Quantum Geometry in Molecular Electronic Structure Theory: Non-adiabatic Effects in Magnetic Fields and Relativistic Frameworks

Zur Erlangung des akademischen Grades eines

DOKTORS DER NATURWISSENSCHAFTEN

(Dr. rer. nat.)

von der KIT-Fakultät für Chemie und Biowissenschaften

des Karlsruher Instituts für Technologie (KIT)

genehmigte

DISSERTATION

von

M.Sc. Dominik Mario Steinmetz

1. Referent: Prof. Dr. Willem Klopper
2. Referent: Prof. Dr. Florian Weigend
Tag der mündlichen Prüfung: 23.07.2026

Für Min

Abstract

The vast majority of electronic structure theory employs the adiabatic Born-Oppenheimer approximation, where the electronic wave function is parametrically dependent on the set of all nuclear coordinates. Such a coupling between a wave function and parameters can be described using the framework of quantum geometry, with the quantum geometric tensor as the central quality, that encompasses properties such as the change in distance or phase of the wave function under displacement of a nuclear coordinate. The spectral representation of the molecular quantum geometric tensor shows that it contains an implicit dependence on all excited states through a sum over non-adiabatic coupling matrix elements. These elements describe the coupling of different electronic states via nuclear motion.

This thesis is concerned with the theoretical framework of quantum geometry applied to molecular electronic structure theory. First, a derivation of the molecular quantum geometric tensor is shown. Afterwards, the Born-Oppenheimer approximation is rigorously applied to systems in external fields. Here, the molecular Berry curvature, the imaginary part of the quantum geometric tensor, is shown to enter the nuclear equations of motion. Additionally, a novel relation of the Berry curvature to the geometry gradient of the pseudomomentum is derived. Within this work, established quantum chemical methods were utilized to compute quantum geometric quantities. Existing linear-response frameworks of Hartree-Fock and current density functional theory are extended to handle the quantum geometric tensor for systems in external magnetic fields and relativistic frameworks. Finally, these implementations were applied to a variety of molecular systems, to demonstrate underlying quantum geometric properties and investigate their influence on experimentally measurable features: Atomic partial charges are calculated based on the molecular Berry curvature in the presence of an external magnetic field. A relation of these charges to another model based on the molecular electric dipole moment is demonstrated. A thorough investigation of the Berry curvature from current density function theory is presented, where a comparison to a full configuration interaction reference is shown. Next, the molecular Berry curvature of relativistic open-shell systems is presented and the implications of time-reversal symmetry for such systems are discussed. Lastly, the effects of spin-orbit coupling on the diagonal Born-Oppenheimer correction are investigated by applying it to various molecular systems.

Zusammenfassung

Der größte Teil aller Elektronenstrukturtheorie verwendet die Born-Oppenheimer Näherung, bei der die elektronische Wellenfunktion parametrisch von der Menge aller Kernkoordinaten abhängt. Diese Kopplung zwischen einer Wellenfunktion und Parametern kann im Rahmen der Quantengeometrie beschrieben werden. In diesem Rahmen ist der Quantengeometrietensor die zentrale Größe, der Eigenschaften wie die Änderung des Abstands oder der Phase der Wellenfunktion bei infinitesimaler Auslenkung einer Kernkoordinate vereint. Die spektrale Darstellung des Quantengeometrietensors zeigt, dass er eine implizite Abhängigkeit von allen angeregten Zuständen, in Form einer Summe über nicht-adiabatische Kopplungsmatrixelemente enthält. Diese Matrixelemente beschreiben die Kopplung verschiedener elektronischer Zustände durch die Kernbewegung.

Diese Arbeit beschäftigt sich mit dem theoretischen Hintergrund der Quantengeometrie angewendet auf Elektronenstrukturtheorie von Molekülen. Zuerst wird die Herleitung des molekularen Quantengeometrietensors gezeigt. Danach wird die Born-Oppenheimer Näherung rigoros auf Systeme in externen Magnetfeldern angewendet. Dabei wird gezeigt, wie die Berry Krümmung, der Imaginärteil des Quantengeometrietensors, in den Bewegungsgleichungen der Atomkerne auftritt. Zusätzlich wird ein neuer Zusammenhang zwischen der Berry Krümmung und der Kernableitung des elektronischen Pseudoimpulses hergeleitet. In dieser Arbeit werden etablierte Methoden der Quantenchemie genutzt, um den Quantengeometrietensor für molekulare Systeme in externen Magnetfeldern oder im Rahmen relativistischer Betrachtungen zu berechnen. Die Implementierung dieser Methoden wird anschließend auf verschiedene Systeme angewendet, um deren zugrunde liegende quantengeometrische Eigenschaften aufzuzeigen und ihren Einfluss auf experimentell messbare Größen zu betrachten: Auf der Berry Krümmung basierende Partialladungen für Moleküle in externen Magnetfeldern werden untersucht. Ein Zusammenhang zwischen diesem Ladungsmodell und einem auf dem elektrischen Dipolmoment basierenden Modell wird erläutert. Eine gründliche Untersuchung der Berry Krümmung im Rahmen der Stromdichte-Dichtefunktionaltheorie wird durchgeführt, wobei ein Vergleich mit Ergebnissen der Full-CI (Configuration Interaction) Methode gezogen wird. Weiterhin wird die molekulare Berry-Krümmung von offenschaligen Systemen in einer relativistischen Betrachtung gezeigt und die Implikation von Zeitumkehrsymmetrie für solche Systeme wird diskutiert. Zuletzt wird der Einfluss von Spin-Bahn-Kopplung auf die diagonale Born-Oppenheimer Korrektur verschiedenster Moleküle untersucht.

Contents

Part I.

Introduction

1. Introduction

The idea that geometry governs the behavior of physical systems is as old as classical mechanics.[1] Still, its implications for quantum mechanics continue to reveal new and surprising physics to this day.[2–4] The application of geometric principles to quantum mechanics has emerged as a relevant and powerful tool in modern physics: The central insight dates back to the seminal work of Michael Berry[2], in which he shows how a wave function that is coupled to a set of external parameters changes upon adiabatic shift within the parameter space.[5] More importantly, the curvature of this space has physical consequences that are measurable.[6–11] Provost and Vallee cast these discoveries into a geometric formulation to analyze the Hilbert space of the manifold of electronic states.[3] The information about this space is contained in the quantum geometric tensor.[2–4,12–21] Its real part is the Fubini-Study metric which measures the distance between quantum states.[15,19,20,22,23] Its imaginary part is the Berry curvature which determines the geometric phase that a state accumulates along a closed path in the parameter space.[2,5,12,13,19,20]

Within the context of crystalline solids, these geometric objects have become well-established tools to describe physical processes. Quantum geometric quantities such as the Berry curvature are at the heart of phenomena like the anomalous Hall effect,[17,24,25] non-linear optical properties of materials,[26–28] and our understanding of topological insulators.[29,30] Recent advances identified the Fubini-Study metric as a key quantity in explaining nontraditional types of superconductivity.[31,32] Similarly, it has been reported to play a central role in the theory of flat band physics.[33,34] While these advances in quantum geometry have shaped our modern understanding of condensed matter, the developments in the context of molecular systems,[18] especially in the framework of *ab initio* quantum chemistry has received comparatively little attention.

The vast majority of modern quantum chemistry lies within the boundaries set by the adiabatic Born-Oppenheimer (BO) approximation. Therein, the molecular wave function is decoupled into a nuclear and an electronic part.[35–38] In this picture, the electronic wave function parametrically depends on the set of all nuclear coordinates, therefore naturally using the language of quantum geometry.[38,39] In this setting, three key quantities arise for molecular systems: non-adiabatic coupling matrix elements (NACMEs), the Fubini-Study metric, and the molecular Berry curvature. NACMEs describe the coupling of electronic motion and nuclear momentum beyond the adiabatic framework.[36,40,41] The Fubini-Study metric provides a measure of the change in the electronic wave function under nuclear displacement and can be related to the leading order correction to the electronic energy within the BO framework, the diagonal Born–Oppenheimer correction (DBOC).[42,43] Finally, the

Berry curvature emerges from geometric effects in the nuclear equations of motion, where it results in an additional force similar in nature to Lorentz forces.[44–48] For systems where the Hamiltonian is invariant under time-reversal, the wave function of the electronic ground state can be chosen to be real-valued, consequently, its derivative with respect to a nuclear coordinate fulfills the same property.[49,50] Under such conditions, the Berry curvature naturally vanishes.[18] Hence, a non-vanishing Berry curvature can only be obtained whenever time-reversal symmetry is broken. A prominent condition where this symmetry is always broken is in the presence of external magnetic fields.[51–53] Here, the Berry curvature plays a vital role in the accurate description of molecular motion.[54–56] Similarly, under certain conditions, relativistic effects have also been shown to result in a non-vanishing molecular Berry curvature.[57–60]

Still, other external parameters that are coupled to the electronic wave function are commonly encountered in quantum chemistry. Molecular properties that depend on external magnetic or electric fields, or on the molecule's angular momentum can also be expressed in the framework of quantum geometry, which becomes important in the context of vibrational circular dichroism spectroscopy, for instance.[18,61,62] An explicit coupling is achieved by using a finite magnetic field approach. Conditions in the astrophysical context render a particularly compelling motivation. Magnetic white dwarfs and some other celestial objects are known to exhibit magnetic fields of up to 10^5 T, where theoretical results are essential to explain experimental observations.[63–66] For field strengths in this regime, the interaction with the external field competes in strength with the intramolecular electromagnetic interactions, which can lead to novel types of bonding mechanisms.[67] Certainly, these strong magnetic fields exceed any perturbational limit and therefore need to be considered explicitly in a quantum chemical calculation. Such finite-field approaches typically employ London atomic orbitals (LAOs) to ensure the gauge invariance of physical observables.[68] So far, significant progress has been achieved in adapting established quantum chemical methods for this applications, including Hartree–Fock (HF), density function theory (DFT), coupled cluster (CC) theory, full configuration interaction (full-CI), and many more.[53,66,69–79] Within such calculations, time-reversal symmetry is explicitly broken by the magnetic fields resulting in generally complex-valued wave functions and consequently giving rise to a non-vanishing molecular Berry curvature.[43,46,80–83]

The application of the aforementioned computational methods has so far only seen a limited application to quantum geometrical quantities of molecules in external magnetic fields or including relativistic spin-orbit coupling: Implementations for the calculation of the Berry curvature in magnetic fields have been reported within the Hartree-Fock framework, both numerically and analytically.[43,47,53] Additionally, an extension of a numerical finite-differences scheme to full-CI calculations has recently been conducted in literature.[81] Crucially, an analytical implementation within the Kohn–Sham current density functional framework,[84–86] offering an advantageous balance between accuracy and computational cost, had not been achieved.

Therefore, the central aim of this thesis is to derive the quantum geometric framework for molecules and demonstrate where it can be applied in molecular

electronic structure theory. Because of its relation to the adiabatic Born-Oppenheimer approximation, molecular quantum geometry is especially useful in beyond-Born-Oppenheimer applications. This work provides the relevant derivations, an efficient implementation in an established quantum chemistry package, and presents several selected applications.

Thus, this thesis makes the quantum geometric framework available in practical quantum chemical calculations for molecular systems. This framework is structurally very similar to the analytical linear-response methods. Consequently, existing Hartree-Fock and KS DFT linear response implementations are a natural starting point. This thesis discusses the different molecular properties that are of interest and how they are related to each other. The majority of this work employs the one-determinant approach from Hartree-Fock and Kohn-Sham DFT, for which the necessary working equations are derived. The implementation of the respective properties has been conducted and is discussed in a dedicated chapter. Lastly, selected applications are shown to demonstrate the calculation of quantum geometric properties for molecular systems. The implementations are publicly available in the TURBOMOLE program suite.[82,83,87,88] Hence, other researchers are encouraged to find broader adoptions of these methods and further drive advances in the field of molecular quantum geometry.

This thesis is structured into three major parts: First, the theoretical background of the thesis is laid out and derivations for molecular quantum geometry are provided. Second, the efficient implementation in TURBOMOLE is presented. Third, selected applications of molecular quantum geometry are shown, including molecules in external magnetic fields and molecules in a relativistic framework.

The following is a short overview of the sections contained in this work. The theoretical framework is presented, starting in section 2. It introduces the general quantum geometry framework. Here, a measure for the quantum distance between different states is discussed in terms of the Fubini-Study metric. Subsequently, the quantum geometric tensor is introduced. Its real part is the aforementioned metric, while its imaginary part is closely related to the Berry curvature.

The quantum geometric tensor depends on an external set of parameters. Section 3 discusses the Born-Oppenheimer approximation, where the nuclear coordinates naturally emerge as external parameters.

Section 4 considers the quantum geometric tensor for the special case of nuclear coordinates as parameters. For complex wave functions, the molecular Berry curvature emerges, which describes the coupling of electronic and nuclear degrees of freedom. It conserves total angular momentum in molecular dynamics simulations and results in Lorentz-like forces acting on nuclei. The molecular Fubini-Study metric is shown to be the central quantity needed for the calculation of the diagonal Born-Oppenheimer correction. Lastly, the geometric vector potential and non-adiabatic coupling matrix elements are discussed, including how they can enter the nuclear Hamiltonian as additional potentials.

Section 5 presents a detailed and rigorous derivation of the nuclear equations of

motion in a semi-classical framework starting from the Born–Oppenheimer approximation. In this section, the previously discussed quantum geometric quantities emerge again: The Berry curvature of a wave function in an external finite magnetic field results in a partial shielding of the bare nuclear charge from the field, effectively counteracting the Lorentz forces. The expression for the diagonal Born–Oppenheimer correction is derived to be a mass-weighted trace over the molecular Fubini-Study metric.

Different intrinsic properties of the molecular Berry curvature are subsequently discussed in section 6, where a connection to the atomic pseudomomentum tensor is derived. This connection reveals a relation to the atomic polar tensor and the geometry derivative of the canonical momentum. Additionally, a relation to the total number of electrons in the system and the external magnetic flux density is established. A special case of the former relation for exact solutions of the Schrödinger equation is additionally provided.

The remaining sections mostly present already established methods of quantum chemistry. The electronic wave function is discussed in section 7 to arrive at the Hartree-Fock equations. Kohn-Sham current density function theory is additionally presented as a one-determinant approach. The electronic Hamiltonian is discussed in section 8. There, the Dirac equation is introduced and manipulated to arrive at a relativistic Hamiltonian within a two-component framework. Additionally, the non-relativistic limit is considered, arriving at the Pauli equation to explicitly treat external magnetic fields.

Section 9 presents the coupled perturbed Hartree-Fock and Kohn-Sham equations within a finite field approach using London atomic orbitals, which need to be solved in order to calculate the derivative of an electronic wave function in one-determinant approaches. For the current density function framework explicit expressions are derived and presented.

Section 10 presents various partial charge models. Berry partial charges are derived based on the Berry curvature in finite magnetic fields. Generalized atomic polar tensor charges, that are based on the geometry derivative of the electric dipole moment, are shown to have a close relation to Berry charges.

The implementation of the quantum geometry framework into the Turbomole program suite is presented in sections 11 to 14. The geometric vector potential is accessible after a ground state calculation, its implementation is discussed in section 11. The implementation of the coupled perturbed Hartree–Fock equations is presented in section 12. The solution vectors of this linear response calculation can subsequently be used to calculate molecular properties. The implementation of these properties is discussed in section 13: The implementation of the molecular Berry curvature, the DBOC, and geometry derivatives of one-electron operators is shown. An implementation to rotate electronically instable wave functions along an instability vector is presented in this section as well. The chapter concludes with an overview of the available functionalities in Turbomole.

In the final part of this work, selected applications of the previously presented methods are shown. External magnetic fields are the focus of sections 15 to 18. The

introductory section 15 presents examples of the molecular Berry curvature for small systems of increasing complexity. Section 16 discusses Berry charges, this partial charge model is applied to molecules with strong ionic character to show certain shortcomings. Afterwards, hetero aromatic systems are investigated, where the planar structure of these molecules results in a direct relation between Berry and generalized atomic polar tensor (GAPT) charges with the electric dipole moment. Additionally, this section demonstrates the basis set convergence of Berry and GAPT charges which both converge to the same limit. Section 17 numerically verifies the general relation between the Berry curvature and the atomic pseudomomentum tensor, and therefore the connection between Berry and GAPT charges. The application of Kohn-Sham current density functional theory is presented in section 18: First, the dissociation of the hydrogen molecule in a magnetic field is investigated, where the DFT Berry curvature is compared to results obtained from full CI. A qualitative disagreement is found for the lowest singlet state, where one-determinant methods show a discontinuity of the Berry curvature at the Coulson-Fischer point of hydrogen. The impact of this discontinuity on MD simulations is estimated. Next, the convergence of the Berry curvature with increasing grids for the numerical integration of the density functional is investigated. Lastly, Berry partial charges from DFT calculations are presented, which offer only small improvements over Hartree–Fock with respect to different metrics.

The last two sections 19 and 20 are concerned with non-adiabatic effects in relativistic frameworks. The relativistic molecular Berry curvature is demonstrated to be dependent on the spin-polarization of different systems in section 19. Here, it is pointed out that the current implementation only features the abelian Berry curvature, which has to be used with care when treating relativistic open-shell molecules. Section 20 presents the diagonal Born–Oppenheimer correction for different small molecules with different electronic structure properties. Non-relativistic, scalar-relativistic, and spin-orbit relativistic frameworks are compared. The dissociation of hydrogen halides reveals that for chemically relevant bond distances, scalar relativistic calculations using effective core potentials offer a great approximation to relativistic approaches that consider spin-orbit coupling. Lastly, a set of closed-shell and open-shell molecules containing light elements is presented. Here, the DBOC of open-shell systems is shown to be significantly influenced by spin-orbit coupling.

Part II.

Theory

This chapter discusses the necessary theory to deal with molecular quantum geometry in the presence of magnetic fields or relativistic effects. The general framework of quantum geometry is introduced first. Here, a measure for the distance between two quantum states is constructed, where the Fubini-Study metric is encountered as the central quantity. Next, the full quantum geometric tensor (QGT) is discussed. While its real part is the aforementioned metric, the QGT is generally complex-valued and Hermitian. The Berry curvature is then identified as the imaginary part of the QGT.

The quantum geometry framework relies on coupling a quantum mechanical wave function to a set of parameters. Introducing the adiabatic Born-Oppenheimer approximation naturally transfers our description of molecular quantum mechanics into the language of quantum geometry. The electronic wave function parametrically depends on the set of all nuclear coordinates. In the resulting manifold, the distance between two states under infinitesimal nuclear displacement provides information on the accuracy of the BO approximation at a given point in the manifold. The curvature of this manifold is found to carry profound physical meaning. In the semi-classical picture of the BO approximation, where the nuclei are plain charged particles, the Berry curvature enters the nuclear equation of motion and results in a Lorentz-like force. The corresponding potential to this force is the geometric vector potential, given its modern formulation by Michael Berry in 1984.[2]

Next, the electronic wave function is discussed and how an approximate solution to the electronic Schrödinger equation can be obtained. This encompasses the introduction of the complex two-component formalism for Hartree-Fock and Kohn-Sham density functional theory (KSDFT). Then, the electronic Hamiltonian is discussed, starting at the relativistic Dirac equation for the free electron. After the extension to many electron systems, two central approximations employed in this work are discussed. First, the relativistic exact two-component (X2C) Hamiltonian in the absence of external magnetic fields. Second, the non-relativistic Hamiltonian for molecules in the presence of external magnetic fields. On this basis, the coupled perturbed Hartree-Fock and Kohn-Sham equations are presented, whose solutions enable the calculation of analytical geometry derivatives of the wave function.

Finally, various types of population analyses are presented, some of which are derived from the quantum geometric framework.

2. The Quantum Geometry Framework

Within quantum mechanics, a system can be described by the Schrödinger equation[89,90]

$$\hat{H}(\boldsymbol{\lambda})|\Psi(\boldsymbol{\lambda})\rangle = E(\boldsymbol{\lambda})|\Psi(\boldsymbol{\lambda})\rangle\,. \tag{2.1}$$

It contains the Hamilton operator $\hat{H}$, the wave function Ψ, and the energy E of the system. These quantities can depend on a set of external parameters $\boldsymbol{\lambda} = \{\lambda_1, \lambda_2, \ldots, \lambda_N\}$, such as external fields, or parameters that describe the structure of the system like crystal lattice parameters or nuclear coordinates. From a geometric point of view, an interesting question is concerned with how much the wave function changes under infinitesimal change of a parameter. A well-behaved metric that measures this property can be thought of as a quantum distance[23] between the original unperturbed state $|\Psi(\boldsymbol{\lambda})\rangle$ and the state after infinitesimal displacement $|\Psi(\boldsymbol{\lambda} + \mathrm{d}\boldsymbol{\lambda})\rangle$. Such a distance can be defined as[3,4,15,23]

$$\mathrm{d}s^2 = 1 - \left|\langle\Psi(\boldsymbol{\lambda})|\Psi(\boldsymbol{\lambda} + \mathrm{d}\boldsymbol{\lambda})\rangle\right|^2. \tag{2.2}$$

Clearly, this distance is bounded $0 \leq \mathrm{d}s^2 \leq 1$, as the overlap of a state with itself is equal to 1, resulting in $\mathrm{d}s^2 = 0$. Similarly, the distance between two orthogonal states will be as large as possible, since they do not overlap, one obtains $\mathrm{d}s^2 = 1$. To evaluate the expression for the quantum distance given in eq. 2.2, the Taylor expansion of the displaced wave function can be considered, yielding[3]

$$\begin{aligned} |\Psi(\boldsymbol{\lambda} + \mathrm{d}\boldsymbol{\lambda})\rangle =& |\Psi(\boldsymbol{\lambda})\rangle + \sum_i |\partial_i \Psi(\boldsymbol{\lambda})\rangle\, \mathrm{d}\lambda_i \\ &+ \frac{1}{2}\sum_{ij} |\partial_i \partial_j \Psi(\boldsymbol{\lambda})\rangle\, \mathrm{d}\lambda_i\, \mathrm{d}\lambda_j + \mathcal{O}(\mathrm{d}\boldsymbol{\lambda}^3)\,, \end{aligned} \tag{2.3}$$

where the short hand notation $\partial_i = \partial/\partial\lambda_i$ was used. Inserting this expansion into the inner product of eq. 2.2 and using the orthonormality of $|\Psi\rangle$ gives

$$\langle\Psi(\boldsymbol{\lambda})|\Psi(\boldsymbol{\lambda} + \mathrm{d}\boldsymbol{\lambda})\rangle = 1 + \sum_i \langle\Psi|\partial_i\Psi\rangle\, \mathrm{d}\lambda_i + \frac{1}{2}\sum_{ij}\langle\Psi|\partial_i\partial_j\Psi\rangle\, \mathrm{d}\lambda_i\, \mathrm{d}\lambda_j + \mathcal{O}(\mathrm{d}\boldsymbol{\lambda}^3)\,, \tag{2.4}$$

where the dependence of the wave function on the set of external parameters was suppressed for the sake of brevity. Evaluating the squared absolute value of this

expression up to second order yields

$$\begin{aligned}\left|\langle\Psi(\boldsymbol{\lambda})|\Psi(\boldsymbol{\lambda}+\mathrm{d}\boldsymbol{\lambda})\rangle\right|^2 =& 1+\sum_i\langle\Psi|\partial_i\Psi\rangle\,\mathrm{d}\lambda_i+\sum_i\langle\partial_i\Psi|\Psi\rangle\,\mathrm{d}\lambda_i\\ &+\frac{1}{2}\sum_{ij}\langle\Psi|\partial_i\partial_j\Psi\rangle\,\mathrm{d}\lambda_i\,\mathrm{d}\lambda_j+\frac{1}{2}\sum_{ij}\langle\partial_i\partial_j\Psi|\Psi\rangle\,\mathrm{d}\lambda_i\,\mathrm{d}\lambda_j\\ &+\sum_{ij}\langle\partial_i\Psi|\Psi\rangle\langle\Psi|\partial_j\Psi\rangle\,\mathrm{d}\lambda_i\,\mathrm{d}\lambda_j+\mathcal{O}(\mathrm{d}\boldsymbol{\lambda}^3)\,.\end{aligned} \tag{2.5}$$

To further simplify this expression, some properties and relations of the quantities of the previous expression are useful. First, taking the derivative of the orthonormality condition, which applies for all choices of the external parameters, gives

$$\begin{aligned}&\langle\Psi|\Psi\rangle=1\\ \Leftrightarrow\quad&\partial_i\langle\Psi|\Psi\rangle=0\\ \Leftrightarrow\quad&\langle\partial_i\Psi|\Psi\rangle+\langle\Psi|\partial_i\Psi\rangle=0\\ \Leftrightarrow\quad&\Re\langle\Psi|\partial_i\Psi\rangle=0\,,\end{aligned} \tag{2.6}$$

meaning that the overlap $\langle\Psi|\partial_i\Psi\rangle$ must be purely imaginary or zero. This identity shows that the sum of all first order contributions in eq. 2.5 vanishes. Next, a similar consideration can be made for the second derivative of the orthonormality condition to arrive at

$$\begin{aligned}&\partial_i\partial_j\langle\Psi|\Psi\rangle=0\\ \Leftrightarrow\quad&\langle\partial_i\partial_j\Psi|\Psi\rangle+\langle\partial_i\Psi|\partial_j\Psi\rangle+\langle\partial_j\Psi|\partial_i\Psi\rangle+\langle\Psi|\partial_i\partial_j\Psi\rangle=0\\ \Leftrightarrow\quad&2\Re\langle\Psi|\partial_i\partial_j\Psi\rangle+2\Re\langle\partial_i\Psi|\partial_j\Psi\rangle=0\\ \Leftrightarrow\quad&\Re\langle\Psi|\partial_i\partial_j\Psi\rangle=-\Re\langle\partial_i\Psi|\partial_j\Psi\rangle\end{aligned} \tag{2.7}$$

Now, the squared absolute value in eq. 2.5 simplifies to

$$\begin{aligned}\left|\langle\Psi(\boldsymbol{\lambda})|\Psi(\boldsymbol{\lambda}+\mathrm{d}\boldsymbol{\lambda})\rangle\right|^2 =& 1+\sum_{ij}\langle\partial_i\Psi|\Psi\rangle\langle\Psi|\partial_j\Psi\rangle\,\mathrm{d}\lambda_i\,\mathrm{d}\lambda_j\\ &-\sum_{ij}\Re\langle\partial_i\Psi|\partial_j\Psi\rangle\,\mathrm{d}\lambda_i\,\mathrm{d}\lambda_j+\mathcal{O}(\mathrm{d}\boldsymbol{\lambda}^3)\,.\end{aligned} \tag{2.8}$$

Notably, the second term in this expression must always be real-valued, since eq. 2.6 shows that the individual overlaps are purely imaginary. This way the final expression for the quantum distance is obtained by inserting into eq. 2.2 and keeping only the leading order terms:

$$\mathrm{d}s^2=\sum_{ij}\Re\Big(\langle\partial_i\Psi|\partial_j\Psi\rangle-\langle\partial_i\Psi|\Psi\rangle\langle\Psi|\partial_j\Psi\rangle\Big)\,\mathrm{d}\lambda_i\,\mathrm{d}\lambda_j\,. \tag{2.9}$$

One important conceptual property that a quantum distance should fulfill is that the distance between two wave functions that only differ in a global phase factor

should vanish.[3] This is because these wave functions describe the same physical state, as they result in identical physical observables. This property can be tested by considering such a wave function

$$|\tilde{\Psi}\rangle = e^{\mathrm{i}\phi}|\Psi\rangle\,, \tag{2.10}$$

where ϕ is real-valued. From the original definition of the quantum distance in eq. 2.2 it becomes apparent that this requirement is indeed met:

$$\begin{aligned} \mathrm{d}s^2 &= 1 - \left|\langle\Psi|\tilde{\Psi}\rangle\right|^2 \\ &= 1 - \left|e^{\mathrm{i}\phi}\langle\Psi|\Psi\rangle\right|^2 \\ &= 0 \end{aligned} \tag{2.11}$$

In the system's Hilbert space, these two wave functions $|\Psi\rangle$ and $|\tilde{\Psi}\rangle$ are parallel to each other. This implies that the quantum distance between two states should not depend on any parallel contributions they have in common. This can be shown by decomposing the wave function into two orthogonal components, one that is parallel to the reference state and the other that is perpendicular to that state

$$|\partial_i\Psi(\boldsymbol{\lambda})\rangle = |\partial_i\Psi(\boldsymbol{\lambda})\rangle^{\parallel\Psi} + |\partial_i\Psi(\boldsymbol{\lambda})\rangle^{\perp\Psi}\,. \tag{2.12}$$

Now, the quantum distance can be computed, where one of the wave functions carries a global phase like shown in eq. 2.10. The derivative of such a function is given by

$$|\partial_i\tilde{\Psi}\rangle = e^{\mathrm{i}\phi}\Big(|\partial_i\Psi\rangle + \mathrm{i}(\partial_i\phi)|\Psi\rangle\Big)\,. \tag{2.13}$$

The second contribution in this expression is parallel to the original state and should therefore not contribute, while the first one simply recovers the derivative of the original wave function:

$$|\partial_i\tilde{\Psi}\rangle^{\perp\Psi} = e^{\mathrm{i}\phi}|\partial_i\Psi\rangle\,, \tag{2.14}$$

$$|\partial_i\tilde{\Psi}\rangle^{\parallel\Psi} = \mathrm{i}(\partial_i\phi)e^{i\phi}|\Psi\rangle\,. \tag{2.15}$$

The perpendicular component can be extracted using the projection operator[11,16]

$$\hat{\mathcal{P}} = 1 - |\Psi\rangle\langle\Psi|\,, \tag{2.16}$$

since

$$\begin{aligned} \hat{\mathcal{P}}|\partial_i\Psi\rangle &= (1 - |\Psi\rangle\langle\Psi|)\left(|\partial_i\Psi\rangle^{\parallel\Psi} + |\partial_i\Psi\rangle^{\perp\Psi}\right) \\ &= |\partial_i\Psi\rangle^{\parallel\Psi} + |\partial_i\Psi\rangle^{\perp\Psi} - |\Psi\rangle\langle\Psi|\partial_i\Psi\rangle^{\parallel\Psi} - |\Psi\rangle\langle\Psi|\partial_i\Psi\rangle^{\perp\Psi} \\ &= |\partial_i\Psi\rangle^{\parallel\Psi} + |\partial_i\Psi\rangle^{\perp\Psi} - |\Psi\rangle\langle\Psi|\partial_i\Psi\rangle^{\parallel\Psi} - 0 \\ &= |\partial_i\Psi\rangle^{\parallel\Psi} + |\partial_i\Psi\rangle^{\perp\Psi} - |\partial_i\Psi\rangle^{\parallel\Psi} \\ &= |\partial_i\Psi\rangle^{\perp\Psi}\,. \end{aligned} \tag{2.17}$$

Evidently, this operator that projects on only the orthogonal contribution to $|\Psi\rangle$ can be identified in the previous definition of the quantum distance in eq. 2.9. This way, one finds[11,12,15,16,23]

$$\mathrm{d}s^2 = \sum_{ij} g_{ij}\,\mathrm{d}\lambda_i\,\mathrm{d}\lambda_j\,, \tag{2.18}$$

with the Fubini–Study metric[11,12,15]

$$g_{ij} = \Re\langle\partial_i\Psi|\hat{\mathcal{P}}|\partial_j\Psi\rangle\,. \tag{2.19}$$

2.1. The Quantum Geometric Tensor

The quantum geometric tensor is defined as[11,16,30,91]

$$Q_{ij} = \langle\partial_i\Psi|\hat{\mathcal{P}}|\partial_j\Psi\rangle\,. \tag{2.20}$$

The previous section derived a measure for a quantum distance and showed how the Fubini-Study metric, which is the real part of the QGT, provides this information.[11] Consequently, the QGT can be used to examine the change in the wave function under displacement of an external parameter. Since the wave function is generally complex valued, the QGT usually holds a non-vanishing imaginary part. Hence, it is common to decompose the QGT into its real and imaginary part:[12,91]

$$Q_{ij} = g_{ij} - \frac{\mathrm{i}}{2}\Omega_{ij}\,. \tag{2.21}$$

The Fubini–Study metric g_{ij} was already discussed in detail in the previous section and describes a distance between states.[11,15,23,91] Similarly, the imaginary part of the QGT is proportional the Berry curvature Ω_{ij}, which provides information about the change in the non-trivial phase induced by adiabatic displacement of the parameters.[12,13,91]

2.1.1. The Spectral Representation of the QGT

From its definition in eq. 2.20, it may appear as if the QGT is only dependent on one state (such as the ground state). By transforming the QGT into its spectral representation, another form can be obtained, from which it is apparent that all quantum mechanical states contribute. Assuming a non-degenerate orthonormal basis for the Hamiltonian, results in the following condition for its eigenvectors:

$$\langle m|n\rangle = \delta_{mn}\,. \tag{2.22}$$

This allows the construction of the projection operator according to

$$\hat{\mathcal{P}} = 1 - |n\rangle\langle n| = \sum_{m\neq n} |m\rangle\langle m|\,. \tag{2.23}$$

This expression can be used to recast the definition of the QGT given in eq. 2.20 to arrive at an expression for an arbitrary state $|n\rangle$ as

$$Q_{ij}^{n} = \sum_{m \neq n} \langle \partial_i n | m \rangle \langle m | \partial_j n \rangle \,. \tag{2.24}$$

In the orthonormal basis, the Schrödinger equation can be written as

$$\hat{H}|n\rangle = E_n |n\rangle \,. \tag{2.25}$$

Taking its derivative with respect to an external parameter gives

$$(\partial_i \hat{H})|n\rangle + \hat{H}|\partial_i n\rangle = (\partial_i E_n)|n\rangle + E_n |\partial_i n\rangle \,. \tag{2.26}$$

Using the orthonormality condition from eq. 2.22 and projecting onto another state $|m\rangle$ results in

$$\langle m|\partial_i \hat{H}|n\rangle + \langle m|\hat{H}|\partial_i n\rangle = (\partial_i E_n)\langle m|n\rangle + E_n \langle m|\partial_i n\rangle \tag{2.27}$$

$$\Leftrightarrow \quad \langle m|\partial_i \hat{H}|n\rangle + E_m \langle m|\partial_i n\rangle = E_n \langle m|\partial_i n\rangle \tag{2.28}$$

$$\Leftrightarrow \qquad \langle m|\partial_i n\rangle = \frac{\langle m|\partial_i \hat{H}|n\rangle}{E_n - E_m} \qquad m \neq n \,. \tag{2.29}$$

Using the identity from eq. 2.29 in the series expansion of the QGT tensor given in eq. 2.24 finally yields its spectral decomposition[11,91]

$$Q_{ij}^{n} = \sum_{m \neq n} \frac{\langle n|\partial_i \hat{H}|m\rangle \langle m|\partial_j \hat{H}|n\rangle}{(E_n - E_m)^2} \,. \tag{2.30}$$

Whether eq. 2.24 or eq. 2.30 is easier to evaluate depends on which derivative is easier to compute.[91] If the Hamiltonian's dependence on the parameter is simple, eq. 2.30 usually takes a manageable form. Otherwise, eq.2.24 can be employed, where the derivative of the wave function is needed.[91]

3. Born-Oppenheimer Approximation

The previous section established the framework of quantum geometry; here a system depends on an external set of parameters. To apply this framework to the electronic structure theory of molecules, the Born-Oppenheimer approximation needs to be introduced. It is one of the most central approximations in quantum chemistry and responsible for making quantum mechanics practicably applicable to molecular systems. The BO approximation also naturally transfers electronic structure theory into the quantum geometry framework, as the electronic wave function parametrically depends on the set of all nuclear coordinates.

3.1. Notation

Throughout this thesis, Hartree atomic units are used, unless stated otherwise. This set of units is defined by setting several common constants equal to one to obtain simpler and more readable equations. Concretely, Hartree atomic units define

$$e = m_e = \hbar = 4\pi\varepsilon_0 = 1\,, \tag{3.1}$$

which are the unit of charge from the elementary charge e, the unit of mass from the mass of an electron m_e, the unit of action from Planck's reduced constant $\hbar$, and Coulomb's constant.[92,93]

Indices for the N_{nuc} nuclei in the molecule are I, J, with their respective coordinates $\mathbf{R}_I, \mathbf{R}_J$, charges Z_I, Z_J, and masses M_I, M_J. Similarly, the indices i, j refer to the N_{el} electrons with coordinates $\mathbf{r}_i, \mathbf{r}_j$. The set of all nuclear coordinates of the system is denoted as $\mathbf{R} = \{\mathbf{R}_1, \mathbf{R}_2, \ldots, \mathbf{R}_{N_{\text{nuc}}}\}$, analogously, the set of all electronic coordinates is $\mathbf{r}$.

3.2. The Molecular Schrödinger Equation

The molecular Schrödinger equation reads[89,90]

$$\mathrm{i}\frac{\partial}{\partial t}\Psi_{\text{mol}} = \hat{H}_{\text{mol}}\Psi_{\text{mol}}\,, \tag{3.2}$$

with the molecular Hamiltonian

$$\hat{H}_{\text{mol}} = \hat{T}_{\text{nuc}} + \hat{T}_{\text{el}} + \hat{V}_{\text{nuc-nuc}} + \hat{V}_{\text{nuc-el}} + \hat{V}_{\text{el-el}}\,. \tag{3.3}$$

It contains the kinetic energy operator of the nuclei, the kinetic energy operator of the electrons, the three Coulomb operators for the interaction between different

nuclei, between the nuclei and electrons, and between the different electrons. The molecular wave function depends on the time coordinate t, the set of all nuclear coordinates $\mathbf{R}$, and the set of all electronic coordinates $\mathbf{r}$

$$\Psi_{\mathrm{mol}}(t, \mathbf{R}, \mathbf{r})\,. \tag{3.4}$$

3.3. Separation of the Molecular Wave Function

The molecular wave function can be approximated as a product of a nuclear and an electronic wave function according to[35,36,38,94]

$$\Psi_{\mathrm{mol}}(t, \mathbf{R}, \mathbf{r}) \approx \Psi_{\mathrm{nuc}}(t, \mathbf{R}) \cdot \Psi_{\mathrm{el}}(\mathbf{r}; \mathbf{R})\,, \tag{3.5}$$

which is known as the Born-Huang ansatz. Here, the nuclear wave function depends on the set of all nuclear coordinates and the time coordinate, whereas the electronic wave function is only explicitly dependent on all electronic coordinates and parametrically dependent on the nuclear coordinates. Note that in the presence of an external magnetic field the center-of-mass motion does not separate in the field-free manner, so that the electronic Hamiltonian does not depend parametrically on the nuclear positions alone.[44,95–98] The Born-Huang ansatz is often justified to be a valid approximation because the nuclei move on a much larger time scale compared to the electrons.[38,99] Therefore, the nuclei experience a near instantaneous response of the electrons when the nuclear geometry changes.

3.4. The Adiabatic Approximation

The previous section established the Born-Huang ansatz for the molecular wave function. Now, the application of the individual operators contained in the molecular Hamiltonian of eq. 3.3 on the wave function needs to be investigated. The different operators are given as:

$$\hat{T}_{\mathrm{nuc}} = \sum_I \frac{1}{2M_I} \hat{\mathbf{P}}_I^2 \tag{3.6}$$

$$\hat{T}_{\mathrm{el}} = \sum_i \frac{1}{2} \hat{\mathbf{p}}_i^2 \tag{3.7}$$

$$\hat{V}_{\text{nuc-nuc}} = \sum_{IJ} \frac{Z_I Z_J}{|\mathbf{R}_I - \mathbf{R}_J|} \tag{3.8}$$

$$\hat{V}_{\text{nuc-el}} = -\sum_{Ii} \frac{Z_I}{|\mathbf{R}_I - \mathbf{r}_i|} \tag{3.9}$$

$$\hat{V}_{\text{el-el}} = \sum_{ij} \frac{1}{|\mathbf{r}_i - \mathbf{r}_j|} \tag{3.10}$$

Here, the canonical momentum operator for the nuclei and electrons are

$$\hat{\mathbf{P}}_I = -\mathrm{i}\boldsymbol{\partial}_I \,, \tag{3.11}$$

$$\hat{\mathbf{p}}_i = -\mathrm{i}\boldsymbol{\partial}_i \,. \tag{3.12}$$

Note that these expressions assume that no external fields are present, the more general case, including magnetic fields, is discussed in greater detail in section 5, where the nuclear equations of motion are derived. Assuming that an orthonormal basis of electronic wave functions $|p\rangle$, $|q\rangle$ with $\langle p|q\rangle = \delta_{pq}$ has been found, all operators in the molecular Hamiltonian from equations 3.6 - 3.10 are diagonal with the exception of the nuclear kinetic energy operator:

$$\langle p|\hat{T}_{\mathrm{nuc}}|q\rangle \neq T_{pq}\delta_{pq} \tag{3.13}$$

This means that all electronic states are still coupled via this operator, rendering an exact solution unfeasible. The Born-Huang approximation simply neglects all off-diagonal elements of this operator[36,100,101]

$$\langle p|\hat{T}_{\mathrm{nuc}}|q\rangle \approx T_{pq}\delta_{pq} \,. \tag{3.14}$$

This way, the molecular Hamiltonian is cast into a diagonal form but an implicit dependence on all electronic states remains. This becomes apparent when evaluating a diagonal element of the nuclear kinetic energy operator:

$$\langle p|\hat{T}_{\mathrm{nuc}}|p\rangle = -\sum_I \frac{1}{2M_I}\langle p|\partial_I^2 p\rangle \,. \tag{3.15}$$

The respective matrix element contains the operator ∂_I^2 which is not Hermitian with respect to the Hilbert space of the electronic degrees of freedom. Hence, the nuclear kinetic energy in the Born-Huang approximation is generally complex. The considerations from eq. 2.7 showed the relation of such matrix elements to a similar integral:

$$\Re\langle p|\partial_I^2 p\rangle = -\Re\langle \boldsymbol{\partial}_I p|\boldsymbol{\partial}_I p\rangle = -\langle \boldsymbol{\partial}_I p|\boldsymbol{\partial}_I p\rangle \,. \tag{3.16}$$

This expression is surprisingly similar to the diagonal elements of the Fubini–Study metric

$$g_{II} = \Re\langle \boldsymbol{\partial}_I p|\boldsymbol{\partial}_I p\rangle - \langle \boldsymbol{\partial}_I p|p\rangle\langle p|\boldsymbol{\partial}_I p\rangle \,, \tag{3.17}$$

it is only missing the projection. The spectral decomposition of such quantities was already provided in eq. 2.30 and clearly demonstrates that all states are implicitly contained, even in the diagonal element $\langle p|\hat{T}_{\mathrm{nuc}}|p\rangle$. Therefore, to obtain a truly adiabatic approximation, the diagonal elements have to be neglected

$$\langle p|\hat{T}_{\mathrm{nuc}}|p\rangle \approx 0 \,. \tag{3.18}$$

This is often called the adiabatic Born-Oppenheimer approximation.[35,36,38] It might seem like the expression in eq. 3.15 is still a valid choice to obtain a first order

correction to the electronic energy.[94] When the Fubini-Study metric was previously discussed in section 2, it was determined that the projection onto all orthogonal states is needed so the metric is gauge-invariant.[15,23] Consequently, if such an energy correction is to be calculated, the mass weighted trace of the Fubini-Study metric should be used instead. From this consideration, the general form of the diagonal Born-Oppenheimer correction can already be predicted, and is derived rigorously in section 5. For now the DBOC reads

$$E^{\mathrm{DBOC}} = \sum_I \frac{g_{II}}{2M_I} \,. \tag{3.19}$$

It is worth noting that these two expressions are equivalent to each other for wave functions that can be chosen to be purely real-valued for all nuclear geometries. Intuitively, this makes sense as the global phase of the wave function is essentially fixed in this case. Still, it is straightforward to see from eq. 3.17 as well. In the discussion of the QGT, eq. 2.6 showed that the overlap $\langle p|\partial_I p\rangle$ has a vanishing real-part and is therefore either zero or purely imaginary. If the wave function is always real, its derivative must also be real valued. Consequently, these overlaps are zero and the diagonal elements of the Fubini–Study metric simplifies to

$$g_{II} = \langle \partial_I p|\partial_I p\rangle \qquad \text{if} \quad |p\rangle \in \mathbb{R} \quad \forall\, \mathbf{R} \,. \tag{3.20}$$

In summary, the adiabatic Born-Oppenheimer approximation employs a product ansatz for the molecular wave function and neglects the coupling between any electronic states by neglecting the corresponding matrix elements of the nuclear kinetic energy operator. This way, an electronic Schrödinger equation

$$\hat{H}\Psi_{\mathrm{el}} = E_{\mathrm{el}}\Psi_{\mathrm{el}} \,, \tag{3.21}$$

can be obtained. The following chapters are mostly concerned with electronic structure, and thus the electronic wave function is simply denoted as Ψ in most subsequent chapters.

4. Nuclear Coordinates as the Parameter Space

In this section, the concept of quantum geometry is used with nuclear coordinates as parameters for the electronic wave function. This choice deserves notable attention, as the nuclear degree of freedom is the most fundamental parameter space employed in the vast majority of quantum chemical calculations. Since the Born-Oppenheimer approximation introduces this choice, any theoretical framework that makes use of it falls into this category.

4.1. The Molecular Berry Curvature

Many molecular properties are closely related to the QGT with respect to nuclear coordinates $Q_{I\alpha J\beta}$, where $\alpha, \beta \in \{x, y, z\}$. Starting with the molecular Berry curvature

$$\Omega_{I\alpha J\beta} = -2\Im \langle \partial_{I\alpha}\Psi | \partial_{J\beta}\Psi \rangle \ , \tag{4.1}$$

which is a quantity that occurs not only in the context of geometrical phases but is also of relevance for nuclear equation of motion in semi-classical molecular dynamics simulations.[2,47,48,80,102,103] Here, the Berry curvature is needed to conserve the total angular momentum by capturing the coupling of electronic and nuclear degrees of freedom.[104] This connection is further explored in section 5. Afterwards, in section 6, several important properties of the molecular Berry curvature are discussed, where its connection to other molecular expectation values is derived.

4.2. The Molecular Fubini-Study Metric

The real part of the QGT, the Fubini-Study metric,

$$g_{I\alpha J\beta} = \Re\Big(\langle \partial_{I\alpha}\Psi | \partial_{J\beta}\Psi \rangle - \langle \partial_{I\alpha}\Psi | \Psi \rangle \langle \Psi | \partial_{J\beta}\Psi \rangle \Big) , \tag{4.2}$$

has a noteworthy connection to the diagonal Born-Oppenheimer correction. This connection was already mentioned in section 3 and is derived later, in section 5. The DBOC is essentially the first-order correction term to the electronic energy in the BO approximation that can be calculated without the nuclear wave function.[36,94] In the absence of external fields, the DBOC is simply the expectation value of the nuclear kinetic energy operator over the electronic wavefunction. A more general

expression for the DBOC,[43] which is derived in section 5, is related to the trace of the Fubini-Study metric:

$$E_{\mathrm{DBOC}} = \sum_I \frac{1}{2M_I} \sum_\alpha g_{I\alpha I\alpha} \,. \tag{4.3}$$

4.3. The Geometric Vector Potential

So far, integrals of the type

$$\langle \Psi_n | \partial_{I\alpha} \Psi_0 \rangle \tag{4.4}$$

have been encountered, for instance in the definition of the Fubini-Study metric in eq. 4.2. There, the overlap of the ground state wave function and its nuclear derivative was used. This quantity emerges in another context as well: It enters the nuclear Hamiltonian as an additional potential that resembles a vector potential.[47,49,50] The exact details of this occurrence is discussed in section 5.3, but also briefly introduced here. The quantity in question is often written down in a slightly modified way as

$$\chi_{I\alpha} = \langle \Psi_0 | \hat{P}_{I\alpha} | \Psi_0 \rangle = -\mathrm{i} \langle \Psi_0 | \partial_{I\alpha} \Psi_0 \rangle \,, \tag{4.5}$$

and has different names found in literature like the geometric vector potential, or Berry connection.[2,5,50] It is a real-valued quantity which is a consequence of the orthonormality of the wave function as previously noted in the discussion of the QGT in section 2. Another important consequence that follows is that in all cases where the electronic wave function can be chosen to be real-valued at all geometries, the geometric vector potential must vanish, since both ψ and $\partial_{I\alpha}\psi$ are real.

4.4. Non-Adiabatic Coupling Matrix Elements

The other kind of integral as shown in eq. 4.4 occurred in the sum over states expression for the QGT in eq. 2.30. Here, the overlap of an excited state wave function and the nuclear derivative of the ground state wavefunction needs to be evaluated. These matrix elements are commonly referred to as first order non-adiabatic coupling matrix elements and are defined as

$$d^{0n}_{I\alpha} = \langle \Psi_n | \partial_{I\alpha} \Psi_0 \rangle \,. \tag{4.6}$$

NACMEs are well-known in the literature[35,41,49,81,105,106] and required for non-adiabatic dynamics simulations among other applications.[61,107–112]

5. Nuclear Equation of Motion

This section establishes the nuclear equation of motion in a semi-classical framework for molecules in an external magnetic field. The derivations shown in this section mostly follow those presented in Ref. [47] and [48]. Here, the inclusion of external fields is considered as well. In this way, the effects of the BO approximation that were already introduced in section 3 are cleanly applied and the respective quantities like the DBOC are derived rigorously.

5.1. Minimal coupling

External magnetic fields can be considered within quantum mechanics from the principle of minimal coupling.[113] The expression of the kinetic energy operator is modified by replacing the canonical momentum operator with the kinetic momentum operator

$$\hat{\boldsymbol{\pi}} = \hat{\mathbf{p}} + \mathbf{A}\,, \tag{5.1}$$

containing the magnetic vector potential $\mathbf{A}$, often simply called the vector potential. It is defined such that its curl gives the magnetic flux density:

$$\mathcal{B} = \boldsymbol{\nabla} \times \mathbf{A}\,. \tag{5.2}$$

The following sections will default to the use of the kinetic momentum operator to explicitly consider external magnetic fields. The field-free case is trivially obtained by setting the external vector potential equal to zero at all points in space.

5.2. Effective Nuclear Hamiltonian and Equations of Motion

To set up an effective nuclear Hamiltonian, a convenient starting point is the full molecular Hamiltonian. After decoupling the electronic and nuclear degrees of freedom, several contributions arise, which can mostly be distinguished as being either an electronic or a nuclear contribution. The total molecular Hamiltonian

$$\hat{H}_{\mathrm{mol}} = \hat{T}_{\mathrm{nuc}} + \hat{V}_{\mathrm{nuc}} + \hat{H}_{\mathrm{el}}\,, \tag{5.3}$$

contains the nuclear kinetic energy operator

$$\hat{T}_{\mathrm{nuc}} = \sum_I \frac{\hat{\boldsymbol{\Pi}}_I^2}{2M_I}\,, \tag{5.4}$$

where the physical nuclear momentum operator is constructed using minimal coupling from the canonical nuclear momentum operator $\hat{\mathbf{P}}_I = -\mathrm{i}\boldsymbol{\nabla}_I$ as

$$\hat{\mathbf{\Pi}}_I = \hat{\mathbf{P}}_I - Z_I \mathbf{A}(\mathbf{R}_I)\,. \tag{5.5}$$

As a reminder, the non-relativistic electronic Hamilton operator is given as

$$\hat{H}_{\mathrm{el}} = \frac{1}{2}\sum_i \hat{\boldsymbol{\pi}}_i^2 - \sum_{iI}\frac{Z_I}{|\mathbf{r}_i - \mathbf{R}_I|} + \sum_{i<j}\frac{1}{|\mathbf{r}_i - \mathbf{r}_j|}\,. \tag{5.6}$$

Now, the Born-Oppenheimer ansatz can be inserted into the molecular Schrödinger equation. This means, that the molecular wave function is taken as a product of two parts: First, the nuclear wave function Ψ^{nuc}, which is explicitly dependent on all nuclear coordinates and the time coordinate. Second, the electronic wave function Ψ^{el}, which is explicitly dependent on all electronic coordinates and parametrically dependent on the nuclear coordinates through the electron-nucleus Coulomb interaction. Then, the molecular wave function can be written as

$$\Psi^{\mathrm{mol}}(\mathbf{R}, \mathbf{r}, t) = \Psi^{\mathrm{nuc}}(\mathbf{R}, t) \cdot \Psi^{\mathrm{el}}(\mathbf{r}; \mathbf{R})\,. \tag{5.7}$$

The goal is to obtain an effective nuclear Hamiltonian by projecting onto the electronic wave function[47]

$$\hat{H}_{\mathrm{eff}}|\Psi^{\mathrm{nuc}}\rangle = \langle\Psi^{\mathrm{el}}|\hat{H}_{\mathrm{mol}}|\Psi^{\mathrm{nuc}}\Psi^{\mathrm{el}}\rangle = \langle\Psi^{\mathrm{el}}|\hat{T}_{\mathrm{nuc}} + \hat{V}_{\mathrm{nuc}} + \hat{H}_{\mathrm{el}}|\Psi^{\mathrm{nuc}}\Psi^{\mathrm{el}}\rangle\,. \tag{5.8}$$

Evaluating the last expression in eq. 5.8 produces several contributions that are of special interest for this work, as they describe the coupling between the electronic and nuclear degrees of freedom.

5.3. Geometric Vector Potential and Scalar Potential

After projecting the molecular Schrödinger equation within the Born-Oppenheimer approximation onto the electronic wave function, different non-adiabatic contributions arise from the nuclear kinetic energy operator. One obtains[47]

$$\begin{aligned}
&\langle\Psi^{\mathrm{el}}|\hat{\mathbf{\Pi}}_I^2|\Psi^{\mathrm{nuc}}\Psi^{\mathrm{el}}\rangle \\
=&\langle\Psi^{\mathrm{el}}|\left(\hat{\mathbf{P}}_I - Z_I\mathbf{A}(\mathbf{R}_I)\right)^2|\Psi^{\mathrm{nuc}}\Psi^{\mathrm{el}}\rangle \\
=&\langle\Psi^{\mathrm{el}}|\Psi^{\mathrm{el}}\hat{\mathbf{P}}_I^2\Psi^{\mathrm{nuc}}\rangle + 2\langle\Psi^{\mathrm{el}}|\hat{\mathbf{P}}_I\Psi^{\mathrm{nuc}}\hat{\mathbf{P}}_I\Psi^{\mathrm{el}}\rangle + \langle\Psi^{\mathrm{el}}|\Psi^{\mathrm{nuc}}\hat{\mathbf{P}}_I^2\Psi^{\mathrm{el}}\rangle \\
&- \langle\Psi^{\mathrm{el}}|Z_I(\hat{\mathbf{P}}_I\mathbf{A}(\mathbf{R}_I))|\Psi^{\mathrm{nuc}}\Psi^{\mathrm{el}}\rangle - 2\langle\Psi^{\mathrm{el}}|Z_I\mathbf{A}(\mathbf{R_I})|\Psi^{\mathrm{el}}\hat{\mathbf{P}}_I\Psi^{\mathrm{nuc}}\rangle \\
&- 2\langle\Psi^{\mathrm{el}}|Z_I\mathbf{A}(\mathbf{R}_I)|\Psi^{\mathrm{nuc}}\hat{\mathbf{P}}_I\Psi^{\mathrm{el}}\rangle + \langle\Psi^{\mathrm{el}}|Z_I^2\mathbf{A}^2(\mathbf{R}_I)|\Psi^{\mathrm{nuc}}\Psi^{\mathrm{el}}\rangle \\
=&\left[(\hat{\mathbf{P}}_I - Z_I\mathbf{A}(\mathbf{R}_I))^2 + 2\langle\Psi^{\mathrm{el}}|\hat{\mathbf{P}}_I\Psi^{\mathrm{el}}\rangle(\hat{\mathbf{P}}_I - Z_I\mathbf{A}(\mathbf{R}_I)) + \langle\Psi^{\mathrm{el}}|\hat{\mathbf{P}}_I^2\Psi^{\mathrm{el}}\rangle\right]|\Psi^{\mathrm{nuc}}\rangle
\end{aligned} \tag{5.9}$$

Using the definition of the geometric vector potential,

$$\boldsymbol{\chi}_I = \langle\Psi^{\mathrm{el}}|\hat{\mathbf{P}}_I|\Psi^{\mathrm{el}}\rangle\,, \tag{5.10}$$

and introducing the scalar potential

$$\Lambda_I = \langle \Psi^{\mathrm{el}} | \hat{\mathbf{P}}_I^2 | \Psi^{\mathrm{el}} \rangle \,, \tag{5.11}$$

the previous expression can be written in a much simpler form as

$$\langle \Psi^{\mathrm{el}} | \hat{\mathbf{\Pi}}_I^2 | \Psi^{\mathrm{nuc}} \Psi^{\mathrm{el}} \rangle = \left[\hat{\mathbf{\Pi}}_I^2 + 2 \boldsymbol{\chi}_I \hat{\mathbf{\Pi}}_I + \Lambda_I \right] | \Psi^{\mathrm{nuc}} \rangle \,. \tag{5.12}$$

The geometric vector potential $\boldsymbol{\chi}_I$ is, as its name suggests, a $3 \times N_{\mathrm{nuc}}$ tensor that contains a 3-vector for each nucleus in the molecule. It is similar to the magnetic vector potential in some regards, which are further explored in section 6. Note that application of the canonical nuclear momentum operator on the component of the geometric vector potential corresponding to the same nucleus results in

$$\begin{aligned} \hat{\mathbf{P}}_I \boldsymbol{\chi}_I &= -\langle \hat{\mathbf{P}}_I \Psi^{\mathrm{el}} | \hat{\mathbf{P}}_I \Psi^{\mathrm{el}} \rangle + \langle \Psi^{\mathrm{el}} | \hat{\mathbf{P}}_I^2 \Psi^{\mathrm{el}} \rangle \\ &= -\langle \hat{\mathbf{P}}_I \Psi^{\mathrm{el}} | \hat{\mathbf{P}}_I \Psi^{\mathrm{el}} \rangle + \Lambda_I \,. \end{aligned} \tag{5.13}$$

Introducing the real-valued expression

$$\Delta_I = \langle \hat{\mathbf{P}}_I \Psi^{\mathrm{el}} | \hat{\mathbf{P}}_I \Psi^{\mathrm{el}} \rangle = \Delta_I^* \,, \tag{5.14}$$

it follows that the scalar potential can be written as

$$\Lambda_I = \Delta_I + \hat{\mathbf{P}}_I \boldsymbol{\chi}_I \,. \tag{5.15}$$

Finally, by defining the geometric scalar potential as

$$\overline{\Delta}_I = \Delta_I - \boldsymbol{\chi}_I^2 \,, \tag{5.16}$$

a concise expression for an effective nuclear momentum operator can be formulated as

$$\begin{aligned} \hat{\overline{\mathbf{\Pi}}}_I &= \hat{\mathbf{\Pi}}_I + \boldsymbol{\chi}_I \\ &= \hat{\mathbf{P}}_I - Z_I \mathbf{A}(\mathbf{R}_I) + \boldsymbol{\chi}_I \,. \end{aligned} \tag{5.17}$$

Now, the quantity involving the projection of the nuclear kinetic energy operator simplifies to

$$\langle \Psi^{\mathrm{el}} | \hat{\mathbf{\Pi}}_I^2 | \Psi^{\mathrm{nuc}} \Psi^{\mathrm{el}} \rangle = \left(\hat{\overline{\mathbf{\Pi}}}_I + \overline{\Delta}_I \right) | \Psi^{\mathrm{nuc}} \rangle \,. \tag{5.18}$$

Note, that at this point the DBOC simply reads

$$E_{\mathrm{DBOC}} = \sum_I \frac{\overline{\Delta}_I}{2M_I} \,. \tag{5.19}$$

For real-valued wave functions, one obtains $\overline{\Delta}_I = \Delta_I$, since the geometric vector potential vanishes from eq. 5.16 and the more familiar expression of the DBOC is

re-obtained. This is equivalent to the expression for the DBOC in equations 3.19 and 4.3, where it was written using the diagonal elements of the Fubini-Study metric. The geometric scalar potential is connected to this metric by the identity

$$\overline{\Delta}_I = \sum_\alpha g_{I\alpha I\alpha} \,. \tag{5.20}$$

Consequently, eq. 4.3 is obtained by insertion of the identity into eq. 5.19:

$$E_{\mathrm{DBOC}} = \sum_I \frac{1}{2M_I} \sum_\alpha g_{I\alpha I\alpha} \,.$$

5.4. Born-Oppenheimer Nuclear Schrödinger Equation

After the algebraic work of the previous section, the effective nuclear Schrödinger equation can be written down as

$$\hat{H}_{\mathrm{eff}} |\Psi^{\mathrm{nuc}}\rangle = (\hat{T} + \hat{U}) |\Psi^{\mathrm{nuc}}\rangle = \mathrm{i} \frac{\partial}{\partial t} |\Psi^{\mathrm{nuc}}\rangle \tag{5.21}$$

with the kinetic energy operator containing the effective nuclear momentum operator

$$\hat{T} = \sum_I \frac{1}{2M_I} \hat{\overline{\mathbf{\Pi}}}_I \,, \tag{5.22}$$

and the remaining internal energy contributions

$$\hat{U} = E_{\mathrm{BO}} + E_{\mathrm{DBOC}} + V_{\mathrm{nuc}} \tag{5.23}$$

resulting in

$$\begin{aligned} \hat{H}_{\mathrm{eff}} &= \hat{T} + E_{\mathrm{BO}} + E_{\mathrm{DBOC}} + V_{\mathrm{nuc}} \\ &= \sum_I \frac{1}{2M_I} \left(\hat{\mathbf{P}}_I - Z_I \mathbf{A}(\mathbf{R}_I) + \boldsymbol{\chi}_I \right)^2 + \langle \Psi^{\mathrm{el}} | \hat{H}_{\mathrm{el}} | \Psi^{\mathrm{el}} \rangle + \sum_I \frac{1}{2M_I} \overline{\Delta}_I + V_{\mathrm{nuc}} \end{aligned} \tag{5.24}$$

This Hamiltonian is the starting point of following sections to derive the equations of nuclear motion.

5.5. Equations of Motion

Having set up an effective nuclear Hamiltonian, the semiclassical picture can be used where equations of motion for the nuclei are derived from classical mechanics. Starting from Eq. 5.24, the equations of motion can now be constructed. The Hamiltonian depends of the spacial coordinates and momenta of the nuclei[47,48,53]

$$H_{\mathrm{eff}}(\mathbf{R}, \mathbf{P}) = \sum_I \frac{1}{2M_I} \left(\hat{\mathbf{P}}_I - Z_I \mathbf{A}(\mathbf{R}_I) + \boldsymbol{\chi}_I \right)^2 + U \,. \tag{5.25}$$

In the fashion of Hamiltonian mechanics, the velocity of a nucleus I is obtained from the derivative of $\hat{H}_{\text{eff}}$ with respect to the momentum

$$\dot{\mathbf{R}}_I = \frac{\partial H_{\text{eff}}(\mathbf{R}, \mathbf{P})}{\partial \mathbf{P}_I} = \frac{1}{M_I} \left(\hat{\mathbf{P}}_I - Z_I \mathbf{A}(\mathbf{R}_I) + \boldsymbol{\chi}_I \right) . \tag{5.26}$$

The force acting on said nucleus is then analogously given by

$$\dot{\mathbf{P}}_I = -\frac{\partial H_{\text{eff}}(\mathbf{R}, \mathbf{P})}{\partial \mathbf{R}_I} . \tag{5.27}$$

These equations require the propagation of the canonical momentum. This is disadvantageous because of its gauge dependency, which would result in the loss of translational invariance.[48]

5.6. Lagrangian Formalism

After the failure of the Hamiltonian mechanics, instead constructing the Lagrangian of the system gives[48,53]

$$\mathcal{L}(\mathbf{R}, \dot{\mathbf{R}}) = \max_{\mathbf{P}} \left(\sum_I \dot{\mathbf{R}}_I \mathbf{P}_I - \partial H_{\text{eff}}(\mathbf{R}, \mathbf{P}) \right) , \tag{5.28}$$

where an expression for $\mathbf{P}_I$ can be obtained from eq. 5.25 as

$$\mathbf{P}_I = M_I \dot{\mathbf{R}}_I + Z_I \mathbf{A}(\mathbf{R}_I) - \boldsymbol{\chi}_I . \tag{5.29}$$

Finally, one obtains

$$\mathcal{L}(\mathbf{R}, \dot{\mathbf{R}}) = \sum_I \dot{\mathbf{R}}_I \left(\frac{1}{2} M_I \dot{\mathbf{R}}_I + Z_I \mathbf{A}(\mathbf{R}_I) - \boldsymbol{\chi}_I \right) - U . \tag{5.30}$$

By separating the velocity-dependent and -independent contributions, the Euler-Lagrange equation

$$\frac{\mathrm{d}}{\mathrm{d}t} \frac{\partial \mathcal{L}(\mathbf{R}, \dot{\mathbf{R}})}{\partial \dot{\mathbf{R}}_I} = \frac{\partial \mathcal{L}(\mathbf{R}, \dot{\mathbf{R}})}{\partial \mathbf{R}_I} , \tag{5.31}$$

can be solved to arrive at[48]

$$M_I \ddot{\mathbf{R}}_I + Z_I \dot{\mathbf{A}}(\mathbf{R}_I) - \dot{\boldsymbol{\chi}}_I = -\frac{\partial U}{\partial \mathbf{R}_I} - Z_I \dot{\mathbf{A}}(\mathbf{R}_I) - \sum_J \left[\frac{\partial \boldsymbol{\chi}_J}{\partial \mathbf{R}_J} \right]^{\mathrm{T}} \dot{\mathbf{R}}_I . \tag{5.32}$$

Using the time derivative of the geometric vector potential

$$\dot{\boldsymbol{\chi}}_I = \sum_J \frac{\partial \boldsymbol{\chi}_I}{\partial \mathbf{R}_J} \frac{\partial \mathbf{R}_J}{\partial t} = \sum_J \frac{\partial \boldsymbol{\chi}_I}{\partial \mathbf{R}_J} \dot{\mathbf{R}}_J , \tag{5.33}$$

one obtains the force acting on nucleus I as

$$\mathbf{F}_I = -\frac{\partial U}{\partial \mathbf{R}_I} - 2Z_I \dot{\mathbf{A}}(\mathbf{R}_I) + \sum_J \frac{\partial \boldsymbol{\chi}_I}{\partial \mathbf{R}_J}\dot{\mathbf{R}}_J - \sum_J \left[\frac{\partial \boldsymbol{\chi}_J}{\partial \mathbf{R}_I}\right]^{\mathrm{T}} \dot{\mathbf{R}}_J \,. \tag{5.34}$$

Here, the two contributions involving derivatives of the geometric vector potential can be written using the Berry curvature[43,47,48,53,82]

$$\boldsymbol{\Omega}_{IJ} = \frac{\partial \boldsymbol{\chi}_I}{\partial \mathbf{R}_J} - \left[\frac{\partial \boldsymbol{\chi}_J}{\partial \mathbf{R}_I}\right]^{\mathrm{T}} \,. \tag{5.35}$$

Note, that this expression can be written as

$$\Omega_{I\alpha J\beta} = \partial_{J\beta}\chi_{I\alpha} - \partial_{I\alpha}\chi_{J\beta} \,, \tag{5.36}$$

which resembles a curl. A similar expression can be obtained for the magnetic flux density by using the well-known equivalence of the cross product and multiplication with an anti-symmetric matrix:

$$\mathbf{a} \times \mathbf{b} = \begin{pmatrix} a_1 \\ a_2 \\ a_3 \end{pmatrix} \times \begin{pmatrix} b_1 \\ b_2 \\ b_3 \end{pmatrix} = \begin{pmatrix} 0 & -a_3 & a_2 \\ a_3 & 0 & -a_1 \\ -a_2 & a_1 & 0 \end{pmatrix} \begin{pmatrix} b_1 \\ b_2 \\ b_3 \end{pmatrix} \,. \tag{5.37}$$

Accordingly, a magnetic flux density matrix can be defined as[47]

$$\tilde{\mathcal{B}} = \begin{pmatrix} 0 & -\mathcal{B}_z & \mathcal{B}_y \\ \mathcal{B}_z & 0 & -\mathcal{B}_x \\ -\mathcal{B}_y & \mathcal{B}_x & 0 \end{pmatrix} \,. \tag{5.38}$$

Using the definition of the magnetic flux density via the magnetic vector potential yields

$$\tilde{\mathcal{B}}_{\alpha\beta} = \partial_\beta A_\alpha - \partial_\alpha A_\beta \,, \tag{5.39}$$

which highlights the similarity of the geometric and magnetic vector potential. Both are gauge dependent quantities with a curl that is gauge-invariant. In this analogy, the Berry curvature has similar properties to a magnetic vector field, although great caution is advised when using this picture. Later sections explore much more natural interpretations that become more obvious after more algebraic work. The time derivative of the magnetic vector potential within the symmetric gauge is simply obtained as

$$\dot{\mathbf{A}}(\mathbf{R}_I) = \frac{\partial \mathbf{A}(\mathbf{R}_I)}{\partial \mathbf{R}_I}\dot{\mathbf{R}}_I = -\frac{1}{2}\dot{\mathbf{R}}_I \times \mathcal{B} \,. \tag{5.40}$$

This identity, together with the definition of the Berry curvature from eq. 5.35, simplifies the force acting on a nucleus I from eq. 5.34 to[48]

$$\mathbf{F}_I = -\frac{\partial U}{\partial \mathbf{R}_I} + Z_I \dot{\mathbf{R}}_I \times \mathcal{B} + \sum_J \boldsymbol{\Omega}_{IJ}\dot{\mathbf{R}}_J \,. \tag{5.41}$$

Three contributions to the force on nucleus I can now be identified: First, the gradient of the electronic energy, which contains the Born-Oppenheimer energy and the DBOC. Second, the Lorentz force acting on the bare nuclear charge Z_I due to the external magnetic field. Third, the so called Berry force, that couples the velocities of all nuclei via the Berry curvature. One can therefore write[48]

$$\mathbf{F}_I(\mathbf{R}, \dot{\mathbf{R}}) = \mathbf{F}_I^{\mathrm{el}}(\mathbf{R}) + \mathbf{F}_I^{\mathrm{L}}(\dot{\mathbf{R}}) + \mathbf{F}_I^{\mathrm{B}}(\mathbf{R}, \dot{\mathbf{R}})\,. \tag{5.42}$$

For the sake of clarity, eq. 5.42 shows the explicit dependence of each force, the electronic energy is only depended on the molecular geometry $\mathbf{R}$, while the Lorentz force only depends on the velocity of all the corresponding nuclei. The Berry force, on the other hand, depends on all nuclear coordinates and all velocities.

6. The Berry Curvature, Properties and Sum Rules

This section explores some known properties of the molecular Berry curvature. Furthermore, a different way of interpreting the Berry curvature is explored.

In eq. 5.35 and 5.36 of the previous section, the Berry curvature $\mathbf{\Omega}$ was introduced as

$$\Omega_{I\alpha J\beta} = \partial_{J\beta}\chi_{I\alpha} - \partial_{I\alpha}\chi_{J\beta}\,.$$

In this notation, the resemblance to the magnetic field and the magnetic vector potential becomes obvious by recalling that $\mathcal{B} = \boldsymbol{\nabla} \times \mathbf{A}$. Similar to the these magnetic quantities, the Berry curvature is gauge-invariant, while the geometric vector potential is gauge-dependent.[47] Analogously to the magnetic vector potential, the gradient of any scalar field can be added to $\boldsymbol{\chi}$ without changing the resulting Berry curvature. By inserting the definition of the geometric vector potential, we obtain the following expression for one 3×3 block of the Berry curvature which recovers the definition via the QGT from section 4:[43,47,48,53]

$$\begin{aligned}\mathbf{\Omega}_{IJ} &= \mathrm{i}\left(\left\langle \frac{\partial\Psi}{\partial\mathbf{R}_I}\middle|\frac{\partial\Psi}{\partial\mathbf{R}_J}\right\rangle - \left\langle \frac{\partial\Psi}{\partial\mathbf{R}_J}\middle|\frac{\partial\Psi}{\partial\mathbf{R}_I}\right\rangle\right) \\ &= -2\Im\left(\left\langle \frac{\partial\Psi}{\partial\mathbf{R}_I}\middle|\frac{\partial\Psi}{\partial\mathbf{R}_J}\right\rangle\right)\,.\end{aligned} \tag{6.1}$$

From the definition it also becomes apparent that the Berry curvature is a real-valued, anti-symmetric $3N_{\mathrm{nuc}} \times 3N_{\mathrm{nuc}}$ matrix that contains 3×3 matrices $\mathbf{\Omega}_{IJ}$ for each pair of nuclei. These individual 3×3 matrices usually do not show any symmetry, except for the notable exception of the diagonal blocks, which retain the anti-symmetry.

At this point it might be useful, for our understanding of the Berry curvature, to return to eq. 5.42, where the force acting on a nucleus I in a magnetic field was derived. The Lorentz and Berry force,

$$\mathbf{F}_I^{\mathrm{LB}} = Z_I\dot{\mathbf{R}}_I \times \mathcal{B} + \sum_J \mathbf{\Omega}_{IJ}\dot{\mathbf{R}}_J\,, \tag{6.2}$$

can be rewritten by decomposing each block IJ of the Berry curvature into its symmetric and anti-symmetric part according to[47,53,80]

$$\mathbf{\Omega}_{IJ} = \mathbf{\Omega}_{IJ}^{\mathrm{sym}} + \mathbf{\Omega}_{IJ}^{\mathrm{asym}}\,, \tag{6.3}$$

$$\mathbf{\Omega}_{IJ}^{\mathrm{sym}} = \frac{1}{2}\left(\mathbf{\Omega}_{IJ} + \mathbf{\Omega}_{IJ}^{\mathrm{T}}\right)\,, \tag{6.4}$$

$$\boldsymbol{\Omega}_{IJ}^{\text{asym}} = \frac{1}{2}\left(\boldsymbol{\Omega}_{IJ} - \boldsymbol{\Omega}_{IJ}^{\text{T}}\right) . \tag{6.5}$$

Using the equivalence of the cross product and multiplication with an anti-symmetric matrix from eq. 5.37, one arrives at

$$\mathbf{F}_I^{\text{LB}} = Z_I \dot{\mathbf{R}}_I \times \mathcal{B} + \sum_J \boldsymbol{\omega}_{IJ}^{\text{asym}} \times \dot{\mathbf{R}}_{IJ} + \sum_J \boldsymbol{\Omega}_{IJ}^{\text{sym}} \dot{\mathbf{R}}_J \, . \tag{6.6}$$

Where the vector $\boldsymbol{\omega}_{IJ}^{\text{asym}}$ is defined as

$$\boldsymbol{\omega}_{IJ}^{\text{asym}} = \begin{pmatrix} \Omega_{IzJy}^{\text{asym}} \\ \Omega_{IxJz}^{\text{asym}} \\ \Omega_{IyJx}^{\text{asym}} \end{pmatrix} . \tag{6.7}$$

By introducing a quantity Q resembling a charge population as[47]

$$Q_{IJ}\mathcal{B} = -\boldsymbol{\omega}_{IJ}^{\text{asym}} , \tag{6.8}$$

the force becomes

$$\mathbf{F}_I^{\text{LB}} = -\sum_J \left(\delta_{IJ} Z_I + Q_{IJ}\right) \mathcal{B} \times \dot{\mathbf{R}}_J + \sum_J \boldsymbol{\Omega}_{IJ}^{\text{sym}} \dot{\mathbf{R}}_J \, . \tag{6.9}$$

By decomposing the Berry force into individual contributions from the symmetric and anti-symmetric parts, the Lorentz force acting on the bare nuclear charge Z_I can be combined with the latter part of the Berry force. This now allows for the definition of the so-called Berry atomic partial charge of the nucleus I as[53,80]

$$q_I = Z_I + \sum_J Q_{IJ} \, . \tag{6.10}$$

This paves the way to another interpretation of the Berry curvature that emerges due to an external magnetic field. In a molecule that moves in a magnetic field, the nucleus does not experience the full Lorentz force acting on its bare nuclear charge. Instead, the electrons in the vicinity of the nucleus screen the magnetic field and somewhat shield the nucleus in this way.[53,80] This interpretation is investigated in the later sections 16 and 18.4, where Berry charges are calculated for some molecules and relations to other partial charge models, that are already established in the literature, are drawn.

6.1. Sum Rules of the Molecular Berry Curvature

At this point, it is useful to derive some properties of the molecular Berry curvature. They are obtained from summing the molecular Berry curvature over one or both of its nuclear indices. Summation over both indices yields the number of electrons in the system times a component of the magnetic flux density,

$$\sum_{IJ} \Omega_{I\alpha J\beta} = -N_{\text{el}} \sum_\gamma \varepsilon_{\alpha\beta\gamma} \mathcal{B}_\gamma \, , \tag{6.11}$$

as stated by the *magnetic-translational sum rule* which was first derived by Peters, Culpitt, Tellgren and Helgaker in Ref. [46]. Here, the Levi-Civita tensor $\varepsilon_{\alpha\beta\gamma}$ was used. Whereas summation over only one nuclear index yields a derivative of the electronic pseudomomentum vector,

$$\sum_J \Omega_{I\alpha J\beta} = \frac{\partial k_\beta}{\partial R_{I\alpha}}\,, \tag{6.12}$$

as given by the *pseudomomentum-translational sum rule* that was first presented in the context of this work in Ref. [82] together with Pausch. The pseudomomentum operator is defined as

$$\hat{\mathbf{k}} = \hat{\boldsymbol{\pi}} - \mathcal{B} \times \hat{\mathbf{r}}\,. \tag{6.13}$$

The remainder of this section is a summary of the derivations of these two sum rules, more details can be found in Ref. [46] and Ref. [82].

6.1.1. The Coulomb Gauge

Before continuing with the derivation, a convenient choice of the magnetic vector potential within molecular quantum mechanics is introduced in this section. The Coulomb gauge is constructed such that the magnetic vector potential is divergence-less

$$\boldsymbol{\nabla} \cdot \mathbf{A} = 0\,, \tag{6.14}$$

which is a useful property in quantum chemistry, because this way also $\hat{\mathbf{p}} \cdot \mathbf{A} = 0$. Furthermore, for static homogeneous external magnetic fields in the Coulomb gauge, $\mathbf{A}$ can be chosen in the symmetric gauge[99] as

$$\mathbf{A}(\mathbf{r}, \mathbf{O}) = \frac{1}{2}\mathcal{B} \times (\mathbf{r} - \mathbf{O})\,, \tag{6.15}$$

where the choice of the gauge origin $\mathbf{O}$ is arbitrary. It is common to write $\mathbf{r}^{\mathbf{O}} = \mathbf{r} - \mathbf{O}$ for the sake of readability.

6.2. The Pseudomomentum-Translational Sum Rule

Throughout the derivation it is often important which quantities depend on the set of all electronic coordinates $\mathbf{r}$, the set of all nuclear coordinates $\mathbf{R}$, or the gauge-origin of the magnetic vector potential $\mathbf{O}$. Therefore, the dependence is mostly written out explicitly in this section. Starting off, the expectation value of one component of the electronic pseudomomentum is given as

$$k_\alpha(\mathbf{R}) = \langle \Psi(\mathbf{r}, \mathbf{R}, \mathbf{O}) | \hat{k}_\alpha(\mathbf{r}, \mathbf{O}) | \Psi(\mathbf{r}, \mathbf{R}, \mathbf{O}) \rangle\,, \tag{6.16}$$

inserting the definition of the electronic kinetic momentum operator $\hat{\boldsymbol{\pi}}$ together with the magnetic vector potential in the symmetric gauge, one component of the

pseudomomentum operator becomes

$$\hat{k}_\alpha = \hat{p}_\alpha + \frac{1}{2}\sum_{\beta\gamma} \varepsilon_{\alpha\beta\gamma} \left(\hat{r}_\beta + O_\beta\right) \mathcal{B}_\gamma \,. \tag{6.17}$$

As indicated by its dependencies, the expectation value of the pseudomomentum operator is gauge-invariant, even though it contains the gauge origin in this expression. Now Eq. 6.12 becomes

$$\sum_I \Omega_{I\alpha J\beta} = \frac{\partial p_\beta(\mathbf{R},\mathbf{O})}{\partial R_{I\alpha}} - \frac{1}{2}\mathcal{B}_\alpha \sum_\gamma \varepsilon_{\alpha\beta\gamma} \frac{\partial \mu_\gamma(\mathbf{R},\mathbf{O})}{\partial R_{I\alpha}} \,, \tag{6.18}$$

were the expectation values on the right-hand side are given as

$$p_\alpha(\mathbf{R},\mathbf{O}) = \langle \Psi(\mathbf{r},\mathbf{R},\mathbf{O}) | \hat{p}_\alpha \Psi(\mathbf{r},\mathbf{R},\mathbf{O}) \rangle \,, \tag{6.19}$$

$$\mu_\alpha(\mathbf{R},\mathbf{O}) = -\langle \Psi(\mathbf{r},\mathbf{R},\mathbf{O}) | (\hat{r}_\alpha - O_\alpha) \Psi(\mathbf{r},\mathbf{R},\mathbf{O}) \rangle \,. \tag{6.20}$$

In the same fashion, the expectation value of the kinetic momentum operator can be evaluated as

$$\pi_\alpha(\mathbf{R},\mathbf{O}) = \langle \Psi(\mathbf{r},\mathbf{R},\mathbf{O}) | \hat{\pi}_\alpha \Psi(\mathbf{r},\mathbf{R},\mathbf{O}) \rangle \,, \tag{6.21}$$

which describes the general motion of the electrons.[82]

6.3. The Limit of a Complete Basis

In a complete basis, the pseudomomentum-translational sum rule can be cast into a simpler form, which is now discussed.

In a bound state with stationary nuclei, the electrons should not carry an overall kinetic momentum, and fulfill the continuity equation. Therefore, for an electronic ground state the expectation value of the kinetic momentum operator needs to vanish[67,82]

$$\boldsymbol{\pi} = 0 \,. \tag{6.22}$$

Insertion into the definition of the pseudomomentum in eq. 6.13 gives

$$\mathbf{k} = \mathcal{B} \times \boldsymbol{\mu} \,, \tag{6.23}$$

and the following expression is obtained for the sum rule:[82]

$$\sum_J \Omega_{I\alpha J\beta} = -\mathcal{B}_\alpha \sum_\gamma \frac{\partial \mu_\gamma(\mathbf{R},\mathbf{O})}{\partial R_{I\alpha}} \,. \tag{6.24}$$

As mentioned earlier, this form of the pseudomomentum-translational sum rule is only valid in a complete basis. This expression was obtained by exploiting the vanishing expectation value of the kinetic momentum operator under such conditions. Still, this property can be understood in another way by investigating the different

contributions to the electronic kinetic momentum operator. Using its definition from the principle of minimal coupling and the vector potential in the symmetric gauge yields

$$\hat{\boldsymbol{\pi}} = \hat{\mathbf{p}} + \frac{1}{2}\mathcal{B} \times (\hat{\mathbf{r}} - \mathbf{O}) \,. \tag{6.25}$$

Notably, the first contribution contains solely the canonical momentum operator, while the second contains the position operator. The momentum operator has an exact representation in momentum space, whereas the position operator has an exact representation in coordinate space. These two spaces are related by a Fourier transformation, which is only exact within a complete basis. Therefore, the gauge dependency of the electronic canonical momentum and of the dipole moment do not cancel each other necessarily when employing a finite basis set.[82]

6.4. Derivation of the Pseudomomentum-Translational Sum Rule

This section's aim is to show a summary of this derivation of the pseudomomentum-translational sum rule. A more detailed version of the derivation can be found in Ref. [82] and is structurally similar to the derivation of the magnetic-translational sum rule derived by Peters *et al.* in Ref. [46].

Starting off, the definition of the Berry curvature from eq.5.35 is used, and summed over one nuclear index, one then obtains

$$\sum_J \Omega_{I\alpha J\beta}(\mathbf{R}) = \sum_J \frac{\partial}{\partial R_{J\beta}} \chi_{I\alpha}(\mathbf{R}, \mathbf{O}) - \frac{\partial}{\partial R_{I\alpha}} \sum_J \chi_{J\beta}(\mathbf{R}, \mathbf{O}) \,. \tag{6.26}$$

The first term in eq. 6.26 can be simplified by defining the sum of the nuclear derivative operators over all nuclear coordinates as a translation of all nuclear coordinates by some displacement vector, while leaving the gauge origin unchanged. Such a translation, along a vector $\mathbf{T}$, can be written as

$$\mathbf{R} + \mathbf{R}_\mathrm{T} = \begin{pmatrix} \mathbf{R}_1 + \mathbf{T} \\ \mathbf{R}_2 + \mathbf{T} \\ \vdots \end{pmatrix} \,. \tag{6.27}$$

In this way, the sum over derivatives is given by

$$\sum_J \frac{\partial}{\partial R_{J\beta}} = \frac{\partial}{\partial T_\beta} \,. \tag{6.28}$$

The second term in eq. 6.26 can also be simplified by defining the total nuclear canonical momentum operator as

$$\hat{P}_\beta^\mathrm{tot} = \sum_J \hat{P}_{J\beta} \,. \tag{6.29}$$

Using the two aforementioned relations, eq. 6.26 is obtained as

$$\sum_J \Omega_{I\alpha J\beta}(\mathbf{R}) = \frac{\partial}{\partial T_\beta}\langle\Psi|\hat{P}_{I\alpha}\Psi\rangle - \frac{\partial}{\partial R_{I\alpha}}\langle\Psi|\hat{P}^{\mathrm{tot}}_{\beta}\Psi\rangle\,. \tag{6.30}$$

In doing so, the sum of the Berry curvature elements over one nuclear index is expressed as a translation of one element of the nuclear canonical momentum and a nuclear derivative of the total nuclear canonical momentum of the system. To evaluate the expectation value of the total nuclear canonical momentum operator, one needs to investigate the effect of a translation of all nuclear coordinates on the wave function. The electronic Hamiltonian after such a translation can be obtained from a unitary transformation[46]

$$\hat{H}^{\mathrm{el}}(\mathbf{r},\mathbf{R}+\mathbf{R}_{\mathrm{T}},\mathbf{O}) = \hat{U}(\mathbf{R},\mathbf{T},\mathbf{O})\hat{H}^{\mathrm{el}}(\mathbf{r},\mathbf{R},\mathbf{O})\hat{U}^{\dagger}(\mathbf{R},\mathbf{T},\mathbf{O})\,, \tag{6.31}$$

the electronic wave function can then be transformed accordingly. It can be shown, that such a unitary transformation is given by[46]

$$\hat{U}(\mathbf{R},\mathbf{T},\mathbf{O}) = \exp\left(-\mathrm{i}\mathbf{T}\hat{\mathbf{k}} + \mathrm{i}\eta(\mathbf{R},\mathbf{T},\mathbf{O})\right)\,, \tag{6.32}$$

where $\eta(\mathbf{R},\mathbf{T},\mathbf{O})$ is an arbitrary gauge function. Application of this transformation to the total nuclear canonical momentum operator yields

$$\hat{P}^{\mathrm{U,tot}}_{\alpha}(\mathbf{R},\mathbf{T},\mathbf{O}) = \hat{U}^{\dagger}(\mathbf{R},\mathbf{T},\mathbf{O})\hat{P}^{\mathrm{tot}}_{\alpha}(\mathbf{R},\mathbf{T},\mathbf{O})\hat{U}(\mathbf{R},\mathbf{T},\mathbf{O})\,. \tag{6.33}$$

From here, the Baker-Campbell-Hausdorff expansion can be applied as higher order terms vanish and the expansion terminates early to arrive at[46]

$$\hat{P}^{\mathrm{U,tot}}_{\alpha}(\mathbf{R},\mathbf{T},\mathbf{O}) = -\mathrm{i}\frac{\partial}{\partial T_\alpha} - \hat{k}_\alpha + \hat{\gamma}_\alpha(\mathbf{R},\mathbf{T},\mathbf{O}) - \frac{1}{2}N_{\mathrm{el}}\left(\mathcal{B}\times\mathbf{T}\right)_\alpha\,, \tag{6.34}$$

where $\hat{\boldsymbol{\gamma}}$ is the derivative of the gauge function η from eq. 6.32 with respect to $\mathbf{T}$

$$\hat{\boldsymbol{\gamma}}(\mathbf{R},\mathbf{T},\mathbf{O}) = \frac{\partial\eta(\mathbf{R},\mathbf{T},\mathbf{O})}{\partial\mathbf{T}}\,. \tag{6.35}$$

Next, the application of the total nuclear canonical momentum operator on the electronic wave function of the displaced reference system needs to be calculated. After building the limit of $\mathbf{T}\to\mathbf{0}$ and eliminating any vanishing contributions, eq. 6.30 can be rewritten as[82]

$$\sum_J \Omega_{I\alpha J\beta}(\mathbf{R}) = \frac{\partial}{\partial T_\beta}\langle\Psi|\hat{P}_{I\alpha}\Psi\rangle - \frac{\partial\hat{\gamma}_\beta(\mathbf{R},\mathbf{O})}{\partial R_{I\alpha}} + \frac{\partial\hat{k}_\beta(\mathbf{R},\mathbf{O})}{\partial R_{I\alpha}}\,. \tag{6.36}$$

At this point, by comparison to the final sum rule in eq. 6.12, all that is left to show is that the following identity holds:

$$\frac{\partial}{\partial T_\beta}\langle\Psi|\hat{P}_{I\alpha}\Psi\rangle = \frac{\partial\hat{\gamma}_\beta(\mathbf{R},\mathbf{O})}{\partial R_{I\alpha}}\,. \tag{6.37}$$

This identity states that the translation of the geometric vector potential may at most result in the displacement of the gauge function. For a vector potential, this is the expected behavior, but the property is proven here nonetheless. Using the product rule, one obtains

$$\frac{\partial}{\partial T_\beta}\langle\Psi|\hat{P}_{I\alpha}\Psi\rangle = -\left\langle \hat{P}^{\mathrm{tot}}_\beta\Psi\middle|\frac{\partial\Psi}{\partial R_{I\alpha}}\right\rangle + \left\langle\Psi\middle|\frac{\partial}{\partial R_{I\alpha}}\hat{P}^{\mathrm{tot}}_\beta\Psi\right\rangle . \tag{6.38}$$

Using the hermiticity of $\hat{\boldsymbol{\gamma}}$ and $\hat{\mathbf{k}}$, this expression can be further written as

$$\frac{\partial}{\partial T_\beta}\langle\Psi|\hat{P}_{I\alpha}\Psi\rangle = -\left\langle\Psi\middle|(\hat{\gamma}_\beta - \hat{k}_\beta)\frac{\partial\Psi}{\partial R_{I\alpha}}\right\rangle + \left\langle\Psi\middle|\frac{\partial}{\partial R_{I\alpha}}(\hat{\gamma}_\beta - \hat{k}_\beta)\Psi\right\rangle . \tag{6.39}$$

The pseudomomentum operator commutes with the nuclear canonical momentum operator, since the former does not explicitly depend on any nuclear coordinate. Therefore, the last contribution in eq. 6.39 amounts to

$$\left\langle\Psi\middle|\frac{\partial}{\partial R_{I\alpha}}(\hat{\gamma}_\beta - \hat{k}_\beta)\Psi\right\rangle = \left\langle\Psi\middle|(\hat{\gamma}_\beta - \hat{k}_\beta)\frac{\partial\Psi}{\partial R_{I\alpha}}\right\rangle + \frac{\partial\gamma_\beta}{\partial R_{I\alpha}} . \tag{6.40}$$

Using these relations eq. 6.36 can be cast into

$$\begin{aligned}\sum_J \Omega_{I\alpha J\beta} &= \frac{\partial\gamma_\beta}{\partial R_{I\alpha}} - \frac{\partial\gamma_\beta}{\partial R_{I\alpha}} + \frac{\partial k_\beta}{\partial R_{I\alpha}} \\ &= \frac{\partial k_\beta}{\partial R_{I\alpha}} ,\end{aligned} \tag{6.41}$$

which is the pseudomomentum translational sum rule.

7. The Electronic Wavefunction

Section 3 established the adiabatic Born-Oppenheimer approximation, where the total molecular wave function was decoupled into an electronic and a nuclear part. So far, mostly an exact solution to the electronic Schrödinger equation has been considered. One central aim of this work is to make the quantum geometric quantities that have been discussed so far available from standard methods of computational electronic structure theory. For this purpose, the following chapter discusses different approaches to calculate an approximate solution to the Schrödinger equation. For the remainder of this thesis only the complex-valued two-component framework is considered, if not noted otherwise.

7.1. The Slater Determinant

The Pauli exclusion principle[114] requires fermionic wave functions to change their sign when the coordinates of two such particles are exchanged. To satisfy this requirement, the electronic wave function can be chosen as a single Slater determinant[115]

$$\Psi = \begin{vmatrix} \psi_1(\mathbf{x}_1) & \psi_2(\mathbf{x}_1) & \cdots & \psi_n(\mathbf{x}_1) \\ \psi_1(\mathbf{x}_2) & \psi_2(\mathbf{x}_2) & \cdots & \psi_n(\mathbf{x}_2) \\ \vdots & \vdots & \ddots & \vdots \\ \psi_1(\mathbf{x}_n) & \psi_2(\mathbf{x}_n) & \cdots & \psi_n(\mathbf{x}_n) \end{vmatrix}, \tag{7.1}$$

that contains one-electron wave functions $\psi(\mathbf{x})$. Here, the coordinate $\mathbf{x}_i$ contains space- and spin- coordinates of the particle.

7.2. Linear Combination of Atomic Orbitals

One approach to construct the one-electron wave functions is the so-called linear combination of atomic orbitals (LCAO)[37,116–119]

$$\psi_p(\mathbf{x}) = \sum_{\mu\tau} C^{\tau}_{\mu p} \chi_\mu(\mathbf{r}) \tau \,, \tag{7.2}$$

with a set of atomic orbitals (AOs) $\chi^\tau_\mu(\mathbf{r})$ and the expansion coefficients $C_{\mu p}$. The spin-function τ takes care of the orthonormality of the spin components. Such a set of AOs is commonly referred to as a basis set, that contains fixed, pre-optimized functions. This approach is applicable to different types of one-electron wave functions, the

most common one being molecular orbitals (MOs). The two-component formalism presented here employs spinors as one-electron functions

$$\psi_p = \begin{pmatrix} \psi_p^{\uparrow} \\ \psi_p^{\downarrow} \end{pmatrix} . \tag{7.3}$$

A spinor can contain any normalized linear combination of alpha and beta spin functions, here marked with $\uparrow$ and $\downarrow$ respectively. Basis functions can be chosen as Gaussian-type orbitals (GTOs)[120]

$$\chi_\mu(\mathbf{r}) = N_\mu (x - R_x^\mu)^{l_\mu} (y - R_y^\mu)^{m_\mu} (z - R_z^\mu)^{n_\mu} \exp\left(-\zeta_\mu (\mathbf{r} - \mathbf{R}^\mu)^2\right) , \tag{7.4}$$

which are centered at $\mathbf{R}^\mu$ and have normalization coefficients N_μ. The sum $L = l_\mu + m_\mu + n_\mu$ of the integer exponents of the monomials specifies the angular momentum of the basis function, with $L = 0$ representing an s-type orbital, $L = 1$ a p-type orbital and so on. A single GTO of this form is called a primitive basis function. For higher efficiency, some primitive functions of equal angular momentum are contracted in a linear combination with fixed coefficients and exponents.[121]

7.3. London Atomic Orbitals

For calculations in external magnetic fields, additional considerations have to be taken into account if finite basis sets are used. The magnetic vector potential in the symmetric gauge has already been introduced in equations 6.14 and 6.15. This definition included the arbitrary gauge origin $\mathbf{O}$. Any transformation

$$\mathbf{A}'(\mathbf{r}) = \mathbf{A}(\mathbf{r}) - \boldsymbol{\nabla}\Lambda(\mathbf{r}) , \tag{7.5}$$

with a scalar field $\Lambda(\mathbf{r})$ results in the same magnetic field because the curl of a gradient field always vanishes

$$\boldsymbol{\nabla} \times \mathbf{A}'(\mathbf{r}) = \boldsymbol{\nabla} \times (\mathbf{A}(\mathbf{r}) - \boldsymbol{\nabla}\Lambda(\mathbf{r})) = \boldsymbol{\nabla} \times \mathbf{A}(\mathbf{r}) . \tag{7.6}$$

A shift of the underlying gauge origin to $\mathbf{O}'$ can be achieved by using

$$\Lambda(\mathbf{r}) = \mathbf{A}(\mathbf{O}') \cdot \mathbf{r} = \frac{1}{2} \mathcal{B} \times (\mathbf{O}' - \mathbf{O}) \cdot \mathbf{r} , \tag{7.7}$$

which vanishes if the new gauge origin coincides with the coordinate origin. Physical quantities like the Hamilton operator then need to be transformed accordingly[53]

$$\hat{H}' = e^{-\mathrm{i}\Lambda(\mathbf{r})} \hat{H} e^{\mathrm{i}\Lambda(\mathbf{r})} . \tag{7.8}$$

Any observable like the energy must be independent of such transformations, since they describe the same magnetic field. This means that the wave functions corresponding to the two different Hamilton operators need to be connected by a phase factor that cancels the transformation of the Hamiltonian[122]

$$\Psi' = e^{-\mathrm{i}\Lambda(\mathbf{r})} \Psi , \tag{7.9}$$

to ensure gauge independent electronic properties.[123] Therefore, the wave function also becomes dependent on the choice of gauge and carries information about said choice. As a consequence, the wave function can no longer be chosen to be real-valued without loss of generality when external magnetic fields are involved.[69] Since the exact wave function obtains a multiplicative factor from the gauge transformation, each basis function would essentially absorb the same factor

$$\chi'_\mu(\mathbf{r}) = \exp\left(-\frac{\mathrm{i}}{2}\mathcal{B} \times (\mathbf{O}' - \mathbf{O}) \cdot \mathbf{r}\right) \chi_\mu(\mathbf{r})\,. \tag{7.10}$$

This plane wave factor oscillates over all of space, which is generally not described well by a finite basis set of atom-centered GTOs. One approach to deal with this problem is to premultiply all basis functions with the necessary plane wave factor to handle this requirement naturally. These so-called London atomic orbitals or gauge-including atomic orbitals (GIAOs) read[68,124,125]

$$\xi_\mu(\mathbf{r}) = \exp\left(-\frac{\mathrm{i}}{2}\mathcal{B} \times (\mathbf{R}^\mu - \mathbf{O}) \cdot \mathbf{r}\right) \chi_\mu(\mathbf{r})\,. \tag{7.11}$$

Comparison with eq. 7.10 shows that this is equivalent to a gauge transformation where the gauge origin is shifted onto the basis function's center.

7.4. Hartree-Fock Theory

Inserting the definition of the Slater determinant into the electronic Schrödinger equation and minimizing the energy via the variational principle[93], the Hartree-Fock equations are obtained[92,93,126]

$$\hat{F}\psi_p = \epsilon_p \psi_p\,, \tag{7.12}$$

with the Fock operator

$$\hat{F} = \hat{h}_{\mathrm{core}} + \hat{J} - \hat{K}\,. \tag{7.13}$$

It consists of the core Hamiltonian, containing all one-particle contributions like the kinetic energy, the electron-nucleus attraction and magnetic field dependent contributions, namely the paramagnetic and diamagnetic terms. Additionally, the Fock operator contains the Coulomb operator $\hat{J}$ and the exchange operator $\hat{K}$. The former describes the electrostatic interaction of the electrons between each other, while the latter is a consequence of the construction of the Slater determinant and the indistinguishability of the electrons. In contrast to the Schrödinger equation where the Hamiltonian acts on the many-particle wave function, the Hartree-Fock equations are coupled effective one-particle equations. Using the LCAO approach from eq. 7.3 to expand the molecular orbitals in a finite basis leads to the two-component Roothaan-Hall equation[119,127]

$$\begin{pmatrix} \mathbf{F}^{\uparrow\uparrow} & \mathbf{F}^{\uparrow\downarrow} \\ \mathbf{F}^{\downarrow\uparrow} & \mathbf{F}^{\downarrow\downarrow} \end{pmatrix} \begin{pmatrix} \mathbf{C}^{\uparrow} \\ \mathbf{C}^{\downarrow} \end{pmatrix} = \begin{pmatrix} \mathbf{S} & \mathbf{0} \\ \mathbf{0} & \mathbf{S} \end{pmatrix} \begin{pmatrix} \mathbf{C}^{\uparrow} \\ \mathbf{C}^{\downarrow} \end{pmatrix} \boldsymbol{\epsilon}\,, \tag{7.14}$$

with the Fock matrices $\mathbf{F}^{\sigma\tau}$, the spinor coefficient matrix $\mathbf{C}^{\sigma}$, the diagonal matrix $\boldsymbol{\epsilon}$ containing the orbital energies and the overlap matrix $\mathbf{S}$ containing the matrix elements

$$S_{\mu\nu} = \langle \xi_\mu | \xi_\nu \rangle \ . \tag{7.15}$$

Before going into more detail, the Pauli spin-matrices[114] can be introduced, as they will provide an alternative decomposition of spin-dependent quantities. They are defined as

$$\boldsymbol{\sigma}_x = \begin{pmatrix} 0 & 1 \\ 1 & 0 \end{pmatrix} , \qquad \boldsymbol{\sigma}_y = \begin{pmatrix} 0 & -\mathrm{i} \\ \mathrm{i} & 0 \end{pmatrix} , \qquad \boldsymbol{\sigma}_z = \begin{pmatrix} 1 & 0 \\ 0 & -1 \end{pmatrix} , \tag{7.16}$$

these matrices are useful in the description of spin, as they are closely related to the special unitary group of second order SU(2). Therefore, it will prove itself useful to also define

$$\boldsymbol{\sigma}_0 = \begin{pmatrix} 1 & 0 \\ 0 & 1 \end{pmatrix} , \tag{7.17}$$

to describe a spin-free quantity. The whole Fock matrix can be conveniently decomposed according to the Pauli matrices as[70]

$$\mathbf{F} = \begin{pmatrix} \mathbf{F}^{\uparrow\uparrow} & \mathbf{F}^{\uparrow\downarrow} \\ \mathbf{F}^{\downarrow\uparrow} & \mathbf{F}^{\downarrow\downarrow} \end{pmatrix} = \sum_{m \in 0,x,y,z} \boldsymbol{\sigma}_m \otimes \mathbf{F}_m \, . \tag{7.18}$$

Then, the Fock matrix contribution which is totally symmetrical with regards to spin,

$$\mathbf{F}_0 = \mathbf{h}_0 + \mathbf{J}_0[\mathbf{D}_0] - \mathbf{K}_0[\mathbf{D}_0] \, , \tag{7.19}$$

contains the matrix elements over

$$\hat{\mathbf{h}}_0 = \frac{1}{2}\hat{\mathbf{p}}^2 - \sum_I \frac{Z_I}{|\mathbf{R}_I - r|} + \frac{1}{2}\mathcal{B} \cdot \hat{\mathbf{l}}^{\mathbf{O}} + \frac{1}{8}\left[\mathcal{B}^2 \left(\mathbf{r}^{\mathbf{O}}\right)^2 + \left(\mathcal{B} \cdot \mathbf{r}^{\mathbf{O}}\right)^2\right] , \tag{7.20}$$

and the electron-electron Coulomb interaction $\mathbf{J}_0$ with the matrix elements

$$J_{\mu\nu,0} = \sum_{\mu\nu\kappa\lambda} (\mu\nu|\kappa\lambda) D_{\lambda\kappa,0} \, , \tag{7.21}$$

and the exchange contribution

$$K_{\mu\nu,m}[\mathbf{D}_m] = \sum_{\mu\nu\kappa\lambda} (\mu\lambda|\kappa\nu) D_{\lambda\kappa,m} \, . \tag{7.22}$$

The Coulomb and exchange matrices in turn contain the two-electron integral

$$(\mu\nu|\kappa\lambda) = \int\int \xi_\mu^*(\mathbf{r}_1)\xi_\nu(\mathbf{r}_1) \frac{1}{|\mathbf{r}_1 - \mathbf{r}_2|} \xi_\kappa^*(\mathbf{r}_2)\xi_\lambda(\mathbf{r}_2) \, \mathrm{d}\mathbf{r}_1 \, \mathrm{d}\mathbf{r}_2 \, , \tag{7.23}$$

and different contributions of the density matrix

$$D_{\mu\nu,0}^{\sigma\tau} = \sum_i C_{\mu i}^{\sigma} C_{\nu i}^{\tau *} \, . \tag{7.24}$$

The different spin contributions to the Fock matrix are

$$\mathbf{F}_n = \mathbf{F}_n^{\mathrm{Z}} - \mathbf{K}_n[\mathbf{D}_n] \quad \text{with} \quad n \in x, y, z\,. \tag{7.25}$$

Here, $\mathbf{F}_n^{\mathrm{Z}}$ is the spin-Zeeman contribution

$$\mathbf{F}_n^{\mathrm{Z}} = -\frac{1}{2}\mathcal{B}_n \boldsymbol{\sigma}_n \otimes \mathbf{S}\,. \tag{7.26}$$

In practice, the Roothaan-Hall equations need to be solved iteratively, as the Fock matrix is dependent on its eigenvectors through the density matrix. Usually, a start guess for the coefficients is provided by simpler methods such as the extended Hückel theory[128] or a superposition of atomic densities.[129–131] From there, the so-called self-consistent field (SCF) procedure is started, where the Fock matrix is repeatedly constructed from the coefficients of the last iteration until certain criteria no longer change significantly between two iterations. This is called a mean-field process, as the Hartree-Fock equation for one electron contains the mean-field of all other electrons in the system. Possible convergence criteria are the change in electronic energy or the change of the density matrix. Note, that state of the art implementations of the SCF procedure only very rarely follow this simple scheme of diagonalization of the Fock matrix and subsequent construction of the density matrix. Different convergence accelerating techniques such as DIIS[132,133] (direct inversion of the iterative subspace) or a hybrid procedure[134] with a diagonalization-free step can be used in conjunction with convergence stabilizing techniques like damping or level-shifting.

7.5. Kohn-Sham Density Functional Theory

Within the Hartree-Fock theory, the many-electron wave function is approximated as a single Slater determinant. The Slater determinant is build from one-electron wave functions, which are optimized within the mean-field SCF procedure. As a consequence, electron correlation is neglected. Within the context of quantum chemistry, the correlation energy E_{c} of a system is defined as the difference between the exact energy and the Hartree-Fock Energy as[135]

$$E_{\mathrm{c}} = E_{\mathrm{exact}} - E_{\mathrm{HF}}\,. \tag{7.27}$$

The correlation energy is always non-positive, as the Hartree-Fock method is variational and therefore the Hartree-Fock energy can only be at or above the exact energy.[37,93,136] There is a plethora of methods that aim to capture correlation effects. One large family of such methods are post-Hartree-Fock methods that build upon the Hartree-Fock ground state wave function and treat correlation on top of it. Such methods include but are not limited to Møller-Plesset (MP) perturbation theory, coupled-cluster, or configuration interaction (CI) theory. Another way to include electron correlation effects is the approach of density functional theory. The theoretical starting point for DFT are the Hohenberg-Kohn theorems.[137] Simplified, these

theorems state that there exists a one-to-one correspondence between the electron density $\rho(\mathbf{r})$ and the external potential, and therefore also a functional that produces the energy when given the electron density

$$E_{\text{exact}} = E[\rho(\mathbf{r})]\,. \tag{7.28}$$

The exact functional is not known and in practice different approximations have to be made. Especially the kinetic energy functional has no generally satisfactory approximations for molecular systems. Kohn and Sham proposed a solution, where the electron density is once again computed from a Slater determinant that contains non-interacting one-electron wave functions that result in the same density as the fully interacting system. Then, the kinetic energy can be calculated analogously to Hartree-Fock. Kohn-Sham DFT[138] now is one of the most widely used quantum chemical methods.[139–141] The reintroduction of a reference wave function means that all one-electron quantities and the electron-electron Coulomb interaction can be calculated from the orbitals in a straightforward manner. What remains are the exchange and correlation contributions that are described as the exchange-correlation energy E_{xc}. Numerous exchange-correlation functionals exist in the literature and can be categorized into different families. Functionals from the local density approximation (LDA)[142,143] family only depend on the ground state density

$$E_{\text{xc}}^{\text{LDA}}\left[\rho(\mathbf{r})\right]\,, \tag{7.29}$$

the general gradient approximation (GGA)[144] additionally includes the gradient of the density

$$E_{\text{xc}}^{\text{GGA}}\left[\rho(\mathbf{r}), \boldsymbol{\nabla}\rho(\mathbf{r})\right]\,, \tag{7.30}$$

and the meta-generalized gradient approximation (mGGA)[145] also includes the kinetic energy density

$$E_{\text{xc}}^{\text{mGGA}}\left[\rho(\mathbf{r}), \boldsymbol{\nabla}\rho(\mathbf{r}), \tau(\mathbf{r})\right]\,. \tag{7.31}$$

Hybrid functionals also include Hartree-Fock exchange. Global hybrids[146] mix a fixed percentage of HF exchange into the functional while range-separated hybrids[147] scale the amount of HF exchange based on inter-electronic distance. Local hybrid functionals mix different amounts of HF exchange based on certain properties of the density at each point in space.[148] Lastly, double hybrid functionals include contributions similar to expressions found in post-HF methods such as MP perturbation theory.[149] The electronic density, its gradient and the kinetic energy density are easily accessible from the occupied KS orbitals

$$\rho(\mathbf{r}) = \sum_i \psi_i(\mathbf{r})\psi_i^*(\mathbf{r}) \tag{7.32}$$

$$\boldsymbol{\nabla}\rho(\mathbf{r}) = \sum_i \Big(\left[\boldsymbol{\nabla}\psi_i(\mathbf{r})\right]\psi_i^*(\mathbf{r}) + \psi_i(\mathbf{r})\left[\boldsymbol{\nabla}\psi_i^*(\mathbf{r})\right] \Big)\,, \tag{7.33}$$

$$\tau(\mathbf{r}) = \frac{1}{2}\sum_i \left[\hat{\mathbf{p}}\psi_i(\mathbf{r})\right] \cdot \left[\hat{\mathbf{p}}\psi_i(\mathbf{r})\right]^*\,. \tag{7.34}$$

Alternatively they can be expressed using the different Pauli contributions of the density matrix. For example the ground state density can be calculated as

$$\rho_m(\mathbf{r}) = \sum_{\mu\nu} D_{\mu\nu,m} \xi_\mu(\mathbf{r}) \xi_\nu(\mathbf{r})^* \quad \text{with} \quad m \in 0, x, y, z\,. \tag{7.35}$$

This way, the total electronic density ρ_0 can be obtained as well as spin-densities for the different directions of spin polarization. Magnetic fields and relativistic effects such as spin-orbit coupling introduce one more consideration to be made, as they induce currents that have to be taken into account.[85,86,150,151] One way to accomplish this is to use the physical kinetic energy density[84,152,153]

$$\tilde{\tau}_m(\mathbf{r}) = \tau_m(\mathbf{r}) - \frac{|\mathbf{j}^{\mathrm{p}}_m(\mathbf{r})|^2}{2\rho_m(\mathbf{r})}\,, \tag{7.36}$$

which in turn depends on the paramagnetic current density

$$\mathbf{j}^{\mathrm{p}}_m = \frac{1}{2} \sum_{\mu\nu} D_{\mu\nu,m} \Big(\left[\boldsymbol{\nabla} \xi_\mu(\mathbf{r})\right] \xi^*_\nu(\mathbf{r}) - \xi_\mu(\mathbf{r}) \left[\boldsymbol{\nabla} \xi^*_\nu(\mathbf{r})\right] \Big)\,. \tag{7.37}$$

This framework is commonly called current density function theory (cDFT).[84,152] The Fock operator of KSDFT is structurally very similar to the HF Fock operator

$$\hat{F}_{\mathrm{KS}} = \hat{T} + \hat{V} + \hat{J} + \hat{V}_{\mathrm{xc}}\,, \tag{7.38}$$

with the exchange-correlation potential

$$\hat{V}_{\mathrm{xc}} = \frac{\partial E_{\mathrm{xc}}}{\partial \rho(\mathbf{r})}\,, \tag{7.39}$$

with its equivalent matrix representation

$$V^{\mathrm{xc}}_{\mu\nu,m} = \frac{\partial E_{\mathrm{xc}}}{\partial D_{\mu\nu,m}} = \int \frac{\partial f_{\mathrm{xc}}}{\partial D_{\mu\nu,m}}\, \mathrm{d}\mathbf{r}\,. \tag{7.40}$$

Depending on the family of the density functional, this expression can be evaluated using the chain rule for derivatives. The density, its gradient and the kinetic energy density depend on the density matrix

$$V^{\mathrm{xc}}_{\mu\nu,m} = \left(\frac{\partial f_{\mathrm{xc}}}{\partial \rho_m} \frac{\partial \rho_m}{\partial D_{\mu\nu,m}} + \frac{\partial f_{\mathrm{xc}}}{\partial \boldsymbol{\nabla} \rho_m} \frac{\partial \boldsymbol{\nabla} \rho_m}{\partial D_{\mu\nu,m}} + \frac{\partial f_{\mathrm{xc}}}{\partial \tilde{\tau}_m} \frac{\partial \tilde{\tau}_m}{\partial D_{\mu\nu,m}} \right) \mathrm{d}\mathbf{r}\,. \tag{7.41}$$

Each derivative with respect to a density matrix element in eq. 7.41 can be further transformed using the chain rule until a product containing basis functions is obtained. For example, the contribution containing the derivative of the electron density simply results in

$$\frac{\partial f_{\mathrm{xc}}}{\partial \rho_m} \frac{\partial \rho_m}{\partial D_{\mu\nu,m}} = \frac{\partial f_{\mathrm{xc}}}{\partial \rho_m} \xi_\mu(\mathbf{r}) \xi^*_\nu(\mathbf{r})\,. \tag{7.42}$$

In state of the art implementations, the integration over such expressions for different DFT contributions is evaluated by numerical integration schemes on a three dimensional grid.[154]

8. The Electronic Hamiltonian

In this section, different approaches for constructing the electronic Hamiltonian are discussed. It begins with the Dirac equation for the description of relativistic systems. Afterwards, two distinct cases are considered: First, the non-relativistic limit is presented, where the Pauli equation is obtained to explicitly treat the presence of external fields. Second, a decoupling for the Dirac equation is shown for the absence of external fields. Here, a two-component framework is obtained to treat relativistic effects for electronic systems.

8.1. The Dirac-Hamiltonian

To obtain a relativistic equation that is analogous to the non-relativistic Schrödinger equation, Dirac used the correspondence principle on the well-known mass-energy equivalence of special relativity.[155] After some algebraic work to handle the squared energy expression, his equation[113] reads

$$\left(\boldsymbol{\beta} c^2 + c\overrightarrow{\boldsymbol{\alpha}} \cdot \hat{\boldsymbol{\pi}}\right) \Psi = \mathrm{i}\frac{\partial}{\partial t}\Psi \,, \tag{8.1}$$

with the speed of light in a vacuum c. The two operators on the left-hand side describe the rest energy and the kinetic energy of a free particle. To simplify the notation of later equations, the vector containing all three Pauli spin matrices is written as

$$\overrightarrow{\boldsymbol{\sigma}} = \begin{pmatrix} \boldsymbol{\sigma}_x \\ \boldsymbol{\sigma}_y \\ \boldsymbol{\sigma}_z \end{pmatrix} . \tag{8.2}$$

The expression for the rest energy contains the 4×4 matrix

$$\boldsymbol{\beta} = \begin{pmatrix} \boldsymbol{\sigma}_0 & \mathbf{0}_2 \\ \mathbf{0}_2 & -\boldsymbol{\sigma}_0 \end{pmatrix} , \tag{8.3}$$

while the expression for the kinetic energy contains the vector $\overrightarrow{\boldsymbol{\alpha}}$ with three individual 4×4 matrices that read

$$\boldsymbol{\alpha}_m = \begin{pmatrix} \mathbf{0}_2 & \boldsymbol{\sigma}_m \\ \boldsymbol{\sigma}_m & \mathbf{0}_2 \end{pmatrix} \qquad \text{with}\, m \in \{x, y, z\} \,, \tag{8.4}$$

where $\mathbf{0}_2$ is the 2×2 zero matrix. The presence of the Pauli spin matrices shows that the Dirac equation intrinsically contains a description of the electronic spin. In contrast, the Schrödinger equation does not contain such a description naturally and

spin needs to be introduced in a more *ad hoc* manner. From the dimensions of $\overrightarrow{\boldsymbol{\alpha}}$ and $\boldsymbol{\beta}$ it is apparent that the wave function Ψ in the Dirac equation must also be a vector with four components

$$\Psi = \begin{pmatrix} \Psi_\mathrm{L} \\ \Psi_\mathrm{S} \end{pmatrix} , \tag{8.5}$$

which is commonly written in terms of the so called large component Ψ_L and small component Ψ_S, which are two-component wave functions. It is useful to write down the time independent Dirac equation while explicitly showing both two-component wave functions

$$\begin{pmatrix} c^2\boldsymbol{\sigma}_0 & c\overrightarrow{\boldsymbol{\sigma}}\cdot\hat{\boldsymbol{\pi}} \\ c\overrightarrow{\boldsymbol{\sigma}}\cdot\hat{\boldsymbol{\pi}} & -c^2\boldsymbol{\sigma}_0 \end{pmatrix} \begin{pmatrix} \Psi_\mathrm{L} \\ \Psi_\mathrm{S} \end{pmatrix} = E \begin{pmatrix} \Psi_\mathrm{L} \\ \Psi_\mathrm{S} \end{pmatrix} . \tag{8.6}$$

The Dirac equation gives rise not only to electronic states, but also to positronic states. Therefore, it is useful to decouple the electronic and positronic states, since most often only the electronic states are of interest in quantum chemistry.

8.2. Many Electron Systems

The previous section introduced the Dirac-Hamiltonian for one free particle. For a proper description of molecular systems, usually many electrons within a potential need to be considered. Inclusion of a potential energy operator $\hat{\mathbf{V}}$, typically the Coulomb potential of the nuclei in the molecule's rest frame, is straightforward. Additionally, the diagonal of the Hamiltonian is often shifted down by c^2 which recovers the electronic energies of the Schrödinger equation in a non-relativistic limit. These modifications give the following one-electron Dirac-Hamilton operator:

$$\hat{h}_\mathrm{Dirac} = (\boldsymbol{\beta} - \mathbf{1}_4)\, c^2 + c\overrightarrow{\boldsymbol{\alpha}}\cdot\hat{\boldsymbol{\pi}} + \mathbf{1}_4\hat{V} . \tag{8.7}$$

The generalization to many-electron systems requires summing over all individual one-electron contributions and the addition of the two-electron Coulomb operator

$$\hat{g}(i,j) = \frac{1}{|\mathbf{r}_i - \mathbf{r}_j|} , \tag{8.8}$$

to arrive at the Dirac-Coulomb-Hamiltonian[99,156,157]

$$\hat{H}_\mathrm{DC} = \sum_i \hat{h}_\mathrm{Dirac}(i) + \sum_{i<j} \hat{g}(i,j) . \tag{8.9}$$

Although the Dirac-Coulomb-Hamiltonian finds wide application in the literature, it entails a few mostly undesired properties. Namely, Lorentz invariancy is not fully preserved[99,157] or that occupation of positronic states is possible and could lead to the so-called variational collapse[158].

8.3. The Pauli Equation

In this section, the non-relativistic limit to the four-component Dirac equation is considered. The starting point is the time-independent Dirac-equation 8.6, where the modifications discussed in the previous section 8.2 are included to treat many-electron systems. Evaluation of the matrix vector product gives the two coupled equations

$$\hat{\mathbf{V}}\Psi_\mathrm{L} + c\overrightarrow{\boldsymbol{\sigma}} \cdot \hat{\boldsymbol{\pi}}\Psi_\mathrm{S} = E\Psi_\mathrm{L}\,, \tag{8.10}$$

$$c\overrightarrow{\boldsymbol{\sigma}} \cdot \hat{\boldsymbol{\pi}}\Psi_\mathrm{L} + \left(\hat{\mathbf{V}} - 2c^2\right)\Psi_\mathrm{S} = E\Psi_\mathrm{S}\,. \tag{8.11}$$

Rearranging the second equation results in

$$\frac{\overrightarrow{\boldsymbol{\sigma}} \cdot \hat{\boldsymbol{\pi}}}{2c}\Psi_\mathrm{L} = \left(1 + \frac{E - \hat{\mathbf{V}}}{2c^2}\right)\Psi_\mathrm{S}\,. \tag{8.12}$$

Defining the inverse of the compound operator on the right-hand side as $\hat{Y}$ one obtains

$$\Psi_\mathrm{S} = \hat{Y}\frac{\overrightarrow{\boldsymbol{\sigma}} \cdot \hat{\boldsymbol{\pi}}}{2c}\Psi_\mathrm{L}\,. \tag{8.13}$$

Using the geometric series or equivalently expanding $\hat{Y}$ in a Taylor series in orders of $1/c^2$ produces

$$\hat{Y} = \left(1 + \frac{E - \hat{\mathbf{V}}}{2c^2}\right)^{-1} = 1 - \frac{E - \hat{\mathbf{V}}}{2c^2} + \left(\frac{E - \hat{\mathbf{V}}}{2c^2}\right)^2 + \ldots\,. \tag{8.14}$$

Considering the non-relativistic limit $c \to \infty$, only the first term does not vanish, yielding $\hat{Y} = 1$. Substitution back into eq. 8.10 gives the Pauli equation[114]

$$\left(\frac{1}{2}\left(\overrightarrow{\boldsymbol{\sigma}} \cdot \hat{\boldsymbol{\pi}}\right)^2 + \hat{\mathbf{V}}\right)\Psi_\mathrm{L} = E\Psi_\mathrm{L}\,, \tag{8.15}$$

where evaluation of the squared operator gives rise to several contributions originating from the magnetic vector potential. Using the Dirac identity[99]

$$\left(\overrightarrow{\boldsymbol{\sigma}} \cdot \mathbf{a}\right) \cdot \left(\overrightarrow{\boldsymbol{\sigma}} \cdot \mathbf{b}\right) = \boldsymbol{\sigma}_0 + \mathrm{i}\overrightarrow{\boldsymbol{\sigma}} \cdot (\mathbf{a} \times \mathbf{b})\,, \tag{8.16}$$

one finds

$$\left(\overrightarrow{\boldsymbol{\sigma}} \cdot \hat{\boldsymbol{\pi}}\right)^2 = \boldsymbol{\sigma}_0\hat{\boldsymbol{\pi}}^2 + \overrightarrow{\boldsymbol{\sigma}} \cdot \mathcal{B}\,. \tag{8.17}$$

The squared kinetic momentum operator in the symmetric gauge, introduced in eq. 6.15, reads

$$\hat{\boldsymbol{\pi}}^2 = \hat{\mathbf{p}}^2 + \mathcal{B} \cdot (\mathbf{r}^\mathbf{O} \times \hat{\mathbf{p}}) + \frac{1}{4}\left[\mathcal{B}^2\left(\mathbf{r}^\mathbf{O}\right)^2 - \left(\mathcal{B} \cdot \mathbf{r}^\mathbf{O}\right)^2\right]\,, \tag{8.18}$$

from where different contributions to the Hamiltonian in the Pauli equation 8.15 can finally be identified. The field free Hamiltonian is contained within this expression as

$$\hat{H}_0 = \frac{1}{2}\hat{\mathbf{p}}^2 + \hat{V}\,. \tag{8.19}$$

Two paramagnetic contributions, that are linear in $\mathcal{B}$, can be found.[136] By noticing an angular momentum operator in eq. 8.18 as $\hat{\boldsymbol{l}}^{\mathbf{O}} = \mathbf{r}^{\mathbf{O}} \times \hat{\mathbf{p}}$, the orbital-Zeeman contribution is obtained as

$$\hat{H}_{\mathrm{BL}} = \frac{1}{2}\mathcal{B} \cdot \hat{\boldsymbol{l}}^{\mathbf{O}} \,, \tag{8.20}$$

while the spin-Zeeman contribution reads

$$\hat{H}_{\mathrm{BS}} = \frac{1}{2}\mathcal{B} \cdot \overrightarrow{\boldsymbol{\sigma}} \,. \tag{8.21}$$

Lastly, the diamagnetic contribution, which is quadratic in the magnetic fields is[136]

$$\hat{H}_{\mathrm{dia}} = \frac{1}{8}\left[\mathcal{B}^2 \left(\mathbf{r}^{\mathbf{O}}\right)^2 - \left(\mathcal{B} \cdot \mathbf{r}^{\mathbf{O}}\right)^2\right] \,. \tag{8.22}$$

In conclusion, a non-relativistic two-component equation can be derived that explicitly includes the external magnetic field. In the absence of a field, the equation recovers the field-free two-component Schrödinger equation.

8.4. Exact Two-Component Decoupling

The aim of this chapter is to introduce the exact two-component Hamiltonian[159–163] for relativistic quantum chemical calculations. The necessary setup was discussed in previous sections: Section 8.3 concluded by attempting to decouple electronic and positronic states by a Taylor expansion of the operator. The previous sections 7.4 and 7.5 discussed how expansion of the Hartree-Fock or KS-DFT equations in a finite basis lead to matrix eigenvalue equations.

Recall the one-electron Dirac Hamiltonian from eq. 8.7, which does not include the electron-electron interaction potential

$$\hat{h}_{\mathrm{Dirac}} = \left(\boldsymbol{\beta} - \mathbf{1}_4\right) c^2 + c\overrightarrow{\boldsymbol{\alpha}} \cdot \hat{\boldsymbol{\pi}} + \mathbf{1}_4 \hat{V} \,. \tag{8.23}$$

The non relativistic limit of eq. 8.13

$$\Psi_{\mathrm{S}} = \frac{\overrightarrow{\boldsymbol{\sigma}} \cdot \hat{\boldsymbol{\pi}}}{2c} \Psi_{\mathrm{L}} \,, \tag{8.24}$$

provides a relation between the large and small component of the wave function. This relation needs to be preserved in the basis set expansion and is called the restricted magnetic balance condition.[158,164] Following this relation, the LCAO for a spinor of the large and small component respectively reads

$$\psi_{\mathrm{L},p} = \sum_{\mu} C^{\mathrm{L}}_{\mu p} \xi_{\mu} \,, \tag{8.25}$$

$$\psi_{\mathrm{S},p} = \sum_{\mu} C^{\mathrm{S}}_{\mu p} \frac{\overrightarrow{\boldsymbol{\sigma}} \cdot \hat{\boldsymbol{\pi}}}{2c} \xi_{\mu} \,. \tag{8.26}$$

Expansion of the Dirac equation in this basis then gives

$$\begin{pmatrix} \mathcal{V} & \mathcal{T} \\ \mathcal{T} & \frac{1}{4c^2}\mathcal{W} - \mathcal{T} \end{pmatrix} \begin{pmatrix} \mathbf{C}_+^{\mathrm{L}} & \mathbf{C}_-^{\mathrm{L}} \\ \mathbf{C}_+^{\mathrm{S}} & \mathbf{C}_-^{\mathrm{S}} \end{pmatrix} = \begin{pmatrix} \mathcal{S} & \mathbf{0}_2 \\ \mathbf{0}_2 & \frac{1}{2c^2}\mathcal{T} \end{pmatrix} \begin{pmatrix} \mathbf{C}_+^{\mathrm{L}} & \mathbf{C}_-^{\mathrm{L}} \\ \mathbf{C}_+^{\mathrm{S}} & \mathbf{C}_-^{\mathrm{S}} \end{pmatrix} \begin{pmatrix} \boldsymbol{\epsilon}_+ & \mathbf{0}_2 \\ \mathbf{0}_2 & \boldsymbol{\epsilon}_- \end{pmatrix}, \tag{8.27}$$

which is a generalized matrix eigenvalue equation, similarly to the previously discussed Roothaan-Hall equation. Calligraphically written matrices in eq. 8.27 are themselves 2×2 supermatrices. $\mathcal{S}$, $\mathcal{T}$ and $\mathcal{V}$ are given by the Kronecker product of the overlap, kinetic energy and electron-nucleus attraction matrices in AO basis

$$\mathcal{M} = \boldsymbol{\sigma}_0 \otimes \mathbf{M} = \begin{pmatrix} \mathbf{M} & \mathbf{0} \\ \mathbf{0} & \mathbf{M} \end{pmatrix} \quad \text{with} \quad \mathcal{M} = \mathcal{S}, \mathcal{T}, \mathcal{V}\,. \tag{8.28}$$

The matrix representation of the relativistically modified potential is not block diagonal, as its matrix elements are given by the integral over the operator[165,166]

$$\hat{W} = (\overrightarrow{\boldsymbol{\sigma}} \cdot \hat{\boldsymbol{\pi}})\hat{V}(\overrightarrow{\boldsymbol{\sigma}} \cdot \hat{\boldsymbol{\pi}})\,, \tag{8.29}$$

therefore the $\mathcal{W}$ matrix can be written as[157]

$$\mathcal{W} = \begin{pmatrix} \mathbf{W}_0 + \mathrm{i}\mathbf{W}_z & \mathrm{i}\mathbf{W}_x + \mathbf{W}_y \\ \mathrm{i}\mathbf{W}_x - \mathbf{W}_y & \mathbf{W}_0 - \mathrm{i}\mathbf{W}_z \end{pmatrix}. \tag{8.30}$$

Here, the individual contributions can be calculated from

$$W_{0,\mu\nu} = \langle \xi_\mu | \hat{\boldsymbol{\pi}} \cdot (\hat{V}\hat{\boldsymbol{\pi}}) | \xi_\nu \rangle\,, \tag{8.31}$$

and

$$W_{n,\mu\nu} = \langle \xi_\mu | [\hat{\boldsymbol{\pi}} \times (\hat{V}\hat{\boldsymbol{\pi}})]_n | \xi_\nu \rangle \quad \text{with} \quad n \in x, y, z\,. \tag{8.32}$$

In a subsequent step, the decoupling of the electronic and positronic states can be carried out. This decoupling is achieved after the expansion in a finite basis. Here, the one-electron Dirac matrix can be block diagonalized by applying a unitary transformation

$$\begin{pmatrix} \mathbf{U}_{\mathrm{LL}} & \mathbf{U}_{\mathrm{LS}} \\ \mathbf{U}_{\mathrm{SL}} & \mathbf{U}_{\mathrm{SS}} \end{pmatrix}^\dagger \begin{pmatrix} \mathcal{V} & \mathcal{T} \\ \mathcal{T} & \frac{1}{4c^2}\mathcal{W} - \mathcal{T} \end{pmatrix} \begin{pmatrix} \mathbf{U}_{\mathrm{LL}} & \mathbf{U}_{\mathrm{LS}} \\ \mathbf{U}_{\mathrm{SL}} & \mathbf{U}_{\mathrm{SS}} \end{pmatrix} = \begin{pmatrix} \mathbf{h}_+ & \mathbf{0}_2 \\ \mathbf{0}_2 & \mathbf{h}_- \end{pmatrix} \tag{8.33}$$

The corresponding decoupling operator $\hat{U}$ was derived by Heully *et. al*[167] as

$$\begin{pmatrix} \hat{U}_{\mathrm{LL}} & \hat{U}_{\mathrm{LS}} \\ \hat{U}_{\mathrm{SL}} & \hat{U}_{\mathrm{SS}} \end{pmatrix} = \begin{pmatrix} 1 & -\hat{X} \\ \hat{X} & 1 \end{pmatrix} \begin{pmatrix} \hat{R} & 0 \\ 0 & \hat{R} \end{pmatrix}, \tag{8.34}$$

where $\hat{X}$ decouples the states and $\hat{R}$ renormalizes each component. The decoupling operator already showed up in the derivation of the Dirac equation as

$$\hat{X} = \hat{Y}\frac{\overrightarrow{\boldsymbol{\sigma}} \cdot \hat{\boldsymbol{\pi}}}{2c}\,, \tag{8.35}$$

which is difficult to work with, since the $\hat{Y}$ operator is energy dependent. Now, that the Dirac equation has been cast into a matrix representation, the decoupling can be constructed from the eigenvectors of the four-component Dirac equation as

$$\mathbf{X} = \mathbf{C}_+^{\mathrm{S}} (\mathbf{C}_+^{\mathrm{L}})^{-1} \,. \tag{8.36}$$

Once the decoupling matrices have been constructed, the electronic part of the one-electron Hamiltonian[157]

$$\begin{aligned} \mathbf{h}_+ &= \begin{pmatrix} \mathbf{U}_{\mathrm{LL}} \\ \mathbf{U}_{\mathrm{SL}} \end{pmatrix}^\dagger \begin{pmatrix} \mathcal{V} & \mathcal{T} \\ \mathcal{T} & \frac{1}{2c^2}\mathcal{W} - \mathcal{T} \end{pmatrix} \begin{pmatrix} \mathbf{U}_{\mathrm{LL}} \\ \mathbf{U}_{\mathrm{SL}} \end{pmatrix} \\ &= \mathbf{R}^\dagger \left[\mathcal{V} + \mathbf{X}^\dagger \mathcal{T} + \mathcal{T}\mathbf{X} + \mathbf{X}^\dagger \left(\frac{1}{2c^2}\mathcal{W} - \mathcal{T} \right) \mathbf{X} \right] \mathbf{R} \,, \end{aligned} \tag{8.37}$$

can be computed and used as the one-electron contribution in a relativistic calculation. On a practical note, it is important to point out that this decoupling needs to be done in the decontracted basis, because the large and small component show different requirements on the basis set.[160,168,169] An additional consequence of this approach is that any derivative of the one-electron part of the Hamiltonian matrix is no longer a simple derivative of an integral. Here, the derivative of the decoupling enters as well and therefore the derivative of the eigenvectors of the Dirac matrix.[170]

9. Coupled Perturbed Hartree-Fock and Kohn-Sham Equations

The previous chapters discussed how to obtain an approximate solution to the electronic Schrödinger equation and how to set up electronic Hamiltonians for a relativistic framework and for molecules in external magnetic fields. Quantum geometric properties like the Berry curvature or the Fubini-Study metric depend on the geometry derivative of the electronic wave function. The solutions of the coupled perturbed Hartree-Fock (CPHF) or Kohn-Sham (CPKS) equations provide this derivative in practical calculations and are discussed in this section.

9.1. Derivative Spinor Functions

To construct the derivative of a Slater determinant with respect to any perturbation λ, the derivative of the individual spinor functions needs to be determined. Within the LCAO approach this leads to

$$\frac{\partial \psi_i}{\partial \lambda} = \sum_{\tau\mu} C^{\tau}_{\mu i} \frac{\partial \xi_\mu}{\partial \lambda} + \sum_{\tau\mu} \frac{\partial C^{\tau}_{\mu i}}{\partial \lambda} \xi_\mu \,, \tag{9.1}$$

where the first sum contains derivatives of the basis function which are straightforward to build analytically. The second sum contains the derivative of the spinor coefficients. This derivative can be expanded in the basis of the unperturbed spinor coefficients as

$$\frac{\partial C^{\tau}_{\mu i}}{\partial \lambda} = \sum_{p} C^{\tau}_{\mu p} U^{\tau}_{p i} \,. \tag{9.2}$$

Please note that only the derivative of occupied spinor functions is needed to compute derivative properties of the ground state Slater determinant. The equations that produce this $\mathbf{U}$ matrix are called the coupled perturbed Hartree-Fock or Kohn-Sham equations respectively.[136,171,172] These equations are obtained from the derivative of certain properties known about the underlying SCF equations. Namely the orthonormality of the spinors

$$S_{pq} = \sum_{\mu\nu\tau} C^{\tau *}_{\mu p} S_{\mu\nu} C^{\tau}_{\nu q} = \left[\mathbf{C}^\dagger \mathbf{S} \mathbf{C}\right]_{pq} = \delta_{pq} \,, \tag{9.3}$$

and Brillouin's theorem[173]

$$F_{ai} = \sum_{\mu\nu\sigma\tau} C^{\sigma *}_{\mu a} F^{\sigma\tau}_{\mu\nu} C^{\tau}_{\nu i} = \left[\mathbf{C}^\dagger \mathbf{F} \mathbf{C}\right]_{ai} = 0 \,. \tag{9.4}$$

9.2. Derivation of the CPHF equations

The derivations in this section mostly follow Ref. [43] from Culpitt *et al.* Taking the derivative of eq. 9.3 via the product rule gives

$$\begin{aligned}\frac{\partial S_{pq}}{\partial \lambda} &= \left[\frac{\partial \mathbf{C}^\dagger}{\partial \lambda}\mathbf{S}\mathbf{C}\right]_{pq} + \left[\mathbf{C}^\dagger\frac{\partial \mathbf{S}}{\partial \lambda}\mathbf{C}\right]_{pq} + \left[\mathbf{C}^\dagger\mathbf{S}\frac{\partial \mathbf{C}}{\partial \lambda}\right]_{pq} \\ &= \left[\mathbf{U}^\dagger\mathbf{C}^\dagger\mathbf{S}\mathbf{C}\right]_{pq} + \left[\mathbf{C}^\dagger\frac{\partial \mathbf{S}}{\partial \lambda}\mathbf{C}\right]_{pq} + \left[\mathbf{C}^\dagger\mathbf{S}\mathbf{C}\mathbf{U}\right]_{pq} \\ &= U^*_{qp} + \mathcal{S}^\lambda_{pq} + U_{pq} \\ &= 0\,.\end{aligned} \tag{9.5}$$

Here, the matrix elements $\mathcal{S}_{pq}$ contain derivative integrals that are transformed into the unperturbed spinor basis

$$\mathcal{S}_{pq} = \sum_{\tau\mu\nu} C^{\tau *}_{\mu p}\frac{\partial S_{\mu\nu}}{\partial \lambda}C^{\tau}_{\nu q}\,. \tag{9.6}$$

This kind of matrix, where only the integrals are derivatives is commonly encountered within the context of the CPHF equations and is denoted using curly letters ($\mathcal{S}, \mathcal{F}$). From eq. 9.5 it becomes apparent that the diagonal of $\mathbf{U}$ can be chosen freely as long as they satisfy the condition

$$U^*_{pp} + U_{pp} + \mathcal{S}_{pp} = 0\,, \tag{9.7}$$

similarly, the occupied-occupied block can be chosen as

$$U_{ij} = -\frac{1}{2}\mathcal{S}_{ij}\,, \tag{9.8}$$

without loss of generality. To obtain a condition for the occupied-virtual block of the $\mathbf{U}$ matrix, the derivative of Brillouin's theorem in eq. 9.4 needs to be formed. This is very similar to the derivative of the overlap matrix and results in the following expression for one derivative matrix element

$$\frac{\partial F_{ai}}{\partial \lambda} = \sum_p U^*_{pa}F_{pi} + \mathcal{F}_{ai} + \sum_p F_{ap}U_{pi} = 0\,, \tag{9.9}$$

inserting Brillouin's theorem again eliminates the off-diagonal blocks, leading to

$$\frac{\partial F_{ai}}{\partial \lambda} = \sum_j U^*_{ja}F_{ji} + \mathcal{F}_{ai} + \sum_b F_{ab}U_{bi} = 0\,. \tag{9.10}$$

Using the canonicity of the Fock matrix, eq. 9.10 can be written as

$$\frac{\partial F_{ai}}{\partial \lambda} = U^*_{ia}\epsilon_i + \mathcal{F}_{ai} + U_{ai}\epsilon_a = 0\,, \tag{9.11}$$

which still contains both, the occupied-virtual and virtual-occupied block of the **U** matrix. To eliminate one of the blocks, the corresponding case of eq. 9.5 can be considered to obtain:

$$\begin{aligned} & U_{ia}^{*} + \mathcal{S}_{ai} + U_{ai} = 0 \\ \Leftrightarrow \quad & U_{ia}^{*} = -\mathcal{S}_{ai} - U_{ai} \,. \end{aligned} \tag{9.12}$$

Using this identity, the final expression for the occupied-virtual block becomes

$$\begin{aligned} & \mathcal{F}_{ai} + U_{ai}\epsilon_a = \epsilon_i \left(\mathcal{S}_{ai} + U_{ai}\right) \\ \Leftrightarrow \quad & \left(\epsilon_a - \epsilon_i\right) U_{ai} = \epsilon_i \mathcal{S}_{ai} - \mathcal{F}_{ai} \,. \end{aligned} \tag{9.13}$$

All that remains is to treat $\mathcal{F}_{ai}$, since the Fock matrix contains the ground state density matrix and is therefore dependent on the occupied block of the coefficient matrix itself. The Fock matrix can generally be written as consisting of a density independent one-electron part and a density dependent two-electron part

$$F_{ai} = h_{ai} + G_{ai}[\mathbf{D}] \,. \tag{9.14}$$

Taking the derivative only of the AO contributions leads to two contributions originating from the two-electron term from the chain rule

$$\mathcal{F}_{ai} = \hbar_{ai} + \mathcal{G}_{ai}[\mathbf{D}] + G_{ai}[\mathbf{D}^{\lambda}] \,, \tag{9.15}$$

where the superscript λ on the density matrix indicates that it is the derivative density matrix. From this, the last remaining contribution that contains the **U** matrix emerges

$$\begin{aligned} \frac{\partial D_{\mu\nu}^{\sigma\tau}}{\partial \lambda} = [\mathbf{D}^{\lambda}]_{\mu\nu}^{\sigma\tau} &= \sum_{ip} C_{\mu p}^{\sigma} U_{pi} C_{\nu i}^{\tau *} + \sum_{ip} C_{\mu i}^{\sigma} C_{\nu p}^{\tau *} U_{pi}^{*} \\ &= \sum_{ia} C_{\mu a}^{\sigma} U_{ai} C_{\nu i}^{\tau *} + \sum_{ia} C_{\mu i}^{\sigma} C_{\nu a}^{\tau *} U_{ai}^{*} - \sum_{ij} C_{\mu i}^{\sigma} \mathcal{S}_{ij} C_{\nu j}^{\tau *} \,. \end{aligned} \tag{9.16}$$

Taking a look at the other contributions in eq. 9.15, one encounters the AO derivative one-particle Hamiltonian as

$$\hbar_{ai} = \sum_{\mu\nu\sigma\tau} C_{\mu a}^{\sigma *} \frac{\partial h_{\mu\nu}^{\sigma\tau}}{\partial \lambda} C_{\nu i}^{\tau} \,, \tag{9.17}$$

and the AO derivative two-particle term as

$$\mathcal{G}_{ai}[\mathbf{D}] = \sum_{\substack{\mu\nu\kappa\iota \\ \sigma\tau\sigma'\tau'}} C_{\mu a}^{\sigma *} C_{\nu i}^{\tau} \frac{\partial (\mu\nu||\kappa\iota)}{\partial \lambda} D_{\iota\kappa}^{\sigma'\tau'} \,. \tag{9.18}$$

The third contribution containing the derivative density matrix again gives rise to several terms:

$$\begin{aligned} G_{ai}[\mathbf{D}^{\lambda}] &= \sum_{\kappa\iota\sigma\tau} (ai||\kappa\iota) \left(\sum_{jb} C_{\iota b}^{\sigma} U_{bj} C_{\kappa j}^{\tau *} + \sum_{jb} C_{\iota j}^{\sigma} C_{\kappa b}^{\tau *} U_{bj}^{*} - \sum_{kl} C_{\iota k}^{\sigma} \mathcal{S}_{kl} C_{\kappa l}^{\tau *} \right) \\ &= \sum_{jb} (ai||jb) U_{bj} + \sum_{jb} (ai||bj) U_{bj}^{*} - \sum_{kl} (ai||lk) \mathcal{S}_{kl} \end{aligned} \tag{9.19}$$

Before setting up the CPHF equations, another auxiliary quantity can be defined such that the final expression is more concise. The Fock-like matrix that only contains derivatives of AO integrals, is written as

$$\mathscr{F}_{ai}^{(\lambda)} = \mathscr{h}_{ai} + \mathscr{G}_{ai}[\mathbf{D}] \,. \tag{9.20}$$

From here, it is straightforward to set up the CPHF equations by substituting all expressions into eq. 9.13, obtaining

$$(\epsilon_a - \epsilon_i)\, U_{ai} + \sum_{jb}(ai||jb)U_{bj} + \sum_{jb}(ai||bj)U_{bj}^* = \epsilon_i \mathcal{S}_{ai} - \mathscr{F}_{ai}^{(\lambda)} + \sum_{kl}(ai||lk)\mathcal{S}_{kl} \,. \tag{9.21}$$

Identifying the coefficients of $\mathbf{U}$ and $\mathbf{U}^*$ respectively, leads to the two matrices

$$A_{ai,bj} = (\epsilon_a - \epsilon_i)\, \delta_{ij}\delta_{ab} + (ai||jb) \,, \tag{9.22}$$

and

$$B_{ai,bj} = (ai||bj) \,. \tag{9.23}$$

The right-hand side of eq. 9.21 is summarized as

$$F_{ai}^{\mathrm{RHS}} = \epsilon_i \mathcal{S}_{ai} - \mathscr{F}_{ai}^{(\lambda)} + \sum_{kl}(ai||lk)\mathcal{S}_{kl} \,, \tag{9.24}$$

leading to an even more concise way to write down the CPHF equations

$$\mathbf{AU} + \mathbf{BU}^* = \mathbf{F}^{\mathrm{RHS}} \,. \tag{9.25}$$

9.3. Conversion to a Hermitian System of Equations

The form presented in eq. 9.25 is usually not implemented in standard quantum chemistry software. The main disadvantage is that the operator

$$\mathcal{L}(\mathbf{U}) = \mathbf{AU} + \mathbf{BU}^* \,, \tag{9.26}$$

is not a linear operator over $\mathbb{C}$ since

$$\mathcal{L}(z\mathbf{U}) = z\mathbf{AU} + z^*\mathbf{BU}^* \neq z\mathbf{AU} + z\mathbf{BU}^* = z\mathcal{L}(\mathbf{U}) \,. \tag{9.27}$$

Many approaches to solve large linear systems of equations are only applicable for complex linear operators, such as commonly used Krylov subspace methods.[174] Constructing an operator that fulfills this requirement is easily achieved by additionally considering the complex conjugate of eq. 9.25, leading to

$$\begin{pmatrix} \mathbf{A} & \mathbf{B} \\ \mathbf{B}^* & \mathbf{A}^* \end{pmatrix} \begin{pmatrix} \mathbf{U} \\ \mathbf{U}^* \end{pmatrix} = \begin{pmatrix} \mathbf{F}^{\mathrm{RHS}} \\ \mathbf{F}^{\mathrm{RHS}*} \end{pmatrix} \,, \tag{9.28}$$

where now

$$\mathcal{L}'(\mathbf{V}) = \begin{pmatrix} \mathbf{A} & \mathbf{B} \\ \mathbf{B}^* & \mathbf{A}^* \end{pmatrix} \mathbf{V} \,, \tag{9.29}$$

is not only linear over $\mathbb{C}$ but also Hermitian. Note, that the 2×2 super-matrix containing the $\mathbf{A}$ and $\mathbf{B}$ matrices is commonly referred to as the electronic Hessian, since it is related to the second derivative of the electronic energy with respect to orbital rotations. The electronic Hessian is an important and recurring matrix within linear response theory, and not only occurs in the calculation of static properties, but also in the calculation of excitation energies within time-dependent perturbation theory or the investigation of electronic instabilities.[175–181] This similarity also means that any implementation that can compute the product of the electronic Hessian with an arbitrary vector, can be modified for all of the previously mentioned applications.

9.4. Coupled Perturbed Kohn-Sham Equations

The presentation of the CPKS equations in this section follows Ref. [83] which was published in collaboration with Kronenberger, Appenzeller, and Pausch. So far, only the Hartree-Fock Fock operator has been considered, where the two-electron interaction solely consists of the Coulomb and exchange contributions. Now, the Kohn-Sham Fock operator containing the exchange correlation contribution is discussed. In a very similar fashion to the derivation presented in the previous section, two terms arise from the exchange-correlation part. One term depends only on the ground state density, which enters the CPKS equations on the right-hand side. The other term depends on the $\mathbf{U}$ matrix through the derivative density matrix, hence, it enters the electronic Hessian on the left-hand side of the CPKS equations. Considering the general KS Fock matrix

$$\mathbf{F}^{\mathrm{KS}} = \mathbf{h} + \mathbf{G}[\mathbf{D}] + \mathbf{V}^{\mathrm{xc}}[\mathbf{D}]\,, \tag{9.30}$$

where $\mathbf{G}$ contains the Coulomb integrals, and, in the case of hybrid functionals, scaled exchange integrals.

9.4.1. CPKS Equations for LDAs

To start of, the LDA case is discussed where one spin contribution to the exchange-correlation matrix can be written as

$$V^{\mathrm{xc}}_{\mu\nu,m} = \frac{\partial E_{\mathrm{xc}}}{\partial D_{\mu\nu,m}} = \int \frac{\partial f^{\mathrm{xc}}}{\partial \rho_m} \frac{\partial \rho_m}{\partial D_{\mu\nu,m}}\,\mathrm{d}\mathbf{r} = \int \frac{\partial f^{\mathrm{xc}}}{\partial \rho_m} \xi_\mu \xi^*_\nu\,. \tag{9.31}$$

Taking the derivative with respect to a perturbation leads to

$$\frac{\partial V^{\mathrm{xc}}_{\mu\nu,m}}{\partial \lambda} = \int \left(\sum_l \frac{\partial^2 f^{\mathrm{xc}}}{\partial \rho_m \rho_l} \frac{\partial \rho_l}{\partial \lambda} \frac{\partial \rho_m}{\partial D_{\mu\nu,m}} + \frac{\partial f^{\mathrm{xc}}}{\partial \rho_m} \frac{\partial^2 \rho_m}{\partial \lambda \partial D_{\mu\nu,m}}\,\mathrm{d}\mathbf{r} \right)\,, \tag{9.32}$$

where the identity

$$\frac{\partial f^{\mathrm{xc}}}{\partial \lambda} = \sum_{l \in 0,x,y,z} \frac{\partial f^{\mathrm{xc}}}{\partial \rho_l} \frac{\partial \rho_l}{\partial \lambda}\,, \tag{9.33}$$

and the span of the sum over l was not written out for the sake of conciseness. The derivative of the electronic ground state density is given by

$$\begin{aligned}\frac{\partial \rho_l}{\partial \lambda} &= \frac{\partial}{\partial \lambda} \sum_{\mu\nu} D_{\mu\nu,l} \xi_\mu \xi_\nu^* \\ &= \sum_{\mu\nu} D^\lambda_{\mu\nu,l} \xi_\mu \xi_\nu^* + \sum_{\mu\nu} D_{\mu\nu,l} \frac{\partial(\xi_\mu \xi_\nu^*)}{\partial \lambda} \,.\end{aligned} \tag{9.34}$$

From here, the two distinct contributions that emerge can be written down in the style of the previous section as

$$\mathcal{V}^{\mathrm{xc}}_{\mu\nu,m}[\mathbf{D}^\lambda] = \int \left(\xi_\mu \xi_\nu^* \sum_l \frac{\partial^2 f^{\mathrm{xc}}}{\partial \rho_m \rho_l} \sum_{\kappa\iota} D^\lambda_{\kappa\iota,l} \xi_\mu \xi_\nu^* \right) \mathrm{d}\mathbf{r} \,, \tag{9.35}$$

and

$$\mathcal{V}^{\mathrm{xc},(\lambda)}_{\mu\nu,m}[\mathbf{D}_m] = \int \left(\frac{\partial f^{\mathrm{xc}}}{\partial \rho_m} \frac{\partial(\xi_\mu \xi_\nu^*)}{\partial \lambda} + \sum_l \frac{\partial^2 f^{\mathrm{xc}}}{\partial \rho_m \rho_l} \xi_\mu \xi_\nu^* \sum_{\kappa\iota} D_{\kappa\iota,l} \frac{\partial(\xi_\kappa \xi_\iota^*)}{\partial \lambda} \, \mathrm{d}\mathbf{r} \right) . \tag{9.36}$$

Eq. 9.35 is the DFT kernel contracted with the derivative density matrix. The LDA exchange-correlation kernel is given by

$$\begin{aligned}K^{\mathrm{xc,\ LDA}}_{\mu\nu\kappa\iota,ml} &= \frac{\partial^2 E^{\mathrm{xc,LDA}}}{\partial D_{\mu\nu,m} \partial D_{\kappa\iota,l}} \\ &= \iint \frac{\partial^2 f^{\mathrm{xc}}}{\partial \rho_m \rho_l} \frac{\partial \rho_m}{\partial D_{\mu\nu,m}} \frac{\partial \rho_l}{\partial D_{\kappa\iota,l}} \delta(\mathbf{r} - \mathbf{r}') \, \mathrm{d}\mathbf{r} \, \mathrm{d}\mathbf{r}' \\ &= \iint \frac{\partial^2 f^{\mathrm{xc}}}{\partial \rho_m \rho_l} \xi_\mu \xi_\nu^* \xi_\kappa \xi_\iota^* \, \mathrm{d}\mathbf{r} \,,\end{aligned} \tag{9.37}$$

so one can write

$$\mathcal{V}^{\mathrm{xc}}_{\mu\nu,m}[\mathbf{D}^\lambda] = \sum_{l\kappa\iota} K^{\mathrm{xc,\ LDA}}_{\mu\nu\kappa\iota,ml} D^\lambda_{\kappa\iota,l} \,. \tag{9.38}$$

The perturbed density matrix can again be decomposed into two contributions containing the $\mathbf{U}$ matrix and one contribution, corresponding to the occupied-occupied block, containing the AO derivative overlap matrix $\mathcal{S}$. Transformation into the occupied-virtual block then leads to

$$\mathcal{V}^{\mathrm{xc}}_{ai}[\mathbf{D}^\lambda] = \sum_{bj} \left(K^{\mathrm{xc}}_{aijb} U_{bj} + K^{\mathrm{xc}}_{aibj} U^*_{bj} \right) - \sum_{kj} K^{\mathrm{xc}}_{aijk} \mathcal{S}_{kj} \,. \tag{9.39}$$

Consequently, the CPKS equations can be set up for the general LDA case. The form of the CPKS equations is analogous to the CPHF equations in eq. 9.28. The main difference arises from slightly modified expressions for the involved quantities:

$$A^{\mathrm{KS}}_{ai,bj} = (\epsilon_a - \epsilon_i) \, \delta_{ij} \delta_{ab} + (ai|jb) - c_x (ab|ji) + K^{\mathrm{xc}}_{aijb} \,, \tag{9.40}$$

$$B^{\mathrm{KS}}_{ai,bj} = (ai|bj) - c_x (aj|bi) + K^{\mathrm{xc}}_{aibj} \,, \tag{9.41}$$

$$F^{\mathrm{RHS,\ KS}}_{ai} = \epsilon_i \mathcal{S}_{ai} - \mathcal{F}^{(\lambda)}_{ai} + \sum_{kj} \left[(ai|jk) - c_x (ak|ji) + K^{\mathrm{xc}}_{aijk} \right] \mathcal{S}_{kj} \,. \tag{9.42}$$

9.4.2. CPKS Equations for GGAs

The objective of this section is to showcase the expressions involved in the CPKS working equations for GGA functionals. As a reminder, the exchange-correlation potential matrix is given by

$$V_{\mu\nu,m}^{\mathrm{GGA}} = \int \left(\frac{\partial f^{\mathrm{xc}}}{\partial \rho_m} \frac{\partial \rho_m}{\partial D_{\mu\nu,m}} + \frac{\partial f^{\mathrm{xc}}}{\partial \boldsymbol{\nabla} \rho_m} \frac{\partial \boldsymbol{\nabla} \rho_m}{\partial D_{\mu\nu,m}} \right) \mathrm{d}\mathbf{r} \,. \tag{9.43}$$

From this expression, the derivative of the potential is then obtained as

$$\begin{aligned} \frac{\partial V_{\mu\nu,m}^{\mathrm{GGA}}}{\partial \lambda} = \int \Bigg[& \frac{\partial f^{\mathrm{xc}}}{\partial \rho_m} \frac{\partial^2 \rho_m}{\partial \lambda \partial D_{\mu\nu,m}} + \frac{\partial f^{\mathrm{xc}}}{\partial \boldsymbol{\nabla} \rho_m} \frac{\partial^2 \boldsymbol{\nabla} \rho_m}{\partial \lambda \partial D_{\mu\nu,m}} \\ & + \sum_l \left(\frac{\partial^2 f^{\mathrm{xc}}}{\partial \rho_l \partial \rho_m} \frac{\partial \rho_l}{\partial \lambda} + \frac{\partial^2 f^{\mathrm{xc}}}{\partial \boldsymbol{\nabla} \rho_l \partial \rho_m} \frac{\partial \boldsymbol{\nabla} \rho_l}{\partial \lambda} \right) \frac{\partial \rho_m}{\partial D_{\mu\nu,m}} \\ & + \sum_l \left(\frac{\partial^2 f^{\mathrm{xc}}}{\partial \rho_l \partial \boldsymbol{\nabla} \rho_m} \frac{\partial \rho_l}{\partial \lambda} + \frac{\partial^2 f^{\mathrm{xc}}}{\partial \boldsymbol{\nabla} \rho_l \partial \boldsymbol{\nabla} \rho_m} \frac{\partial \boldsymbol{\nabla} \rho_l}{\partial \lambda} \right) \frac{\partial \boldsymbol{\nabla} \rho_m}{\partial D_{\mu\nu,m}} \Bigg] \mathbf{dr} \,. \end{aligned} \tag{9.44}$$

It should be noted that most implementations that actually calculate the value of the exchange-correlation functional do not take the individual values of the $\boldsymbol{\nabla}\rho_m$ vector, but its squared absolute value. This approach becomes more convenient when switching to the basis of individual alpha and beta spins instead of the Pauli spin-matrix basis. Then, one can define

$$\gamma_{\sigma\tau} = [\boldsymbol{\nabla} \rho_\sigma] \cdot [\boldsymbol{\nabla} \rho_\tau] \,, \tag{9.45}$$

where the expressions that need to be inserted into the equations are consequently given by

$$\frac{\partial \gamma_{\sigma\tau}}{\partial \boldsymbol{\nabla} \rho_\sigma} = \begin{cases} 2\boldsymbol{\nabla} \rho_\sigma & \text{if } \sigma = \tau \,, \\ \boldsymbol{\nabla} \rho_\tau & \text{else} \,. \end{cases} \tag{9.46}$$

9.4.3. CPKS Equations for mGGAs

Similar to the previous section, the necessary expression for the CPKS equations for mGGAs are provided here. As shown in equations 7.36 and 7.37, for mGGAs the paramagnetic current density $\mathbf{j}_m^{\mathrm{p}}$ enters the expressions. The exchange-correlation potential matrix is given by

$$\begin{aligned} V_{\mu\nu,m}^{\mathrm{mGGA}} = \int \Bigg\{ & \frac{\partial f^{\mathrm{xc}}}{\partial \rho_m} \frac{\partial \rho_m}{\partial D_{\mu\nu,m}} + \frac{\partial f^{\mathrm{xc}}}{\partial \boldsymbol{\nabla} \rho_m} \frac{\partial \boldsymbol{\nabla} \rho_m}{\partial D_{\mu\nu,m}} \\ & + \frac{\partial f^{\mathrm{xc}}}{\partial \bar{\tau}_m} \frac{\partial \tau_m}{\partial D_{\mu\nu,m}} - \frac{\partial f^{\mathrm{xc}}}{\partial \bar{\tau}_m} \frac{\mathbf{j}_m^{\mathrm{p}}}{\rho_m} \frac{\partial \mathbf{j}_m^{\mathrm{p}}}{\partial D_{\mu\nu,m}} \\ & + \frac{\partial f^{\mathrm{xc}}}{\partial \bar{\tau}_m} \frac{|\mathbf{j}_m^{\mathrm{p}}|^2}{2\rho_m^2} \frac{\partial \rho_m}{\partial D_{\mu\nu,m}} \Bigg\} \mathrm{d}\mathbf{r} \,. \end{aligned} \tag{9.47}$$

The derivative matrix elements can then be written as

$$
\begin{aligned}
\frac{\partial V^{\mathrm{mGGA}}_{\mu\nu,m}}{\partial\lambda} &= \frac{\partial V^{\mathrm{GGA}}_{\mu\nu,m}}{\partial\lambda} + \int\Bigg\{ \frac{\partial f^{\mathrm{xc}}}{\partial\bar{\tau}_m}\frac{|\mathbf{j}^{\mathrm{p}}_m|^2}{2\rho_m^2}\frac{\partial^2\rho_m}{\partial\lambda\partial D_{\mu\nu,m}} \\
&+ \frac{\partial f^{\mathrm{xc}}}{\partial\bar{\tau}_m}\left(\frac{\partial^2\tau_m}{\partial\lambda\partial D_{\mu\nu,m}} - \frac{\mathbf{j}^{\mathrm{p}}_m}{\rho_m}\frac{\partial^2\mathbf{j}^{\mathrm{p}}_m}{\partial\lambda\partial D_{\mu\nu,m}}\right) \\
&- \frac{\partial f^{\mathrm{xc}}}{\partial\bar{\tau}_m}\left(\frac{1}{\rho_m}\frac{\partial\mathbf{j}^{\mathrm{p}}_m}{\partial\lambda} - \frac{\mathbf{j}^{\mathrm{p}}_m}{\rho_m^2}\frac{\partial\rho_m}{\partial\lambda}\right)\frac{\partial\mathbf{j}^{\mathrm{p}}_m}{\partial D_{\mu\nu,m}} \\
&+ \frac{\partial f^{\mathrm{xc}}}{\partial\bar{\tau}_m}\left(\frac{\mathbf{j}^{\mathrm{p}}_m}{\rho_m^2}\frac{\partial\mathbf{j}^{\mathrm{p}}_m}{\partial\lambda} - \frac{|\mathbf{j}^{\mathrm{p}}_m|^2}{\rho_m^3}\frac{\partial\rho_m}{\partial\lambda}\right)\frac{\partial\rho_m}{\partial D_{\mu\nu,m}} \\
&+ \sum_l \frac{\partial^2 f^{\mathrm{xc}}}{\partial\bar{\tau}_l\partial\rho_m}\left(\frac{\partial\tau_l}{\partial\lambda} - \frac{\mathbf{j}^{\mathrm{p}}_l}{\rho_l}\frac{\partial\mathbf{j}^{\mathrm{p}}_l}{\partial\lambda} + \frac{|\mathbf{j}^{\mathrm{p}}_l|^2}{2\rho_l^2}\frac{\partial\rho_l}{\partial\lambda}\right)\frac{\partial\rho_m}{\partial D_{\mu\nu,m}} \\
&+ \sum_l \frac{\partial^2 f^{\mathrm{xc}}}{\partial\bar{\tau}_l\partial\boldsymbol{\nabla}\rho_m}\left(\frac{\partial\tau_l}{\partial\lambda} - \frac{\mathbf{j}^{\mathrm{p}}_l}{\rho_l}\frac{\partial\mathbf{j}^{\mathrm{p}}_l}{\partial\lambda} + \frac{|\mathbf{j}^{\mathrm{p}}_l|^2}{2\rho_l^2}\frac{\partial\rho_l}{\partial\lambda}\right)\frac{\partial\boldsymbol{\nabla}\rho_m}{\partial D_{\mu\nu,m}} \\
&+ \sum_l \left(\frac{\partial^2 f^{\mathrm{xc}}}{\partial\rho_l\bar{\tau}_m}\frac{\partial\rho_l}{\partial\lambda} + \frac{\partial^2 f^{\mathrm{xc}}}{\partial\boldsymbol{\nabla}\rho_l\partial\bar{\tau}_m}\frac{\partial\boldsymbol{\nabla}\rho_l}{\partial\lambda}\right)\frac{\partial\tau_m}{\partial D_{\mu\nu,m}} \\
&+ \sum_l \frac{\partial^2 f^{\mathrm{xc}}}{\partial\bar{\tau}_l\partial\bar{\tau}_m}\left(\frac{\partial\tau_l}{\partial\lambda} - \frac{\mathbf{j}^{\mathrm{p}}_l}{\rho_l}\frac{\partial\mathbf{j}^{\mathrm{p}}_l}{\partial\lambda} + \frac{|\mathbf{j}^{\mathrm{p}}_l|^2}{2\rho_l^2}\frac{\partial\rho_l}{\partial\lambda}\right)\frac{\partial\tau_m}{\partial D_{\mu\nu,m}} \\
&+ \sum_l \left(\frac{\partial^2 f^{\mathrm{xc}}}{\partial\rho_l\partial\bar{\tau}_m}\frac{\partial\rho_l}{\partial\lambda} + \frac{\partial^2 f^{\mathrm{xc}}}{\partial\boldsymbol{\nabla}\rho_l\partial\bar{\tau}_m}\frac{\partial\boldsymbol{\nabla}\rho_l}{\partial\lambda}\right) \\
&\qquad\times\left(-\frac{\mathbf{j}^{\mathrm{p}}_m}{\rho_m}\frac{\partial\mathbf{j}^{\mathrm{p}}_m}{\partial D_{\mu\nu,m}} + \frac{|\mathbf{j}^{\mathrm{p}}_m|^2}{2\rho_m^2}\frac{\partial\rho_m}{\partial D_{\mu\nu,m}}\right) \\
&+ \sum_l \frac{\partial^2 f_{\mathbf{xc}}}{\partial\bar{\tau}_l\partial\bar{\tau}_m}\left(\frac{\partial\tau_l}{\partial\lambda} - \frac{\mathbf{j}^{\mathrm{p}}_l}{\rho_l}\frac{\partial\mathbf{j}^{\mathrm{p}}_l}{\partial\lambda} + \frac{|\mathbf{j}^{\mathrm{p}}_l|^2}{2\rho_l^2}\frac{\partial\rho_l}{\partial\lambda}\right) \\
&\qquad\times\left(-\frac{\mathbf{j}^{\mathrm{p}}_m}{\rho_m}\frac{\partial\mathbf{j}^{\mathrm{p}}_m}{\partial D_{\mu\nu,m}} + \frac{|\mathbf{j}^{\mathrm{p}}_m|^2}{2\rho_m^2}\frac{\partial\rho_m}{\partial D_{\mu\nu,m}}\right)\Bigg\}\mathbf{dr}\,.
\end{aligned}
\tag{9.48}
$$

10. Population Analyses

This section's objective is the introduction of some different population analyses. One special family of population analyses are methods that construct atomic partial charges. Such charges are a very intuitive way for any chemist to think about the electronic structure of a molecule in crude approximation and can be used to explain stability, reactivity and many other properties of the system.[182] In the context of this work, atomic partial charges aid in the interpretation of the Berry curvature in external magnetic fields. Section 6 discussed how the molecular Berry curvature is closely related to molecular properties such as the electronic dipole moment and the total number of electrons in the system. As a consequence, a quantity resembling atomic partial charges can be defined from the forces acting on a nucleus due to the Berry curvature.

10.1. Berry Atomic Partial Charges

The Berry charge population Q_{IJ} was defined in eq. 6.8 and can be obtained from the antisymmetric part of the Berry curvature.[53,80] As a reminder, eq. 6.8 reads

$$Q_{IJ}\mathcal{B} = -\boldsymbol{\omega}_{IJ}^{\text{asym}} ,$$

where the vector $\boldsymbol{\omega}$ was defined in eq. 6.7 as

$$\boldsymbol{\omega}_{IJ}^{\text{asym}} = \begin{pmatrix} \Omega_{IzJy}^{\text{asym}} \\ \Omega_{IxJz}^{\text{asym}} \\ \Omega_{IyJx}^{\text{asym}} \end{pmatrix} .$$

The electronic contribution to the atomic partial charge of the nucleus I can then be obtained by summation over the other nuclear index. Addition of the nuclear charge Z_I finally results in the total atomic partial charge

$$q_I = Z_I + \sum_J Q_{IJ}. \tag{10.1}$$

In the non-relativistic case, the Berry curvature, and therefore the Berry charge population, vanishes in the zero-field case. Since Berry charges are consequently only formally defined in a finite magnetic field, for a given molecular geometry, three sets of partial charges can be obtained. These three cases differ in the direction of the magnetic field, which can be chosen to coincide with the Cartesian axes without loss of generality. Each of these sets is referred to as $q_I^{x,\text{Berry}}$, $q_I^{y,\text{Berry}}$, and $q_I^{z,\text{Berry}}$, respectively. Generally, these partial charges are not equivalent

$$q_I^{x,\text{Berry}} \neq q_I^{y,\text{Berry}} \neq q_I^{z,\text{Berry}} . \tag{10.2}$$

Some obvious exception exists of course, like highly symmetric systems, such as diatomic homo-nuclear molecules with their bond axis aligned with the magnetic field vector, where two of these sets are equivalent. The isotropic average of these sets of Berry charges are invariant with respect to rotations of the magnetic field axis, and can be defined as[53,80]

$$q_{I,\mathrm{rot}}^{\mathrm{Berry}} = \frac{1}{3}\left(q_I^{x,\mathrm{Berry}} + q_I^{y,\mathrm{Berry}} + q_I^{z,\mathrm{Berry}}\right) . \tag{10.3}$$

Even though a finite magnetic field is needed for a non-vanishing Berry curvature and consequently Berry charges, the value of the Berry charges themselves converge rapidly towards the zero-field limit. For many molecular systems, charges calculated in a magnetic field of about $10^{-4}B_0 \approx 23.5\,T$ already show several converged decimal places.

10.2. Generalized Atomic Polar Tensor Charges

Another well-known kind of population analysis are the so-called generalized atomic polar tensor charges.[183–185] They are based on the atomic polar tensor (APT), which is a $3 \times 3 \times N_{\mathrm{nuc}}$ tensor defined as

$$T_{I,\alpha\beta} = \frac{\partial \mu_\beta}{\partial R_{I\alpha}} . \tag{10.4}$$

The APT gives rise to a very intuitive definition of atomic partial charges. Considering how the electronic dipole moment of a system changes when one nucleus is displaced, one can think about how much electronic charges this nucleus drags with it. This quantity is just given by the corresponding element of the APT, the derivative of the electronic dipole moment with respect to a nuclear coordinate. Similarly to the Berry charges, an isotropic average of the diagonal element of the APT is defined as the GAPT charge

$$q_I^{\mathrm{GAPT}} = \frac{1}{3}\left(T_{I,xx} + T_{I,yy} + T_{I,zz}\right) . \tag{10.5}$$

In Ref. [80], Peters *et al.* noticed a striking similarity between the values of Berry and GAPT charges. The relation between these types of partial charges can be well understood with the help of the pseudomomentum-translational sum rule in eq. 6.12, and more specifically its special case for complete basis sets in eq. 6.24.

10.2.1. Relation between GAPT and Berry Charges

This section summarizes the respective section of Ref. [82], where this relation was proven in collaboration with Pausch. Previously, Berry charges were derived in eq. 6.10 during the investigation of the effective nuclear Hamiltonian. There, a charge population was defined first, which depends on the antisymmetric part of the

individual blocks of the Berry curvature. Alternatively, and in resemblance to the APT, the pseudomomentum tensor can be defined as

$$\omega_{I,\alpha\beta} = \sum_J \Omega_{I\alpha J\beta} = \frac{\partial k_\beta}{\partial R_{I\alpha}}\,, \tag{10.6}$$

from this, the Berry charge can be obtained from the following identity:

$$q_I^{\alpha,\mathrm{Berry}} \mathcal{B}_\alpha = \frac{1}{2} \sum_{\beta\gamma} \varepsilon_{\alpha\beta\gamma} \omega_{I,\alpha\beta}\,. \tag{10.7}$$

With this expression, the Berry charge for the different directions of the magnetic field can be investigated, starting with the z-direction. Construction of the corresponding elements of the pseudomomentum tensor then yields

$$\omega_{I,xy} = \frac{\partial k_y}{\partial R_{Ix}} = \frac{\partial p_y}{\partial R_{Ix}} + \frac{\mathcal{B}_z}{2} \frac{\partial \mu_x}{\partial R_{Ix}}\,, \tag{10.8}$$

and

$$\omega_{I,yx} = \frac{\partial k_x}{\partial R_{Iy}} = \frac{\partial p_x}{\partial R_{Iy}} - \frac{\mathcal{B}_z}{2} \frac{\partial \mu_y}{\partial R_{Iy}}\,. \tag{10.9}$$

Inserting these expressions for the elements of $\boldsymbol{\omega}$ into eq. 10.7 produces an expression for the Berry charge with the magnetic field along the z-axis[82]

$$q_I^{z,\mathrm{Berry}} = \frac{1}{2\mathcal{B}_z} \left(\frac{\partial p_y}{\partial R_{Ix}} - \frac{\partial p_x}{\partial R_{Iy}} \right) + \frac{1}{4} \left(T_{I,xx} + T_{I,yy} \right)\,. \tag{10.10}$$

Cyclic permutation of all cartesian indices can be applied to obtain the analogous expression for the other directions of the magnetic field. The rotationally averaged Berry charge is then found to be

$$\begin{aligned} q_{I,\mathrm{rot}}^{\mathrm{Berry}} =& \frac{1}{6\mathcal{B}_x} \left(\frac{\partial p_z}{\partial R_{Iy}} - \frac{\partial p_y}{\partial R_{Iz}} \right) + \frac{1}{6\mathcal{B}_y} \left(\frac{\partial p_x}{\partial R_{Iz}} - \frac{\partial p_z}{\partial R_{Ix}} \right) + \frac{1}{6\mathcal{B}_z} \left(\frac{\partial p_y}{\partial R_{Ix}} - \frac{\partial p_x}{\partial R_{Iy}} \right) \\ &+ \frac{1}{6} \left(T_{I,xx} + T_{I,yy} + T_{I,zz} \right) \end{aligned} \tag{10.11}$$

Considering that the magnetic field strength in the different calculations is the same, just with differing directions, one can set

$$\mathcal{B}_x = \mathcal{B}_y = \mathcal{B}_z = B\,, \tag{10.12}$$

to simplify eq. 10.11. Additionally, the definition of the GAPT charge from eq. 10.5 can be inserted to arrive at

$$q_{I,\mathrm{rot}}^{\mathrm{Berry}} = \frac{1}{6B} \sum_{\alpha\beta\gamma} \varepsilon_{\alpha\beta\gamma} \frac{\partial p_\gamma}{\partial R_{I\beta}} + \frac{1}{2} q_I^{\mathrm{GAPT}}\,. \tag{10.13}$$

From this equation it becomes apparent that the Berry charge is essentially an equal mix of GAPT charges and another contribution that similarly resembles an atomic partial charge. For convenience, this type of partial charge is called a momentum partial charge and is then simply defined from the derivative canonical momentum expectation values as

$$q_I^{\mathrm{mom}} = \frac{1}{3B} \sum_{\alpha\beta\gamma} \varepsilon_{\alpha\beta\gamma} \frac{\partial p_\gamma}{\partial R_{I\beta}} \,. \tag{10.14}$$

Even though this definition explicitly contains the magnetic field strength, the zero field limit of these charges does not vanish and can be calculated perturbatively as[82]

$$\lim_{|\mathcal{B}|\to 0} q_I^{\mathrm{mom}} = \frac{1}{3} \sum_{\alpha\beta\gamma} \varepsilon_{\alpha\beta\gamma} \left. \frac{\partial^2 p_\gamma}{\partial R_{I\beta} \partial \mathcal{B}_\alpha} \right|_{|\mathcal{B}|=0} \,. \tag{10.15}$$

So far, eq. 10.13 already established the general relation between Berry and GAPT charges. However, an even stronger connection presents itself in a finite basis. Under these conditions, eq. 6.24 says that the sum of the Berry curvature over one nucleus is equal to a component of the APT scaled with the magnetic field strength. Therefore, in the limit of a complete basis one obtains

$$q_{I,\mathrm{rot}}^{\mathrm{Berry}} = q_I^{\mathrm{GAPT}} \qquad \text{for basis} \to \infty \,. \tag{10.16}$$

Trivially, it also follows that the momentum charges converge towards the same value. Hence, in a finite basis set any difference between Berry and GAPT charges solely stems from the incompleteness of the employed basis set.

10.3. Mulliken Charges

The Mulliken population analysis[186] is one of the most widely known methods to obtain atomic partial charges. It is based on the simple observation that integration of the electron density over all of space gives the total number of electrons in the system, therefore

$$\sum_{\mu\nu} D_{\mu\nu,0} S_{\nu\mu} = N_{\mathrm{el}} \,. \tag{10.17}$$

To obtain a partial charge from here, one has to apply a rule to distribute the electronic charge among the nuclei. Within the Mulliken population analysis this distribution is based on where each basis function is centered. The Mulliken charge population,

$$Q_\nu^{\mathrm{Mull}} = \sum_{\mu} D_{\mu\nu,0} S_{\nu\mu} \tag{10.18}$$

is summed over all basis function that are centered on a specific atom to produce the electronic partial charge of said atom. The total Mulliken charge can then be written as

$$q_I^{\mathrm{Mull}} = Z_I - \sum_{\mu\in I} Q_\mu^{\mathrm{Mull}} \,. \tag{10.19}$$

This way of constructing the partial charge has a few advantages besides its extremely low computational cost: Firstly, the summation in eq. 10.19 can be decomposed even further. For example, one might be interested in how much orbitals of certain angular momentum contribute to each charge. Second, the trace of the product of the spin-symmetric part of the density matrix and the overlap matrix produces the total number of electrons. If instead a spin contribution of the density matrix is used in the equation, a kind of spin charge can be calculated. Such a charge can the be used to crudely locate unpaired spins on atoms in the system. Despite this, the Mulliken population analysis has a variety of shortcoming.[187–190] For instance, by definition it is strongly dependent on the choice of the basis set. This means that there is usually no way to systematically converge these charges. This issue can at least partly be resolved by using the very similar Löwdin charges[191,192], among others.

Part III.

Implementation

Overview

The theoretical framework of this thesis was presented in part II, the implementation of the relevant quantities into the TURBOMOLE program suite is presented in this part. The geometric vector potential is discussed in section 11, followed by the coupled perturbed Hartree-Fock and Kohn-Sham equations in section 12. Equipped with these topics, the implementation of various molecular properties is presented in section 13, including the Berry curvature, the diagonal Born–Oppenheimer correction, and the derivatives of one-electron expectation values. This makes the atomic polar tensor and the related GAPT charges available. Section 13.4 contains a short discussion about the rotation of instable electronic wave functions along an instability vector. Lastly, an overview of the available functionalities in TURBOMOLE that are related to this work is provided in section 14.

Almost all implementation work discussed in this chapter is in the complex-valued two-component framework for calculations in external magnetic fields or including relativistic effects. The only exception is a paragraph in section 13.2, where the implementation of the DBOC into the `aoforce` module for real-valued one-component wave functions is summarized.

11. The Geometric Vector Potential

11.1. The Working Equation

The geometric vector potential was encountered when deriving the nuclear equations of motion as an additional potential that enters the nuclear Hamiltonian.[44,47,193–195] It was defined in eq. 5.10 as

$$\boldsymbol{\chi}_I = \langle \Psi | \hat{\mathbf{P}}_I | \Psi \rangle \,.$$

When investigating the effect that the canonical nuclear momentum operator has on an effective one-electron wave function, a particular property of the Slater determinant can be used. The Hartree product is a simple product of the individual spinors

$$\Psi_{\text{Hartree}} = \psi_1(\mathbf{x}_1) \cdot \psi_2(\mathbf{x}_2) \cdot \ldots \cdot \psi_{N_{\text{el}}}(\mathbf{x}_{N_{\text{el}}}) \,. \tag{11.1}$$

To obtain a Slater determinant starting from the Hartree product, the anti-symmetry operator[93]

$$\mathcal{A} = \frac{1}{\sqrt{N_{\text{el}}!}} \sum_{Q \in S_N} \text{sgn}(\hat{Q}) \hat{Q} \,, \tag{11.2}$$

can be used, where the sum runs over all $N!$ symmetry elements of the symmetric group S_N, and $\hat{Q}$ is the corresponding symmetry operator. To account for the right sign, each term is multiplied by the signature of the symmetry operator, or, equivalently, with the parity of the permutation. The Slater determinant can then be expressed as

$$\Psi = \mathcal{A} \Psi_{\text{Hartree}} \,. \tag{11.3}$$

Now, the application of the momentum operator with subsequent projection back onto the ground state Slater determinant can be written as

$$\langle \Psi | \hat{P}_{I\alpha} | \Psi \rangle = \langle \Psi | \hat{\mathcal{A}} (\hat{P}_{I\alpha} \Psi_{\text{Hartree}}) \rangle = \sum_i^{N_{\text{el}}} \langle \Psi | \hat{\mathcal{A}} \left[\left(\hat{P}_{I\alpha} \psi_i(\mathbf{x}_i) \right) \prod_{j \neq i}^{N_{\text{el}}} \psi_j(\mathbf{x}_j) \right] \rangle \,. \tag{11.4}$$

Using the orthonormality of the spinor functions, this expression can be simplified. The overlap of spinor functions that are contained in the bra and ket of the expression is equal to one. Therefore, only the overlap of the respective spinor that is different in both functions remains. Since $\hat{\mathcal{A}}$ is hermitian and idempotent up to the normalization constant, the Slater determinant can also be written using the Hartree product. Then, only a trace over one-electron contributions remains

$$\langle \Psi | \hat{P}_{I\alpha} | \Psi \rangle = \sum_i^{N_{\text{el}}} \langle \psi_i | \hat{P}_{I\alpha} | \psi_i \rangle \,. \tag{11.5}$$

Inserting the LCAO into this equation and using the expansion of a derivative coefficients in the basis of all unperturbed coefficients leads to

$$\begin{aligned}
\chi_{I\alpha} &= -\mathrm{i}\sum_{\mu\nu\sigma}\sum_{i} C^{\sigma *}_{\mu i}(\nabla_{I\alpha} C^{\sigma}_{\nu i})\langle\xi_\mu|\xi_\nu\rangle + \sum_{\mu\nu} D_{\nu\mu,0}\langle\xi_\mu|\hat{P}_{I\alpha}|\xi_\nu\rangle \\
&= -\mathrm{i}\sum_{\mu\nu\sigma}\sum_{iq} C^{\sigma *}_{\mu i} C^{\sigma}_{\nu q} U^{I\alpha}_{qi}\langle\xi_\mu|\xi_\nu\rangle + \sum_{\mu\nu} D_{\nu\mu,0}\langle\xi_\mu|\hat{P}_{I\alpha}|\xi_\nu\rangle \\
&= -\mathrm{i}\sum_{iq} U^{I\alpha}_{qi}\langle\psi_i|\psi_q\rangle + \sum_{\mu\nu} D_{\nu\mu,0}\langle\xi_\mu|\hat{P}_{I\alpha}|\xi_\nu\rangle \\
&= -\mathrm{i}\sum_{i} U^{I\alpha}_{ii} + \sum_{\mu\nu} D_{\nu\mu,0}\langle\xi_\mu|\hat{P}_{I\alpha}|\xi_\nu\rangle\,,
\end{aligned} \tag{11.6}$$

where the superscript $I\alpha$ of U indicates that the respective perturbation is the displacement of the nuclear coordinate $R_{I\alpha}$. An explicit expression for the occupied-occupied block of the $\mathbf{U}$ matrix was derived in eq. 9.8, which then yields

$$\begin{aligned}
\chi_{I\alpha} =& -\mathrm{i}\sum_{i} U^{I}_{ii} + \sum_{\mu\nu} D_{\nu\mu,0}\langle\xi_\mu|\hat{P}_{I\alpha}|\xi_\nu\rangle \\
=& \frac{\mathrm{i}}{2}\sum_{i} \mathcal{S}^{I\alpha}_{ii} + \sum_{\mu\nu} D_{\nu\mu,0}\langle\xi_\mu|\hat{P}_{I\alpha}|\xi_\nu\rangle \\
=& -\frac{1}{2}\sum_{i}\Big(\langle\hat{P}_{I\alpha}\psi_i|\psi_i\rangle + \langle\psi_i|\hat{P}_{I\alpha}\psi_i\rangle\Big) + \sum_{\mu\nu} D_{\nu\mu,0}\langle\xi_\mu|\hat{P}_{I\alpha}|\xi_\nu\rangle \\
=& \frac{1}{2}\sum_{\mu\nu} D_{\nu\mu,0}\Big(\langle\xi_\mu|\hat{P}_{I\alpha}\xi_\nu\rangle - \langle\hat{P}_{I\alpha}\xi_\mu|\xi_\nu\rangle\Big)\,.
\end{aligned} \tag{11.7}$$

This final expression for one column of the geometric vector potential most notably does not require the solution of the CPHF/KS equations.[83] Thus, it can simply be calculated at the end of any ground state calculation in a very similar fashion to any other one-electron expectation value. One only needs to calculate the respective integrals in AO basis, which are just overlap integrals where one function is a derivative, and then calculate their trace with the density matrix. The geometric vector potential is strictly real-valued: Eq. 2.6 showed that the overlap of a wave function with its own geometry derivative must be purely imaginary. The integrals in the working equation of the geometric vector potential only differ from this overlap by the factors of i. Consequently, the geometric vector potential is generally real-valued, whereas it vanishes for purely real-valued wave functions.

11.2. Implementation Details

The implementation of the geometric vector potential resides within the `ridft` module of TURBOMOLE. A vastly simplified schematic of the workflow is shown in figure 11.1. If a two-component calculation is performed in the presence of an external magnetic field or with the relativistic X2C Hamiltonian, and the keyword `berry` is set in the control file, the geometric vector potential is calculated. The

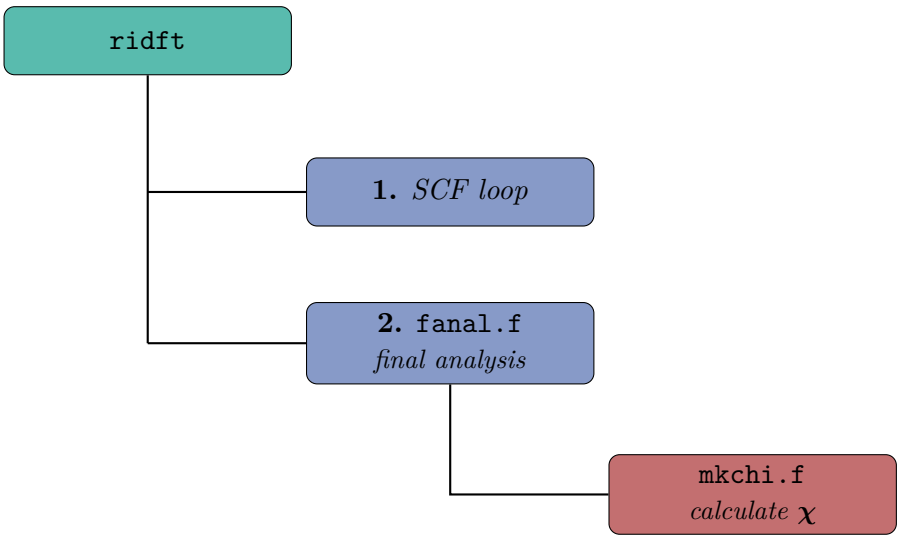

Figure 11.1.: Simplified schematic of the workflow of `ridft`. The TURBOMOLE module is depicted in green, already existing routine in blue, and routines that were implemented within the scope of this work in red.

routine responsible for handling the calculation is `mkchi`, where eq. 11.7 is evaluated. The spin symmetric part of the ground state density is passed to the routine as it is needed in several other places. The derivative integrals are provided by the `lndnloop` routine, which handles the computation of all one-electron integrals over LAOs. The required subtractive linear combination is one of the cases that is internally handled by the routine. The output of `lndnloop` always consists of only the lower triangle of the whole matrix. Therefore, if the number of basis functions is N_{basis}, not the full number of N_{basis}^2 integrals of the general matrix M is provided but only the $N_{\text{basis}}(N_{\text{basis}}+1)/2$ elements

$$M_{\mu\nu} \quad \text{with } \mu \geq \nu\,. \tag{11.8}$$

In the case of the subtractive linear combination of ket- and bra-derivative overlap matrices required for the geometric vector potential

$$T_{\mu\nu}^{I\alpha} = \langle \xi_\mu | \nabla_{I\alpha} \xi_\nu \rangle - \langle \nabla_{I\alpha} \xi_\mu | \xi_\nu \rangle\,, \tag{11.9}$$

`lndnloop` outputs the lower triangles of all $3N_{\text{nuc}}$ different derivatives. In particular, this matrix is skew-hermitian $T_{\mu\nu}^{I\alpha} = -T_{\nu\mu}^{I\alpha *}$. Exploiting this symmetry and the

hermiticity of the ground state density matrix, yields

$$\begin{aligned}
\chi_{I\alpha} &= \frac{\mathrm{i}}{2} \sum_{\mu\nu} D_{\nu\mu,0} T^{I\alpha}_{\mu\nu} \\
&= \frac{1}{2} \Im \left(\sum_{\mu\nu} D_{\nu\mu,0} T^{I\alpha}_{\mu\nu} \right) \\
&= \frac{1}{2} \sum_{\mu\nu} \Re(D_{\nu\mu,0}) \Im(T^{I\alpha}_{\mu\nu}) + \Im(D_{\nu\mu,0}) \Re(T^{I\alpha}_{\mu\nu}) \\
&= \frac{1}{2} \sum_{\mu \geq \nu} (2 - \delta_{\mu\nu}) \left[\Re(D_{\nu\mu,0}) \Im(T^{I\alpha}_{\mu\nu}) + \Im(D_{\nu\mu,0}) \Re(T^{I\alpha}_{\mu\nu}) \right] \\
&= \frac{1}{2} \sum_{\mu \geq \nu} (2 - \delta_{\mu\nu}) \left[\Re(D_{\mu\nu,0}) \Im(T^{I\alpha}_{\mu\nu}) - \Im(D_{\mu\nu,0}) \Re(T^{I\alpha}_{\mu\nu}) \right] .
\end{aligned} \tag{11.10}$$

In this way, only the lower triangle of each matrix is needed for the calculation. Additionally, by decomposing both factors into their respective real and imaginary part, only the required total real part of the geometric vector potential is computed. The prefactor $(2 - \delta_{\mu\nu})$ that multiplies all off-diagonal elements by two while leaving the diagonal unchanged, is a common occurrence in traces of the product of two matrices. For this reason, many places in the implementation multiply the corresponding elements of the density matrix with each factor at the very beginning, so no repeated if-else branches are needed in every loop.

12. The Coupled Perturbed Hartree–Fock and Kohn–Sham Equations

The calculation of the geometric vector potential presented in section 11 did not require the solution of the CPHF/CPKS equations, since it involved a special case where only the occupied-occupied space of the orbital rotation entered the final expression. Since this is not the case for general nuclear derivatives, the CPHF/CPKS equations need to be solved to compute other quantities like the Berry curvature or the atomic polar tensor. Section 12.1 discusses the general complex two-component CPHF/CPKS solver that was already implemented in TURBOMOLE and was presented by Kehry *et al.* in Ref. [196]. Afterwards, the construction of the right-hand side (rhs) of the linear response equations for nuclear derivatives is discussed. This implementation work was done in collaboration with Pausch for the general structure and the Hartree–Fock framework, which was presented in Ref. [82]. The implementation of the rhs for the Kohn-Sham cDFT framework was additionally done in collaboration with Kronenberger and is described in Ref. [83].

12.1. The CPHF Solver

This section provides an overview of the general complex solver for the linear response equations presented in Ref. [196]. The system of linear equations that needs to be solved for static properties is always of the form provided in eq. 9.28 and reads

$$\begin{pmatrix} \mathbf{A} & \mathbf{B} \\ \mathbf{B}^* & \mathbf{A}^* \end{pmatrix} \begin{pmatrix} \mathbf{U} \\ \mathbf{U}^* \end{pmatrix} = \begin{pmatrix} \mathbf{F}^{\mathrm{RHS}} \\ \mathbf{F}^{\mathrm{RHS}*} \end{pmatrix} ,$$

where the matrices $\mathbf{A}$ and $\mathbf{B}$ were defined in equations 9.22 and 9.23, respectively.[43,175,197] Their expressions are repeated here as

$$A_{ai,bj} = (\epsilon_a - \epsilon_i)\, \delta_{ij}\delta_{ab} + (ai||jb)\,,$$

$$B_{ai,bj} = (ai||bj)\,.$$

The system of linear equations can be written down in a concise manner by using the electronic Hessian and by combining the solution and rhs vector into one variable respectively to obtain

$$\mathbf{Hu} = \mathbf{f}^{\mathrm{RHS}}\,. \tag{12.1}$$

The basic principle of the solver is to transform the equations into a subspace using a set of orthonormal vectors $\mathbf{v}_i$ according to[157]

$$\mathbf{H}^{\mathrm{sub}} = \mathbf{V}^\dagger\mathbf{H}\mathbf{V} = \mathbf{V}^\dagger\mathbf{W}\,, \tag{12.2}$$

where all vectors $\mathbf{v}_i$ have been collected in the rectangular matrix $\mathbf{V}$. The matrix $\mathbf{W}$ analogously contains all individual matrix vector product $\mathbf{w}_i = \mathbf{H}\mathbf{v}_i$. The rhs vector can be transformed into the subspace accordingly as

$$\mathbf{f}^{\mathrm{RHS,sub}} = \mathbf{V}^\dagger \mathbf{f}^{\mathrm{RHS}} \,. \tag{12.3}$$

Next, the problem is solved in the subspace by for example Cholesky decomposition of $\mathbf{H}^{\mathrm{sub}}$ to obtain subspace solution vectors

$$\mathbf{H}^{\mathrm{sub}} \mathbf{t}^{\mathrm{sub}} = \mathbf{f}^{\mathrm{RHS,sub}} \,. \tag{12.4}$$

The solution vector can then be transformed into the full space

$$\mathbf{t} = \mathbf{V}\mathbf{t}^{\mathrm{sub}} \,, \tag{12.5}$$

resulting in an approximate solution to the original problem. Convergence is tested via the norm of the residue vector

$$\mathbf{r} = \mathbf{H}\mathbf{t} - \mathbf{f}^{\mathrm{RHS}} \,. \tag{12.6}$$

It is important to note that the evaluation of the residue vector does not necessitate the evaluation of a matrix vector product involving the electronic Hessian. It is accessible by using an identity with the already calculated set of matrix vector products as

$$\mathbf{H}\mathbf{t} = \mathbf{H}\mathbf{V}\mathbf{t}^{\mathrm{sub}} = \mathbf{W}\mathbf{t}^{\mathrm{sub}} \,. \tag{12.7}$$

If the residual norm is larger than the convergence threshold, the subspace is expanded by additional $\mathbf{v}$ vectors. To obtain these new vectors, preconditioning using the approximate diagonal of the electronic Hessian can be used.[174] The diagonal can be approximated via

$$A_{ai,ai} \approx M_{ai,ai} = \epsilon_a - \epsilon_i \,, \tag{12.8}$$

to obtain a new subspace vector as[157]

$$\mathbf{v}^{\mathrm{new}} = \mathbf{M}^{-1}\mathbf{t} - \mathbf{M}^{-1}\mathbf{r} \,. \tag{12.9}$$

Before adding a new vector to the projection matrix it usually needs to be orthonormalized with respect to the already existing set of vectors. With the expanded subspace, this procedure is repeated until convergence is reached.

12.1.1. The Matrix Vector Product

The definition of the $\mathbf{A}$ and $\mathbf{B}$ matrices was so far only given in the spinor basis. The transformation of the four-center integrals from AO to spinor basis scales with the fifth power of the number of basis functions. Additionally, the total number of spinor basis integrals can get quite large. This transformation can be avoided however, by using an integral direct procedure where the matrix vector product is

evaluated without explicitly constructing the electronic Hessian.[136,197,198] A similar procedure is later needed to form the rhs of the linear response equations for geometry derivatives. For this reason, the general contraction of a four-center integral in spinor basis is shown, which leads to a form that can be evaluated entirely in the AO basis. Considering the contraction of any matrix $\mathbf{U}$ with the respective integrals to obtain a matrix vector product $\mathbf{P}$, one obtains

$$\begin{aligned} P_{pq} &= \sum_{rs} (pq|rs) U_{sr} \\ &= \sum_{rs} \sum_{\mu\nu\kappa\lambda} C^*_{\mu p} C_{\nu q} C^*_{\kappa r} C_{\lambda s} (\mu\nu|\kappa\lambda) U_{sr} \\ &= \sum_{\mu\nu} C^*_{\mu p} C_{\nu q} \sum_{\kappa\lambda} (\mu\nu|\kappa\lambda) \sum_{rs} C^*_{\kappa r} C_{\lambda s} U_{sr} \,. \end{aligned} \tag{12.10}$$

Therefore, the first step in evaluating the matrix vector product consists of transforming $\mathbf{U}$ to the AO basis as

$$\mathbf{U}^{\mathrm{AO}} = \sum_{rs} C_{\lambda s} U_{sr} C^*_{\kappa r} \,. \tag{12.11}$$

Next, the four-center integrals are simply contracted with $\mathbf{U}^{\mathrm{AO}}$. This step is very similar to the calculation of the two-electron contribution to the Fock matrix during the SCF procedure. The main difference is that $\mathbf{U}^{\mathrm{AO}}$ generally shows no symmetry while the ground state density used for the Fock matrix is hermitian. The Fock-like matrix that is obtained from this contraction can then be transformed into the spinor basis to obtain the final quantity. The indices p, q, r, s are usually restricted to different combinations of the occupied or virtual space, depending on the exact expression for the matrix vector product.

12.2. The CPHF Right Hand Side

In this section, the integral direct construction of the rhs of the linear response equations for geometry derivatives is presented. The one-component zero field case is well known from the computation of vibrational frequencies.[199] The working equations for a two-component framework including external magnetic fields for Hartree-Fock were derived by Culpitt *et al.* in Ref. [43]. The extension to KSDFT was then presented together with Kronenberger, Appenzeller, and Pausch in Ref. [83]. Here, only the implementation of the Hartree-Fock framework is discussed. The implementation resides within the `escf` module, and a vastly simplified schematic of its workflow is shown in figure 12.1: First, the rhs is constructed. Second, the CPHF/KS equations are solved. Finally, molecular properties like the Berry curvature and the DBOC are calculated. The solver was briefly described in section 12.1, while the calculation of the molecular properties is the topic of section 13.

The expression for the rhs was given in eq. 9.24, which is repeated here for the sake of clarity:

$$F^{\mathrm{RHS},I\alpha}_{ai} = \epsilon_i \mathcal{S}^{I\alpha}_{ai} - \mathcal{F}^{(I\alpha)}_{ai} + \sum_{kl} (ai||lk) \mathcal{S}^{I\alpha}_{kl} \,.$$

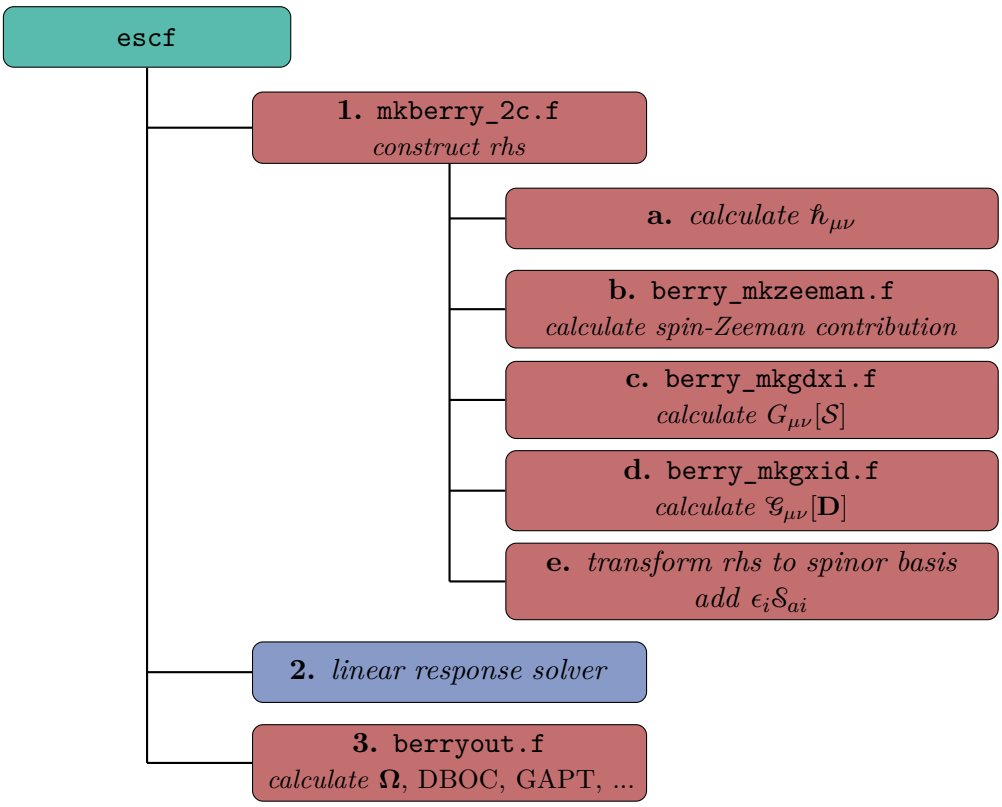

Figure 12.1.: Simplified schematic of the workflow of `escf`. The TURBOMOLE module is depicted in green, already existing routine in blue, and routines that were implemented within the scope of this work in red.

The rhs needs to be constructed for each nuclear-cartesian component $I\alpha$, this index will be suppressed in this chapter so equations are easier to read. The second (a, b, and d in figure 12.1) and third (c in figure 12.1) terms are calculated first and written to the rhs in AO basis, which is kept in memory. Then, the rhs is transformed into the spinor basis and the first term is added (e in figure 12.1). Afterwards, the final rhs is written to disk, from where it is repeatedly read whenever needed during the solving of the CPHF equations. The third term of the rhs is calculated as described for the general matrix vector product in section 12.1: The AO derivative overlap matrix is transformed into the spinor basis

$$\mathcal{S}_{kl}^{I\alpha} = \sum_{\mu\nu} C_{\mu k}^{*} C_{\nu l} \Big(\langle \nabla_{I\alpha} \xi_\mu | \xi_\nu \rangle + \langle \xi_\mu | \nabla_{I\alpha} \xi_\nu \rangle \Big) , \tag{12.12}$$

and subsequently transformed again using the spinor coefficients to obtain the density-like matrix needed for the contractions:

$$\mathcal{S}_{\kappa\lambda}^{\mathrm{AO},I\alpha} = \sum_{kl} C_{\kappa k} C_{\lambda l}^{*} \mathcal{S}_{kl}^{I\alpha} . \tag{12.13}$$

Since the summation only runs over occupied indices, the two transformation steps

can be combined into one by using the ground state density

$$\mathcal{S}^{\mathrm{AO},I\alpha}_{\kappa\lambda} = \sum_{\mu\nu} D_{\kappa\mu,0} D_{\nu\lambda,0} \Big(\langle \nabla_{I\alpha} \xi_\mu | \xi_\nu \rangle + \langle \xi_\mu | \nabla_{I\alpha} \xi_\nu \rangle \Big) \,. \tag{12.14}$$

The $\mathcal{S}^{\mathrm{AO}}$ matrix can then be used for the contraction with the fourcenter integrals and is then written to the AO basis rhs.

The second term of the rhs reads

$$\mathcal{F}^{(I\alpha)}_{ai} = \hbar^{I\alpha}_{ai} + \mathcal{G}^{I\alpha}_{ai}[\mathbf{D}] \,, \tag{12.15}$$

and contains the contributions to the Fock matrix, where only AO integrals carry a derivative. The two electron part of this contribution in AO basis is given as

$$\mathcal{G}^{\sigma\tau,I\alpha}_{\mu\nu}[\mathbf{D}] = \sum_{\kappa\lambda} \frac{\partial (\mu\nu||\kappa\lambda)}{\partial R_{I\alpha}} D^{\sigma\tau}_{\lambda\kappa} \,, \tag{12.16}$$

where the geometry derivative of the four-center integrals is contracted with the ground state density matrix. A very similar quantity is present in the expression for analytic gradients of the Hartree-Fock energy. For gradients, a second contraction with the density matrix has to be performed to obtain a scalar quantity. Consequently, any implementation of analytical gradients can be modified by dropping the second contraction to obtain this contribution to the rhs. Analytical gradients for calculations in magnetic fields as well as for relativistic X2C calculations were already present in TURBOMOLE, so only small modifications had to be made.[53,170]

The derivative one-electron Hamilton matrix $\hbar$ consists of several different terms depending on the presence of external fields or relativistic effects. It always contains the derivatives of the electron-nucleus Coulomb operator and of the kinetic energy operator of the electrons. Within the X2C framework, the derivative of the decoupling matrix enters as well and necessitates the solution of another system of linear equations similar to the CPHF equations.[170,200] For calculations in external magnetic fields, the derivatives of the spin-Zeeman and orbital-Zeeman contributions enter additionally. Once again, these quantities contracted with the ground state density matrix are required for the calculation of analytical gradients. Therefore, these necessary AO derivatives were already implemented in TURBOMOLE and can simply be added to the rhs. At this points, all contributions that can be calculated in the AO basis are gathered and can be transformed into the occupied-virtual block of the spinor basis.

Finally, the first term of eq. 9.24 can be computed by transforming the derivative overlap matrix into the occupied-virtual block and scaling it by the respective orbital energies. The contribution is then added to the rhs to complete the expression given in eq. 9.24. In the implementation, all $3N_{\mathrm{nuc}}$ rhs vectors are calculated simultaneously and are then all written to disk.

13. Molecular Linear Response Properties

This section presents details on the working equations and implementation details of molecular properties that depend on the linear response vectors, like the Berry curvature, the DBOC, GAPT charges, and the atomic pseudomomentum tensor. Currently, all of these quantities are evaluated within the `berryout` routine at the end of an `escf` calculation. An implementation of the DBOC has also been completed for one-component real-valued wavefunctions, potentially including ECPs, into the `aoforce` module together with Hamm. The details and limitations of the aforementioned implementation are summarized in section 13.2.2.

13.1. The Molecular Berry Curvature

This section aims to show how the Berry curvature tensor can be computed after the CPHF/KS equations have been solved. Since the previous section 11 already explored the same aspect for the geometric vector potential in great detail, this section is more concise. Most expressions shown in this section were first derived by Culpitt *et al.* in Ref. [43]. The general procedure to deal with nuclear derivatives of Slater determinants was already shown and the procedure changes only marginally for the Berry curvature. Recalling its definition from eq. 6.1

$$\Omega_{I\alpha J\beta} = -2\Im\langle\nabla_{I\alpha}\Psi|\nabla_{J\beta}\Psi\rangle\,,$$

the same algebraic considerations can be taken again to deal with the derivative Slater determinants, leading to

$$\begin{aligned}\langle\nabla_{I\alpha}\Psi|\nabla_{J\beta}\Psi\rangle = &\sum_i\langle\nabla_{I\alpha}\psi_i|\nabla_{J\beta}\psi_i\rangle \\ &-\sum_i\sum_{j\neq i}\langle\nabla_{I\alpha}\psi_i|\psi_j\rangle\langle\psi_j|\nabla_{J\beta}\psi_i\rangle \\ &-\sum_i\sum_{j\neq i}\langle\psi_i|\nabla_{I\alpha}\psi_i\rangle\langle\psi_j|\nabla_{J\beta}\psi_j\rangle\,.\end{aligned} \tag{13.1}$$

From here once again, each derivative spinor function is decomposed within the LCAO approach into a part where the basis function carries the derivative and another where the coefficients are derivatives. Next, the expansion of the derivative

coefficients is inserted. At the end, one arrives at the following expression:[43]

$$\begin{aligned}\langle \nabla_{I\alpha}\Psi | \nabla_{J\beta}\Psi\rangle = &\sum_i \langle \psi_i^{(I\alpha)} | \psi_i^{(J\beta)}\rangle - \sum_{ir} \langle \psi_i^{(I\alpha)} | \psi_r\rangle\langle \psi_r | \psi_i^{(J\beta)}\rangle \\ &+ \sum_{ai} \left[\langle \psi_a | \psi_i^{(I\alpha)}\rangle + U_{ai}^{I\alpha}\right]^* \cdot \left[\langle \psi_a | \psi_i^{(J\beta)}\rangle + U_{ai}^{J\beta}\right] \\ &- \sum_{ij} \left[\langle \psi_i | \psi_i^{(I\alpha)}\rangle + U_{ii}^{I\alpha}\right] \cdot \left[\langle \psi_j | \psi_j^{(J\beta)}\rangle + U_{jj}^{J\beta}\right] .\end{aligned} \tag{13.2}$$

Here $\psi_i^{(I\alpha)}$ contains basis functions that are a derivative with respect to the Cartesian nuclear coordinate $I\alpha$ and are transformed using the unperturbed coefficients of spinor i. This equation can be used to calculate any element of the quantum geometric tensor, since the Berry curvature is related to its imaginary part, any strictly real-valued term does not contribute to the Berry curvature. Hence, the following working equation can be obtained for the Berry curvature:

$$\begin{aligned}\Omega_{I\alpha J\beta} = -2\Im\Bigg(&\sum_i \langle \psi_i^{(I\alpha)} | \psi_i^{(J\beta)}\rangle + \sum_{ai} U_{ai}^{I\alpha *} U_{ai}^{J\beta} \\ &+ \sum_{ai} \langle \psi_a | \psi_i^{(J\beta)}\rangle U_{ai}^{I\alpha *} + \sum_{ai} \langle \psi_i^{(I\alpha)} | \psi_a\rangle U_{ai}^{J\beta} \\ &- \sum_{ij} \langle \psi_i^{(I\alpha)} | \psi_j\rangle\langle \psi_j | \psi_i^{(J\beta)}\rangle \Bigg) .\end{aligned} \tag{13.3}$$

13.1.1. Implementation Details

The working equation for the Berry curvature was given in eq. 13.3. In the actual implementation, the overall anti-symmetry of the Berry curvature as well as symmetry relations between the individual contributions from the working equation are exploited.

The first term is calculated from the trace of the ground state density matrix and a double derivative overlap matrix as

$$\langle \psi_i^{(I\alpha)} | \psi_i^{(J\beta)}\rangle = \sum_{\mu\nu} D_{\nu\mu,0} \langle \nabla_{I\alpha}\xi_\mu | \nabla_{J\beta}\xi_\nu\rangle . \tag{13.4}$$

As mentioned in the implementation details of the geometric vector potential, the integral routine for LAOs only outputs the lower triangle of each matrix. Since the overlap matrix with a derivative in the bra and ket is not hermitian if $I \neq J \vee \alpha \neq \beta$, special care is needed for this contraction. Exploiting the respective symmetries

between matrix elements and dropping any purely real-valued contributions yields

$$\begin{aligned}
&\Im\left(\sum_{\mu\nu} D_{\nu\mu,0}\langle\nabla_{I\alpha}\xi_\mu|\nabla_{J\beta}\xi_\nu\rangle\right)\\
=&\sum_{\mu\nu}\Re(D_{\nu\mu,0})\Im\langle\nabla_{I\alpha}\xi_\mu|\nabla_{J\beta}\xi_\nu\rangle + \sum_{\mu\nu}\Im(D_{\nu\mu,0})\Re\langle\nabla_{I\alpha}\xi_\mu|\nabla_{J\beta}\xi_\nu\rangle\\
=&\sum_{\mu\geq\nu}\frac{1}{2}(2-\delta_{\mu\nu})\Re(D_{\mu\nu,0})\Big[\Im\langle\nabla_{I\alpha}\xi_\mu|\nabla_{J\beta}\xi_\nu\rangle - \Im\langle\nabla_{J\beta}\xi_\mu|\nabla_{I\alpha}\xi_\nu\rangle\Big]\\
&-\sum_{\mu\geq\nu}\Im(D_{\mu\nu,0})\Big[\Re\langle\nabla_{I\alpha}\xi_\mu|\nabla_{J\beta}\xi_\nu\rangle - \Re\langle\nabla_{J\beta}\xi_\mu|\nabla_{I\alpha}\xi_\nu\rangle\Big].
\end{aligned} \tag{13.5}$$

Here, the factor responsible for scaling the diagonal contributions $\mu = \nu$ by 0.5 in the second contribution is omitted since the density matrix is hermitian and therefore $\Im(D_{\mu\mu,0}) = 0$. During the calculation of this quantity, the lower triangle of all $9N_{\text{nuc}}^2$ double derivative matrices are kept in memory, for very large systems the memory requirements can quickly grow as it scales with the second power of both, the number of nuclei in the system and the number of basis functions. All other similar quantities either only contain one geometry derivative or only need to be saved in the occupied-virtual basis, which would result in less memory requirements for usual systems.

The second term of eq. 13.3 is very straightforward to implement, as it is just given by the cross product of different linear response vectors.

The third term and fourth term in eq. 13.3 are related to each other according to

$$\sum_{ai}\langle\psi_a|\psi_i^{(J\beta)}\rangle U_{ai}^{I\alpha *} = \left(\sum_{ai}\langle\psi_i^{(J\beta)}|\psi_a\rangle U_{ai}^{I\alpha}\right)^*, \tag{13.6}$$

for this reason, only the fourth term is calculated for all combinations of I and J. For this contribution, the overlap matrix with a derivative function in the bra needs to be transformed into the occupied-virtual space of the spinor basis. To achieve this, the full bra-derivative overlap matrix needs to be constructed first. Since the matrix is not hermitian, the upper triangle of the matrix needs to be constructed from the ket derivative matrix as

$$\langle\nabla_{I\alpha}\xi_\mu|\xi_\nu\rangle = \langle\xi_\nu|\nabla_{I\alpha}\xi_\mu\rangle^*. \tag{13.7}$$

The full bra-derivative matrix is then decomposed into a symmetric and an anti-symmetric part and passed to the transformation routine for the occupied-virtual block to obtain $\langle\psi_i^{(I\alpha)}|\psi_a\rangle$. These $3N_{\text{nuc}}$ matrices are all kept in memory and subsequently contracted with different U matrices to obtain the respective contribution to the Berry curvature. In this final contraction step only the imaginary part of the product is calculated once again. For the first term, the bra-derivative overlap matrix is transformed into the occupied-occupied block of the spinor basis. The

$3N_{\mathrm{nuc}}$ matrices are kept in memory and contracted with each other according to

$$\begin{aligned} &- \Im\left(\sum_{ij}\langle\psi_i^{(I\alpha)}|\psi_j\rangle\langle\psi_j|\psi_i^{(J\beta)}\rangle\right) \\ =& -\sum_{ij}\Im\langle\psi_i^{(I\alpha)}|\psi_j\rangle\Re\langle\psi_j|\psi_i^{(J\beta)}\rangle + \Re\langle\psi_i^{(I\alpha)}|\psi_j\rangle\Im\langle\psi_j|\psi_i^{(J\beta)}\rangle \\ =& -\sum_{ij}\Im\langle\psi_i^{(I\alpha)}|\psi_j\rangle\Re\langle\psi_i^{(J\beta)}|\psi_j\rangle - \Re\langle\psi_i^{(I\alpha)}|\psi_j\rangle\Im\langle\psi_i^{(J\beta)}|\psi_j\rangle\,. \end{aligned} \tag{13.8}$$

With all individual contributions gathered, they are multiplied by the missing factor of two from eq. 13.3 to obtain the final Berry curvature. The non-redundant 3×3 blocks of the Berry curvature are printed into the output of `escf`. Additionally, the whole $3N_{\mathrm{nuc}} \times 3N_{\mathrm{nuc}}$ matrix is written to a file named `berrycur` with a total of 14 decimal places.

From the Berry curvature, the Berry charge population is computed using a modification of eq. 6.8:

$$Q_{IJ} = \frac{1}{2|\mathcal{B}|^2}\Big[(\Omega_{IzJy} - \Omega_{IyJz})\mathcal{B}_x + (\Omega_{IxJz} - \Omega_{IzJx})\mathcal{B}_y + (\Omega_{IyJx} - \Omega_{IxJy})\mathcal{B}_z\Big]\,. \tag{13.9}$$

Summation over one index of the charge population results in the electronic contribution to the Berry partial charge

$$q_I^{\mathrm{Berry,el}} = \sum_J Q_{IJ}\,. \tag{13.10}$$

The output then shows a list of all nuclei in the molecule, their nuclear charge, their electronic Berry charge, and the Berry partial charge as the sum of the latter two. The total sum of the Berry partial charges is additionally provided which should equal the total molecular charge up to the numerical precision dictated by the convergence criteria.

13.2. The Diagonal Born-Oppenheimer Correction

The DBOC was defined in eq. 5.19 and was previously determined to be related to the diagonal elements of the real part of the quantum geometric tensor and the geometric vector potential. Therefore, a working equation for the DBOC can be constructed from the already established equations 11.7 and 13.2. One element of the geometric scalar potential is obtained as

$$\overline{\boldsymbol{\Delta}}_I = \sum_i\langle\psi_i^{(I)}|\psi_i^{(I)}\rangle - \sum_{ir}\left|\langle\psi_i^{(I)}|\psi_r\rangle\right|^2 + \sum_{ai}\left|\langle\psi_a|\psi_i^{(I)}\rangle + U_{ai}^I\right|^2, \tag{13.11}$$

from which the DBOC can be obtained according to eq. 5.19 as

$$E_{\mathrm{DBOC}} = \sum_I \frac{\overline{\Delta}_I}{2M_I}\,.$$

13.2.1. Implementation Details - Complex Two-Component `escf`

Most contributions to the DBOC in eq. 13.11 are very similar to certain terms encountered in the working equation for the molecular Berry curvature in eq. 13.3. Indeed, the very first term in eq. 13.11 occurring for the geometric scalar potential is obtained from the diagonal elements of the first term of the Berry curvature. While the Berry curvature needs the total imaginary part of the respective integral, the DBOC needs its real part. Therefore, both contributions are calculated simultaneously in the fashion described in section 13.1. The second term in eq. 13.11 is related to the third, fourth and fifth term of the Berry curvature working equation. Its evaluation involves the occupied-occupied and occupied-virtual blocks of the bra-derivative overlap matrix. The squared absolute value of the respective quantity is simply added to the geometric scalar potential when they are available in memory from the calculation of the Berry curvature. Similarly, the third term of the geometric scalar potential of eq. 13.11 is straightforward to calculate. All $3N_{\mathrm{nuc}}$ linear response vectors $\mathbf{U}$ are held in memory for the most part of the routine handling the calculation of the molecular properties. When the bra-derivative overlap matrices have been transformed into the occupied-virtual block of the spinor basis as needed for the Berry curvature, the third term of the geometric scalar potential is calculated. At the very end, the elements of the geometric scalar potential are scaled with the respective nuclear masses and summed according to eq. 5.19 to obtain the final DBOC. The output features the contributions of each nucleus including each nuclear mass that was used in the calculation. Per default TURBOMOLE uses isotope-averaged atomic masses, it is therefore advisable to define the mass of each nucleus in the molecule before a calculation, especially if an isotope-specific DBOC needs to be calculated. Notably, the masses can also be changed after the `escf` calculation, because the linear response vectors are saved on disk afterwards. Therefore, after modifying the nuclear masses, a computationally undemanding recalculation of the molecular properties can be invoked using `escf -proper`.

13.2.2. Implementation Details - Real One-Component `aoforce`

For the implementation of the DBOC for real valued wave functions in the `aoforce` module, the working equation is slightly modified by manipulating the squared absolute values

$$\begin{aligned}\overline{\Delta}_{I\alpha} &= \sum_i \langle\psi_i^{(I\alpha)}|\psi_i^{(I\alpha)}\rangle - \sum_{ir}\langle\psi_i^{(I\alpha)}|\psi_r\rangle^2 + \sum_{ai}\left(\langle\psi_a|\psi_i^{(I\alpha)}\rangle + U_{ai}^{I\alpha}\right)^2 \\ &= \sum_i \langle\psi_i^{(I\alpha)}|\psi_i^{(I\alpha)}\rangle - \sum_{ij}\langle\psi_i^{(I\alpha)}|\psi_j\rangle^2 + \sum_{ai}\left[(U_{ai}^{I\alpha})^2 + \langle\psi_a|\psi_i^{(I\alpha)}\rangle U_{ai}^{I\alpha}\right] .\end{aligned} \tag{13.12}$$

Almost all quantities involved in this expression are already needed for the calculation of the second derivative of the SCF energy.[198] The exception is the ket-derivative overlap matrix transformed into the occupied-virtual block of the MO basis. This matrix is, however, needed for the construction of the `aoforce` rhs. Since it needs

to be multiplied with the linear response solution vectors that are not yet available during the rhs evaluation, the $3N_{\text{nuc}}$ MO basis matrices are written to disk and saved for later processing. After the CPHF equations have been solved and the second derivative of the SCF energy is constructed, an array for the geometric vector potential is passed to the relevant subroutines, where all necessary contributions are gathered. Notably, the third term of eq. 13.12 is evaluated at the point where the only **U**-dependent contribution to the SCF energy derivative is calculated, at which point the integrals that were saved to disk are processed.

13.3. Derivatives of One-Electron Operators

The quantities investigated in sections 11, 13.1, and 13.2, namely the geometric vector potential, the Berry curvature, and the DBOC, cannot be written as a derivative of the electronic energy. In Ref. [39], Resta shows that any adiabatic linear-response property can be expressed as a sum of a one-electron contribution and a quantum geometric contribution containing the QGT. For a general time-dependent operator that can be written as a derivative of the Hamiltonian

$$\hat{O} = \partial_{\lambda_1} \hat{H} \,, \tag{13.13}$$

the time evolution the respective observable is obtained as[39]

$$\begin{aligned} O(t) &= \partial_{\lambda_1} E^{\text{el}} - \sum_i \Omega_{\lambda_1 \lambda_i} \dot{\lambda}_i(t) \\ &= \langle \Psi | \hat{O} | \Psi \rangle - \sum_i \Omega_{\lambda_1 \lambda_i} \dot{\lambda}_i(t) \,. \end{aligned} \tag{13.14}$$

In many cases, one of these contributions vanishes. Properties where only the one-electron contribution remains include but are not limited to: electronic dipole moments, magnetic dipole moments, quadrupole moments, and different momentum operators like the canonical or pseudomomentum operator, or the rotational g-factor. These expectation values can be calculated from the matrix representation of their respective operator $\hat{O}$ and the spin-symmetric part of the ground state density as

$$\langle O \rangle = \text{Tr}(\mathbf{O}\mathbf{D}_0) = \sum_{\mu\nu} O_{\mu\nu} D_{\nu\mu,0} \,. \tag{13.15}$$

From here the derivative of the expectation value can be computed via the product rule, as

$$\nabla_{I\alpha} \langle O \rangle = \text{Tr}(\mathbf{O}^{I\alpha}\mathbf{D}_0) + \text{Tr}(\mathbf{O}\mathbf{D}_0^{I\alpha}) \,, \tag{13.16}$$

where the superscript $I\alpha$ indicates a derivative. Depending on the operator $\hat{O}$, the calculation of the derivative AO integrals can have different degrees of computational complexity. The derivative density matrix can be constructed from the spinor coefficient matrix and the matrix **U** as

$$\mathbf{D}^{I\alpha} = \nabla_{I\alpha} \left(\mathbf{C}_{\text{occ}} \mathbf{C}_{\text{occ}}^\dagger \right) = (\nabla_{I\alpha} \mathbf{C}_{\text{occ}}) \mathbf{C}_{\text{occ}}^\dagger + \mathbf{C}_{\text{occ}} (\nabla_{I\alpha} \mathbf{C}_{\text{occ}})^\dagger \,. \tag{13.17}$$

Inserting the expansion for the derivative coefficients from eq. 9.2 leads to the following equation for one element of the derivative density matrix

$$D_{\mu\nu}^{\sigma\tau,I\alpha} = \sum_{ai} C_{\mu i}^{\sigma} C_{\nu a}^{\tau *} U_{ai}^{I\alpha *} + \sum_{ai} C_{\mu a}^{\sigma} C_{\nu i}^{\tau *} U_{ai}^{I\alpha} - \sum_{ij} C_{\mu i}^{\sigma} C_{\nu j}^{\tau *} \Re(\mathcal{S}_{ij}^{I\alpha}) \,. \tag{13.18}$$

After constructing the derivative density matrix, the derivative of any one-electron expectation value can be calculated, as long as the necessary integrals in AO basis are accessible.

13.3.1. Implementation Details

Currently, the `escf` output includes the geometry derivatives of the electric dipole moments, the canonical momentum, and the pseudomomentum. For this purpose, the derivative density matrix is constructed according to eq. 9.2 by first evaluating the full derivative coefficients matrix for one Cartesian nuclear component from the unperturbed spinor coefficients, the linear response vectors, as well as the real part of the derivative overlap matrix transformed into the occupied-occupied block. Afterwards, eq. 13.17 is used to construct the derivative density matrix itself. All quantities involved in this calculation have already been discussed in section 13.1 in more detail.

In the next step, the different derivative one-electron expectation values can be constructed using a modification of eq. 13.16:

$$\nabla_{I\alpha} \langle O \rangle = \sum_{\mu\nu} \langle \xi_\mu | \hat{O} | \xi_\nu \rangle D_{\nu\mu,0}^{I\alpha} + \sum_{\mu\nu} \left(\nabla_{I\alpha} \langle \xi_\mu | \hat{O} | \xi_\nu \rangle \right) D_{\nu\mu,0} \tag{13.19}$$

As previously mentioned, this requires the AO integrals over the non-derivative operator as well as the geometry derivative of that integral. The derivative of the canonical momentum operator is calculated and printed to the output unmodified. It will be needed later to compute the atomic pseudomomentum tensor. Next, the geometry derivative of the electric dipole moment, namely the electronic contribution to the atomic polar tensor

$$T_{I,\alpha\beta} = \frac{\partial \mu_\beta}{\partial R_{I\alpha}} \,,$$

is calculated and given in the output. Section 10.2 introduced the generalized atomic polar tensor charges, their definition was provided in eq. 10.5:

$$q_I^{\mathrm{GAPT}} = \frac{1}{3} \left(T_{I,xx} + T_{I,yy} + T_{I,zz} \right) \,.$$

Using that equation and the nuclear charges, the GAPT partial charges are computed. Their report in the output features the electronic and nuclear contributions to the partial charge in addition to their sum. Similarly to the Berry charges, the total sum is given as well and should reproduce the total molecular charge generally to a high degree depending on the convergence criteria. Finally, the derivative

canonical momentum, the APT, and the magnetic flux density vector can be used to evaluate the atomic pseudomomentum tensor from a modification of eq. 6.17. Using the magnetic vector potential in the Coulomb gauge, one component of the pseudomomentum tensor can be obtained as

$$\frac{\partial p_\beta}{\partial R_{I\alpha}} - \left[\mathbf{A}\left(\frac{\partial \boldsymbol{\mu}}{\partial R_{I\alpha}}\right)\right]_\beta , \tag{13.20}$$

which is then also reported in the output of `escf`.

In principle this procedure can be easily expanded to any other geometry derivative as long as it can be computed from the first derivative of the spinor coefficients or of the ground state density matrix.

13.4. Rotating Electronically Instable Wave Functions

After converging the SCF procedure, there is no guarantee that the global minimum was found. Instead, one might find only a local minimum, or not even a minimum but some kind of stationary point resembling a saddle point with respect to orbital rotations. If such a saddle point is converged, the electronic wave function is said to show an electronic instability.[201,202] A rather trivial example for this might be the hydrogen molecule in a very strong magnetic field, where at some point the triplet state will be the ground state because of the pronounced spin-Zeeman contribution. If one now converges the singlet state in a two-component calculation, the lower triplet state becomes accessible from an orbital rotation. This kind of stability analysis is analogous to the investigation of molecular geometries via vibrational frequencies. Thus, the quantity of interest for electronic instabilities are the eigenvalues of the electronic Hessian given in equations 9.22 and 9.23

$$\begin{pmatrix} \mathbf{A} & \mathbf{B} \\ \mathbf{B}^* & \mathbf{A}^* \end{pmatrix} \begin{pmatrix} \mathbf{X} \\ \mathbf{Y} \end{pmatrix} = \omega \begin{pmatrix} \mathbf{X} \\ \mathbf{Y} \end{pmatrix} . \tag{13.21}$$

It is desirable to converge to a local minimum, not a saddle point, because a lower energy state is a better approximation to the exact solution according to the variational principle.[201,203] Using the spin-unrestricted two-component framework, it is rather common, especially for certain groups of molecules, to converge to an electronically instable state. Hence, a procedure to get rid of such instabilities can be of great value. For geometric transition states this is commonly done, one simply displaces the molecular geometry along the normal mode corresponding to the negative eigenvalue (or imaginary vibrational frequency for that matter). Analogously, the electronic wave function can essentially be rotated along the corresponding eigenvector of the electronic Hessian as previously reported in the literature.[202] To achieve this, Goings *et al.* proposed in Ref. [202] that a unitary matrix can be constructed from the $\mathbf{X}$ vector of eq. 13.21 as

$$\mathbf{R} = \exp\begin{pmatrix} \mathbf{0} & -\eta\mathbf{X}^\dagger \\ \eta\mathbf{X} & \mathbf{0} \end{pmatrix} , \tag{13.22}$$

where the real valued scalar parameter η is a scaling factor, resembling a step width along the instability vector. Then, a new set of coefficients can be constructed as

$$\mathbf{C}^{\text{new}} = \mathbf{C}\mathbf{R}\,. \tag{13.23}$$

The effect of applying the orbital rotation $\mathbf{R}$ becomes more apparent when looking at the Taylor expansion of eq. 13.22:

$$\mathbf{R} = \mathbf{1} + \eta \begin{pmatrix} \mathbf{0} & -\mathbf{X}^\dagger \\ \mathbf{X} & \mathbf{0} \end{pmatrix} + \dots\,. \tag{13.24}$$

Therefore, the new set of spinor coefficients mostly consists of the unperturbed original coefficients with a certain amount of the rotated wave function mixed in. The skew-hermitian matrix occurring in the linear term applies differently to the occupied and virtual space of the coefficients, respectively. Because the $\mathbf{X}$ matrix is spanned in the occupied-virtual space, the zeroth and first order contributions to the individual blocks of the new coefficients become

$$\mathbf{C}_{\text{occ}}^{\text{new}} = \mathbf{C}_{\text{occ}} - \eta \mathbf{C}_{\text{virt}} \mathbf{X}^\dagger\,, \tag{13.25}$$

and

$$\mathbf{C}_{\text{virt}}^{\text{new}} = \mathbf{C}_{\text{virt}} + \eta \mathbf{C}_{\text{occ}} \mathbf{X}\,. \tag{13.26}$$

After the new coefficients are obtained from one of the presented equations, the SCF procedure can be restarted from there, which can help to find an energetically lower lying state. Note that the exact procedure to compute the new coefficients is not too important. The most important aspect is to break the symmetry corresponding to the saddle point, and afterwards the SCF algorithm usually finds "downhill" on its own. This is again similar to the breakage of symmetry in a geometry optimization to find a local minimum starting at a transition state: If the SCF procedure is started with a spin-symmetric singlet wave function, but the lowest state is a triplet with different alpha and beta spin contributions, this spin-symmetry needs to be broken first for the SCF algorithm to find the lower state.

13.4.1. Implementation Details

Electronic instabilities and how to potentially eliminate them from a calculation were shortly discussed in the previous paragraphs. There, an approach proposed by Goings *et al.* from Ref. [202] was discussed, where the spinor coefficients of an SCF calculation are rotated via a unitary matrix that is constructed from an eigenvector of the electronic Hessian. The definition of this matrix was provided in eq. 13.22, where $\mathbf{X}$ is part of the eigenvalue of the electronic hessian, and η is a real-valued scaling factor. The implementation into the `escf` module of TURBOMOLE was shortly summarized in Ref. [83]. Here, the matrix exponential is approximated as

$$\mathbf{R} \approx \left[\mathbf{1} + \frac{1}{128} \begin{pmatrix} \mathbf{0} & -\eta\mathbf{X}^\dagger \\ \eta\mathbf{X} & \mathbf{0} \end{pmatrix} \right]^{128}\,, \tag{13.27}$$

by repeatedly squaring the matrix in brackets. Afterwards, the original spinor coefficients $\mathbf{C}$ are transformed into the new set as

$$\mathbf{C}^{\text{new}} = \mathbf{CR}\,. \tag{13.28}$$

The rotated spinor coefficients are written into files named `new_spinor.r` and `new_spinor.i`, respectively. The format of these files is equivalent to the regular spinor files from TURBOMOLE and they can just be renamed to restart the calculation from there. In practice, it is advisable to start the new calculation in another directory, e.g. a subdirectory created using the `cpc` script or TURBOMOLE. The main reason for this recommendation is that the scaling parameter η might not have been correctly tuned the first time and a new set of rotated coefficients needs to be constructed. In this case the spinor coefficients and electronic hessian eigenvectors of the original calculation are required. The scaling parameter is set with the `rotate_step <float>` keyword in the `control` file, where the value `<float>` defines η. To aid in the tuning of this parameter, the output of `escf` contains the absolute value of the largest coefficient found in the $\mathbf{R}$ matrix as a measure of the largest mixing between two spinors. Additionally, the indices of these two spinors are provided. Generally, η can be chosen in the range of 10^{-4} to 1, where a resulting maximal mixing of about 0.05 is the recommended starting point. If the SCF calculation that is started using the new spinor coefficients converges to the same energy as the original calculation, the scaling parameter should generally be chosen such that a larger mixing is obtained. Alternatively, if the electronic hessian has several negative eigenvalues, rotating along multiple different vectors can be attempted. The number of the eigenvector along which the rotation is conducted can be specified using the `rotate_instab <n>` keyword, where `<n>` is the number of the vector according to the output of `escf`.

14. Overview of the Available Functionalities

This section summarizes the functionalities available in TURBOMOLE that were discussed in this work, as well as some related functionalities. The necessary keywords and suggested parameters like convergence criteria are provided.

14.1. Magnetic Field Definition in `define`

In the last menu of `define`, the magnetic field can be specified using the `b` option. There, one can specify the exact magnetic flux density vector by providing its three Cartesian components. Alternatively, its direction and magnitude can be specified. The magnetic flux density can be set in atomic units B_0 or in SI-units using Tesla T. For DFT calculations it is often necessary to align the magnetic field with the Cartesian z-axis due to restrictions in the implementation. If the magnetic flux density vector is not already parallel to the z-axis and the option `zfield` is activated in `define`, the user will be asked if the molecule and field vector should be rotated such that the latter is parallel to the z-axis. After leaving the `b` menu, the options `soghf` and `coulex` will be set if the user does not object, thereby activating the two-component framework by default.

14.2. SCF Functionalities

One-component SCF calculations in external magnetic fields can be performed using the `dscf` module with Hartree-Fock or most DFT functionals. Some benchmarks for the one-component calculation can be found in Ref. [83] and were implemented by Appenzeller and Pausch. Two-component calculations in external magnetic fields are available in the `ridft` module featuring Hartree-Fock as well as most DFT functionals. Additionally, relativistic effects using the X2C Hamiltonian can be included with or without the presence of external magnetic fields.

14.3. The Geometric Vector Potential

The calculation of the geometric vector potential is available within the `ridft` module for any two-component calculation if the keyword `berry` is set. It is advisable to set the `denconv 1d-<n>` keyword reasonably high, where `<n>` roughly corresponds to the number of converged decimal places of the geometric vector potential. The implementation of the geometric vector potential is compatible with all functionalities

of the complex two-component `ridft` module, including Hartree-Fock and most types of DFT functionals.

14.4. The Molecular Berry Curvature

14.4.1. Analytical – Linear Response Calculation

The calculation of the molecular Berry curvature is available within the `escf` module for two-component calculations including either external magnetic fields or the relativistic X2C Hamiltonian. Notably, the combination of these two is currently only available for SCF calculations. The missing component for the Berry curvature is the analytical derivative of the X2C decoupling in the presence of magnetic fields. To calculate the Berry curvature the keywords `scfinstab polly` and `berry` need to be set in the control file. The underlying SCF calculation should be tightly converged by setting `scfconv <n>` and `denconv 1d-<n>`. For small molecules `<n>` can usually be chosen in the range of 10–12. The convergence criterion for the norm of the linear response vectors can be set using `rpaconv <m>`, where reasonable values for `<m>` are one or two below `<n>`. Additionally, if convergence problems during the linear response calculation are encountered, it is often advisable to set `scftol 1d-<l>`, where `<l>` can be set as high as needed. Many calculations in this work set `scftol 1d-40` as a preventive measure. The calculation of the Berry curvature in external magnetic fields is currently supported for Hartree–Fock calculations. DFT calculations with the magnetic field aligned with the z-axis support the following types of functionals: LDAs, GGAs, mGGAs, and global as well as range-separated hybrids thereof. For X2C calculations, only Hartree–Fock is currently available. For DFT linear response calculations, the keyword `kramers` needs to be set in `escf` to exploit time-reversal symmetry. However, for these calculations the Berry curvature always vanishes; more details are provided in section 19.

14.4.2. Numerical – Finite Differences

As an alternative to the analytical calculation using `escf`, a TURBOMOLE script was implemented in collaboration with Pausch to calculate the Berry curvature numerically in a one- or two-component framework as suggested in references [47] and [53]. The `NumBerry` script can be used equivalently to the `NumForce` script. It works by building the derivatives of the wave function numerically and relies on transforming the phases of individual MOs or spinors to fit that of the reference calculation. This procedure limits the numerical accuracy greatly. For this reason, a small nuclear displacement of about $10^{-4}\,a_0$ is recommended together with tight convergence criteria for the SCF energy and ground state density using `scfconv <n>` and `denconv 1d-<n>`. The `NumBerry` script is available for one-component magnetic fields calculations using the `dscf` module. Additionally, the two-component framework using the `ridft` module can handle external magnetic fields, the relativistic

X2C Hamiltonian, or their combination.

14.5. The Diagonal Born Oppenheimer Correction

14.5.1. Complex two-component `escf`

The calculation of the DBOC requires the same computational infrastructure as the Berry curvature, as such the same keywords as given in section 14.4 are needed. The convergence criteria should also be set in a way similar to the Berry curvature calculation.

14.5.2. Real-valued one-component `aoforce`

Similarly, the DBOC requires the same infrastructure as `aoforce` calculations in C_1-symmetry, but is only calculated if the keyword `nosalc` is set in the control file due to limitations of the DBOC implementation. Additionally, the full molecular Hessian needs to be constructed, meaning `les` may not be set to only calculate the lowest few eigenvalues. Convergence criteria for the preceding SCF and the CPHF calculations should be set as described in section 14.4.

14.6. Rotating Instable Wave Functions

After any two-component instability calculation using the `escf` module with the keyword `scfinstab complex`, the spinor coefficients can be rotated along any computed eigenvector of the electronic hessian. The number of the vector can be chosen using the keyword `rotate_instab <`*n*`>`, and the step width is specified using `rotate_step <`*float*`>`. The new spinor coefficients are then written to the files `new_spinor.r` and `new_spinor.i`. The rotation of the wave function can be cheaply recalculated using `escf --proper`.

Part IV.

Applications

15. The Molecular Berry Curvature

This introductory section lays out some of the principle properties of the molecular Berry curvature. As such, some small systems are investigated to explore different properties of the Berry curvature based on examples of increasing complexity.

15.1. The Molecular Berry Curvature of Individual Atoms

One of the simplest possible systems is the hydrogen atom in a magnetic field. The Berry curvature of the H-atom in the presence of a magnetic field with a flux density of $0.1\,B_0$ solely along the z-axis is shown in table 15.1.

	x	y	z
x	0	-0.1	0
y	0.1	0	0
z	0	0	0

Table 15.1.: Berry curvature of the hydrogen atom in the presence of a magnetic field with a flux density of $0.1\,B_0$ along the z-axis. Values given in $[eB_0]$.

For a single atom, the Berry curvature is a 3×3 matrix, where several fundamental properties are already apparent. First, the overall anti-symmetry of the Berry curvature $\mathbf{\Omega}^{\mathrm{T}} = -\mathbf{\Omega}$ is clearly visible. Second, the magnetic translational sum rule is easily verified.[46] The rule states that summation over both nuclear indices of the molecular Berry curvature is related to the magnetic flux density and the total number of electrons in the system. The rule was already provided in eq. 6.11 but is repeated here for the sake of clarity:

$$\sum_{IJ} \Omega_{I\alpha J\beta} = -N_{\mathrm{el}} \sum_{\gamma} \varepsilon_{\alpha\beta\gamma} \mathcal{B}_{\gamma}\,.$$

For the special case of the hydrogen atom with the magnetic flux density vector along the z-axis this expression simplifies to

$$\begin{aligned} & \Omega_{\alpha\beta} = -N_{\mathrm{el}} \varepsilon_{\alpha\beta z} \mathcal{B}_z \\ \Leftrightarrow \quad & \Omega_{xy} = -N_{\mathrm{el}} \mathcal{B}_z = -0.1\, eB_0 \\ \Leftrightarrow \quad & \Omega_{yx} = N_{\mathrm{el}} \mathcal{B}_z = 0.1\, eB_0\,. \end{aligned} \tag{15.1}$$

Additionally, the rule dictates that all other Berry curvature elements must vanish. As another consequence of the relations shown in eq. 15.1, it is rather intuitive that

an atomic partial charge can be formulated based on the Berry curvature. Applying the equation provided in section 10.1, the trivial electronic partial charge of $1\,e$ is obtained for the hydrogen atom. In a related manner, the forces acting on the hydrogen nucleus can be examined. The nuclear equations of motion were presented in section 5, where equation 5.41 was obtained. It yielded:

$$\mathbf{F}_I = -\frac{\partial U}{\partial \mathbf{R}_I} + Z_I \dot{\mathbf{R}}_I \times \mathcal{B} + \sum_J \mathbf{\Omega}_{IJ} \dot{\mathbf{R}}_J \,.$$

The three contributions to the force were identified in eq. 5.42 as the BO force, which is just the gradient of the electronic energy, the Lorentz force acting on the bare nuclear charge, and the Berry force. Intuitively, a particle carrying no charge should not experience any deflecting Lorentz forces in an external magnetic field. Consequently, the Berry force should cancel the bare Lorentz force exactly in the case of the hydrogen atom. Eq. 5.37 established the equivalence of the vector vector cross product and the matrix vector product of an antisymmetric matrix. Since the Berry curvature is antisymmetric and the number of electrons is equal to the nuclear charge, the relations in eq. 15.1 make sure that the resulting Lorentz and Berry forces cancel exactly. The Berry forces simply read

$$F_x^{\mathrm{B}} = \Omega_{xy} v_y = -0.1\, eB_0 \cdot v_y \,, \tag{15.2}$$

$$F_y^{\mathrm{B}} = \Omega_{yx} v_x = 0.1\, eB_0 \cdot v_x \,, \tag{15.3}$$

with the velocity of the hydrogen nucleus in the y-direction v_y, as all other Berry curvature elements are zero.

15.1.1. Skew Magnetic Fields

If the magnetic flux density vector is no longer aligned with the z-axis, the Berry curvature takes on a more complicated form. By rotating the whole system, consisting of the molecule and the magnetic flux density vector, the latter can be aligned with a certain axis again. From this consideration, it is evident how the Berry curvature of a single atom will change under such rotation. Table 15.2 shows the Berry curvature of the hydrogen atom, where the magnetic flux density vector is oriented in the Cartesian $(1, 2, 3)^{\mathrm{T}}$ direction with a magnitude of $0.1\, B_0$. This choice results in $\mathcal{B} \approx (0.026\,726, 0.053\,452, 0.080\,178)^{\mathrm{T}}$.

	x	y	z
x	0	−0.080 178 372 574	0.053 452 248 382
y	0.080 178 372 574	0	−0.026 726 124 191
z	−0.053 452 248 382	0.026 726 124 191	0

Table 15.2.: Berry curvature of the hydrogen atom with a magnetic flux density of $0.1\, B_0$ along the Cartesian $(1, 2, 3)^{\mathrm{T}}$ direction. Values given in $[eB_0]$.

This time the magnetic translational sum rule dictates the following ratios between the non-redundant Berry curvature elements:

$$\Omega_{yz} : \Omega_{zx} : \Omega_{xy} = 1 : 2 : 3\,. \tag{15.4}$$

The Berry curvature shown for the skew magnetic field in table 15.2 can equivalently be obtained from a 3D-rotation of the matrix given in table 15.1 where the field was aligned with the z-axis.

15.1.2. The Nitrogen Atom

For the sake of completeness, the nitrogen atom in the presence of a magnetic field with a flux density of $0.1\,B_0$ is briefly discussed as an example of a many-electron atom. The molecular Berry curvature is presented in table 15.3.

	x	y	z
x	0	-0.7	0
y	0.7	0	0
z	0	0	0

Table 15.3.: Berry curvature of the nitrogen atom with a magnetic flux density of $0.1\,B_0$ along the z-axis. Values given in $[eB_0]$.

As expected, all but two elements vanish and the absolute value of the two non-zero elements gives the total number of electrons, which is seven, scaled with the magnetic flux density.

To summarize, the Berry curvature of any atomic system in an external magnetic field is trivially obtained from the total number of electrons in the system and the magnetic flux density vector. On a more practical note, the only non-vanishing contribution of the working equation for the Berry curvature within the CPHF framework is the first term on the right hand side in eq. 13.3. All contributions that contain the derivative of the coefficients vanish for a system containing a single atom.

15.2. The Molecular Berry Curvature of Diatomic Molecules

Having presented the properties of the molecular Berry curvature for atoms, this section moves on to diatomic molecules. The general structure of the molecular Berry curvature of a system containing two nuclei A and B is

$$\boldsymbol{\Omega} = \begin{pmatrix} \boldsymbol{\Omega}_{\mathrm{AA}} & \boldsymbol{\Omega}_{\mathrm{AB}} \\ \boldsymbol{\Omega}_{\mathrm{BA}} & \boldsymbol{\Omega}_{\mathrm{BB}} \end{pmatrix}\,, \tag{15.5}$$

which is a $3N_{\mathrm{nuc}} \times 3N_{\mathrm{nuc}} = 6 \times 6$ matrix. It consists of individual 3×3 matrices for each pair of nuclei. From the overall antisymmetry of the Berry curvature, it follows

that the blocks on the diagonal $\mathbf{\Omega}_{IJ}$ are antisymmetric themselves. Accordingly, the off-diagonal block are related to each other as

$$\mathbf{\Omega}_{\mathrm{AB}}^{\mathrm{T}} = -\mathbf{\Omega}_{\mathrm{BA}}\,, \tag{15.6}$$

while the individual block generally retains no internal symmetry.

15.2.1. The Helium Dimer

A simple system that can be considered is the helium dimer with the nuclei on the cartesian x-axis and the magnetic field along the z-axis. There are only two non-redundant Berry curvature elements, all other elements can be obtained from the internal symmetry of the Berry curvature or the point group symmetry of the system.[204] These elements are:

$$\Omega_{1x1y} = -\Omega_{1y1x} = \Omega_{2x2y} = -\Omega_{2y2x} =: a\,, \tag{15.7}$$

$$\Omega_{1x2y} = -\Omega_{2y1x} = \Omega_{2x1y} = -\Omega_{2x1y} =: b\,, \tag{15.8}$$

resulting in the Berry curvature

$$\mathbf{\Omega} = \left(\begin{array}{ccc|ccc} 0 & a & 0 & 0 & b & 0 \\ -a & 0 & 0 & -b & 0 & 0 \\ 0 & 0 & 0 & 0 & 0 & 0 \\ \hline 0 & b & 0 & 0 & a & 0 \\ -b & 0 & 0 & -a & 0 & 0 \\ 0 & 0 & 0 & 0 & 0 & 0 \end{array}\right)\,. \tag{15.9}$$

The magnetic translational sum rule now yields

$$\begin{aligned} & 2a + 2b = -N_{\mathrm{el}}\mathcal{B}_z = -0.4\,eB_0 \\ \Leftrightarrow \qquad & a + b = -0.2\,eB_0\,, \end{aligned} \tag{15.10}$$

relating both elements of the Berry curvature to each other. If both nuclei are infinitely far away from each other so that they do not interact at all, the limit of two individual atoms is recovered again. As expected, this trivially yields $a = -0.2\,eB_0$ and $b = 0\,eB_0$. With decreasing bond distance, as the electronic structure of the helium atoms starts to interact, a gradual shift from the Berry curvature element a to b is expected, while their sum must remain constant according to eq. 15.10. This is presented in Figure 15.1, where both non-redundant Berry curvature elements are shown for varying interatomic distances. Starting at large distances, one element is very close to zero, while the other element starts at $-0.2\,eB_0$. The cross element Ω_{1x2y} then gradually starts to increase in absolute value with a decreasing interatomic distance. At some point, the element of the diagonal block approaches zero and then changes its sign. Additionally, from figure 15.1 it is evident that the sum of these elements does indeed equal $-0.1\,eB_0$ as clearly indicated by the mirror symmetry of the curves.

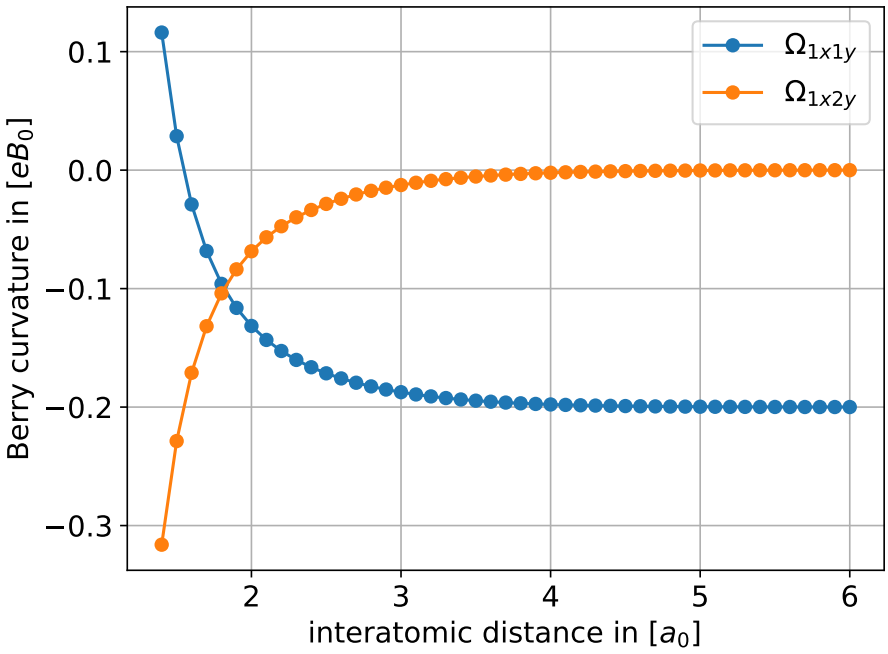

Figure 15.1.: Non-redundant Berry curvature elements of the helium dimer for different interatomic distances along the x-axis. Calculations used Hartree-Fock with a decontracted aug-cc-pVTZ basis set[205] and a magnetic flux density of $0.1\,B_0$ along the z-axis.

15.2.2. The Lithium Hydride Molecule

The lithium hydride molecule aligned with the x-axis with a magnetic flux density of $0.1\,B_0$ along the z-axis lowers the point group symmetry compared to the helium dimer.[204,206] In this case, the Berry curvature will generally have the form

$$\boldsymbol{\Omega} = \left(\begin{array}{ccc|ccc} 0 & a & 0 & 0 & b & 0 \\ -a & 0 & 0 & -c & 0 & 0 \\ 0 & 0 & 0 & 0 & 0 & 0 \\ \hline 0 & c & 0 & 0 & d & 0 \\ -b & 0 & 0 & -d & 0 & 0 \\ 0 & 0 & 0 & 0 & 0 & 0 \end{array}\right), \tag{15.11}$$

where the off-diagonal block no longer shows any internal symmetry. This time, the magnetic translational sum rule yields

$$a + b + c + d = -N_{\mathrm{el}}\mathcal{B}_z = -0.4\,eB_0\,. \tag{15.12}$$

Three of the non-redundant Berry curvature elements of the LiH molecule are depicted in figure 15.2. With an increasing interatomic distance, both fragments hold onto two electrons each, which is similar to the helium dimer. Consequently, the blue and orange curves generally resemble those of the helium dimer. In the more symmetric

He_2, the elements $1x2y$ and $1y2x$ were simply related via $\Omega_{1x2y} = -\Omega_{1y2x}$. For the LiH molecule this symmetry is broken. Therefore, the green and orange curves still show a remnant of this symmetry. Especially for large bond distance, when the blue curve is close to the dissociation limit of $-0.2\,eB_0$, the orange and green curve show a similar but opposite slope. When the bond distances decrease and approach the equilibrium distance of about $3\,a_0$, the broken symmetry is clearly visible.

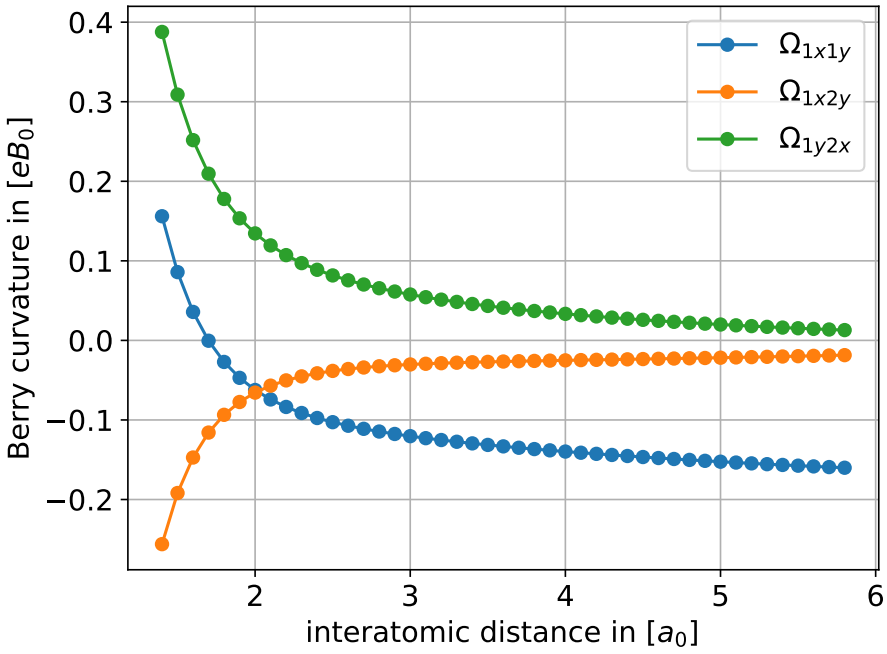

Figure 15.2.: Three non-redundant Berry curvature elements of the lithium hydride molecule for different interatomic distances along the x-axis. Calculations used Hartree–Fock with a decontracted aug-cc-pVTZ basis set[207–209] and a magnetic flux density of $0.1\,B_0$ along the z-axis.

Concluding this introductory section on the molecular Berry curvature, several basic properties have been encountered. Systems consisting of a single atom have been studied and their Berry curvature is directly related to the total number of electrons in the system and the magnetic flux density. Next, diatomic systems were discussed, for which the limit of large interatomic systems simply recovers the Berry curvature of isolated atoms. When the interatomic distance decreases, the coupling occurring in the off-diagonal blocks of the Berry curvature was found to depend on the molecular symmetry.

15.3. Zero-Field Convergence of the Berry Curvature

Some of the following sections consider quantities that are related to the Berry curvature in the limit of a vanishing external magnetic field. This convergence

behavior is introduced here. As before, a natural starting point for the discussion are atomic systems. As established in eq. 15.1, the xy-element of the Berry curvature of an atom in a magnetic field aligned with the z-axis is given by

$$\Omega_{xy} = -N_{\mathrm{el}} \mathcal{B}_z \,.$$

Evidently, the Berry curvature itself vanishes in the zero-field limit. What does not vanish, however, is the quotient of the Berry curvature and the magnetic flux density or equivalently, from L'Hôpital's rule, its derivative with respect to the flux density

$$\lim_{\mathcal{B}_z \to 0} \frac{\Omega_{xy}}{\mathcal{B}_z} = \left. \frac{\partial \Omega_{xy}}{\partial \mathcal{B}_z} \right|_{\mathcal{B}_z = 0} = -N_{\mathrm{el}} \neq 0 \,. \tag{15.13}$$

For molecular systems, this ratio also generally does not vanish.[53] Consequently, quantities like Berry partial charges can be defined in the zero-field limit and will not vanish. To illustrate this, table 15.4 shows results for the water molecule for different magnitudes of magnetic flux density. Three different Berry curvature elements are shown divided by the respective magnetic flux density. The three elements are chosen in a way that their order of magnitude is different from each other to show the convergence not only for the largest elements in absolute value. The results show

$\lvert\mathcal{B}\rvert$	$\mathrm{O}_x\mathrm{O}_y$	$\mathrm{O}_x\mathrm{H}_{1y}$	$\mathrm{O}_y\mathrm{H}_{2z}$
$10^{-1}\,B_0$	-8.33264	-0.11181	0.04098
$10^{-2}\,B_0$	-8.29024	-0.13749	0.04206
$10^{-3}\,B_0$	-8.28983	-0.13774	0.04207
$10^{-4}\,B_0$	-8.28983	-0.13774	0.04207
$10^{-5}\,B_0$	-8.28982	-0.13774	0.04207

Table 15.4.: Three different Berry curvature elements of the water molecule divided by the magnetic flux density. Calculations used Hartree-Fock and the decontracted aug-cc-pVTZ basis set.[207,208] Values for the Berry curvature per magnetic flux density given in $[e]$.

that several digits are already converged for a flux density of $|\mathcal{B}| = 10^{-3}\,B_0$ and the qualitative limit is captured even earlier for the elements under investigation. With decreasing flux density, the results systematically converge towards a limit. Convergence of even a few digits is achieved relatively fast. In practical calculation, caution is somewhat advised, however. For these values, and similarly for Berry charges, one needs to divide a Berry curvature element by the magnetic flux density. But clearly, both of these elements are of similar magnitude, as their ratio converges. Consequently, for small flux densities, a small Berry curvature element is divided by a similarly small value. This procedure easily introduces numerical noise into the result, for a calculation with $|\mathcal{B}| = 10^{-5}\,B_0$ the values of the Berry curvature needs to be converged to nine decimal places, only to obtain four significant digits in the final result. For these reasons, if only qualitative results are required for a zero-field analysis, it may be advisable to conduct the calculations with flux densities in the range of $10^{-4}\,B_0$.

16. Berry Partial Charges

This section investigates atomic partial charges calculated from the Berry curvature as first suggested in references [53] and [80]. The discussion starts with their application to molecules that exhibit strong ionic character. For this purpose, they are compared to different well-known partial charge models. Next, the basis set convergence of Berry charges is investigated. Peters *et al.* already noticed the resemblance of Berry and GAPT charges in Ref. [80]. The pseudomomentum translational sum rule provides their exact relation and is validated numerically during the discussion of the basis set convergence. Finally, the electric dipole moment of different molecules is computed based on partial charges, revealing several intrinsic properties of Berry and GAPT charges.

The results presented in this section were published together with Pausch in Ref. [82] and the discussion follows the structure and reasoning developed there.

16.1. Computational Details

If not stated otherwise, geometries were optimized in the absence of a magnetic field using DFT with the PBE functional and the def2-TZVP basis set.[144,210] For geometry optimizations, TURBOMOLE grid 4[199] was used for the numerical integration of the exchange-correlation functional and the resolution of the identity approximation for the Coulomb contribution (RI-J) was used. For the RI-J integrals, the corresponding def2-TZVP auxiliary basis was used.[211] The individual SCF energy was converged up to at least $10^{-6}\,E_\mathrm{h}$ and its gradient up to $10^{-4}\,E_\mathrm{h}/\mathrm{a}_0$. All molecular coordinates can be found in the supporting information of Ref. [82].

In section 16.2 on molecules with strong ionic character, geometry optimization for trihalomethyl cations and methylmagnesium bromide used the PBE0 functional.[212] Partial charges were subsequently calculated using Hartree-Fock and the def2-TZVP basis set. Mulliken[186] and Kollman[213,214] charges were calculated in the absence of external fields, while Berry and GAPT charges were obtained from Hartree-Fock calculations with a magnetic flux density of $10^{-4}\,B_0$. SCF energies were converged to $10^{-12}\,E_\mathrm{h}$ and the norm of the density matrix up to 10^{-14}. The norm of the linear response solution vectors was converged up to 10^{-10}.

Calculations on the basis set convergence of Berry charges in section 16.3 used Hartree-Fock and a magnetic flux density of $10^{-6}\,B_0$. The Dunning basis set cc-pVXZ and their augmented counterparts aug-cc-pVXZ for X ∈ D, T, Q, 5 were used.[207–209] SCF energies were converged up to $10^{-14}\,E_\mathrm{h}$ and the norm of the density matrix up to 10^{-14}. Linear response vectors were converged up to a norm of 10^{-13}.

Section 16.4 on the electric dipole moment derived from partial charges, the

geometries of furan, pyrrole, and thiophene were optimized using grid 3^{199} for the DFT calculations. The methods used to calculate partial charges as well as the convergence criteria are identical to those applied to the molecules with ionic character of section 16.2.

16.2. Molecules with Strong Ionic Character

An interesting class of molecules to investigate in a population analysis are molecules that exhibit strong ionic character. While partial charges are not observable properties of molecules and cannot be measured, such systems provide clear trends that can be qualitatively compared to partial charge models.

16.2.1. Methylmagnesium Bromide

One family of molecules that show strong ionic character are Grignard reagents which are of great relevance in organic chemistry.[215,216] As a member of this family, methylmagnesium bromide is investigated using four different types of population analysis are applied to these molecules: Berry partial charges,[53,80] generalized atomic polar tensor charges,[183–185] Mulliken charges,[186] and charges from an electrostatic potential fit using Kollman's parameterization.[213,214] These population analyses fall into one of three families. First, Berry and GAPT charges are based on a physical quantity, the Berry curvature and the nuclear derivative of the electronic dipole moment, respectively. They make use of known relations of these quantities with the total number of electrons in the system and make little assumptions about how to separate the electron density among the atoms in the system. Second, Mulliken charges distribute the electron density based on the basis set. The contribution of any basis function to the electron density is solely accounted to the nucleus that the basis function is centered on. Third, the Kollman parameterization constructs the atomic partial charges in such a way that the electrostatic potential of the partial charges matches the true electrostatic potential as well as possible. The calculated partial charges are shown in table 16.1 and are visualized in figure 16.1.

Atom	Berry	GAPT	Mulliken	Kollman
C	−0.3141	−0.3461	−0.7914	−0.5308
H	−0.0504	−0.0430	0.1319	0.0638
Mg	1.1341	1.1579	0.9158	0.8076
Br	−0.6689	−0.6827	−0.5202	−0.4682

Table 16.1.: Partial charges in $[e]$ for CH_3MgBr. All calculations were performed on the HF/def2-TZVP level of theory. Berry and GAPT charges were evaluated at $|\mathcal{B}| = 10^{-4}B_0$. Reproduced from Ref. [82], licensed under CC BY.

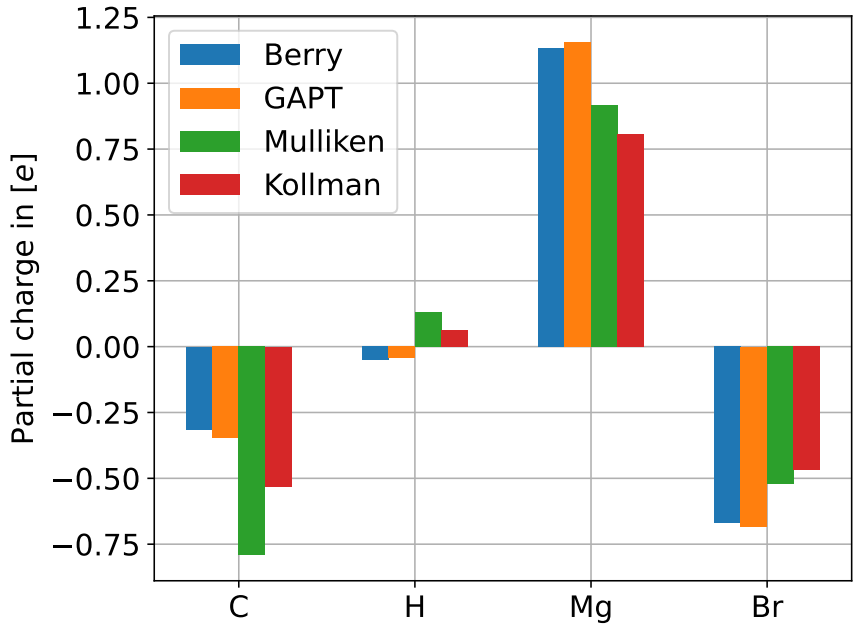

Figure 16.1.: Visualization of the partial charges in [e] for CH_3MgBr presented in table 16.1. Reproduced from Ref. [82], licensed under CC BY.

All four population analyses depicted in figure 16.1 are in qualitative agreement. They predict moderate negative charges for the carbon and bromine atom, close to no charge to the hydrogen atom, and a substantial positive charge on the magnesium atom. As expected, results obtained from the Berry or GAPT population analyses show great resemblance as explained previously. These two methods predict a partial charge of around $+1.15\,e$ for the magnesium atom, while Kollman predict only about $+0.81\,e$, and Mulliken about $+0.91\,e$. The largest deviation is therefore about 40 % between GAPT and Kollman. A discrepancy of similar size is found for the carbon atom. Here, Berry and GAPT analyses result in charges around $-0.33\,e$, whereas Kollman predicts $-0.53\,e$, corresponding to an absolute difference of $0.2\,e$. For the carbon atom, the Mulliken charge of $-0.79\,e$ is significantly larger in absolute value than the other charges, deviating by more than a factor of two from the respective Berry and GAPT charge. A similar trend can again be found for the bromine atom, where Berry and GAPT charge predict about $-0.67\,e$, while the Kollman charge of $0.47\,e$ differs by $0.2\,e$. The Mulliken charge falls between the other charge models, resulting in the largest relative deviation of about 30 %. The different partial charges for the hydrogen atoms hardly show a significant deviation from each other. The largest absolute difference of about $0.18\,e$ between the Berry and Mulliken charge in comparable to the difference of the other atoms. Still, the hydrogens are predicted to carry close to no partial charge by all methods.

16.2.2. The Trihalomethyl Cations

Another family of molecules falling into the category with strong ionic character are the trihalomethyl cations,[217,218] their resonance structure is depicted in figure 16.2.

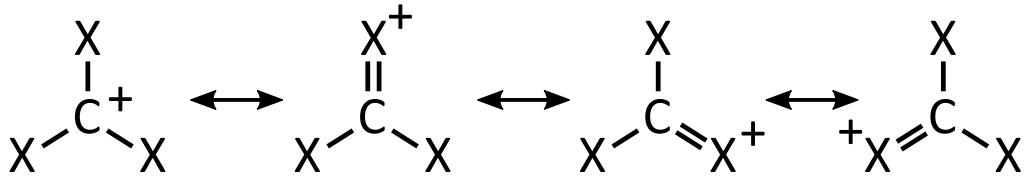

Figure 16.2.: Resonance structure of the trihalomethyl cation. Reproduced from Ref. [82], licensed under CC BY.

Atom	Berry	GAPT	Mulliken	Kollman
$\mathbf{C}F_3^+$	2.0009	2.0457	0.9768	0.9976
$\mathbf{C}Cl_3^+$	1.4241	1.4497	0.1761	−0.1304
$\mathbf{C}Br_3^+$	1.1845	1.2038	0.0527	−0.3179
$C\mathbf{F}_3^+$	−0.3336	−0.3486	0.0077	0.0008
$C\mathbf{Cl}_3^+$	−0.1414	−0.1499	0.2746	0.3768
$C\mathbf{Br}_3^+$	−0.0615	−0.0679	0.3158	0.4397

Table 16.2.: Partial charges in $[e]$ for CF_3^+, CCl_3^+, and CBr_3^+. The element in bold letters indicates the nucleus of the partial charge. All calculations were performed on the HF/def2-TZVP level of theory. Berry and GAPT charges were evaluated at $|\mathcal{B}| = 10^{-4}B_0$. Reproduced from Ref. [82], licensed under CC BY.

Here, molecules of type CX_3^+, where X = F, Cl, Br, have been investigated. These molecules are especially interesting, as it is known that the central carbon atom is assigned an increasingly negative partial charge, depending on the nuclear charge of the halogen atom.[219,220] This trend should be captured by the partial charges, at least qualitatively. Here, the same partial charge models as in the previous section on methylmagnesium bromide are applied. The partial charges calculated using the four different methods can be found in table 16.2 and are also visualized in figure 16.3. Since the halogen atoms in the trihalomethyl cations are symmetry equivalent, only the partial charges of one of them are shown. From the results in figure 16.3, it is apparent that Berry and GAPT charges produce results that are very similar. The largest difference between the two methods is less than $0.05\,e$ for the carbon atom in the triflouro cation. This is expected, because the pseudomomentum-translational sum rule dictates that these partial charges converge in the limit of a complete basis. The def2-TZVP basis set that was employed in the calculations seems to be sufficiently large to clearly show this property, even though convergence has not yet been reached. In contrast, the difference of these two methods to Mulliken or Kollman

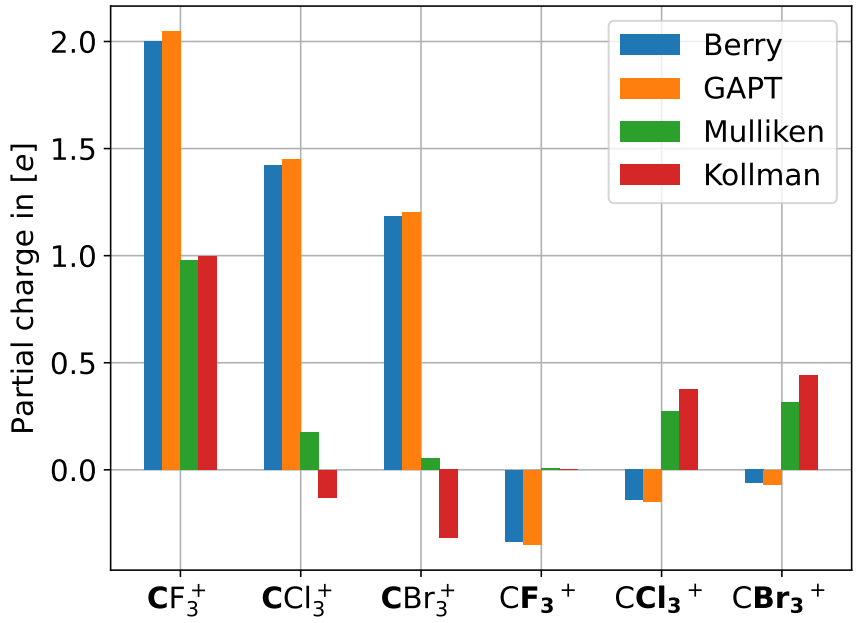

Figure 16.3.: Partial charges of the trihalomethyl cations CX_3^+ from table 16.2 Reproduced from Ref. [82], licensed under CC BY.

charges is much more noticeable, and is larger than $1\,e$ for all systems investigated here. Berry and GAPT charges both predict a high positive partial charge on the carbon atom of CF_3^+. Here, the carbon atom has a partial charge of about $+2\,e$ as predicted by these two methods. Conversely, Mulliken and Kollman predict about $+1\,e$. For the heavier homologues this discrepancy becomes even more pronounced: For the CCl_3^+ and CBr_3^+ molecules, the Kollman population analysis produces a partial negative charge on the carbon atom. On the other hand, Mulliken charges remain positive but close to neutral, with the larger charge occurring in CBr_3^+, where the carbon atom has a charge of less than $0.2\,e$. Interestingly, the Berry and GAPT charges predict a heavy ionic character with the carbon atom carrying a charge of more than $+1\,e$ in both CCl_3^+ and CBr_3^+. Such heavily charged carbenium ions not only defy chemical intuition of these systems but are not backed up by experimental data. Ref. [220] discusses theoretical and experimental findings of these properties and conclude that the halogen atoms in CCl_3^+, and CBr_3^+ should be modeled with a positive charge. For trihalomethy cations, Berry and GAPT charges appear as clear outliers when compared to Mulliken or Kollman charges. Since they also fail to reproduce the experimental data even qualitatively, these molecular systems with strong ionic character expose shortcomings of the aforementioned methods.

Summarizing the results obtained for methylmagnesium bromide and trihalomethyl cations, the connection between Berry and GAPT charges can clearly be seen. As shown in section 6.24, both models produce the same partial charges in the limit of a complete basis. Even in a finite basis, the models are expected to perform similarly,

provided some base level minimum size of the basis set. As a direct consequence, Berry charges show the same limitations that GAPT charges are known for in the literature.[221,222] Compared to electrostatic potential fits like Kollman's method, Berry and GAPT charges almost always show quantitative disagreement and in some cases even qualitative disagreement. The molecules investigated in this section are challenging systems to be described by any population analysis and where picked explicitly to demonstrate the shortcomings of Berry and GAPT charges.

16.3. Basis Set Convergence of Berry Charges

Section 16.2 explored Berry partial charges in comparison to GAPT charge and two other models. From these results it became apparent that Berry and GAPT charges in a finite basis tend to produce very similar results. This connection is expected as the pseudomomentum-translational sum rule dictates their relation. In section 6.3 and 10.2.1, it was shown that Berry and GAPT charges converge to the same value in the limit of a complete basis. Additionally, eq. 10.14 introduced another partial charge model termed momentum charges. Since the pseudomomentum-translational sum rule not only provides a relation between the isotropic averages of Berry and GAPT charges, but also between the individual tensor elements of the pseudomomentum and atomic polar tensor, the following quantities are defined:

$$q_I^{xy,\mathrm{mom}} = \frac{2}{\mathcal{B}_z}\frac{\partial p_y}{\partial R_{Ix}}\,, \tag{16.1}$$

$$q_I^{yx,\mathrm{mom}} = -\frac{2}{\mathcal{B}_z}\frac{\partial p_x}{\partial R_{Iy}}\,, \tag{16.2}$$

Equations 16.1 and 16.2 represent individual components of the momentum charges. In the limit of a complete basis, a relation between these components and the individual APT charges can be established as

$$q_I^{x,\mathrm{APT}} = q_I^{xy,\mathrm{mom}} = \frac{\omega_{I,xy}}{\mathcal{B}_z}\,, \tag{16.3}$$

$$q_I^{y,\mathrm{APT}} = q_I^{yx,\mathrm{mom}} = -\frac{\omega_{I,yx}}{\mathcal{B}_z}\,, \tag{16.4}$$

In this section, the aforementioned convergence and relation of the different charge models is investigated on the lithium hydride molecule in a magnetic field of $10^{-6}\,B_0$ along the Cartesian z-axis. Two orientations of the molecule with respect to the magnetic field are considered, first the parallel and second the perpendicular orientation. Calculations were carried out using the (aug-)cc-pVXZ basis sets with X = D, T, Q, 5.

16.3.1. Parallel Orientation to the Magnetic Field

Starting the discussion with the parallel orientation, the total system, consisting of the molecule and the magnetic field, shows C_∞ symmetry.[204] Therefore, the pseudomomentum tensor shows an overall antisymmetry $\omega_{I,xy} = -\omega_{I,yx}$. Likewise, the two relevant components of the GAPT charges are equivalent $q_I^{x,\mathrm{APT}} = q_I^{y,\mathrm{APT}}$. For this reason, only the results for the quantities occurring in eq. 16.4 are shown.

Basis set	$q_\mathrm{H}^{y,\mathrm{APT}}$	$q_\mathrm{H}^{yx,\mathrm{mom}}$	$-\omega_{\mathrm{H},yx}/\mathcal{B}_z$
cc-pVDZ	–1.7725	–1.6628	–1.7176
cc-pVTZ	–1.7777	–1.7533	–1.7655
cc-pVQZ	–1.7801	–1.7718	–1.7760
cc-pV5Z	–1.7810	–1.7783	–1.7797
aug-cc-pVDZ	–1.7844	–1.7809	–1.7827
aug-cc-pVTZ	–1.7818	–1.7770	–1.7794
aug-cc-pVQZ	–1.7815	–1.7803	–1.7809
aug-cc-pV5Z	–1.7815	–1.7810	–1.7812

Table 16.3.: Results for one component of the APT charge, and the corresponding element of the momentum charge and the pseudomomentum tensor divided by the magnetic flux density. The LiH molecule has its bond axis aligned with the z-axis and the magnetic field vector with $|\mathcal{B}| = 10^{-6}\,B_0$. All calculations were performed with Hartree-Fock using different Dunning basis sets. The convergence of the partial charges of the hydrogen atom in LiH is shown with increasing basis set size, values given in $[e]$. Reproduced from Ref. [82], licensed under CC BY.

It is evident from the results in table 16.3 that the values of the APT charge, the momentum charge and the respective atomic pseudomomentum tensor converge to the same limit. The largest basis set employed in the calculations, the aug-cc-pV5Z basis, consists of six s-, five p-, four d-, three f-, and two g-functions on the hydrogen and up to two h-functions on the lithium. In this basis, the absolute difference between the APT and momentum charge is only $0.0005\,e$, which translates to a relative deviation of only 0.03 %. Since the atomic pseudomomentum tensor per magnetic flux density is the average of these two quantities, it resides just in between them. The findings in table 16.3 also demonstrate that the values of the APT charges converge towards the basis set limit much faster than the other two quantities. Comparing the results obtained in the cc-pVDZ and cc-pV5Z basis sets, the difference in the APT charge is only about $0.0085\,e$, corresponding to a deviation of less than 0.5 % between basis sets. The difference for the momentum charges however amounts to $0.115\,e$, corresponding to a 6.5 % deviation. Evidently, for this system, the momentum charges and as a direct consequence the pseudomomentum tensor elements per magnetic flux density converge orders of magnitude slower than the APT charges. In section 6.3 the cause for this difference was already addressed. Momentum charges

and the pseudomomentum tensor impose very different requirements on the basis set than the APT. While the derivative of the canonical momentum has an exact representation in momentum space, the APT has an exact representation in real space. Consequently, the pseudomomentum tensor does not have an exact representation in either space, because it is the average of both quantities. All calculations made use of atom-centered GTO basis sets in real space. Hence, a rapid convergence of the APT charges is no surprise. In contrast, a high quality description of the pseudomomentum tensor requires a large basis in real space.

16.3.2. Perpendicular Orientation to the Magnetic Field

Next, the lithium hydride molecule with its bond axis perpendicular to the magnetic field is discussed. The symmetry of the system is reduced when compared to the parallel alignment and is now only C_s.[204] Therefore, the symmetry of the APT and pseudomomentum tensor can no longer be exploited when presenting the results, since generally $q_I^{x,\mathrm{APT}} \neq q_I^{y,\mathrm{APT}}$ and $\omega_{I,xy} \neq -\omega_{I,yx}$. The results for the perpendicular orientation are shown in table 16.4. Clearly, the values of the APT charge $q_\mathrm{H}^{y,\mathrm{APT}}$, the momentum charge $q_\mathrm{H}^{yx,\mathrm{mom}}$, and the corresponding element of the pseudomomentum tensor per magnetic flux density $\omega_{\mathrm{H},yx}/\mathcal{B}_z$ are equivalent to those obtained for the parallel orientation of the molecule. The other set of quantities corresponding to

Basis set	$q_\mathrm{H}^{x,\mathrm{APT}}$	$q_\mathrm{H}^{xy,\mathrm{mom}}$	$\omega_{\mathrm{H},xy}/\mathcal{B}_z$	$q_\mathrm{H}^{y,\mathrm{APT}}$	$q_\mathrm{H}^{yx,\mathrm{mom}}$	$-\omega_{\mathrm{H},yx}/\mathcal{B}_z$
cc-pVDZ	–1.4326	–1.3151	–1.3738	–1.7725	–1.6628	–1.7176
cc-pVTZ	–1.4780	–1.4554	–1.4667	–1.7777	–1.7533	–1.7655
cc-pVQZ	–1.4818	–1.4635	–1.4727	–1.7801	–1.7718	–1.7760
cc-pV5Z	–1.4860	–1.4753	–1.4806	–1.7810	–1.7783	–1.7797
aug-cc-pVDZ	–1.4639	–1.4392	–1.4515	–1.7844	–1.7809	–1.7827
aug-cc-pVTZ	–1.4882	–1.4361	–1.4622	–1.7818	–1.7770	–1.7794
aug-cc-pVQZ	–1.4883	–1.4884	–1.4884	–1.7815	–1.7803	–1.7809
aug-cc-pV5Z	–1.4882	–1.4885	–1.4883	–1.7815	–1.7810	–1.7812

Table 16.4.: Results for one component of the APT charge, and the corresponding element of the momentum charge and the pseudomomentum tensor divided by the magnetic flux density. The LiH molecule has its bond axis perpendicular to the z-axis that contains the magnetic field vector with $|\mathcal{B}| = 10^{-6}\,B_0$. All calculations were performed with Hartree-Fock using the different Dunning basis sets. The convergence of the partial charges of the hydrogen atom in LiH is shown with increasing basis set size, values given in $[e]$. Reproduced from Ref. [82], licensed under CC BY.

$q_\mathrm{H}^{x,\mathrm{APT}}$ shows differing values. Here, a slower convergence is observed in comparison to those obtained in the parallel orientation. This effect is quite evident from the APT and momentum charges calculated in the cc-pV5Z basis set. Their difference

is still about 0.01 e or 0.7 % and therefore much worse than the same values of the augmented basis sets. For this system, the general performance of the augmented basis sets is significantly better compared to the non-augmented ones. Results obtained from the aug-cc-pVQZ basis are already converged to the basis set limit and are numerically equivalent to those from the larger basis. Notably, convergence of the APT charges is achieved more rapidly than that of the momentum charges once again. The largest absolute deviation for the non-augmented basis sets is about 0.05 e for the APT charges, corresponding to 3.6 %. Conversely, momentum charges show a maximum deviation of 0.16 e or almost 11 % which is about three times that of the APT charges. These results suggest that the aug-cc-pVQZ is sufficient, at least for the systems under investigation, to obtain a reasonable description of the APT and momentum charges. This observation also holds for Berry charges, because they are just the average of APT and momentum charges.

16.3.3. Investigation of Basis Set Abnormality

Although the previous findings are in line with the expected basis set dependence of the APT and Berry charges, one peculiarity can be observed. In the results for the perpendicular alignment in table 16.4, APT charges have basically reached convergence with the aug-cc-pVTZ basis set. The momentum charges, however, are still off by more than 0.05 e or 3.5 %. Strangely, the value obtained from the non-augmented analogous basis set, cc-pVTZ, is closer to the limit than that of the augmented basis set. It should be stressed that the aug-cc-pVTZ basis set contains all functions that are in the cc-pVTZ basis set, and only extends the basis by one contracted function per angular momentum. Therefore, it is unexpected that the augmented basis set, which is larger than the non-augmeted one, produces worse results in this case. To investigate this aberration, the calculations were repeated while subsequently discarding some of the diffuse functions of the augmented basis set.

The results of the detailed basis set investation are presented in table 16.5. Evidently, the APT charges are hardly affected by dropping diffuse functions from the basis set, the largest absolute difference is just below 0.003 e. For the APT charge, discarding diffuse functions centered on the hydrogen atom seems to have a greater influence than discarding those on the lithium atom. Note that the total molecular charge is zero and therefore the influence on the partial charge of the lithium atom is equal in absolute value to that of the hydrogen. Hence, this effect appears not to stem from the fact that the basis functions are located on the atom whose partial charge is calculated. In contrast, the momentum charges are greatly affected by removing diffuse functions, with the largest difference being close to 0.1 e, which is two orders of magnitude larger than the influence on APT charges. Notably, the diffuse p- and d-functions seem to be especially important for a good description of the momentum charges. Removal of these functions results in a much greater negative partial charge of the hydrogen atom, even more negative than the partial charge obtained with the aug-cc-pV5Z basis. Similarly to the APT charges, removal of basis functions

Basis set	$q_{\mathrm{H}}^{x,\mathrm{APT}}$	$q_{\mathrm{H}}^{xy,\mathrm{mom}}$	$q_{\mathrm{H}}^{y,\mathrm{APT}}$	$q_{\mathrm{H}}^{yx,\mathrm{mom}}$
H w/o aug(s)	–1.4869	–1.4178	–1.7816	–1.7773
H w/o aug(p)	–1.4890	–1.5131	–1.7823	–1.7802
H w/o aug(d)	–1.4892	–1.5048	–1.7818	–1.7700
H w/o aug(p,d)	–1.4897	–1.5135	–1.7815	–1.7729
H w/o aug(s,p,d)	–1.4871	–1.5002	–1.7813	–1.7706
Li w/o aug(s)	–1.4880	–1.4325	–1.7817	–1.7765
Li w/o aug(p)	–1.4881	–1.4321	–1.7818	–1.7781
Li w/o aug(d)	–1.4878	–1.4340	–1.7816	–1.7787
Li w/o aug(f)	–1.4883	–1.4479	–1.7817	–1.7773

Table 16.5.: Results for the APT and momentum charges of LiH molecules perpendicular to the magnetic fields axis. All calculations were performed with Hartree–Fock and a magnetic flux density of $10^{-6}\,B_0$. Only partial charges for the hydrogen atom in $[e]$ are shown, where some diffuse functions of the aug-cc-pVTZ basis set were omitted in the calculation. Reproduced from Ref. [82], licensed under CC BY.

centered on the hydrogen atom has a much bigger impact on the partial charge than removal of those centered on the lithium atom.

In summary, APT charges converge much faster towards the basis set limit than momentum charges, and as a direct consequence Berry charges or more generally the elements of the atomic pseudomomentum tensor. Additionally, it seems that diffuse functions play an important role in the description of momentum charges and the pseudomomentum tensor. The external magnetic field induces a plane-wave character in the wave function as discussed in section 7.3. For this character to be captured at all in real space when making use of atom centered basis functions, diffuse functions seem to be strictly necessary.[82] Since the atomic pseudomomentum tensor is given by the sum of the molecular Berry curvature over one nuclear index, this suggests that a comparable behavior can be expected for the Berry curvature. Especially the calculations on the perpendicular alignment of the lithium hydride molecule with respect to the magnetic field axis shows that different components of these quantities can converge to the basis set limit with vastly different speeds.

16.4. Electric Dipole Moments of Heteroaromatic Molecules

Section 16.2 showed how different partial charge models perform based on their application on molecules that show a strong ionic character. Here, their performance was judged on the basis of experimental evidence, as well as other calculations. Since atomic partial charges are not directly observable quantities, the assessment of partial charges is generally hard. Other molecular properties that are constructed from the partial charges however, can indeed be easily compared to experimental data and can therefore be used to categorize their performance. The electric dipole moment is an intuitive quantity for this. Eq. 6.20 provides a way to calculate the dipole moment quantum mechanically, directly from the wave function or electron density. Meanwhile, the classical definition of the dipole can be used under the assumption that partial charges are exactly located at the position of the corresponding atom. In this way, one component of the molecular dipole moment may be obtained as

$$\mu_\alpha := \sum_I q_I(\mathbf{R}) R_{I\alpha} \,. \tag{16.5}$$

However, this definition does not come without repercussion: Taking the derivative of eq. 16.5 with respect to a nuclear coordinate leads to

$$\frac{\partial \mu_\alpha}{\partial R_{J\beta}} = q_J(\mathbf{R})\delta_{\alpha\beta} + \sum_I \frac{\partial q_I(\mathbf{R})}{\partial R_{J\beta}} R_{I\alpha} \,. \tag{16.6}$$

The troublesome part of this equation comes from the dependence of the partial charge on the nuclear geometry and therefore on its own position within the molecule. In contrast, a classical charge does not carry this dependence, and one could also impose the following condition on the derivative of the dipole moment:

$$\frac{\partial \mu_\alpha}{\partial R_{J\beta}} \stackrel{!}{=} q_J(\mathbf{R})\delta_{\alpha\beta} \,. \tag{16.7}$$

This requirement would be fulfilled by classical charges, whereas the definition of the dipole moment in eq. 16.5 generally contradicts it. The condition in eq. 16.7 does, however, lose information about the relation between partial charges and the dipole moment. Solving eq. 16.7 for the value of the dipole moment would necessitate the introduction of an arbitrary integration constant. As a consequence, any partial charge can generally only fulfill either eq. 16.5 or 16.7, with a few notable exceptions that are discussed at a later point. Importantly, any generic partial charge model will usually fulfill neither of these conditions exactly. A prime candidate to obey eq. 16.7 are APT charges and consequently Berry charges. The derivative of the dipole moment is at the heart of the definition of the APT charges and is therefore closely related to Berry charges as well. Thus, one would expect these models to not necessarily produce results that are in line with the condition in eq. 16.5. Conversely, an electrostatic potential fit like the one based on Kollman's parametrization, is

much closer aligned with the first condition. Accordingly, one would expect these charges to produce a very reasonable approximation to the electric dipole moment as obtained from the wave function according to eq. 6.20. One model that does not clearly lean towards either of the two conditions, are Mulliken charges, since they are directly constructed from the density matrix based on which basis function is centered on which atom.

One special case for these conditions was reported in Ref. [223] and concerns planar molecules. If the molecule resides within the xz-plane, any derivative $\partial q_I / \partial R_{Jy}$ vanishes due to symmetry. Consequently, the element of the yy-element of the APT exactly produces the electric dipole moment of the system. An analogous relation for the Berry charges exists and can be found from the relation of the atomic pseudomomentum tensor and the APT, which yields the linear combination

$$\begin{aligned} q_I^{x+z-y,\mathrm{Berry}} &= q_I^{x,\mathrm{Berry}} + q_I^{z,\mathrm{Berry}} - q_I^{y,\mathrm{Berry}} \\ &= 3q_{I,\mathrm{rot}}^{\mathrm{Berry}} - 2q_I^{y,\mathrm{Berry}} , \end{aligned} \tag{16.8}$$

which corresponds to the APT charge q_I^y. Note again, that these two charges, the Berry linear combination $q_I^{x+z-y,\mathrm{Berry}}$, and the APT charge $q_I^{y,\mathrm{APT}}$ converge towards the same value in the limit of a complete basis. These two special charges are investigated in addition to the normal Berry and GAPT charges in this section.

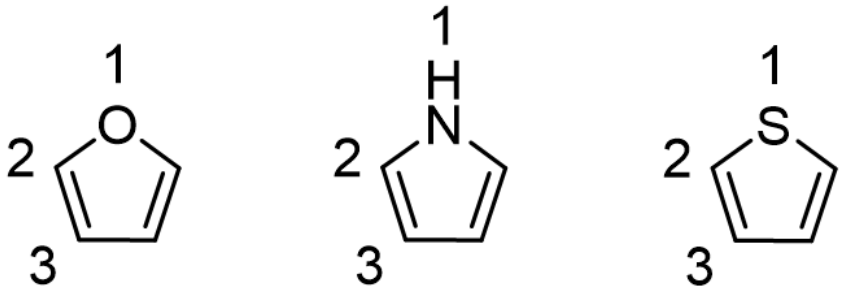

Figure 16.4.: Molecular structures of furan, pyrrole, and thiophene with numbers indicating different positions. Reproduced from Ref. [82], licensed under CC BY.

The different partial charge models discussed so far are applied to furan, pyrrole, and thiophene. The structures of these five-membered rings can be found in figure 16.4. Evidently, these molecules are interesting system to investigate, as they are planar and therefore fall into the special case reported in Ref. [223]. Additionally, pyrrole is well known for its inverted electric dipole moment when compared to furan and thiophene.[224] While any population analysis can not be expected to exactly reproduce the molecular dipole moment as previously discussed, they should predict the dipole moment at least qualitatively.

Atom	Berry	Berry^{x+z-y}	GAPT	APT^{yy}	Mulliken	Kollman
1O	−0.4978	−0.1540	−0.5159	−0.1702	−0.3373	−0.1206
2C	0.1582	−0.0896	0.1669	−0.0817	0.0581	−0.1127
3C	−0.0719	−0.2111	−0.0792	−0.2157	−0.1839	−0.1916
2H	0.0909	0.1982	0.0926	0.2000	0.1530	0.1906
3H	0.0716	0.1794	0.0776	0.1824	−0.1414	0.1741

Table 16.6.: Different partial charges calculated for the furan molecule. Atoms are numbered following the scheme in figure 16.4, hydrogen atoms are denoted with the number of the respective atom they are bonded to. Partial charges are calculated with Hartree-Fock using the def2-TZVP basis for a magnetic flux density of $10^{-4}\,B_0$ and are given in $[e]$. Reproduced from Ref. [82], licensed under CC BY.

Results for the furan molecule can be found in table 16.6. Like all molecules investigated in this section, it shows C_{2v} symmetry and therefore only non-redundant charges are shown. Some clear trends can be seen, as expected, Berry and GAPT charges produce very similar results. Their biggest absolute deviation is about the partial charge of the oxygen atom and only amounts to less than $0.02\,e$. In a very similar fashion, the two special partial charge models, APT^{yy} and Berry^{x+z-y}, agree very well with each other. Here, the biggest difference is also in the partial charge of the oxygen atom and is also less than $0.02\,e$. A vastly different picture emerges when comparing the two groups. The two modified population analyses do not agree with their unmodified counterparts at all. A large difference of around $0.35\,e$ can be found between them for the partial charge of oxygen. Crucially, they predict differing signs for the 2C partial charge. Berry and GAPT charges are slightly positive with more than $+0.15\,e$, whereas the modified variants produce a small negative charge of about $-0.01\,e$. Mulliken and Kollman charges notably align with one or the other group of population analyses. For Mulliken charges, results more closely align with the unmodified Berry and GAPT charges, where the largest deviation is again found for the oxygen atom and amounts to around $0.18\,e$. Kollman charges agree with the values of the modified Berry and APT charges quiet well. Here, the largest deviation occurs on the oxygen atom and constitutes to less than $0.05\,e$.

Partial charges of the pyrrole molecule are listed in table 16.7. The overall conclusion is similar to that of furan. Berry and GAPT charges agree with each other very well. The biggest absolute difference once again occurs for the hetero atom in the system, with about $0.04\,e$. The modified population analyses predict very similar charges that strongly differ from those obtained with the unmodified methods. Namely, the 2C carbon is expected to carry a charge that is partially negative from the modified variants. The Berry and GAPT charges conversely are slightly positive. Still, the difference between the two modified variants is most notable for the nitrogen atom, where the largest deviation is just above $0.06\,e$. Contrary to the furan molecule,

Atom	Berry	Berry^{x+z-y}	GAPT	APT^{yy}	Mulliken	Kollman
1N	−0.3512	−0.2285	−0.3895	−0.2910	−0.3214	−0.1083
1H	0.2379	0.3094	0.2511	0.3239	0.2511	0.3030
2C	0.0206	−0.1883	0.0371	−0.1423	−0.0608	−0.2847
3C	−0.0949	−0.2321	−0.1094	−0.2654	−0.1771	−0.1946
2H	0.0766	0.2051	0.0778	0.2016	0.1451	0.2088
3H	0.0543	0.1748	0.0638	0.1896	0.1280	0.1732

Table 16.7.: Different partial charges calculated for the pyrrole molecule. Atoms are numbered following the scheme in figure 16.4, hydrogen atoms are denoted with the number of the respective atom they are bonded to. Partial charges are calculated with Hartree–Fock using the def2-TZVP basis for a magnetic flux density of $10^{-4}\,B_0$ and are given in $[e]$. Reproduced from Ref. [82], licensed under CC BY.

Mulliken charges resemble the results from the modified Berry and yy-APT charges much closer. This time, Kollman charges show a much larger deviation from the modified variants compared to furan. The largest difference is close to $0.2\,e$ for the nitrogen atom, when compared to the modified APT charge. Kollman charges predict a higher negative charge on the carbon atoms when compared to all other methods.

Atom	Berry	Berry^{x+z-y}	GAPT	APT^{yy}	Mulliken	Kollman
1S	−0.0515	0.0973	−0.0647	0.0897	0.1427	0.0539
2C	−0.0129	−0.2704	−0.0007	−0.2484	−0.1893	−0.2785
3C	−0.0920	−0.1409	−0.1082	−0.1666	−0.1734	−0.1357
2H	0.0780	0.1895	0.0818	0.1885	0.1568	0.2294
3H	0.0527	0.1731	0.0595	0.1816	0.1346	0.1579

Table 16.8.: Different partial charges calculated for the thiophene molecule. Atoms are numbered following the scheme in figure 16.4, hydrogen atoms are denoted with the number of the respective atom they are bonded to. Partial charges are calculated with Hartree–Fock using the def2-TZVP basis for a magnetic flux density of $10^{-4}\,B_0$ and are given in $[e]$. Reproduced from Ref. [82], licensed under CC BY.

Partial charges of the thiophene molecule are shown in table 16.8. Berry and GAPT charges show the greatest resemblance so far. They show a small negative charge for the sulfur atom, in contrast to all other methods that predict a slightly positive charge. The two modified models still perform similarly, this time the largest difference between them is no longer on the hetero atom: A deviation of almost $0.01\,e$ is found on the 2C atom. Kollman charges generally agree with the modified models and their largest difference occurs on the sulfur atom and amounts to about $0.04\,e$. Mulliken charges are closer aligned to Kollman and the modified Berry and APT charges. The most notable differences are about a significantly higher positive

charge of the sulfur and a more negatively charged 2C atom, respectively.

Table 16.9 lists the electric dipole moments calculated via different methods. The reference method, referred to as 'Density' in the table, contains the expectation value of the dipole moment evaluated from eq. 6.20. The other values are calculated from the molecular geometry and the partial charges of the individual molecules given in tables 16.6, 16.7, and 16.8. The difference between dipole moments obtained from partial charges and the reference values from the electronic density are visualized in figure 16.5.

Model	Furan	Pyrrole	Thiophene
Density	−0.3123	0.7573	−0.2760
Berry	−0.8278	0.4373	−0.0191
Berry^{x+z-y}	−0.2888	0.7637	−0.3110
GAPT	−0.8655	0.4208	−0.0225
APT^{yy}	−0.3123	0.7573	−0.2760
Mulliken	−0.4808	0.4397	0.2265
Kollman	−0.3046	0.7535	−0.2641

Table 16.9.: Electric dipole moments for furan, pyrrole, and thiophene. The 'Density' model refers to the dipole moment expectation value over the ground state wave function obtained from eq. 6.20. Dipole moments in the other rows are calculated using eq. 16.5 and the corresponding partial charges from tables 16.6, 16.7, and 16.8. Values are given in units of $[ea_0]$. Reproduced from Ref. [82], licensed under CC BY.

Focusing on the absolute value found in table 16.9 first, all methods generally agree qualitatively with the dipole moment obtained from the density. Furan and thiophene are observed to have a negative dipole moment in all but one case no matter which partial charge model is used and are therefore in line with the reference expectation values. Similarly, all models predict the dipole moment of pyrrole to have a different sign than the other heterocycles. This is the expected result, as previously explained, pyrrole exhibits a characteristic inverse dipole moment. Still, the degree of quantitative agreement greatly differs between the different partial charge models. Berry and GAPT charges vastly overestimate the dipole moment of furan. For both models, the absolute deviation is more the $0.5\,ea_0$, resulting in a dipole moment that is wrong by about a factor of three. The dipole moment of pyrrole is only recovered with about 60 % of the true magnitude, corresponding to an absolute difference of more than $0.3\,ea_0$. Notably, Mulliken charges basically predict the same result for pyrrole as Berry and GAPT charges do. Thiophene's dipole moment is predicted to almost vanish based on Berry and GAPT charges, while the reference value is about $0.28\,ea_0$. Overall, Berry and GAPT charge seem unfit to accurately predict electric dipole moments. For GAPT charges this behavior has already been reported in the literature.[221] Still, mainly because of their close relation via the pseudomomentum translational sum rule, Berry charge exhibit the same shortcomings.

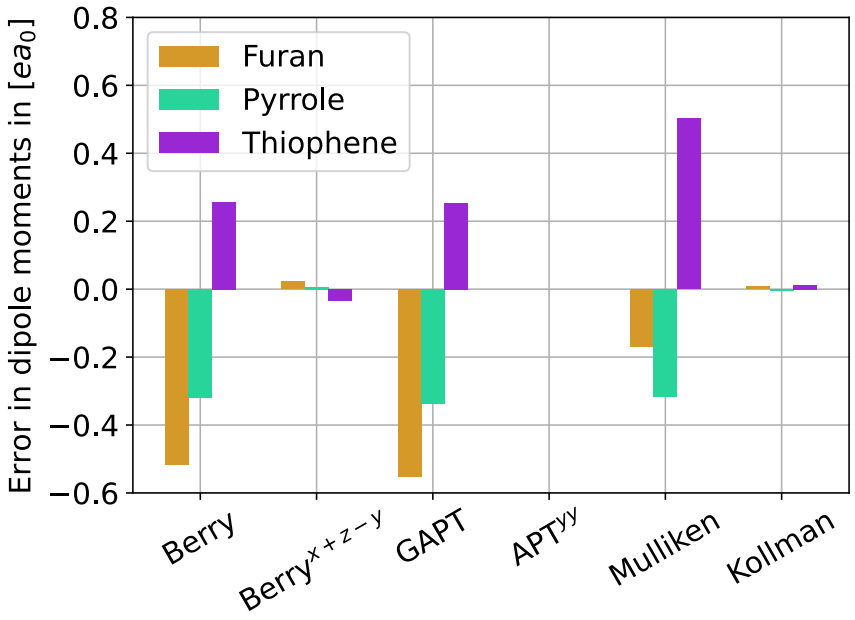

Figure 16.5.: Deviation of the electric dipole moments calculated from the different partial charge models to the reference value obtained as the expectation value of the ground state wave function. Differences are calculated from the dipole moments found in table 16.9. Reproduced from Ref. [82], licensed under CC BY.

Generally, Mulliken charges also seem to be unfit in predicting dipole moments. For furan, Mulliken charges overestimate the dipole moment by more than 50 %. While this is much better than the severe overestimation from Berry and GAPT charges, it still translates to a deviation of almost $0.17\,ea_0$. As previously stated, the dipole moment of pyrrole is described in a very similar fashion from Berry and GAPT charges, where a large deviation was found. But the worst agreement of all molecules is found for thiophene. Mulliken charges fail completely to reproduce the reference value. While the order of magnitude is correct, the sign is flipped. This results in an absolute difference of more than $0.5\,ea_0$ while failing to recover the right qualitative value.

The modified partial charge methods perform better than the non-modified models. As discussed in the introductory paragraph of this section, the yy-component of the APT charges are expected to exactly reproduce the electric dipole moment for these molecules. This is most apparent from the vanishing errors shown in figure 16.5. While table 16.9 only provides values up to four decimal places, this property is fulfilled for at least ten digits for all molecules investigated here. Consequently, the modified Berry^{x+z-y} charges also perform well in reproducing the dipole moment. The largest error is only about $0.03\,ea_0$ with respect to the reference expectation values. Again, the difference in yy-APT charges and the modified Berry charges

solely stems from the incompleteness of the basis set.

Kollman charges also predict the dipole moments with great accuracy. Here, the largest absolute deviation observed amounts to about $0.01\,ea_0$. As discussed, this is actually expected, since the electrostatic potential fit calculates the partial charges in such a way that the overall potential of the electronic system is reproduced as close as possible.

Overall, figure 16.5 demonstrates the great performance of APT^{yy}, Berry^{x+z-y}, and Kollman charges in reproducing the electric dipole moments. It needs to be stressed however, that this property only holds true for the special case of planar molecules. For any non-planar molecule, there will generally not be a linear combination of individual elements of the APT or the pseudomomentum tensor that relates to the dipole moment with such accuracy. The figure also very clearly shows that Berry, GAPT, and Mulliken charges are generally unfit to predict the electric dipole moment of molecules. Still, these charges are essential in describing different processes involving nuclear motion. The APT is the central quantity involved in calculating intensities in IR vibrational spectroscopy. Similarly, Berry charges are needed in the correct description of molecular rotations and vibrations in external magnetic fields.[54,55]

17. Pseudomomentum-Translational Sum Rule

Section 6 discussed different properties of the molecular Berry curvature. Among them were two relations of the Berry curvature summed over one or both nuclear indices, namely the pseudomomentum-translational sum rule and the magnetic-translational sum rule.[46,82] Both relations are numerically verified in this section. The reference system is a water molecule in the xz-plane with its bond distance and angle from the zero-field geometry. A skew magnetic field was applied in the $(1, 2, 3)^{\mathrm{T}}$-direction with a magnetic flux density of $|\mathcal{B}| = 0.1\,B_0$. This combination of molecular geometry and the choice of the direction of the magnetic field eliminates any point group symmetry in the system, resulting in C_1 symmetry.[204,206] Results presented in this section were published together with Pausch in Ref. [82] and the discussion follows the structure and reasoning developed there.

17.1. Computational Details

The geometry of the water molecule was optimized in the absence of a magnetic field using DFT with the PBE functional and the def2-TZVP basis set. The molecular coordinates can be found in the supporting information of Ref. [82]. Results for the Berry curvature and related quantities were obtained using Hartree–Fock and the def2-TZVP basis set. Very tight convergence criteria were used for the SCF calculations, with the energy being converged up to $10^{-12}\,E_{\mathrm{h}}$ and the norm of the density matrix up to 10^{-12}. Linear response vectors were converged up to a norm of 10^{-10}.

17.2. Berry Curvature of the Water Molecule

The pseudomomentum-translational sum rule, given in eq. 6.12, states that the molecular Berry curvature summed over one nuclear index is equal to the geometry gradient of the pseudomomentum. Similarly, the magnetic-translational sum rule, given in eq. 6.11, states that the sum over both nuclear indices results in an antisymmetric 3×3 matrix containing the elements of the magnetic flux density vector times the number of electrons. Hence, to demonstrate these two sum rules, only the molecular Berry curvature and the atomic pseudomomentum tensor need to be calculated. All relevant quantities and their relation to each other is shown in figure 17.1.

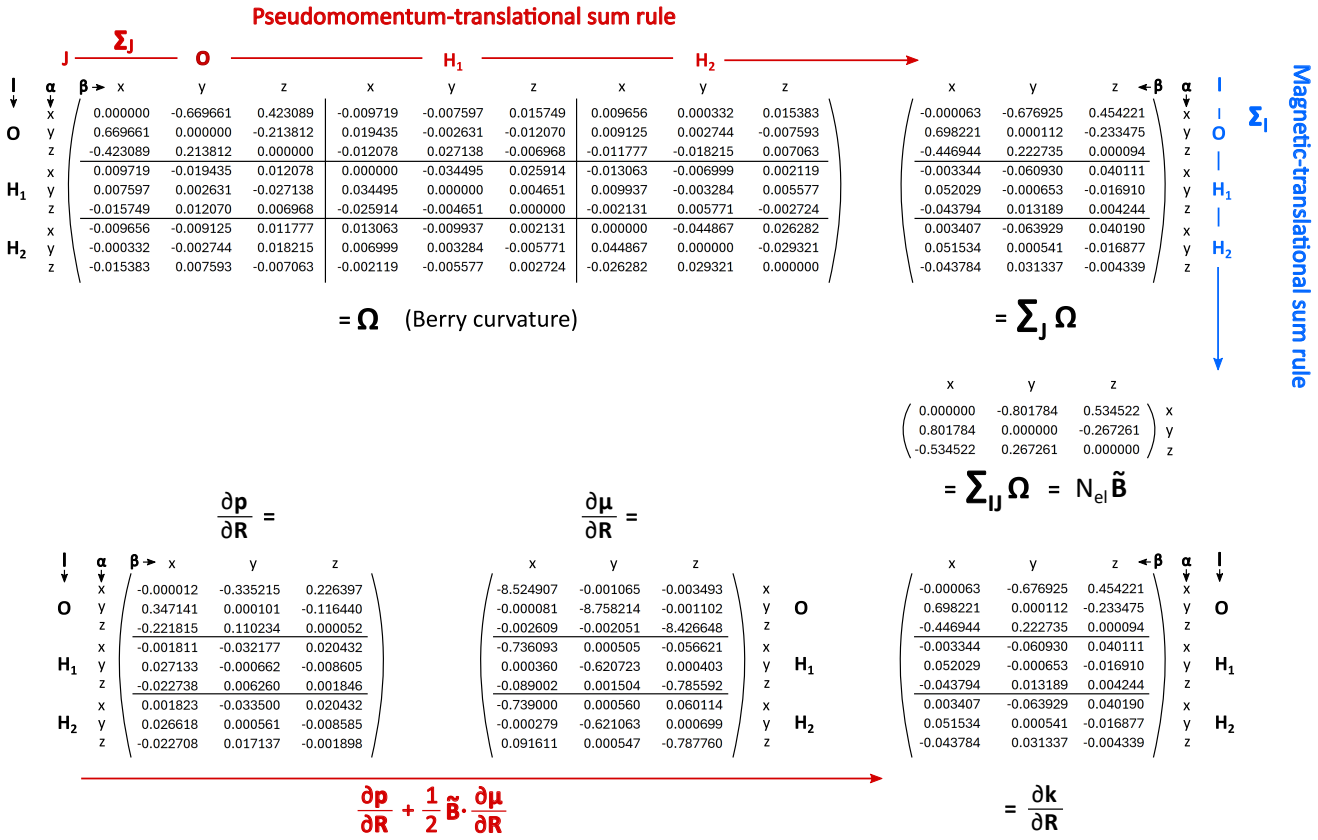

Figure 17.1.: Schematic representation of the molecular Berry curvature and the atomic pseudomomentum tensor, and how they relate to each other via the pseudomomentum-translational sum rule (shown in red). Additionally, by performing a second summation, their relation to the total number of electrons in the system and the magnetic flux density via the magnetic-translational sum rule (given in blue) is depicted. The system under investigation is the water molecule in a skew magnetic field, summation is always performed over one nuclear coordinate at a time. As a comparison, the nuclear derivative of the pseudomomentum tensor is calculated via its definition in eq. 6.13 from the gradient of the electric dipole moment and the canonical momentum. All sum rules shown here are fulfilled up to numerical precision. Reproduced from Ref. [82], licensed under CC BY.

The molecular Berry curvature of the water molecule is shown on the top left in figure 17.1. The red arrow on the top of the figure indicates that summation over the second nuclear index of the Berry curvature results in a $3 \times 3N_{\mathrm{nuc}}$ matrix, that is equal to the nuclear derivative of the electric pseudomomentum, according to the pseudomomentum-translational sum rule given in eq. 6.12. As a numerical validation, this quantity is additionally calculated from its definition in eq. 6.13. This computation is depicted on the bottom of figure 17.1. Here, the derivative of the canonical momentum is shown on the bottom left, with the derivative of the electric dipole moment next to it. From both of these quantities and the magnetic flux density, the derivative of the pseudomomentum is obtained and shown on the bottom right, as indicated by the accompanying red arrow. Evidently, this matrix is equal to the one obtained in the upper row of the figure. From here, summation over the remaining nuclear index is indicated by the blue arrow, to obtain the total number of electrons in the system $N_{\mathrm{el}} = 10$ scaled with the elements of the magnetic flux density vector. From the magnitude and direction of magnetic flux one obtains $\mathcal{B} \approx (0.026\,726\,1, 0.053\,452\,2, 0.080\,178\,4)^{\mathrm{T}}$. The latter relation is given by the magnetic-translational sum rule as first presented in Ref. [46].

18. Molecular Berry Curvature within Density Functional Theory

This section presents the application of Kohn-Sham current density functional theory to the Berry curvature. The necessary theory was laid out in section 9.4, where the coupled perturbed Kohn-Sham equations were shown. To investigate the inclusion of correlation effects on the Berry curvature, section 18.2 conducts a benchmark on the hydrogen molecule, where results from different approximate density functionals and from Hartree-Fock calculations are compared to results obtained from full-CI calculations of Ref. [81]. Next, the convergence of the Berry curvature with respect to the grid size used during the numerical integration of the exchange-correlation functional is presented in section 18.3. In section 18.4, Berry charges are revisited, where the electric dipole moment of furan is discussed. Results presented in this section were published together with Kronenberger, Appenzeller, and Pausch in Ref. [83] and the discussion follows the structure and reasoning developed therein.

18.1. Computational Details

The energy of restricted KSDFT calculations in section 18.2 has been converged to at least $10^{-14}\,E_\mathrm{h}$ and the norm of the density matrix up to 10^{-12}. Afterwards, the Berry curvature was calculated numerically from a finite difference scheme with a nuclear displacement of $10^{-3}\,\mathrm{a}_0$.[47,53] Spin unrestricted results were obtained with the analytical scheme presented in this work. Here, energies were converged up to $10^{-12}\,E_\mathrm{h}$, while the norm of the density matrix was converged up to 10^{-12}. The norm of the linear response vectors was converged to 10^{-9}. The magnetic flux density vector was oriented along the z-axis with a magnitude of $0.1\,B_0$ with the molecular bond axis along the x-axis. All calculations used the decontracted aug-cc-pVTZ basis set. The numerical integration of the exchange-correlation functional used the Turbomole grid 5.[199] Section 18.3 is concerned with the grid convergence using the decontracted cc-pVTZ basis and a magnetic flux density of $0.1\,B_0$. SCF energies were converged up to $10^{-8}\,E_\mathrm{h}$, the norm of the density matrix up to 10^{-8}, and the norm of the linear response vectors up to 10^{-7}. To investigate the convergence, grids of size 3, 4, and 5 were used.[199] Berry charges in section 18.4 have been calculated for a magnetic flux density of $10^{-4}\,B_0$ using the def2-TZVP basis set. SCF energies were converged up to $10^{-12}\,E_\mathrm{h}$, the norm of the density matrix up to 10^{-14}, and the norm of the linear response vectors up to 10^{-10}. For the numerical integration, Turbomole grid 5 was employed.

18.2. Benchmarking the DFT Berry Curvature of H_2

The first system under investigation for the molecular Berry curvature within the density functional theory framework is the hydrogen molecule. Recently, this system has been used to simulate rovibrational spectra in external magnetic fields.[54,55] Such studies were thus far only possible using the Hartree-Fock method.[47,48] In a related work, Culpitt *et al.* conducted a similar study applying the full configuration interaction method (full-CI) to the system.[81] There, they calculated non-adiabatic coupling matrix elements and the molecular Berry curvature for different electronic states of the hydrogen molecule. This section compares the molecular Berry curvature obtained for different DFT functionals with the full-CI reference values from Ref. [81]. It needs to be stressed, however, that even a calculation employing the exact exchange-correlation functional would not generally yield the exact Berry curvature as obtained from full-CI.[83] Still, it is likely that the DFT Berry curvature offers a general improvement of the results obtained from Hartree-Fock because the effects of correlation are taken into account. In the DFT calculations, the following approximate density functionals were used: The GGA functional PBE[144], the global hybrids PBE0[212] and B3LYP[146,225,226], and the range-separated hybrid CAM-B3LYP.[147] Additionally, the *m*GGA functional TASK[227] was used. Its implementation in the Libxc[228–230] library was used. Since the KS DFT reference wave function is still a single Slater determinant, expectation values for the $\hat{S}_z$ and $\hat{S}^2$ operators generally no longer correspond to those obtained for an eigenfunction. In contrast, the full-CI wave function is an exact eigenfunction to both of these operators. A general two-component spin-noncollinear approach also does not provide eigenfunctions to the spin operators. If the magnetic field axis is aligned with the Cartesian z-axis, additional constrains can be introduced to preserve certain symmetries.[179,231] By preserving the $\hat{S}_z$ symmetry, the unrestricted Kohn-Sham (UKS) solution is obtained. Analogously, the restricted Kohn-Sham (RKS) solution is recovered if $\hat{S}^2$ is also retained.[53,231] The RKS and UKS solutions for the hydrogen molecule are equivalent up to the Coulson–Fischer (CF) point.[232,233] The CF point is an avoided crossing of the spin states. There, the $\hat{S}^2$-expectation value is not continuously differentiable. For the hydrogen molecule, this corresponds to the so-called triplet instability, where the $\hat{S}^2$-expectation value of the lowest lying unrestricted solution stops being equal to zero. In Ref. [233] investigations of the Berry curvature without external fields have already been reported under such conditions.

The hydrogen molecule with its bond axis perpendicular to the magnetic field vector shows two non-redundant elements of the molecular Berry curvature. If the magnetic field vector is aligned with the z-axis, those elements are the Ω_{1x1y} and Ω_{1x2y} elements, where the indices 1 and 2 refer to the different hydrogen nuclei in the molecule. All other non-vanishing elements of the Berry curvature are either obtained from the point group symmetry of the system, being C_{2h},[204,206] or from the overall anti-symmetry of the Berry curvature $\Omega_{I\alpha J\beta} = -\Omega_{J\beta I\alpha}$. The pseudomomentum-translational sum rule in conjunction with the point group symmetry additionally relates these two Berry curvature elements to each other. For the remainder of this

discussion, most of the time the Berry curvature element per magnetic flux density is discussed. This quantity not only relates to atomic partial charges as discussed in section 16 but is also easier to handle, regardless of the magnetic field strength, since the numerical values will be larger.

18.2.1. Singlet State of the Hydrogen Molecule

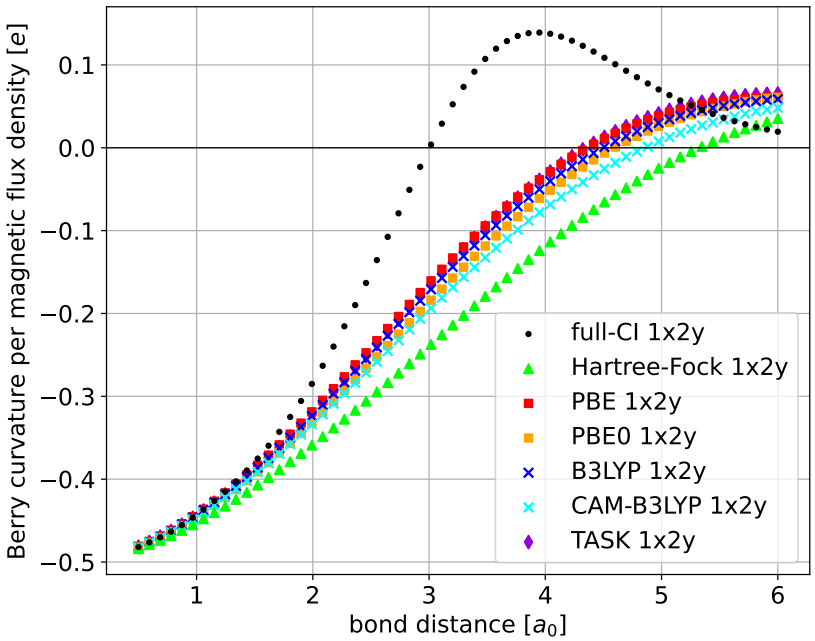

Figure 18.1.: The Ω_{1x2y} Berry curvature element per magnetic flux density of the hydrogen molecules perpendicular to the magnetic flux density vector with $|\mathcal{B}| = 0.1\,B_0$. Results show the lower RKS/RHF solution for different bond distances using the decontracted aug-cc-pVTZ basis set. Full-CI results were reproduced from J. Chem Phys. 161, 184109 (2024),[81] with the permission of AIP Publishing. This figure is reproduced from Ref. [83], licensed under CC BY.

Results for restricted calculations are shown in figure 18.1, where KSDFT calculations using the different functionals are shown as well as results from a Hartree-Fock calculation and the full-CI reference results from Ref. [81]. The full-CI values start off slightly above $-0.5\,e$ and steadily increase until crossing zero at approximately $3\,a_0$. Afterwards, the values continue to approach a maximum value of about $0.14\,e$ at just before $4\,a_0$, at which point the values decrease and start to approach zero. All KSDFT results are very close to each other, the choice of the functional does not seem to have a large influence on the Berry curvature. The DFT values also start

off around $-0.5\,e$ and steadily increase until they cross the zero-line significantly later, at around $4.5\,a_0$. The results then continue to increase and seemingly reach a maximum at some later point. The RHF values are qualitatively very similar to the KSDFT results but are consistently lower. Consequently, the deviation of the Hartree-Fock results is noticeably larger than the deviation between any of the functional approximations. Overall, neither single-determinant approach within a spin-restricted framework recovers the qualitative picture of the full-CI reference. Spin-unrestricted KSDFT and Hartree-Fock results are shown in figure 18.2, where

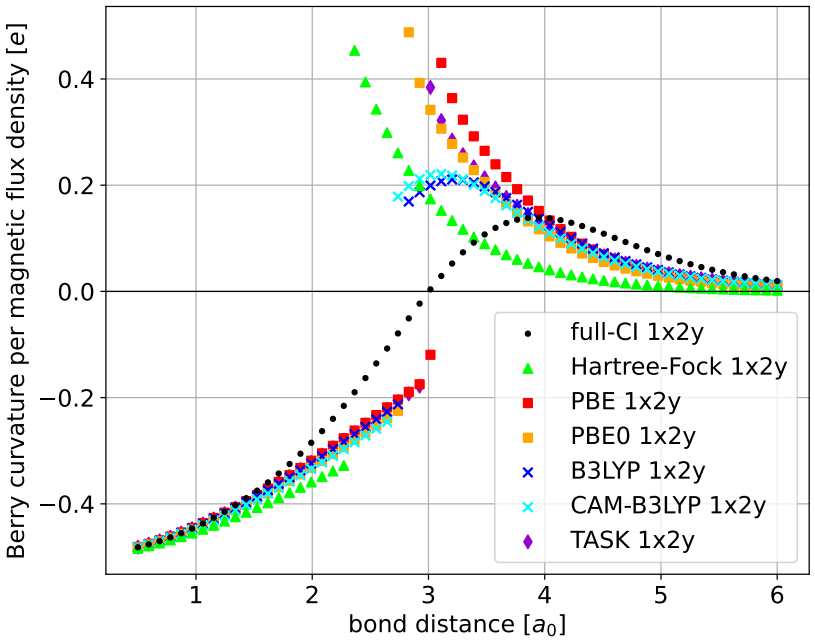

Figure 18.2.: The Ω_{1x2y} Berry curvature element per magnetic flux density of the hydrogen molecules perpendicular to the magnetic flux density vector with $|\mathcal{B}| = 0.1\,B_0$. Results shown of spin-unrestricted solutions for the lowest singlet state at different bond distances using the decontracted aug-cc-pVTZ basis set. Full-CI results were reproduced from J. Chem Phys. 161, 184109 (2024),[81] with the permission of AIP Publishing. This figure is reproduced from Ref. [83], licensed under CC BY.

the full-CI reference values are the same as in figure 18.1. As previously mentioned, for small bond distances, the UKS and UHF results are equivalent to those obtained from the spin-restricted methods. Strikingly, at some point between about $2.3\,a_0$ and $3.1\,a_0$, the Berry curvature exhibits a discontinuity. This point's exact locations, namely the CF point, depends on the underlying method or density functional. Here, the value of the Berry curvature jumps from below zero to somewhere above zero. After the discontinuity, the values decrease steadily and approach $0\,e$ in the

limit of large bond distances. Overall, the qualitative description of the dissociative limit is much better in the spin-unrestricted calculations compared to those of the spin-restricted calculations. The discontinuities found in figure 18.2 can generally be categorized into one of two general cases. In the first case, values after the discontinuity start off rather high at around $0.4\,e$ after which they decrease strictly monotonically. This group includes the Hartree-Fock results as well as the DFT results obtained from PBE, PBE0, and TASK. The second case involves the B3LYP and CAM-B3LYP functionals, where the values after the discontinuity start off just below $0.2\,e$. Afterwards, the values increase until they reach a maximum shortly after, only to then slowly converge towards $0\,e$.

To further investigate these discontinuities, one member of each of the aforementioned cases is now discussed in more detail. Results obtained from the UKS calculation employing the PBE0 functional can be found in figure 18.3. Alongside

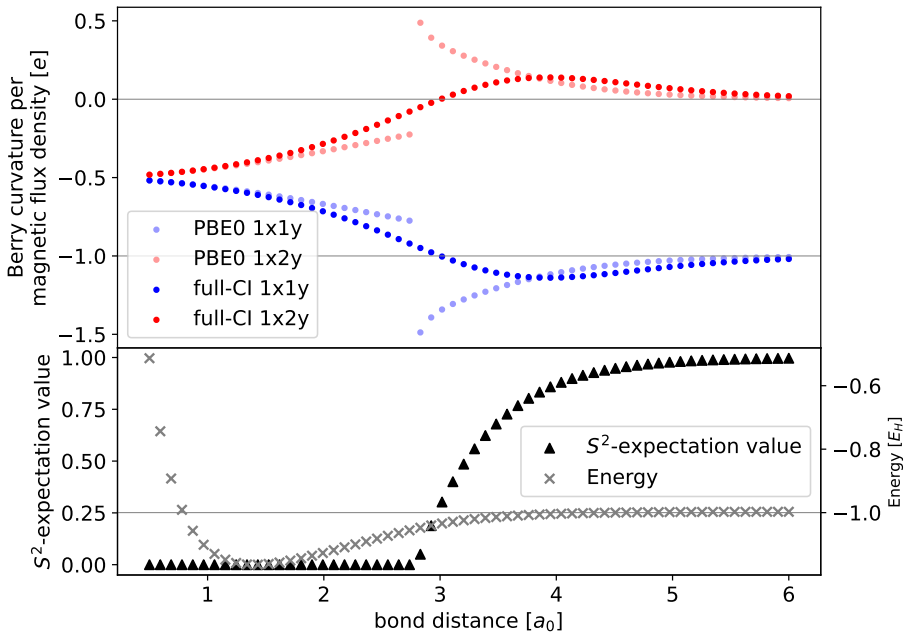

Figure 18.3.: Berry curvature elements Ω_{1x1y} and Ω_{1x2y} per magnetic flux density for the lowest energy singlet state of hydrogen perpendicular to the magnetic flux vector with $|\mathcal{B}| = 0.1\,B_0$. KSDFT results are obtained using the PBE0 functional. Full-CI reference values were reproduced from J. Chem Phys. 161, 184109 (2024),[81] with the permission of AIP Publishing. The lower part of the figure shows the electronic energy and $\hat{S}^2$-expectation value of the UKS calculation. All results used the decontracted aug-cc-pVTZ basis set. This figure is reproduced from Ref. [83], licensed under CC BY.

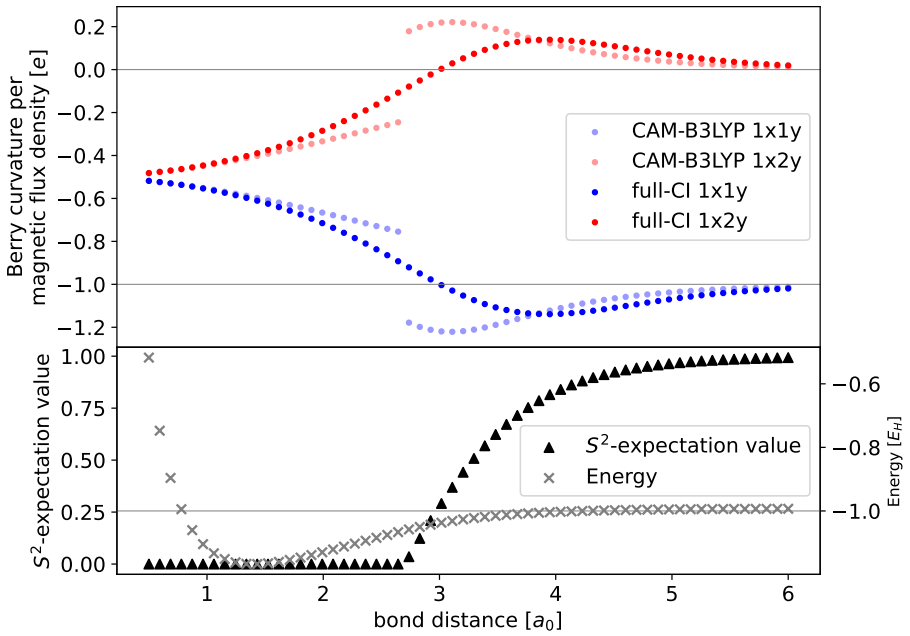

Figure 18.4.: Berry curvature elements Ω_{1x1y} and Ω_{1x2y} per magnetic flux density for the lowest energy singlet state of hydrogen perpendicular to the magnetic flux vector with $|\mathcal{B}| = 0.1\,B_0$. KSDFT results are obtained using the CAM-B3LYP functional. Full-CI reference values were reproduced from J. Chem Phys. 161, 184109 (2024),[81] with the permission of AIP Publishing. The lower part of the figure shows the electronic energy and $\hat{S}^2$-expectation value of the UKS calculation. All results used the decontracted aug-cc-pVTZ basis set. This figure is reproduced from Ref. [83], licensed under CC BY.

both non-redundant Berry curvature elements in the upper part of figure 18.3, the lower part also shows the electronic energy and the $\hat{S}^2$-expectation values from the KSDFT calculation. The electronic energy shows the expected behavior, at very low bond distances the energy is high and quickly decreases until it reaches a minimal value at the equilibrium distance of around $1.4\,a_0$. Afterwards, it steadily increases and converges towards the correct dissociative limit, where the energy of two individual hydrogen atoms is reached. Note that since this is the singlet state, or more precisely $\langle \hat{S}_z \rangle = 0$ in the case of the DFT calculation, the dissociation limit includes the Spin-Zeeman contribution from two opposing electronic spins. Therefore, the energy is similar to that of the zero-field. The $\hat{S}^2$-expectation values paint quite a different picture: For small bond distances $\hat{S}^2$ is strictly zero. At the CF point around $2.8\,a_0$, it suddenly jumps and starts to increase nearly linearly at first. After some time the rate of increase slows down progressively and the $\hat{S}^2$-expectation

value converges towards one. Precisely at the CF point, where the $\hat{S}^2$ function is not continuously differentiable, the discontinuity in the Berry curvature is observed. The cause of this jump in the Berry curvature is a sudden change of the character of the electronic state due to the symmetry breaking. Similar phenomena have already been reported in the literature for zero-field calculations.[233] Results from the spin-unrestricted KSDFT calculations using the CAM-B3LYP functional are visualized in figure 18.4. The general findings from the energy and $\hat{S}^2$-expectation value plots are equal to those for the PBE0 functional. Here, the CF point occurs in a similar region of about $2.7\,a_0$. Before the CF point is reached, the Berry curvature is in great agreement with the other single-determinant methods, as previously discussed. Beyond the CF point, however, the values start off at a magnitude slightly below $0.2\,e$. The values then reach a maximum of $0.22\,e$ at about $3\,a_0$. Finally, they slowly decrease towards $0\,e$ in a continuous fashion. Quantitative agreement with the full-CI reference is still not achieved, but a predominant feature is reproduced nonetheless. CAM-B3LYP and B3LYP results are the only ones that capture the local maximum of the Berry curvature. So far, no apparent reason for this features occurrence was found and is subject to further investigations.

18.2.2. Triplet State of the Hydrogen Molecule

Calculations on the triplet state of the hydrogen molecule perpendicular to the magnetic field can be found in figure 18.5. Reference values from full-CI calculations are again taken from Ref. [81]. In the KSDFT and HF calculations, the triplet state is characterized by $\langle \hat{S}_z \rangle = -1$ and $\langle \hat{S}^2 \rangle = 2$ at all points. Some Hartree–Fock and DFT calculations did not converge for the smallest few bond distances or converged to electronically excited states, therefore, these data points are omitted from the figure. Values from the HF calculations converged the furthest towards small bond distances and indicate that the general result in this region is in agreement with the full-CI reference. The Berry curvature per magnetic flux density seems to start off at $0\,e$ in the limit of decreasing bond distance. It then sharply increases until reaching a maximum in the region around $1.2\,a_0$, independent of the underlying method. The height of the maximum however, is dependent on the method. While the Hartree-Fock and TASK calculations overestimate the maximum value by up to $0.2\,e$, all other density functionals underestimate it. Additionally, all DFT calculations predict the maximum at slightly shorter bond distances than Hartree-Fock and the full-CI reference. Still, all methods show maximum values in the range of approximately $3.7 - 4.2\,e$. Considering the larger magnitude of the Berry curvature in this case compared to the singlet calculations, this is not too much of a deviation and agreement with the reference is observed. Before the maximum however, all DFT results lie above the full-CI values, whereas Hartree-Fock seems to slightly underestimate the Berry curvature with respect to the reference. After the maximum, all results sharply drop and consistently cross the x-axis around $2.3\,a_0$ with only small deviations. Dissociating the molecule further, all methods tend to be in quantitative agreement, as they slowly converge towards $-1\,e$. In summary, KSDFT seems to

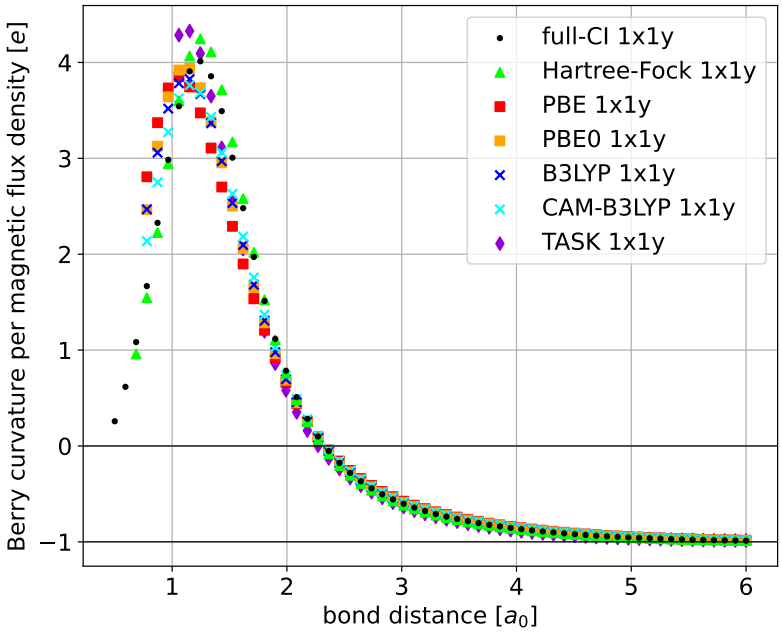

Figure 18.5.: The Ω_{1x1y} Berry curvature element per magnetic flux density of the hydrogen molecules perpendicular to the magnetic flux density vector with $|\mathcal{B}| = 0.1\,B_0$. Results shown of spin-unrestricted solutions for the lowest triplet state at different bond distances using the decontracted aug-cc-pVTZ basis set. Full-CI results were reproduced from J. Chem Phys. 161, 184109 (2024),[81] with the permission of AIP Publishing. This figure is reproduced from Ref. [83], licensed under CC BY.

provide a suitable description of the Berry curvature of the hydrogen molecule near the equilibrium geometry. Large displacements of the geometry can cause a discontinuity to occur in the Berry curvature if the Coulson–Fischer point is encountered. Before the CF point, RKS and UKS calculations result in the same electronic state and properties. While spin-restricted calculations do not show this discontinuity, the dissociation of the hydrogen molecule is not described correctly. On the other hand, spin-unrestricted calculations do reproduce the reference values better, except for the region around the CF point. Conversely, the lowest triplet state of the hydrogen molecule can be described appropriately by UKS and UHF calculations. While the absolute deviations for this system can be larger, the relative differences stay well-behaved, since the values of the Berry curvature reach overall larger values than in the singlet state. Exploratory calculations using the decontracted aug-cc-pVDZ, TZ, and QZ basis sets have been conducted but had no significant effect on the results presented in this section. An investigation of basis set size on the Berry curvature was presented in section 16.3. From there, the basis set effect can be estimated.

18.2.3. Impact of the Discontinuous Berry Curvature on Nuclear Forces

The molecular Berry curvature is essential in molecular dynamics simulations of molecules in external magnetic fields.[47,48,54] To estimate the impact that the discontinuity in the Berry curvature potentially has in these simulations, forces acting on the nuclei near the CF point are computed in this section. Calculations in this section are exclusively based on the PBE results shown in figure 18.2. Section 5 presented the derivation of the nuclear equation of motion in a semiclassical framework.[47,48] The final expression that was obtained for the force acting on one nucleus in the system was given in eq. 5.41. From there, eq. 5.42 identified three different contributions to the force: First, the gradient of the electronic energy within the Born-Oppenheimer approximation F_I^{BO}, which is only dependent on the geometry of the system. Second, the Lorentz force F_I^{L}, which is a classical force acting on moving charged particles in an external magnetic field. As such, it is dependent only on the charge and velocity of the given nucleus. Third, the Berry force F_I^{B}, which screens the Lorentz forces that act on the bare nuclear charge. The Berry force is dependent on the molecular geometry through the Berry curvature and couples the velocity of all nuclei in the molecule. To obtain an estimate of the latter two velocity-dependent forces, the velocity of each nucleus was assumed to be the most probable velocity given by the Maxwell-Boltzmann distribution.[234–236] For a free hydrogen atom this yields

$$v(T) = \sqrt{\frac{2k_bT}{m_{\mathrm{H}}}} \approx 5.8718 \cdot 10^{-5} \frac{a_0 E_{\mathrm{h}}}{\hbar} \cdot \sqrt{\frac{T}{K}}\,. \tag{18.1}$$

Bond distances for the following investigation are $3.02\,a_0$ and $3.11\,a_0$ which correspond to the data points just before and after the CF point. Since the Born-Oppenheimer force is independent of the velocity, the forces for both nuclei just before and beyond the CF point can be found in table 18.1. The molecular bond axis is aligned with the Cartesian x-axis, and the CF point is found significantly past the equilibrium distance of $1.43\,a_0$. Therefore, the BO forces only act along the x-axis and essentially pull the hydrogen nuclei together, since the singlet is a bound state. From the inversion symmetry of the system, one additionally obtains $F_{\mathrm{H}_1}^{\mathrm{BO}} = -F_{\mathrm{H}_2}^{\mathrm{BO}}$. As another consequence of the large displacement with respect to the equilibrium bond distance, the BO forces are large compared to the other contributions.

	before CF	beyond CF
$F_{x,\mathrm{H}_1}^{\mathrm{BO}}$	0.07507	0.06368
$F_{x,\mathrm{H}_2}^{\mathrm{BO}}$	-0.07507	-0.06368

Table 18.1.: Born-Oppenheimer forces acting on the hydrogen nuclei in the H_2 molecule with the bond axis along the x-direction and perpendicular to the magnetic field. Forces are given in atomic units $[E_{\mathrm{h}}/a_0]$. Reproduced from Ref. [83], licensed under CC BY.

The Berry curvature couples the velocity of all nuclei, which means that the direction of movement of one nucleus has a direct influence on the force acting on another nucleus. For this reason, in the following sections, three distinct types of molecular motion are considered. First, a uniform translation of the molecule along the y-axis. Second, a rotation with respect to the magnetic field axis. Third, a vibration where the nuclei move towards each other.

18.2.4. Translatory Molecular Motion

The translatory motion of hydrogen along the y-axis is considered in this subsection. The y-axis is perpendicular to the magnetic field and the bond axis. The velocities are assumed to be $v_{y,\mathrm{H}_1} = v_{y,\mathrm{H}_2} = v(T)$.

T in K	$v(T)$	$F^{\mathrm{L}}_{x,\mathrm{H}_1}$	$F^{\mathrm{B,\ before\ CF}}_{x,\mathrm{H}_1}$	$F^{\mathrm{B,\ after\ CF}}_{x,\mathrm{H}_1}$
100	0.000587	0.000059	-0.000059	-0.000059
500	0.001313	0.000131	-0.000131	-0.000131
1000	0.001857	0.000186	-0.000186	-0.000186

Table 18.2.: Nuclear velocity, Lorentz, and Berry forces during the translatory motion of the hydrogen molecule perpendicular to the magnetic field and bond axes for different temperatures before and after the Coulson–Fischer point. Forces given in $[E_\mathrm{h}/a_0]$. Reproduced from Ref. [83], licensed under CC BY.

All forces of interest are displayed in table 18.2 for three different temperatures. The table only provides forces acting on the first hydrogen nucleus, since the force on the other nucleus is trivially obtained from the symmetry of the system. This exact motion exhibits several special cases when looking at these quantities. First, since the magnetic field vector is aligned with the z-axis and the nuclear velocity is solely along the y-axis, the Lorentz forces only act in the x-direction, as dictated by the cross product. The magnitude of the Lorentz force is therefore simply given by the product of the nuclear charge, the magnetic flux density, and the velocity, yielding $|\mathbf{F}^{\mathrm{L}}_I| = Z_I|\mathcal{B}| \cdot v_I = 0.1 v_I$. A similar relation can be found for the Berry force, which also acts only along the x-axis. The general expression for the Berry force of the hydrogen molecule is

$$F^{\mathrm{B}}_{x,\mathrm{H}_1} = \Omega_{1x1y} v_{1y} + \Omega_{1x2y} v_{2y}\,. \tag{18.2}$$

Since the velocities of both nuclei are identical, the velocity can be taken out of the expression as a common factor. What remains is a sum of two Berry curvature elements that are related via the magnetic translational sum rule.[46] This sum rule dictates that the sum of these elements is equal to the magnetic flux density scaled with a partial charge on the respective atom. From the inversion symmetry of the system, it becomes apparent that both hydrogen nuclei have to share the two electrons in the system equally, resulting in a partial charge of $0\,e$. The Berry force

is then given as a scaled velocity according to

$$\begin{aligned} F^{\mathrm{B}}_{x,\mathrm{H}_1} &= (\Omega_{1x1y} + \Omega_{1x2y})v \\ &= -0.1v\,. \end{aligned} \tag{18.3}$$

Since all relations used to arrive at this expression are independent of the molecule's geometry, it holds true for the calculations before the CF point as well as after the CF point. Notably, the expression for the Berry force is almost equal to that of the Lorentz force, they only differ in their sign. This results in cancellation of both contributions, meaning the translation perpendicular to the magnetic fields and bond axes does not experience any deflecting velocity-dependent forces. Interestingly, the absolute value of the individual forces is this much smaller than that of the BO force, even for an elevated temperature of 1000 K.

18.2.5. Rotatory Molecular Motion

Next, the rotation of the hydrogen molecule with respect to the magnetic field vector is investigated. During this motion, the molecule remains in a plane that is perpendicular to the field vector. Results for the forces acting on the first nucleus at different temperatures are shown in table 18.3.

T in K	$v(T)$	$F^{\mathrm{L}}_{x,\mathrm{H}_1}$	$F^{\mathrm{B,\ before\ CF}}_{x,\mathrm{H}_1}$	$F^{\mathrm{B,\ after\ CF}}_{x,\mathrm{H}_1}$
100	0.000587	0.000059	-0.000045	-0.000109
500	0.001313	0.000131	-0.000100	-0.000244
1000	0.001857	0.000186	-0.000141	-0.000345

Table 18.3.: Nuclear velocity, Lorentz, and Berry forces during the rotation of the hydrogen molecule with respect to the magnetic field vector at temperatures before and beyond the Coulson–Fischer point. Forces given in $[E_\mathrm{h}/a_0]$. Reproduced from Ref. [83], licensed under CC BY.

The velocity of the nuclei was assumed to be $v_{y,\mathrm{H}_1} = -v_{y,\mathrm{H}_2} = v(T)$. Consequently, the Lorentz force acting on the first hydrogen nucleus is equal to the force during the translatory motion, as the respective velocities are identical. The general expression given in eq. 18.2 for the Berry force still holds true. Inserting the nuclear velocities of equal magnitude and differing sign yields

$$F^{\mathrm{B}}_{x,\mathrm{H}_1} = (\Omega_{1x1y} - \Omega_{1x2y})v\,. \tag{18.4}$$

Accordingly, the Berry force is directly depended on the difference of two Berry curvature elements. There is no analytic expression known that relates to this difference. Hence, the Berry forces before and beyond the CF point no longer easily relate to each other as well. Similarly to the translatory forces, the Berry force always shows a different sign than the Lorentz force. Before crossing the CF point, both forces are of comparable magnitude and nearly cancel each other. Beyond the

CF point, however, the Berry force is larger by a factor of nearly 2.5 compared to before the CF point. As a consequence, the sum of these two forces results in a much greater contribution. Still, it is several times smaller than the BO-force from table 18.1.

18.2.6. Vibratory Molecular Motion

The last kind of motion investigated in this section is what would be considered the molecular vibration in the absence of the magnetic field. In this case, the velocities are given as $v_{x,\mathrm{H}_1} = -v_{x,\mathrm{H}_2} = v(T)$ and are strictly aligned with the bond axis. Consequently, both Lorentz, and Berry force solely act along the y-axis. Resulting

T in K	$v(T)$	$F^{\mathrm{L}}_{y,\mathrm{H}_1}$	$F^{\mathrm{B,\ before\ CF}}_{y,\mathrm{H}_1}$	$F^{\mathrm{B,\ after\ CF}}_{y,\mathrm{H}_1}$
100	0.000587	-0.000059	0.000045	0.000109
500	0.001313	-0.000131	0.000100	0.000244
1000	0.001857	-0.000186	0.000141	0.000345

Table 18.4.: Nuclear velocity, Lorentz, and Berry forces during the vibration of the hydrogen molecule at temperatures before and after the Coulson-Fischer point. Forces given in $[E_\mathrm{h}/a_0]$. Reproduced from Ref. [83], licensed under CC BY.

velocities and forces are shown in table 18.4, notably, the absolute value of all forces is identical to those obtained for the rotation of the molecule, but with differing signs. For the Lorentz force, the change of sign is a direct consequence of the cross product of the nuclear velocity with the magnetic flux vector and the way the Cartesian axes are set up. For the Berry forces, a similar argument can be made. Since the non-vanishing velocities are now the x-components instead of the y-components, the respective Berry curvature elements responsible for the force acting on nucleus I are no longer $\Omega_{I\alpha J\beta}$ but $\Omega_{I\beta J\alpha}$. The high point group symmetry of the system together with the overall symmetry of the Berry curvature $\mathbf{\Omega}^\mathrm{T} = -\mathbf{\Omega}$ then results in the overall change in sign. Once again, these arguments are independent of the bond distance and therefore hold before and beyond the CF point. Consequently, the observations made for the rotation of the molecule are also applicable here.

In summary, the Born-Oppenheimer, Lorentz, and Berry forces for the hydrogen molecules have been calculated at two points close to but on different sides of the CF point. The three different modes of motion that were investigated here revealed that for reasonable temperatures, the combined Lorentz and Berry force, which always showed differing signs, were several orders of magnitudes smaller than the BO forces. Additionally, the CF point of this system is far away from the equilibrium distance and is therefore unlikely to be of significant relevance during a conventional MD simulation. Nevertheless, for certain motions, an increase by a factor of 2.5 was observed in the Berry force. If this observation is applicable to other systems

that show a CF point closer to the equilibrium geometry, there could be a more substantial effect on a potential MD simulation.

18.3. Grid Size Effects on the DFT Berry Curvature

A more practical deliberation to be made in the context of DFT calculations is about the dependence of the Berry curvature on the size of the grid that is employed for the numerical integration of the exchange-correlation contribution. It is well known from the literature that some functionals, particularly certain *m*GGAs need very large radial grids for convergence.[237]

18.3.1. Magnetic Translation Sum Rule

One quantity that can be indicative of the quality of the underlying integration grid is the integral over the whole electron density. Trivially, this should yield the number of electrons in the system in exact algebra. When a numerical integral scheme is applied, this is no longer necessarily true. Therefore, this section investigates the magnetic translational sum rule, which is easily related to the total number of electrons in the system as well. For a well converged Hartree-Fock calculation, the total number of electrons is recovered up to machine precision in this way. Hence, different TURBOMOLE grid sizes and different approximate density functionals are investigated about their deviation from the true number of electrons. The system to observe this dependence is the 2-aminopropan-2-ol molecule in a magnetic field with a flux density of $0.1\,B_0$. This molecule offers at least some different atomic species while somewhat resembling general small organic molecules.

	grid 3	grid 4	grid 5
B3LYP	−0.000 591	0.000 084	0.000 089
CAM-B3LYP	−0.000 653	0.000 045	0.000 052
PBE	0.000 196	0.000 848	0.000 762
PBE0	0.000 163	−0.000 021	−0.000 114
TPSS	0.028 272	0.001 306	−0.000 618
TPSSh	0.026 288	0.001 240	−0.000 591
ωb97m	−0.050 008	0.012 499	0.001 473

Table 18.5.: Total molecular charge of the 2-aminopropan-2-ol molecule with different DFT functionals and integration grids as predicted by the magnetic translational sum rule. All calculations used a decontracted cc-pVTZ basis set, results are shown in units of [*e*]. Reproduced from Ref. [83], licensed under CC BY.

The results of the DFT calculations using different functional/grid combinations can be found in table 18.5. It shows the total molecular charge of the system, calculated from the Berry curvature via the magnetic translational sum rule. The

2-aminopropan-2-ol molecule has a total of 42 electrons, adding the nuclear charge should results in exactly $0\,e$. Firstly, these results clearly show that larger grids generally lead to a more precise description of the total charge. Convergence of the GGA functionals that are shown (B3LYP, CAM-B3LPY, PBE, and PBE0) is rather quick. Especially, the B3LYP functional exhibits very fast convergence, with the absolute error in the calculation with grid 5 occurring in the fifth decimal place. Most notably, these functionals seemingly hit convergence with grid 4 already, since grid 5 offers small to no improvement. The cause of this apparent barrier are simply the convergence criteria of the underlying SCF calculations. Still, even the values obtained with the smallest grid offer acceptable accuracy. Next, the *m*GGA functionals TPSS and TPSSh show a much slower convergence with increasing grid size. Even starting off at the smallest grid, their error of around $0.03\,e$ is two order of magnitude larger than that of the GGA functionals. Another order of magnitude is gained from each increasing grid size. Their performance using grid 5 is comparable to that of the PBE family. The worst convergence performance of all is achieved by the ωb97m[238] functional. Calculations with the largest grid still produce an error of more than $0.001\,e$ which is one order of magnitude larger than the error of GGA functionals with the smallest grid. This observation is in agreement with similar investigations of the grid convergence of more recent *m*GGAs.[230,237]

18.3.2. Errors in the Berry Curvature

Another metric worth exploring to investigate how well results are converged with respect to the grid size are the individual elements of the Berry curvature. For this purpose, figure 18.6 shows the root mean square and mean absolute error of all Berry curvature elements of the 2-aminopropan-2-ol molecule when comparing two neighboring grid sizes.
Most observations of the previous section can be easily recognized in the figure again. It clearly shows that all functionals benefit from a larger grid, as the error decreases with increasing grid size in all cases. Additionally, one can see that the B3LYP functional family exhibits the smallest error for these grids, closely followed by the PBE family. The TPSS and TPSSh functionals show significantly larger errors, with the ωb97m functional evidently performing the worst. Notably, inclusion of exact Hartree–Fock exchange seems to play no role in the convergence behavior of the functional, no matter if a global or range-separated hybrid is used. Still, the poor convergence of these *m*GGAs is prominent.

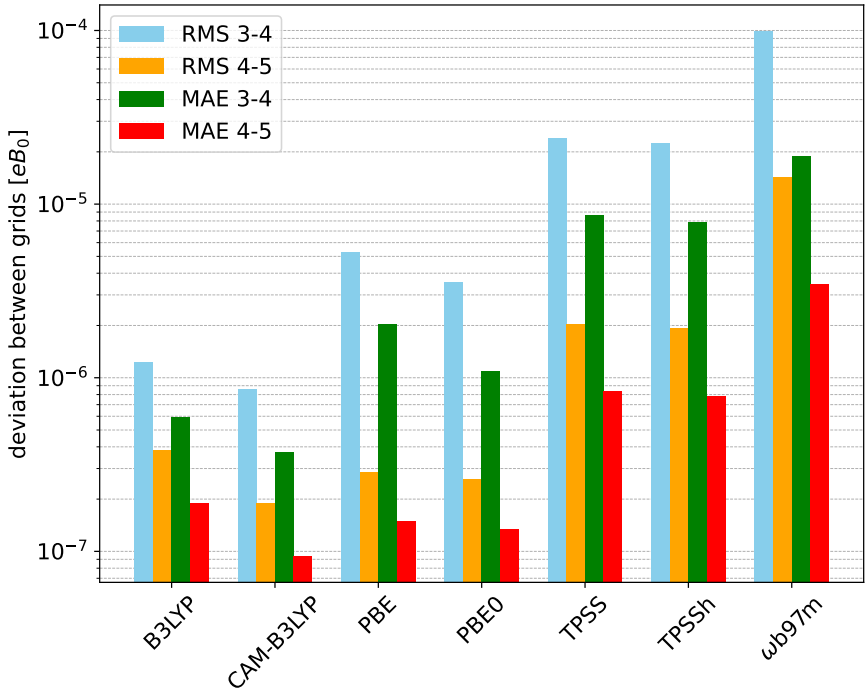

Figure 18.6.: Root mean square (RMS) and mean absolute error (MAE) of all Berry curvature elements of the 2-aminopropan-2-ol molecule between grid 3 and 4 and grid 4 and 5. All calculations used the decontracted cc-pVTZ basis set, results are shown in units of $[eB_0]$. Reproduced from Ref. [83], licensed under CC BY.

18.4. Berry Charges Revisited using DFT

This section revisits the investigations made in section 16.4, where Berry charges were calculated for furan, pyrrole, and thiophene. The Hartree–Fock results in that section exposed several shortcomings of Berry partial charges when describing molecular properties. This section aims at providing an insight into how this observation might change when DFT is employed as the method of choice instead. For this purpose, Berry charges of furan were calculated using different approximate density functionals, which were subsequently used to calculated the electric dipole moment of furan. The functionals used in this section include one LDA functional (SVWN), one pure GGA (PBE), two hybrid GGAs (PBE0, B3LYP), one pure *m*GGA (TPSS), as well as two range-separated hybrid functionals, one belonging to the GGA family (CAM-B3LYP), and another one of the *m*GGA family (MN12-SX).[239]
Results for the Berry partial charges are shown in table 18.6. Starting the discussion with the oxygen atom of furan, one can notice that Hartree-Fock predicts the largest negative charge which amounts to almost $-0.5\,e$. Conversely, all DFT functionals produce values in the range of about $-0.35\,e$ and $-0.43\,e$, resulting in a maximum

	HF	SVWN	PBE	PBE0	B3LYP	CAM-B3LYP	TPSS	MN12-SX
1O	−0.4978	−0.3778	−0.3739	−0.4100	−0.4093	−0.4253	−0.3916	−0.3557
2C	0.1582	0.0946	0.1098	0.1196	0.1233	0.1252	0.1202	0.1091
3C	−0.0719	−0.0911	−0.0706	−0.0767	−0.0691	−0.0790	−0.0601	−0.0641
2H	0.0909	0.0980	0.0792	0.0872	0.0817	0.0906	0.0740	0.0730
3H	0.0716	0.0874	0.0686	0.0749	0.0687	0.0759	0.0617	0.0598

Table 18.6.: Atomic Berry partial charges for furan, calculated using Hartree–Fock and different approximate DFT functionals. All calculations used the def2-TZVP basis set and a magnetic flux density of $10^{-4}\,B_0$. Results given in $[e]$. Reproduced from Ref. [83], licensed under CC BY.

difference of about $0.07\,e$ to the HF value. Meanwhile, the spread of the DFT values is of the same magnitude. This indicates that correlation effects play a significant role, while the exact choice of functional is of less importance. The smallest negative charge is predicted by the MN12-SX functional, which only shows a partial charge of around $-0.36\,e$ for the oxygen atom. The CAM-B3LYP functional on the other hand, produces the largest negative charge among the DFT functionals, which amounts to approximately $-0.43\,e$. A similar trend presents itself for the carbon atom neighboring the oxygen. For this 2C atom, Hartree-Fock predicts the largest charge of all methods. This time SVWN produces the smallest charge of $0.09\,e$, closely followed by MN12-SX and PBE. CAM-B3LYP is again closest to the HF results, differing by only around $0.04\,e$. The carbon atom that is furthest away from the oxygen, 3C, is predicted to show a charge that is close to neutral. All results reside in the range of $-0.06\,e$ to $-0.09\,e$. Likewise, the charge of all hydrogen atoms is shown to be small, with the largest charge of less than $0.1\,e$ that is produced by SVWN for the 3H nucleus.

	Density	Berry
HF	–0.7937	–2.1039
SVWN	–0.6094	–1.6867
PBE	–0.5564	–1.6279
PBE0	–0.6301	–1.7852
B3LYP	–0.6579	–1.7767
CAM-B3LYP	–0.6877	–1.8204
TPSS	–0.5890	–1.7100
MN12-SX	–0.3072	–1.4850

Table 18.7.: Electric dipole moment of furan, calculated from the electronic ground state density and in a classical fashion from the Berry partial charges provided in table 18.6. All calculations used the def2-TZVP basis set and a magnetic flux density of $10^{-4}\,B_0$. Results given in debye. Reproduced from Ref. [83], licensed under CC BY.

Just like in section 16.4, the electric dipole moment of furan was calculated. The results are given in table 18.7, where the dipole moments are computed via two different pathways: First, the electronic ground state density is used to calculate the corresponding expectation value. Second, Berry charges are used to calculate the dipole moment in a classical fashion according to eq. 16.5. As a reference, the experimentally obtained dipole moment of furan in the gas phase is reported to have an absolute value of 0.685 D in Ref. [240]. Overall, the electric dipoles calculated from the ground state density of any method show qualitative agreement with the experiment. The results of the PBE0, B3LYP, and CAM-B3LYP calculations even closely resemble the experimental value. The largest absolute value is again predicted by Hartree–Fock, which gives a dipole moment of almost −0.8 D and consequently overestimated the experimental value by about 15 %. The MN12-SX functional vastly underestimates the dipole moment, which amounts to slightly more than −0.3 D, resulting in an deviation of more than 55 %.

Conversely, all dipole moments based on the Berry partial charges completely fail to reproduce the experimental value or the expectation values obtained from the electron density. These results produce dipole moments that are larger by a factor of 2.5 to 3 with respect to those obtained from the density. Once again, Hartree–Fock predict the largest value with just more than −2.1 D. While the DFT results are closer to experiment, they are still wrong by a factor of around three. MN12-SX again produces the smallest absolute value of around −1.5 D, which still deviates from the experimental value by a factor of two.

In summary, Berry charges based on DFT results show a small improvement of the resulting electric dipole moments but still fail to reproduce the reference values. Therefore, this shortcoming of the Berry charges seems to be conceptual and cannot be traced back to the description of correlation effects.

19. Relativistic Berry curvature

All previous applications dealt with the molecular Berry curvature that emerged from an external magnetic field. However, it may also emerge from spin-orbit coupling,[103] which is often interpreted as an internal magnetic field of the molecule.[166,241,242] Heuristically, this is quite intuitive as spin-orbit effects act like $\hat{L} \cdot \hat{S}$, whereas the spin-Zeeman contribution is proportional to $\mathcal{B} \cdot \hat{S}$. Consequently, their effect on the electronic spin shows some similarities.[243] To start this discussion, the Berry curvature of simple systems is investigated in the following sections. All results presented were obtained in collaboration with Pausch and Franzke and presented in Ref. [244].

19.1. Computational Details

Calculations on the nitric oxide molecule used the generalized Hartree–Fock method with a def2-TZVP basis set. Results for the alanine molecule, metal atoms, and respective complexes were obtained using the x2c-SVPall basis set. These results used the X2C-Hamiltonian for relativistic calculations.

19.1.1. The Relativistic Nitric Oxide Molecule

The NO molecule is a radical and therefore shows an overall spin polarization in its electronic wave function. Two special cases can be considered, one where the spin polarization is aligned with the z-axis, and another one where it is aligned with the opposite direction, along the negative z-axis. Table 19.1 shows the non-redundant elements of the molecular Berry curvature for these two cases. The first case is depicted in table 19.1a, the Berry curvature elements of the diagonal block, $\mathrm{N}_x\mathrm{N}_y$ and $\mathrm{O}_x\mathrm{O}_y$, are identical and amount to approximately $-0.12\,eB_0$, while the off-diagonal element sits around $+0.12\,eB_0$. Results for the second case, with an opposing spin polarization, can be found in table 19.1b. Evidently, the absolute value of each element is equal to that of the first case, while all signs are different. The property that is responsible for the change in sign is that the wave functions of the two cases are related via the time-reversal operator. The Berry curvature of the time-reversed state is consequently given by the negative Berry curvature of the original state. As a comparison, the same molecule was calculated in a non-relativistic framework in an external field with a magnetic flux density of $4000\,\mathrm{T} \approx 0.017\,B_0$, these results are shown in table 19.2. The magnitude of flux density was chosen such that the Berry curvature elements are roughly in the same order of magnitude compared to those obtained from the relativistic calculations. Indeed, the off-diagonal element of the

element	$\boldsymbol{\Omega}$
N_xN_y	−0.122 96
N_xO_y	0.123 00
O_xO_y	−0.122 96

(a) Spin polarization along z-axis

element	$\boldsymbol{\Omega}$
N_xN_y	0.122 96
N_xO_y	−0.123 00
O_xO_y	0.122 96

(b) Spin polarization along negative z-axis

Table 19.1.: Non-redundant Berry curvature elements of the NO molecule calculated without external fields, using Hartree–Fock, the def2-TZVP basis set and the relativistic X2C Hamiltonian. Table 19.1a shows the results where the spin polarization of the electronic wave function are oriented along the z-axis, whereas table 19.1b shows results for the spin polarization along the negative z-axis. Values given in $[eB_0]$. Results reproduced from Ref. [244].

element	$\boldsymbol{\Omega}$
N_xN_y	0.052 07
N_xO_y	−0.170 31
O_xO_y	0.033 28

Table 19.2.: Non-redundant Berry curvature elements of the NO molecule in a non-relativistic calculation with a magnetic flux density of 4000 T along the z-axis. Values given in $[eB_0]$. Results reproduced from Ref. [244].

Berry curvature in the magnetic field amounts to around $-0.17\,eB_0$. The elements of the diagonal blocks of $0.05\,eB_0$ and $0.03\,eB_0$ however, are one magnitude smaller than their relativistic counterparts. Another important observation concerns the sign of the elements. With a magnetic flux density vector along the positive z-axis, the spin polarization is incentivized to align in an anti-parallel direction to the z-axis. Notably, the relativistic calculation with this spin-polarization in table 19.1b shows the same signs for all Berry curvature elements, further suggesting the similarity between spin-orbit coupling and an external magnetic field.

19.2. Metal-Alanine Complexes

Results for the NO molecule demonstrate that application of the time-reversal operator on the electronic wave function results in an overall change of sign in the Berry curvature. As a direct consequence, the Berry curvature for a wave function that is symmetric with respect to time reversal symmetry, must have a vanishing Berry curvature. Even in a one-determinant framework, this is fulfilled for systems that are classically closed shell. One example system is the deprotonated amino acid alanine. On the other hand, atomic systems in a relativistic calculation in the absence of external fields must also have a vanishing Berry curvature as dictated by

the magnetic translational sum rule. This must remain true even if the atom is an open shell system with a wave function that is not symmetric under time-reversal. Even though these two subsystems, the deprotonated alanine and a neutral open shell metal atom, exhibit a vanishing Berry curvature on their own, if they are brought together to interact, the total Berry curvature will generally not vanish.

system	$\|\boldsymbol{\Omega}\|$
$[AlaCu]^-$	0.35217
$[AlaAg]^-$	0.30816
$[AlaAu]^-$	0.33033

Table 19.3.: L^2-norm of the molecular Berry curvature of a complex between deprotonated alanine and the different coinage metal atoms. Calculations used Hartree–Fock, the x2c-SVPall basis set and the X2C relativistic Hamiltonian. The position of the metal atom with respect to the alanine anion is the same in all calculations. Values given in $[eB_0]$. Results reproduced from Ref. [244].

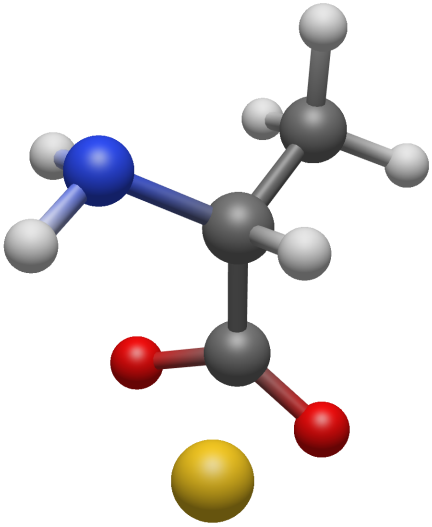

Figure 19.1.: Schematic depiction of the alanine coinage metal complexes of table 19.3. Hydrogen is white, carbon gray, nitrogen blue, oxygen red, and the metal is golden. Reproduced from Ref. [244].

Table 19.3 shows the norm of the molecular Berry curvature of different alanine coinage metal complexes. All calculations used the same geometry, shown in figure 19.1, where the metal atom coordinates to the carboxylate group of the alanine ion. While the magnitude of the spin-orbit coupling energy increases from copper to silver to gold, as their nuclear charges increase, the norm of the Berry curvature does not follow this trend. Instead, the largest Berry curvature norm occurs for the copper alanine complex, closely followed by the gold complex, and the silver complex with

the smallest norm. Still, all norms are very close together, with a deviation of less than $0.05\,eB_0$ between the copper and silver complexes. These results suggest that there is no correlation between the spin-orbit energy of a system and the magnitude of the molecular Berry curvature. A more thorough analysis should, however, be conducted in the future.

19.3. A Consistent Gauge-Covariant Berry Curvature

In relativistic open-shell systems, degenerate spin states give rise to non-Abelian Berry curvature,[14] which cannot be correctly described within a single-determinant framework.[233,245–247] In this context, the Berry curvature takes on a matrix form, to be more precise, a 2×2 matrix in the case of a doubly spin-degenerate state. Applying this to the example of the NO radical from section 19.1.1, the two different states with antiparallel spin-polarization are related by the time-reversal operator

$$\Psi_{\mathrm{SD}}^{\uparrow} = \hat{\mathcal{T}}\Psi_{\mathrm{SD}}^{\downarrow}\,. \tag{19.1}$$

Here the two different states in a one-determinant framework are denoted as $\Psi_{\mathrm{SD}}^{\uparrow}$ and $\Psi_{\mathrm{SD}}^{\downarrow}$. It is important to note that a single Slater determinant is only an approximation to the exact electronic wave function, which would not break time reversal symmetry. The application of the time reversal on the Berry curvature evidently results in a flipping of the overall sign

$$\hat{\mathcal{T}}\boldsymbol{\Omega}\hat{\mathcal{T}}^{-1} = -\boldsymbol{\Omega}\,. \tag{19.2}$$

To capture the whole picture and incorporate the rotation of the spin polarization with the SU(2) symmetry group, the non-abelian Berry curvature would additionally include the cross elements between the two different states, resulting in

$$\begin{pmatrix} \boldsymbol{\Omega}^{\uparrow\uparrow} & \boldsymbol{\Omega}^{\uparrow\downarrow} \\ \boldsymbol{\Omega}^{\downarrow\uparrow} & \boldsymbol{\Omega}^{\downarrow\downarrow} \end{pmatrix}, \tag{19.3}$$

where the following identities relate the different components:

$$\boldsymbol{\Omega}^{\uparrow\uparrow} = -\boldsymbol{\Omega}^{\downarrow\downarrow} \tag{19.4}$$

$$\boldsymbol{\Omega}^{\uparrow\downarrow} = -(\boldsymbol{\Omega}^{\downarrow\uparrow})^{\dagger} \tag{19.5}$$

The implementation of the remaining off-diagonal elements of the non-abelian Berry curvature should be considered in the future to obtain a consistent description of the Berry curvature with respect to the whole spin manifold. The non-abelian Berry curvature is gauge-covariant with respect to spin rotations, whereas the abelian Berry curvature is gauge-invariant.[14,50,245,246,248] Hence, results previously shown for the NO molecules, and the coinage metal complexes are gauge-dependent. Therefore, caution is needed when interpreting these results.

In summary, the molecular Berry curvature is dependent on the spin-polarization of the system. If two states are related to each other by the time-reversal operator,

their abelian Berry curvature only differs in the overall sign. Additionally, the combination of subsystems that both exhibit a vanishing Berry curvature, such as a metal atom and an amino acid, can still have a substantial Berry curvature of its own. Furthermore, the magnitude of the molecular Berry curvature does not seems to correlate with the magnitude of the spin-orbit coupling energy. An extension to the non-abelian Berry curvature is needed for a gauge-covariant description of these relativistic systems.

20. Relativistic DBOC

The diagonal Born-Oppenheimer correction was presented within a quantum geometrical context in section 2 and was also identified in the semiclassical derivation of the nuclear equation of motion in section 5. In the Born-Oppenheimer approximation it originates from the nuclear kinetic energy operator acting on the electronic wave function, and can therefore be calculated as a correction to the electronic energy that goes beyond the BO approximation. While the DBOC is usually small compared to the electronic BO energy, it is important for the accurate prediction of thermochemical properties if the regime of $1\,\mathrm{kJ\,mol^{-1}}$ precision is supposed to be reached.[249] Hence, the DBOC has been investigated with respect to many different aspects in the literature already: To include electron correlation effects, the DBOC has been calculated in the DFT framework[250] and using post-Hartree–Fock methods like coupled cluster or configuration interaction.[251,252] Perturbative approaches like Møller-Plesset theory have also been applied to the DBOC with great success.[253] Additionally, investigations on the basis set convergence of the DBOC have been conducted[254] as well as calculations in external magnetic fields.[43] This section deals with the DBOC in a relativistic framework. Ref. [255] already cast the DBOC into a scalar relativistic framework, where Imafuku *et al.* investigated the effects on bond distances, vibrational frequencies, the heat of formation, inversion barriers, and excitation energies. Together with Hamm, Pausch, Franzke, Harding, and Klopper, the effects of spin-orbit coupling on the DBOC have recently been investigated and are presented in the following sections.

20.1. Computational Details

Calculations on the HEAT test set in section 20.3 were calculated using Hartree–Fock with a relativistic X2C Hamiltonian and a dyall-av3z basis set.[256–258] Molecular geometries were taken from Ref. [249] where they were optimized at the CCSD(T)/cc-pVQZ level of theory. The DBOC requires nuclear masses, which were calculated from the atomic masses retrieved from the NIST database[259] subtracted by the rest mass of the electron from CODATA[260] times the total number of electrons of the corresponding atom. SCF energies for all molecules were converged up to at least $10^{-12}\,E_\mathrm{h}$, the norm of the density matrix at least up to 10^{-12}, and the norm of the linear response vector at least of to 10^{-10}. For the scalar relativistic calculations, the wave function was optimized in a one-component calculation using the `dscf` module, the molecule's orbital coefficients were subsequently expanded to a two-component wave function. Then, the DBOC was calculated using the two-component implementation discussed in this work, where all spin-orbit contributions were set to

zero.

Results for the hydrogen halides in section 20.2 were also obtained from Hartree–Fock calculations. All-electron non-relativistic, scalar relativistic, and SOC relativistic calculations used the decontracted ANO-RCC basis set.[261,262] Calculations using effective core potential (ECPs) used the def2-QZVPP basis set and the corresponding ECP basis.[210,263,264] SCF energies were converged up to $10^{-14}\,E_\mathrm{h}$, the density matrix up to a norm of 10^{-14}, and the linear response vectors up to a norm of 10^{-12}.

20.2. Potential Energy Curve of the Hydrogen Halides

This section is concerned with the DBOC of the hydrogen halides HX, with X being F, Cl, Br, I, or At and how it changes for different interatomic distances. All calculations in this section were done while including four different degrees of relativistic effects: First, a non-relativistic RHF calculation, denoted as "non rel.". Second, a RHF calculation including scalar relativistic effective core potentials, denoted as "ECP scalar rel.". Third, an all electron scalar relativistic calculation denoted as "scalar rel.". Fourth, a relativistic calculation including spin-orbit coupling, denotes as "SOC rel.". Notably, with the basis sets employed in this section, only the atoms I and At actually have ECPs. Therefore, ECP scalar rel. simply means the use of a standard, in this case def2-QZVPP, basis set for the lighter hydrogen halides. Consequently, the difference in non rel. and scalar rel. calculations on for example the HF molecule solely stems from the different basis sets used in these calculations.

The DBOC contribution to the atomization energy of the hydrogen halides is plotted against the interatomic distance in figure 20.1. The bond distance intervals for each system are chosen such that the equilibrium distance of the molecule for each degree of relativity is close to the middle of the plot. The individual equilibrium distances can be found in table 20.1. These results are not the focus of this section but are still summarized here. For HF, HCl, and HBr, close to no effect from the relativistic effects on the bond distance is observed, with the largest difference occurring between the ECP relativistic and scalar relativistic calculations on HBr, which only amounts to about $0.005\,a_0$ or less than 0.3 pm. As mentioned, the only difference between these two calculations is the basis set, consequently this is a pure basis set effect which is seemingly larger than any relativistic effect. For the heavier hydrogen halides, bigger differences can be observed. Here, the largest difference is found between the ECP and SOC relativistic calculations and is approximately $0.055\,a_0$ or close to 3 pm. Evidently, these small deviations hardly matter for the plots shown in figure 20.1. For the curves of HF, HCl, and HBr the individual relativistic description barely results in a notable difference in the DBOC contribution to the atomization energy. The largest deviations are found for the HBr molecule for very large or small interatomic distances, where the SOC relativistic calculations results in a slightly larger DBOC contribution than the other three methods. This overall result is expected, as relativistic effects do not yet play an incredibly important role. Especially the influence of relativity on the DBOC seems to be almost negligible.

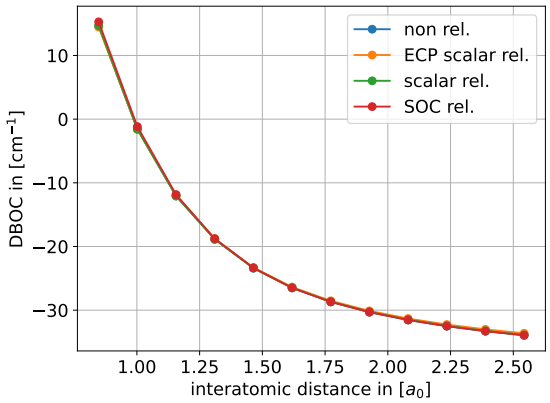

(a) Results for HF

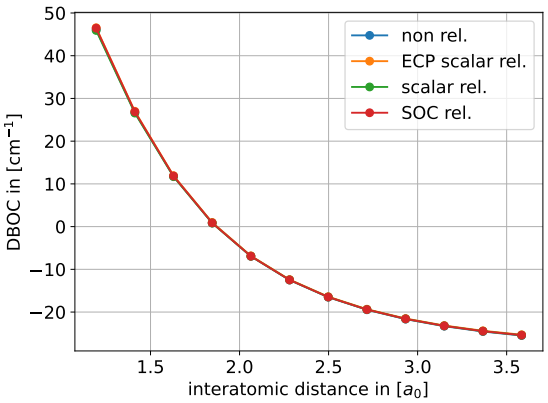

(b) Results for HCl

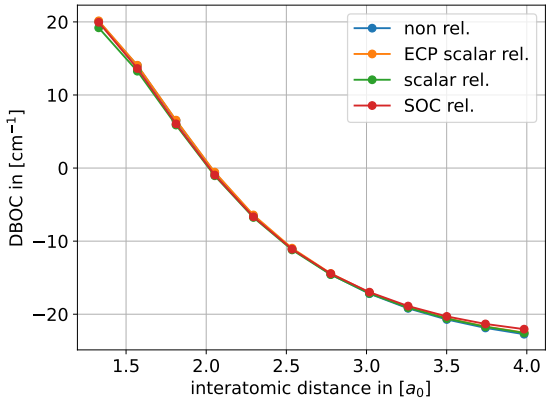

(c) Results for HBr

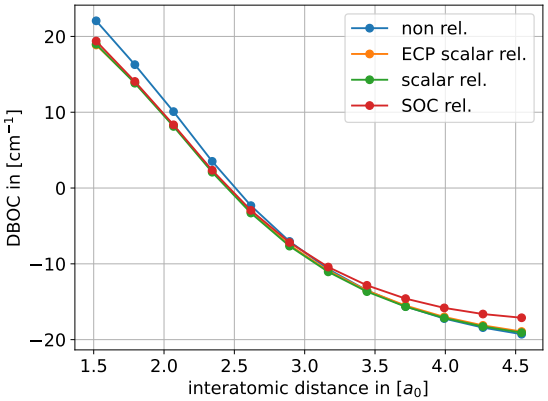

(d) Results for HI

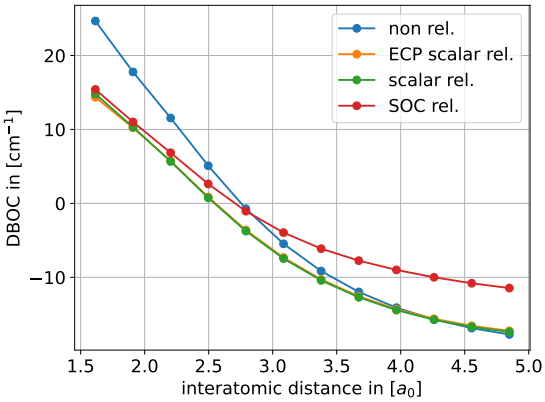

(e) Results for HAt

Figure 20.1.: DBOC contribution to the atomization energy of different hydrogen halides in [cm^{-1}]. Calculations are obtained using Hartree–Fock and included different degrees of relativistic effects: An all electron non-relativistic calculation (non rel.), an ECP scalar relativistic one (ECP scalar rel.), an all electron scalar relativistic one (scalar rel.), and a relativistic calculation including spin-orbit coupling (SOC rel.). The interatomic distance is chosen such that the equilibrium distance of all methods is close to the middle point of the interval.

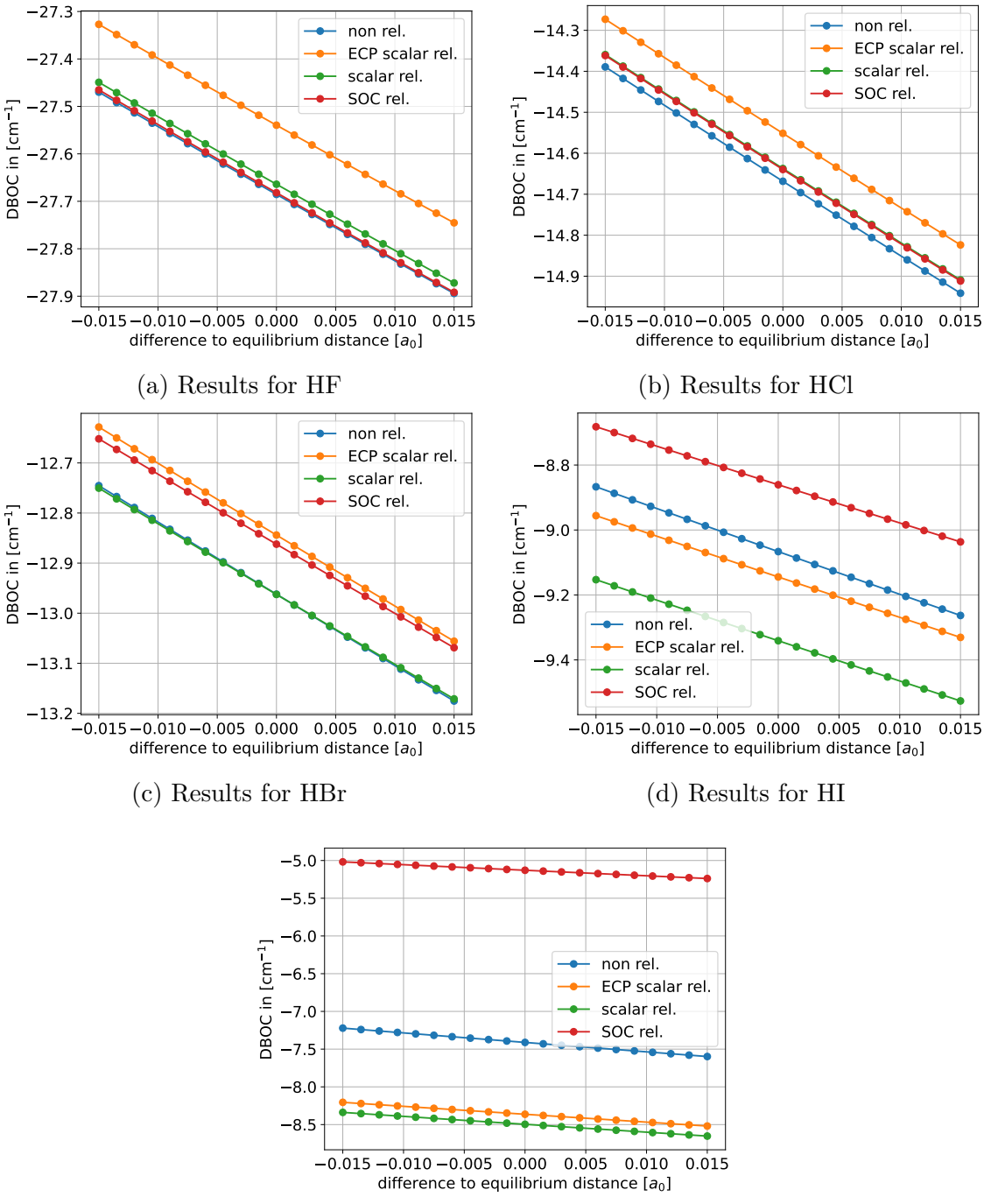

(a) Results for HF

(b) Results for HCl

(c) Results for HBr

(d) Results for HI

(e) Results for HAt

Figure 20.2.: DBOC contribution to the atomization energy of different hydrogen halides in [cm^{-1}]. The results offer a zoomed-in view of the values in figure 20.1 around each individual equilibrium distance.

Another consequence of the great agreement of the different methods is that the difference between the def2-QZVPP and the decontracted ANO-RCC basis set are similarly small for the DBOC. Evidently, both basis sets describe the DBOC of these systems equally well. The first more notable deviations occur for the HI molecule, where the non relativistic results differ from those obtained from any relativistic description. Near an interatomic distance of about $1.52\,a_0$, the deviation to the relativistic methods is in the range of $3 - 4\,\mathrm{cm}^{-1}$. For large bond distances, the SOC relativistic description shows a deviation from all remaining methods. For a bond distances of around $4.54\,a_0$ this deviation amounts to approximately $2\,\mathrm{cm}^{-1}$. A much more pronounced difference between the methods is observed for the HAt molecule, where most curves can be clearly distinguished from each other. The only exception might be the results from the ECP scalar relativistic and all-electron scalar relativistic calculations, which are in quantitative agreement. The largest difference between these two curves occurs for the smallest bond distance that was considered of about $1.62\,a_0$ and amounts to only $0.44\,\mathrm{cm}^{-1}$, further stressing the consistency between the two methods. Looking at the other methods applied to the HAt molecules, the observed trends are similar to those of the HI molecule: For small bond distances, the SOC relativistic calculations generally agrees with both scalar relativistic ones, while the non relativistic calculation shows the largest deviation amounting to almost $10\,\mathrm{cm}^{-1}$. Conversely, for large interatomic distances, the scalar and non relativistic calculations agree with each other, whereas the SOC results differ. Here, a deviation of about $6\,\mathrm{cm}^{-1}$ can be found.

molecule	non rel.	ECP rel.	scalar rel.	SOC rel.
HF	1.6955	1.6952	1.6955	1.6955
HCl	2.3896	2.3891	2.3892	2.3893
HBr	2.6584	2.6586	2.6532	2.6541
HI	3.0351	3.0162	3.0194	3.0248
HAt	3.2301	3.1802	3.1809	3.2353

Table 20.1.: Equilibrium bond distances for the calculations on hydrogen halides shown in figures 20.1 and 20.2, values given in $[a_0]$.

Figure 20.2 offers a zoomed-in view of the atomization DBOC for the hydrogen halides. The region around the respective equilibrium bond distance according to each method is centered in each plot. Additionally, the overall interval shown only amounts to $0.03\,a_0$ in total. Reference [255] looked at similar regions of the DBOC to estimate its influence on bond distances and harmonic vibrational frequencies while including all-electron scalar relativistic effects. The results of figure 20.2 now expand this discussion with scalar relativistic results obtained from ECPs and with calculations including spin-orbit coupling. The most notable observation is that for each molecule, all methods show a linear trend with almost equal slopes. Consequently, the DBOC itself has close to no effect on harmonic frequencies. These observations have already been made in the literature[255] but are seemingly also

applicable to spin-orbit relativistic calculations. Generally, all methods are in very good agreement with each other in this small region around the equilibrium distance. Even for the HAt molecule, where the largest difference occurs between the SOC relativistic and scalar relativistic results, only a deviation of about $3.5\,\mathrm{cm}^{-1}$ can be observed.

In summary, spin-orbit effects on the atomization DBOC of the hydrogen halides has the largest effect for bond distances that are notably larger than the equilibrium bond distance. These effects however are very small for any system investigated here besides HI and HAt. Near the equilibrium distance, all methods investigated in this work show very good agreement, even with the non relativistic calculations. Nevertheless, the main takeaway for practical calculations is about the use of ECPs. If a standard calculation on molecules with heavy atoms is carried out with ECPs, the current implementation makes it possible to subsequently calculate the DBOC without the need of reperforming an all-electron calculation. Especially for closed-shell molecules near their equilibrium bond distances, the results from this section suggest that the scalar relativistic ECP DBOC is in very good agreement with different other methods to include relativistic effects.

20.3. Relativistic DBOC of the HEAT Test Set

As previously mentioned, protocols for thermochemical calculations, such as the HEAT protocol,[249] require the inclusion of different corrections to achieve accuracies below $1\,\mathrm{kJ\,mol^{-1}} \approx 83.6\,\mathrm{cm^{-1}}$. Two individual quantities that are commonly used in such protocols are a correction for relativistic effects on the electronic energy as well as the non-relativistic DBOC. Ref. [255] already investigated the impact of relativity on the DBOC using a scalar relativistic framework and a focus on heavy atoms. This section explores how large the impact is on light open- and closed-shell molecules and if spin-orbit coupling results in a significant contribution on top of scalar relativistic ones. Table 20.2 shows results for the DBOC of the molecules in the HEAT test set. It contains the absolute DBOC of each system as well as the DBOC contribution to the atomization energy. Additionally, the molecules are ordered into three distinct groups: Atoms, closed shell molecules, and open-shell molecules. For each system, the DBOC was calculated in a non-relativistic framework, in a scalar relativistic one, and with the inclusion of spin-orbit coupling (SOC).

For the hydrogen atom, relativistic effects show almost no difference. Scalar relativistic effects increase the absolute DBOC by $0.01\,\mathrm{cm^{-1}}$. The slightly heavier first long-period atoms C, N, O, and F all show a small contribution from the scalar relativistic effects that increases with the nuclear charge. While the DBOC of the carbon atom increases by about $1\,\mathrm{cm^{-1}}$, the effect on the fluorine atom already amounts to $4\,\mathrm{cm^{-1}}$. SOC seemingly only has an effect on the flourine atom, were it further increases the DBOC by a minuscule $0.1\,\mathrm{cm^{-1}}$. The atomization contribution of the DBOC for atomic systems is not well defined and is therefore denoted as $0\,\mathrm{cm^{-1}}$. Results for the closed-shell molecules are comparable to those of the atoms. Scalar relativistic effects consistently results in an increase in the approximate range of $0 - 10\,\mathrm{cm^{-1}}$. To be more precise, the smallest effect is obtained for the hydrogen molecule, were scalar relativistic effects only result in an increase of $0.01\,\mathrm{cm^{-1}}$. The largest effect can be observed for the fluorine molecule and amounts to almost $8.3\,\mathrm{cm^{-1}}$. Most notably, these effects are consistent with the observed effects on the isolated atoms. This becomes evident when investigating the contribution to the atomization energy: There is almost no effect from scalar relativistic effects, the largest influence is observed for H_2O and is just shy of $0.03\,\mathrm{cm^{-1}}$. Including SOC in the calculation has an even smaller effect for these molecules. For the HNO molecule the largest effect on the absolute DBOC can be observed, which is still slightly smaller than $0.009\,\mathrm{cm^{-1}}$. Similarly, the effects of SOC on the atomization DBOC is generally small. An increase in absolute value of about $0.2\,\mathrm{cm^{-1}}$ can be observed for the HF molecule, whereas most other closed-shell molecules exhibit an even smaller effect.

Taking a look at the open-shell molecules in the lower part of table 20.2 reveals a somewhat different picture. Starting off with the absolute DBOC, scalar relativistic effects result in a very similar behavior compared to the closed-shell molecules. The largest effect occurs for the OF molecule and amounts to $7.3\,\mathrm{cm^{-1}}$. Several other molecules show effects of comparable size. For the atomization contribution, this

	DBOC			atomization DBOC		
Molecule	non rel.	scalar rel.	SOC rel.	non rel.	scalar rel.	SOC rel.
H	59.76	59.77	59.77	0.00	0.00	0.00
C	364.27	365.47	365.47	0.00	0.00	0.00
N	440.11	442.08	442.08	0.00	0.00	0.00
O	519.26	522.27	522.27	0.00	0.00	0.00
F	568.76	572.90	573.00	0.00	0.00	0.00
C_2H_2	806.48	808.82	808.83	−41.59	−41.67	−41.66
CO	877.80	882.00	882.00	−5.73	−5.75	−5.75
CO_2	1385.97	1393.18	1393.19	−16.82	−16.84	−16.83
F_2	1135.84	1144.12	1144.12	−1.68	−1.67	−1.88
H_2	101.17	101.18	101.18	−18.36	−18.36	−18.36
H_2O	595.00	598.05	598.06	−43.79	−43.76	−43.76
H_2O_2	1114.70	1120.80	1120.81	−43.35	−43.29	−43.28
HCN	838.32	841.46	841.47	−25.82	−25.86	−25.86
HF	600.37	604.54	604.54	−28.15	−28.13	−28.23
HNO	1038.72	1043.73	1043.72	19.59	19.61	19.60
N_2	873.88	877.81	877.81	−6.34	−6.35	−6.35
NH_3	572.91	574.91	574.92	−46.49	−46.48	−46.47
C_2H	777.02	779.40	794.06	−11.28	−11.32	3.35
CF	930.75	936.09	937.03	−2.28	−2.29	−1.45
CH	453.42	454.64	491.19	29.39	29.40	65.94
CH_2	473.05	474.24	492.00	−10.74	−10.78	6.98
CH_3	527.73	528.93	533.14	−15.82	−15.86	−11.65
CN	810.45	813.62	815.11	6.08	6.06	7.56
HCO	955.43	959.67	966.41	12.14	12.15	18.89
HO_2	1097.34	1103.41	1109.77	−0.94	−0.91	5.45
NH	517.29	519.28	535.07	17.41	17.43	33.22
NH_2	564.03	566.03	576.55	4.39	4.41	14.93
NO	999.72	1005.47	1006.33	40.35	41.11	41.97
O_2	1034.30	1040.33	1042.30	−4.22	−4.22	−2.25
OF	1090.03	1097.29	1097.90	2.01	2.11	2.62
OH	575.46	578.73	587.60	−3.56	−3.32	5.56

Table 20.2.: DBOC and the DBOC contribution to the atomization energy of the molecules in the HEAT test set, given in [cm^{-1}]. Calculations used the dyall-av3z basis set and the X2C Hamiltonian for scalar and spin-orbit relativistic calculations. Molecules are ordered into three groups: Atoms, closed-shell molecules, and open-shell molecules.

results in effects that are still consistently below $1\,\mathrm{cm}^{-1}$ and are consequently in agreement with the effects of the closed-shell molecules. If SOC is considered for the open-shell systems, results change more significantly. Addressing the most notable effects first, there is an increase of more than $36\,\mathrm{cm}^{-1}$ for the CH molecule. This is an erroneous result as it stems from a unphysical symmetry broken solution obtained from the two-component Hartree–Fock calculation. Expectation values of the spin operators reveal that the SCF procedure converged to a different state than the non-relativistic and scalar relativistic calculations: One obtains $\langle \hat{S}_z \rangle = 0.947$ and $\langle \hat{S}^2 \rangle = 2.16$. Conversely, the non-relativistic calculation produced $\langle \hat{S}_z \rangle = 1$ and $\langle \hat{S}^2 \rangle = 0.76$. Therefore, these values of the DBOC are not comparable. Ref. [176] provided a thorough report on the DBOC of the NO_2 molecule, where they varied the bond angle to observe what happens for wave functions that approach an electronic instability. There, they see a sharp increase of the DBOC near the instability, the DBOC diverges when reaching the conical intersection. This is similar to the divergence of the Berry curvature observed by Bian *et al.* in Ref. [233] at the Coulson–Fisher point, which is equivalent to an avoided crossing of spin states in H_2. The effect of SOC on the DBOC of the remaining open-shell molecules fall within more expected bounds, with the largest effect of almost $18\,\mathrm{cm}^{-1}$ for the CH_2 molecule. The SOC contribution of C_2H, NH, and NH_2 are of a similar magnitude and all above $10\,\mathrm{cm}^{-1}$. Comparable observations can be obtained from the atomization DBOC, where the SOC influence is generally on the same order of magnitude. The largest effect (with the exception of the CH molecule) is again found for CH_2 where it amounts to almost $18\,\mathrm{cm}^{-1}$. Several molecules show a SOC contribution to the atomization energy that is larger than $1\,\mathrm{cm}^{-1}$, namely C_2H, CH_2, CH_3, CN, HCO, HO_2, NH, NH_2, O_2, and OH.

In summary of this section, the effects of relativity on the atomization DBOC for the molecules of the HEAT test set is significantly smaller than its effect on the electronic atomization energy, which is in the order of magnitude of $10 - 100\,\mathrm{cm}^{-1}$ for the calculations presented here. In particular, the effect on the atomization of closed-shell molecules is almost negligible. Even for the absolute values of the DBOC the vast majority of the effect is already captured from scalar relativistic effects. In contrast, the effect on open-shell molecules is much more pronounced, especially for the atomization contribution. Here, the influence of spin-orbit relativistic effects is in the single-digit wave number range. Still, the calculation on the CH molecule showcases a shortcoming of the two-component framework without the use of any symmetry restraints, where fictitious electronic states can be found, from which the DBOC can not be obtained in a satisfactory manner.

Part V.

Conclusion and Outlook

21. Conclusion and Outlook

In recent years, quantum geometry has emerged as an increasingly important tool in quantum chemistry, particularly in the context of the Born-Oppenheimer approximation. Therein, nuclear coordinates as external parameters of the electronic wave function result in different quantum geometric quantities, such as the Berry curvature and the diagonal Born-Oppenheimer correction. The aim of this thesis was to further establish the quantum geometric framework in molecular electronic structure theory. This included the derivation of the molecular quantum geometric tensor and a thorough investigation of applications for molecular properties. The implementation of these quantities have been incorporated in the TURBOMOLE program suite. Most notably, the quantum geometry framework was extended to current density functional theory and applied to several molecular systems.

The theoretical section of this work derived the quantum geometric tensor. Starting at the discussion of a measure of quantum distance, the Fubini-Study metric was identified as the real part of the quantum geometric tensor. Afterwards, the Berry curvature was encountered as its imaginary part. The QGT was presented as the central quantity of this framework that encompasses all relevant properties, allowing for a description of beyond Born-Oppenheimer effects. These effects included the diagonal Born-Oppenheimer correction, and the motion of nuclei in external magnetic fields, demonstrating where the QGT can find applications in molecular systems.

To enable the efficient computation of the quantum geometric quantities, the already existing analytical linear-response framework of TURBOMOLE was extended. Consequently, efficient implementations of Hartree-Fock and current density functional theory can now be used for molecular quantum geometry in the context of external magnetic fields and relativistic effects.

Various applications highlighted the impact of quantum geometric quantities for molecules: The Berry curvature is needed for the qualitatively correct description of nuclear motion in magnetic fields, where it is responsible for screening the Lorentz-forces acting on the nuclei. Atomic partial charges were calculated based on the Berry curvature. Moreover, relativistic spin-orbit coupling effects were shown to have a substantial influence on the DBOC of open-shell molecules, even when no heavy elements are present.

In summary, this thesis applied established quantum chemical methods to quantum geometric quantities in complex two-component frameworks for relativistic calculations and external magnetic fields. Their efficient implementation in TURBOMOLE was presented. Subsequently, they were applied to a variety of systems to reveal underlying properties of these quantities and extend their applications to new systems.

Extensions of the work presented in this thesis can be made to many different aspects:

The implementation of the non-abelian Berry curvature was already mentioned in the respective application in section 19. To obtain a consistent, gauge-covariant Berry curvature, time-reversal symmetry needs to be explicitly taken into account. This leads to cross terms between electronic states that are related via the time-reversal operator. To achieve this, multireference methods such as complete active space configuration interaction (CAS-CI) need to be applied to molecular quantum geometry. In such a context, non-abelian extensions to the quantum geometry framework are required. Such an extension would also greatly increase the types of systems that can be investigated: The description of photochemical processes, conical intersections, and transition metal.

The application of the relativistic DBOC including spin-orbit coupling showed the largest effects for open-shell systems. So far, only open-shell systems containing light elements have been investigated. A detailed study of open-shell systems containing heavy elements is subject to further investigation. Systems of interest include organic radicals and aromatic systems, or open-shell metal compounds including transition metals or lanthanides. Furthermore, conditions where the Born-Oppenheimer approximation is known to fail should be investigated. These are fairly common in the vicinity of conical intersections or avoided crossings, as has been demonstrated in this work. A thorough investigation of reaction coordinates in photochemical processes and proton-transfer processes remains the subject of future work.

Implementations for external finite magnetic fields can be extended to a one-component formalism. While ground state calculations and numerical schemes are already available, the analytical linear-response formalism was only very recently implemented in Turbomole by Sinaga and is still limited to static polarizabilities. In this framework, restrictions on the electronic spin can be imposed, which allows to calculate different spin states, even at very high field strengths. In this way, the wave function of some formally excited state can be cleanly converged in the SCF procedure, which is commonly know as ΔSCF. Properties of these states become accessible as well and an extension to excited states within time-dependent perturbation theory offers an interesting direction, particularly in the context of spin-flip time-dependent DFT. The analytical calculation of non-adiabatic coupling matrix elements and the Berry curvature of excited states has so far received only very little attention.

Another, more general extension of molecular quantum geometry is concerned with incorporating other external parameters into the framework. This work primarily focused on the QGT where only nuclear coordinates were considered as parameters. Instead, an external electric or magnetic field can be included. The mixed QGT for nuclear coordinates and a magnetic field is relevant for vibrational circular dichroism, which then presents itself for an interesting application, where the relativistic framework can be applied.

List of Abbreviations and Acronyms

***m*GGA**	*meta* generalized gradient approximation
AO	atomic orbitals
APT	atomic polar tensor
asym	anti-symmetric
aug	augmented
B	Berry
BO	Born-Oppenheimer
CAS-CI	complete active space configuration interaction
CC	coupled cluster
cDFT	current density functional theory
CF	Coulson-Fischer
CI	configuration interaction
CPHF	coupled perturbed Hartree-Fock
CPKS	coupled perturbed Kohn-Sham
DBOC	diagonal Born-Oppenheimer correction
DFT	density functional theory
dia	diamagnetic
DIIS	direct inversion of the iterative subspace
ECP	effective core potential
eff	effective
el	electronic
eq	equation
GAPT	generalized atomic polar tensor

GGA	general gradient approximation
GIAO	gauge-including atomic orbital
GTO	Gaussian-type orbital
HF	Hartree-Fock
KS	Kohn-Sham
KSDFT	Kohn-Sham density functional theory
L	Lorentz
L	large component
LAO	London atomic orbital
LCAO	linear combination of atomic orbitals
LDA	local density approximation
MO	molecular orbital
mol	molecular
Mom	momentum
MP	Møller-Plesset
Mull	Mulliken
NACME	non-adiabatic coupling matrix element
nuc	nuclear
QGT	quantum geometric tensor
Ref	reference
rhs	right-hand side
RI-J	resolution of the identity approximation for the Coulomb integrals
RKS	restricted Kohn-Sham
rot	rotation
S	small component
SCF	self consistent field

SD	Slater determinant
SU(2)	special unitary group of second order
sub	subspace
sym	symmetric
tot	total
UHF	unrestricted Hartree-Fock
UKS	unrestricted Kohn-Sham
X2C	exact two-component
xc	exhange correlation

List of Figures

List of Tables

Permission to Print

This work contains material that was previously published in scientific journals. No permission was needed to be obtained to reuse the following material:

- Section 16 including all figures and tables therein. Section 17 and figure 17.1. Reproduced from *Novel pseudomomentum-translational sum rule for the molecular Berry curvature*, D. Steinmetz, A. Pausch, J. Chem. Phys. 2025, 162, 154109. Licensed under CC BY.
- Section 18 including all figures and tables therein. Reproduced from *The Berry curvature in the framework of current density functional theory for molecules in external magnetic fields*, M. L. Kronenberger, D. Steinmetz, A. Appenzeller, A. Pausch, J. Chem. Phys. 2025, 163, 224114. Licensed under CC BY.

The permission to use the following material in print and electronic form was obtained from the copyright holder:

- Parts of figures 18.1, 18.2, and 18.5. Reproduced from *Non-adiabatic coupling matrix elements in a magnetic field: Geometric gauge dependence and Berry phase*, T. Culpitt, E. I. Tellgren, L. D. M. Peters, T. J. Helgaker, J. Chem. Phys. 2024, 161, 184109.

List of Publications

1. *Novel pseudomomentum-translational sum rule for the molecular Berry curvature*
   D. Steinmetz, A. Pausch
   J. Chem. Phys. **2025**, *162*, 154109.
   DOI: 10.1063/5.0261461

2. *The Berry curvature in the framework of current density functional theory for molecules in external magnetic fields*
   M. L. Kronenberger, **D. Steinmetz**, A. Appenzeller, A. Pausch
   J. Chem. Phys. **2025**, *163*, 224114.
   DOI: 10.1063/5.0300324

Bibliography

(1) Arnold, V. I.; Vogtmann, K.; Weinstein, A., *Mathematical methods of classical mechanics*; Springer: 1989; Vol. 60.

(2) Berry, M. V. *Proc. R. Soc. Lond. A* **1984**, *392*, 45–57.

(3) Provost, J. P.; Vallee, G. *Commun. Math. Phys.* **1980**, *76*, 289–301.

(4) Kolodrubetz, M.; Sels, D.; Mehta, P.; Polkovnikov, A. *Phys. Rep.* **2017**, *697*, 1–87.

(5) Resta, R. *J. Phys.: Condens. Matter* **2000**, *12*, R107.

(6) Ehrenberg, W.; Siday, R. E. *Proc. Phys. Soc. B* **1949**, *62*, 8–21.

(7) Aharonov, Y.; Bohm, D. *Phys. Rev.* **1959**, *115*, 485.

(8) Chambers, R. *Phys. Rev. Lett.* **1960**, *5*, 3–5.

(9) Gianfrate, A.; Bleu, O.; Dominici, L.; Ardizzone, V.; De Giorgi, M.; Ballarini, D.; Lerario, G.; West, K. W.; Pfeiffer, L. N.; Solnyshkov, D. D.; Sanvitto, D.; Malpuech, G. *Nature* **2020**, *578*, 381–385.

(10) Tan, X.; Zhang, D.-W.; Yang, Z.; Chu, J.; Zhu, Y.-Q.; Li, D.; Yang, X.; Song, S.; Han, Z.; Li, Z.; Dong, Y.; Yu, H.-F.; Yan, H.; Zhu, S.-L.; Yu, Y. *Phys. Rev. Lett.* **2019**, *122*, 210401.

(11) Kang, M. et al. *Nat. Phys.* **2025**, *21*, 110–117.

(12) Page, D. N. *Phys. Rev. A* **1987**, *36*, 3479(R)–3481(R).

(13) Simon, B. *Phys. Rev. Lett.* **1983**, *51*, 2167–2170.

(14) Wilczek, F.; Zee, A. *Phys. Rev. Lett.* **1984**, *52*, 2111–2114.

(15) Anandan, J.; Aharonov, Y. *Phys. Rev. Lett.* **1990**, *65*, 1697–1700.

(16) Ma, Y.-Q.; Chen, S.; Fan, H.; Liu, W.-M. *Phys. Rev. B* **2010**, *81*, 245129.

(17) Xiao, D.; Chang, M.-C.; Niu, Q. *Rev. Mod. Phys.* **2010**, *82*, 1959–2007.

(18) Resta, R. *J. Chem. Phys.* **2023**, *158*, 024105.

(19) Requist, R.; Tandetzky, F.; Gross, E. K. U. *Phys. Rev. A* **2016**, *93*, 042108.

(20) Xie, Y.; Liu, R.; Gu, B. *Sci. Adv.* **2025**, *11*, eadz3711.

(21) Yu, J.; Bernevig, B. A.; Queiroz, R.; Rossi, E.; Törmä, P.; Yang, B.-J. *npj Quantum Mater.* **2025**, *10*, 101.

(22) Study, E. *Math. Ann.* **1905**, *60*, 321–378.

(23) Wootters, W. K. *Phys. Rev. D* **1981**, *23*, 357–362.

(24) Bianco, R.; Resta, R.; Souza, I. *Phys. Rev. B* **2014**, *90*, 125153.

(25) Tenasini, G.; Martino, E.; Ubrig, N.; Ghimire, N. J.; Berger, H.; Zaharko, O.; Wu, F.; Mitchell, J. F.; Martin, I.; Forró, L.; Morpurgo, A. F. *Phys. Rev. Res.* **2020**, *2*, 023051.

(26) Holder, T.; Kaplan, D.; Yan, B. *Phys. Rev. Res.* **2020**, *2*, 033100.

(27) Adak, P. C.; Sinha, S.; Agarwal, A.; Deshmukh, M. M. *Nat. Rev. Mater.* **2024**, *9*, 481–498.

(28) Resta, R. *Phys. Rev. B* **2026**, *113*, 125136.

(29) Bradlyn, B.; Elcoro, L.; Cano, J.; Vergniory, M. G.; Wang, Z.; Felser, C.; Aroyo, M. I.; Bernevig, B. A. *Nature* **2017**, *547*, 289–305.

(30) Lysne, M.; Schüler, M.; Werner, P. *Phys. Rev. Lett.* **2023**, *131*, 156901.

(31) Herzog-Arbeitman, J.; Peri, V.; Schindler, F.; Huber, S. D.; Bernevig, B. A. *Phys. Rev. Lett.* **2022**, *128*, 087002.

(32) Ahn, J.; Nagaosa, N. *Phys. Rev. B* **2021**, *104*, L100501.

(33) Peotta, S.; Törmä, P. *Nat. Commun.* **2015**, *6*, 8944.

(34) Hofmann, J. S.; Berg, E.; Chowdhury, D. *Phys. Rev. Lett.* **2023**, *130*, 226001.

(35) Born, M.; Oppenheimer, R. *Ann. Phys.* **1927**, *389*, 457–484.

(36) Born, M.; Huang, K., *Dynamical Theory of Crystal Lattices*; The International Series of Monographs on Physics; Clarendon Press: Oxford, 1954.

(37) Jensen, F., *Introduction to Computational Chemistry, 3rd Edition*; John Wiley & Sons: 2017.

(38) Kutzelnigg, W. *Mol. Phys.* **1997**, *90*, 909–916.

(39) Resta, R. *J. Chem. Phys.* **2025**, *162*, 234102.

(40) Smith, F. T. *Phys. Rev.* **1969**, *179*, 111–123.

(41) Baer, M. *Phys. Rep.* **2002**, *358*, 75–142.

(42) Martinazzo, R.; Burghardt, I. *J. Phys. Chem. Lett.* **2024**, *15*, 10416–10424.

(43) Culpitt, T.; Peters, L. D. M.; Tellgren, E. I.; Helgaker, T. *J. Chem. Phys.* **2022**, *156*, 044121.

(44) Schmelcher, P.; Cederbaum, L. S.; Meyer, H. D. *Phys. Rev. A* **1988**, *38*, 6066–6079.

(45) Ceresoli, D.; Tosatti, E. *Phys. Rev. Lett.* **2002**, *89*, 116402.

(46) Peters, L. D. M.; Culpitt, T.; Tellgren, E. I.; Helgaker, T. *J. Chem. Phys.* **2022**, *157*, 134108.

(47) Culpitt, T.; Peters, L. D. M.; Tellgren, E. I.; Helgaker, T. *J. Chem. Phys.* **2021**, *155*, 024104.

(48) Peters, L. D. M.; Culpitt, T.; Monzel, L.; Tellgren, E. I.; Helgaker, T. *J. Chem. Phys.* **2021**, *155*, 024105.

(49) Mead, C. A.; Truhlar, D. G. *J. Chem. Phys.* **1979**, *70*, 2284–2296.

(50) Mead, C. A. *Rev. Mod. Phys.* **1992**, *64*, 51–85.

(51) Kasper, J. M.; Jenkins, A. J.; Sun, S.; Li, X. *J. Chem. Phys.* **2020**, *153*, 090903.

(52) Kramers, H. A. *Proc. Acad. Amst.* **1930**, *33*, 61–65.

(53) Pausch, A. Development and application of efficient computational methods for molecular spectroscopy in finite magnetic fields, Ph.D. Thesis, Karlsruher Institut für Technologie (KIT), 2022.

(54) Monzel, L.; Pausch, A.; Peters, L. D. M.; Tellgren, E. I.; Helgaker, T.; Klopper, W. *J. Chem. Phys.* **2022**, *157*, 054106.

(55) Tellgren, E. I.; Culpitt, T.; Peters, L. D. M.; Helgaker, T. *J. Chem. Phys.* **2023**, *158*, 124124.

(56) Peters, L. D. M.; Tellgren, E. I.; Helgaker, T. *Mol. Phys.* **2024**, *122*, e2259008.

(57) Chang, M.-C.; Niu, Q. *J. Phys.: Condens. Matter* **2008**, *20*, 193202.

(58) Teh, H.-H.; Dou, W.; Subotnik, J. E. *Phys. Rev. B* **2021**, *104*, L201409.

(59) Gradhand, M.; Fedorov, D. V.; Pientka, F.; Zahn, P.; Mertig, I.; Györffy, B. L. *Phys. Rev. B* **2011**, *84*, 075113.

(60) Shushkov, P. *J. Chem. Phys.* **2024**, *160*, 164105.

(61) Nafie, L. A. *J. Phys. Chem. A* **2004**, *108*, 7222–7231.

(62) Stephens, P. J. *J. Phys. Chem.* **1985**, *89*, 748–752.

(63) Schimeczek, C.; Wunner, G. *Astrophys. J. Suppl. Ser.* **2014**, *212*, 26.

(64) Hollands, M. A.; Stopkowicz, S.; Kitsaras, M.-P.; Hampe, F.; Blaschke, S.; Hermes, J. J. *Mon. Not. R. Astron. Soc.* **2023**, *520*, 3560–3575.

(65) Pemberton, M. J.; Irons, T. J. P.; Helgaker, T.; Teale, A. M. *J. Chem. Phys.* **2022**, *156*, 204113.

(66) Blaschke, S.; Kitsaras, M.-P.; Stopkowicz, S. *Phys. Chem. Chem. Phys.* **2024**, *26*, 28828–28848.

(67) Lange, K. K.; Tellgren, E. I.; Hoffmann, M. R.; Helgaker, T. *Science* **2012**, *337*, 327–331.

(68) London, F. *J. Phys. Radium* **1937**, *8*, 397–409.

(69) Tellgren, E. I.; Soncini, A.; Helgaker, T. *J. Chem. Phys.* **2008**, *129*, 154114.

(70) Sun, S.; Williams-Young, D. B.; Stetina, T. F.; Li, X. *J. Chem. Theory Comput.* **2019**, *15*, 348–356.

(71) Pausch, A.; Klopper, W. *Mol. Phys.* **2020**, *118*, e1736675.

(72) Blaschke, S.; Stopkowicz, S.; Pausch, A. *J. Chem. Phys.* **2024**, *161*, 024117.

(73) Tellgren, E. I.; Teale, A. M.; Furness, J. W.; Lange, K. K.; Ekström, U.; Helgaker, T. *J. Chem. Phys.* **2014**, *140*, 034101.

(74) Irons, T. J. P.; David, G.; Teale, A. M. *J. Chem. Theory Comput.* **2021**, *17*, 2166–2185.

(75) Pausch, A.; Holzer, C. *J. Phys. Chem. Lett.* **2022**, *13*, 4335–4341.

(76) Holzer, C.; Pausch, A.; Klopper, W. *Front. Chem.* **2021**, *9*, 746162.

(77) Stopkowicz, S.; Gauss, J.; Lange, K. K.; Tellgren, E. I.; Helgaker, T. *J. Chem. Phys.* **2015**, *143*, 074110.

(78) Hampe, F.; Stopkowicz, S. *J. Chem. Phys.* **2017**, *146*, 154105.

(79) Kitsaras, M.-P.; Grazioli, L.; Stopkowicz, S. *J. Chem. Phys.* **2024**, *160*, 094112.

(80) Peters, L. D. M.; Culpitt, T.; Tellgren, E. I.; Helgaker, T. *J. Chem. Theory Comput.* **2023**, *19*, 1231–1242.

(81) Culpitt, T.; Tellgren, E. I.; Peters, L. D. M.; Helgaker, T. *J. Chem. Phys.* **2024**, *161*, 184109.

(82) Steinmetz, D.; Pausch, A. *J. Chem. Phys.* **2025**, *162*, 154109.

(83) Kronenberger, M. L.; Steinmetz, D.; Appenzeller, A.; Pausch, A. *J. Chem. Phys.* **2025**, *163*, 224114.

(84) Vignale, G.; Rasolt, M. *Phys. Rev. B* **1988**, *37*, 10685–10696.

(85) Holzer, C.; Franzke, Y. J.; Pausch, A. *J. Chem. Phys.* **2022**, *157*, 204102.

(86) Franzke, Y. J.; Pausch, A.; Holzer, C. *J. Chem. Phys.* **2025**, *162*, 084104.

(87) Balasubramani, S. G. et al. *J. Chem. Phys.* **2020**, *152*, 184107.

(88) Franzke, Y. J. et al. *J. Chem. Theory Comput.* **2023**, *19*, 6859–6890.

(89) Schrödinger, E. *Ann. Phys.* **1926**, *79*, 361–376.

(90) Schrödinger, E. *Ann. Phys.* **1926**, *385*, 437–490.

(91) Cheng, R. Quantum Geometric Tensor (Fubini-Study Metric) in Simple Quantum System: A pedagogical Introduction, 2013.

(92) Hartree, D. R. *Proc. Cambridge Philos. Soc.* **1928**, *24*, 89–110.

(93) Szabo, A.; Ostlund, N. S., *Modern quantum chemistry: introduction to advanced electronic structure theory*; Dover Publications, New York: 1996.

(94) Handy, N. C.; Yamaguchi, Y.; Schaefer III, H. F. *J. Chem. Phys.* **1986**, *84*, 4481–4484.

(95) Avron, J.; Herbst, I.; Simon, B. *Ann. Phys.* **1978**, *114*, 431–451.

(96) Herold, H.; Ruder, H.; Wunner, G. *J. Phys. B: At. Mol. Phys.* **1981**, *14*, 751.

(97) Johnson, B. R.; Hirschfelder, J. O.; Yang, K.-H. *Rev. Mod. Phys.* **1983**, *55*, 109–153.

(98) Schmelcher, P.; Cederbaum, L. S.; Meyer, H.-D. *J. Phys. B: At. Mol. Opt. Phys.* **1988**, *21*, L445.

(99) Reiher, M.; Wolf, A., *Relativistic Quantum Chemistry: The Fundamental Theory of Molecular Science*; John Wiley & Sons, Ltd: 2014.

(100) Ballhausen, C. J.; Hansen, A. E. *Annu. Rev. Phys. Chem.* **1972**, *23*, 15–38.

(101) Handy, N. C.; Lee, A. M. *Chem. Phys. Lett.* **1996**, *252*, 425–430.

(102) Ceresoli, D.; Marchetti, R.; Tosatti, E. *Phys. Rev. B* **2007**, *75*, 161101.

(103) Tao, Z.; Qiu, T.; Subotnik, J. E. *J. Phys. Chem. Lett.* **2023**, *14*, 770–778.

(104) Bian, X.; Tao, Z.; Wu, Y.; Rawlinson, J.; Littlejohn, R. G.; Subotnik, J. E. *Phys. Rev. B* **2023**, *108*, L220304.

(105) Lengsfield III, B. H.; Yarkony, D. R. In *State-Selected and State-to-State Ion–Molecule Reaction Dynamics, Part 2: Theory*, Baer, M., Ng, C.-Y., Eds.; Advances in Chemical Physics, Vol. 82; John Wiley & Sons: 1992, pp 1–71.

(106) Yarkony, D. R. *Chem. Rev.* **2012**, *112*, 481–498.

(107) Yarkony, D. R. *Rev. Mod. Phys.* **1996**, *68*, 985–1013.

(108) Barbatti, M. *WIREs Comput. Mol. Sci.* **2011**, *1*, 620–633.

(109) Mai, S.; Marquetand, P.; González, L. *WIREs Comput. Mol. Sci.* **2018**, *8*, e1370.

(110) Richardson, J. O.; Lawrence, J. E.; Mannouch, J. R. *Annu. Rev. Phys. Chem.* **2025**, *76*, 663–687.

(111) Ghamari, D.; Richardson, J. O. *J. Chem. Phys.* **2026**, *164*, 174101.

(112) Geuther, J. A.; Asnaashari, K.; Richardson, J. O. *J. Chem. Theory Comput.* **2025**, *21*, 2179–2188.

(113) Dirac, P. A. M. *Proc. R. Soc. Lond. A* **1928**, *117*, 610–624.

(114) Pauli, W. *Z. Phys.* **1927**, *43*, 601–623.

(115) Slater, J. C. *Phys. Rev.* **1929**, *34*, 1293–1322.

(116) Lennard-Jones, J. E. *Trans. Faraday Soc.* **1929**, *25*, 668–686.

(117) Mulliken, R. S. *Science* **1967**, *157*, 13–24.

(118) Kutzelnigg, W. *Angew. Chem., Int. Ed. Engl.* **1996**, *35*, 572–586.

(119) Roothaan, C. C. J. *Rev. Mod. Phys.* **1951**, *23*, 69–89.

(120) Boys, S. F. *Proc. R. Soc. Lond. A* **1950**, *200*, 542–554.

(121) Dunning Jr., T. H. *J. Chem. Phys.* **1970**, *53*, 2823–2833.

(122) Hampe, F. Accurate treatment of the electronic structure of atoms and molecules in strong magnetic fields, Ph.D. Thesis, Johannes Gutenberg-Universität Mainz, 2019.

(123) Schmelcher, P.; Cederbaum, L. S. *Phys. Rev. A* **1988**, *37*, 672–681.

(124) Ditchfield, R. *Mol. Phys.* **1974**, *27*, 789–807.

(125) Wolinski, K.; Hinton, J. F.; Pulay, P. *J. Am. Chem. Soc.* **1990**, *112*, 8251–8260.

(126) Fock, V. *Z. Phys.* **1930**, *61*, 126–148.

(127) Hall, G. G. *Proc. R. Soc. Lond. A* **1951**, *205*, 541–552.

(128) Hoffmann, R. *J. Chem. Phys.* **1963**, *39*, 1397–1412.

(129) Almlöf, J.; Faegri Jr., K.; Korsell, K. *J. Comput. Chem.* **1982**, *3*, 385–399.

(130) Van Lenthe, J. H.; Zwaans, R.; Van Dam, H. J. J.; Guest, M. F. *J. Comput. Chem.* **2006**, *27*, 926–932.

(131) Lehtola, S. *J. Chem. Theory Comput.* **2019**, *15*, 1593–1604.

(132) Pulay, P. *Chem. Phys. Lett.* **1980**, *73*, 393–398.

(133) Pulay, P. *J. Comput. Chem.* **1982**, *3*, 556–560.

(134) Baldes, A.; Klopper, W.; Šimunek, J.; Noga, J.; Weigend, F. *J. Comput. Chem.* **2011**, *32*, 3129–3134.

(135) Löwdin, P.-O. *Phys. Rev.* **1955**, *97*, 1509–1520.

(136) Helgaker, T.; Jørgensen, P.; Olsen, J., *Molecular Electronic-Structure Theory*; John Wiley & Sons, Ltd: 2000.

(137) Hohenberg, P.; Kohn, W. *Phys. Rev.* **1964**, *136*, B864–B871.

(138) Kohn, W.; Sham, L. J. *Phys. Rev.* **1965**, *140*, A1133–A1138.

(139) Burke, K. *J. Chem. Phys.* **2012**, *136*, 150901.

(140) Becke, A. D. *J. Chem. Phys.* **2014**, *140*, 18A301.

(141) Jones, R. O. *Rev. Mod. Phys.* **2015**, *87*, 897–923.

(142) Dirac, P. A. M. *Proc. Cambridge Philos. Soc.* **1930**, *26*, 376–385.

(143) Ceperley, D. M.; Alder, B. J. *Phys. Rev. Lett.* **1980**, *45*, 566–569.

(144) Perdew, J. P.; Burke, K.; Ernzerhof, M. *Phys. Rev. Lett.* **1996**, *77*, 3865–3868.

(145) Tao, J.; Perdew, J. P.; Staroverov, V. N.; Scuseria, G. E. *Phys. Rev. Lett.* **2003**, *91*, 146401.

(146) Becke, A. D. *J. Chem. Phys.* **1993**, *98*, 1372–1377.

(147) Yanai, T.; Tew, D. P.; Handy, N. C. *Chem. Phys. Lett.* **2004**, *393*, 51–57.

(148) Jaramillo, J.; Scuseria, G. E.; Ernzerhof, M. *J. Chem. Phys.* **2003**, *118*, 1068–1073.

(149) Grimme, S. *J. Chem. Phys.* **2006**, *124*, 034108.

(150) Desmarais, J. K.; Maul, J.; Civalleri, B.; Erba, A.; Vignale, G.; Pittalis, S. *Phys. Rev. Lett.* **2024**, *132*, 256401.

(151) Desmarais, J. K.; Erba, A.; Vignale, G.; Pittalis, S. *Phys. Rev. Lett.* **2025**, *134*, 106402.

(152) Vignale, G.; Rasolt, M. *Phys. Rev. Lett.* **1987**, *59*, 2360–2363.

(153) Vignale, G.; Rasolt, M.; Geldart, D. J. W. *Phys. Rev. B* **1988**, *37*, 2502.

(154) Becke, A. D. *J. Chem. Phys.* **1988**, *88*, 2547–2553.

(155) Einstein, A. *Ann. Phys.* **1905**, *323*, 639–641.

(156) Sucher, J. *Phys. Rev. A* **1980**, *22*, 348–362.

(157) Franzke, Y. Calculation of NMR Parameters in a Modern Relativistic Density Functional Framework: Theory, Implementation, and Application, Ph.D. Thesis, Karlsruher Institut für Technologie (KIT), 2021.

(158) Stanton, R. E.; Havriliak, S. *J. Chem. Phys.* **1984**, *81*, 1910–1918.

(159) Iliaš, M.; Saue, T. *J. Chem. Phys.* **2007**, *126*, 064102.

(160) Liu, W.; Peng, D. *J. Chem. Phys.* **2009**, *131*, 031104.

(161) Peng, D.; Reiher, M. *Theor. Chem. Acc.* **2012**, *131*, 1081.

(162) Kutzelnigg, W.; Liu, W. *J. Chem. Phys.* **2005**, *123*, 241102.

(163) Saue, T. *ChemPhysChem* **2011**, *12*, 3077–3094.

(164) Dyall, K. G. *J. Chem. Phys.* **1997**, *106*, 9618–9626.

(165) Sun, S.; Li, X. *J. Chem. Theory Comput.* **2020**, *16*, 4533–4542.

(166) Menges, B.; Huynh, B. C.; Visscher, L.; Pausch, A. *Theor. Chem. Acc.* **2026**, *145*, 43.

(167) Heully, J. L.; Lindgren, I.; Lindroth, E.; Lundqvist, S.; Martensson-Pendrill, A. M. *J. Phys. B: At. Mol. Phys.* **1986**, *19*, 2799.

(168) Peng, D.; Middendorf, N.; Weigend, F.; Reiher, M. *J. Chem. Phys.* **2013**, *138*, 184105.

(169) Franzke, Y. J.; Treß, R.; Pazdera, T. M.; Weigend, F. *Phys. Chem. Chem. Phys.* **2019**, *21*, 16658–16664.

(170) Franzke, Y. J.; Middendorf, N.; Weigend, F. *J. Chem. Phys.* **2018**, *148*, 104110.

(171) Pople, J. A.; Krishnan, R.; Schlegel, H. B.; Binkley, J. S. *Int. J. Quantum Chem.* **1979**, *16*, 225–241.

(172) Pulay, P. *Mol. Phys.* **1969**, *17*, 197–204.

(173) Brillouin, L. *J. Phys. Radium* **1932**, *3*, 373–389.

(174) Davidson, E. R. *J. Comput. Phys.* **1975**, *17*, 87–94.

(175) Casida, M. E. *J. Mol. Struct.:THEOCHEM* **2009**, *914*, 3–18.

(176) Thorpe, J. H.; Stanton, J. F. *Mol. Phys.* **2020**, *118*, e1742936.

(177) Olsen, J.; Jørgensen, P. *J. Chem. Phys.* **1985**, *82*, 3235–3264.

(178) Runge, E.; Gross, E. K. U. *Phys. Rev. Lett.* **1984**, *52*, 997–1000.

(179) Stuber, J. L.; Paldus, J. In *Fundamental World of Quantum Chemistry: A Tribute Volume to the Memory of Per-Olov Löwdin*, Brändas, E. J., Kryachko, E. S., Eds.; Kluwer Academic Publishers: Dordrecht, The Netherlands, 2003; Vol. 1, pp 67–139.

(180) Thouless, D. *Nucl. Phys.* **1960**, *21*, 225–232.

(181) Čížek, J.; Paldus, J. *J. Chem. Phys.* **1967**, *47*, 3976–3985.

(182) Vollhardt, K. P. C.; Schore, N. E., *Organische Chemie*; Wiley-VCH: 2020.

(183) Cioslowski, J. *J. Am. Chem. Soc.* **1989**, *111*, 8333–8336.

(184) Cioslowski, J. *Phys. Rev. Lett.* **1989**, *62*, 1469–1471.

(185) Cioslowski, J.; Hamilton, T.; Scuseria, G.; Hess, B. A. J.; Hu, J.; Schaad, L. J.; Dupuis, M. *J. Am. Chem. Soc.* **1990**, *112*, 4183–4186.

(186) Mulliken, R. S. *J. Chem. Phys.* **1955**, *23*, 1833–1840.

(187) Mulliken, R. S. *J. Chem. Phys.* **1962**, *36*, 3428–3439.

(188) Martin, F.; Zipse, H. *J. Comput. Chem.* **2005**, *26*, 97–105.

(189) North, S. C.; Jorgensen, K. R.; Pricetolstoy, J.; Wilson, A. K. *Front. Chem.* **2023**, *11*, 1152500.

(190) Cho, M.; Sylvetsky, N.; Eshafi, S.; Santra, G.; Efremenko, I.; Martin, J. M. L. *ChemPhysChem* **2020**, *21*, 688–696.

(191) Löwdin, P.-O. *J. Chem. Phys.* **1950**, *18*, 365–375.

(192) Baker, J. *Theor. Chim. Acta* **1985**, *68*, 221–229.

(193) Yin, L.; Mead, C. A. *Theor. Chim. Acta* **1992**, *82*, 397–406.

(194) Yin, L.; Mead, C. A. *J. Chem. Phys.* **1994**, *100*, 8125–8131.

(195) Schmelcher, P.; Cederbaum, L. S. *Int. J. Quantum Chem.* **1997**, *64*, 501–511.

(196) Kehry, M.; Franzke, Y. J.; Holzer, C.; Klopper, W. *Mol. Phys.* **2020**, *118*, e1755064.

(197) Frisch, M.; Head-Gordon, M.; Pople, J. *Chem. Phys.* **1990**, *141*, 189–196.

(198) Deglmann, P.; Furche, F.; Ahlrichs, R. *Chem. Phys. Lett.* **2002**, *362*, 511–518.

(199) Treutler, O.; Ahlrichs, R. *J. Chem. Phys.* **1995**, *102*, 346–354.

(200) Cheng, L.; Gauss, J. *J. Chem. Phys.* **2011**, *135*, 084114.

(201) Seeger, R.; Pople, J. A. *J. Chem. Phys.* **1977**, *66*, 3045–3050.

(202) Goings, J. J.; Ding, F.; Frisch, M. J.; Li, X. *J. Chem. Phys.* **2015**, *142*, 154109.

(203) Lehtola, S.; Blockhuys, F.; Van Alsenoy, C. *Molecules* **2020**, *25*, 1218.

(204) Pausch, A.; Gebele, M.; Klopper, W. *J. Chem. Phys.* **2021**, *155*, 201101.

(205) Woon, D. E.; Dunning Jr., T. H. *J. Chem. Phys.* **1994**, *100*, 2975–2988.

(206) Ceulemans, A. J., *Group Theory Applied to Chemistry*; Theoretical Chemistry and Computational Modelling; Springer: Dordrecht, 2013.

(207) Dunning Jr., T. H. *J. Chem. Phys.* **1989**, *90*, 1007–1023.

(208) Kendall, R. A.; Dunning Jr., T. H.; Harrison, R. J. *J. Chem. Phys.* **1992**, *96*, 6796–6806.

(209) Prascher, B. P.; Woon, D. E.; Peterson, K. A.; Dunning Jr., T. H.; Wilson, A. K. *Theor. Chem. Acc.* **2011**, *128*, 69–82.

(210) Weigend, F.; Ahlrichs, R. *Phys. Chem. Chem. Phys.* **2005**, *7*, 3297–3305.

(211) Weigend, F. *Phys. Chem. Chem. Phys.* **2006**, *8*, 1057–1065.

(212) Perdew, J. P.; Ernzerhof, M.; Burke, K. *J. Chem. Phys.* **1996**, *105*, 9982–9985.

(213) Singh, U. C.; Kollman, P. A. *J. Comput. Chem.* **1984**, *5*, 129–145.

(214) Besler, B. H.; Merz Jr., K. M.; Kollman, P. A. *J. Comput. Chem.* **1990**, *11*, 431–439.

(215) Grignard, V. *Compt. rend. Hebd. Séances Acad. Sci.* **1900**, *130*, 1322–1324.

(216) Seyferth, D. *Organometallics* **2009**, *28*, 1598–1605.

(217) Olah, G. A.; Rasul, G.; Yudin, A. K.; Burrichter, A.; Prakash, G. K. S.; Chistyakov, A. L.; Stankevich, I. V.; Akhrem, I. S.; Gambaryan, N. P.; Vol'pin, M. E. *J. Am. Chem. Soc.* **1996**, *118*, 1446–1451.

(218) Prochaska, F. T.; Andrews, L. *J. Am. Chem. Soc.* **1978**, *100*, 2102–2108.

(219) Krossing, I.; Bihlmeier, A.; Raabe, I.; Trapp, N. *Angew. Chem., Int. Ed.* **2003**, *42*, 1531–1534.

(220) Mercier, H. P. A.; Moran, M. D.; Schrobilgen, G. J.; Steinberg, C.; Suontamo, R. J. *J. Am. Chem. Soc.* **2004**, *126*, 5533–5548.

(221) Milani, A.; Castiglioni, C. *J. Mol. Struct.:THEOCHEM* **2010**, *955*, 158–164.

(222) Milani, A.; Castiglioni, C. *J. Phys. Chem. A* **2010**, *114*, 624–632.

(223) Dinur, U.; Hagler, A. T. *J. Chem. Phys.* **1989**, *91*, 2949–2958.

(224) Breitung, E. M.; Shu, C.-F.; McMahon, R. J. *J. Am. Chem. Soc.* **2000**, *122*, 1154–1160.

(225) Lee, C.; Yang, W.; Parr, R. G. *Phys. Rev. B* **1988**, *37*, 785–789.

(226) Stephens, P. J.; Devlin, F. J.; Chabalowski, C. F.; Frisch, M. J. *J. Phys. Chem.* **1994**, *98*, 11623–11627.

(227) Aschebrock, T.; Kümmel, S. *Phys. Rev. Res.* **2019**, *1*, 033082.

(228) Marques, M. A.; Oliveira, M. J.; Burnus, T. *Comput. Phys. Commun.* **2012**, *183*, 2272–2281.

(229) Lehtola, S.; Steigemann, C.; Oliveira, M. J.; Marques, M. A. *SoftwareX* **2018**, *7*, 1–5.

(230) Lehtola, S.; Marques, M. A. L. *J. Chem. Phys.* **2023**, *159*, 114116.

(231) Fukutome, H. *Int. J. Quantum Chem.* **1981**, *20*, 955–1065.

(232) Coulson, C.; Fischer, I. *Philos. Mag.* **1949**, *40*, 386–393.

(233) Bian, X.; Qiu, T.; Chen, J.; Subotnik, J. E. *J. Chem. Phys.* **2022**, *156*, 234107.

(234) Maxwell, J. C. *Philos. Mag.* **1860**, *19*, 19–32.

(235) Boltzmann, L. *Wiener Ber.* **1868**, *58*, 517–560.

(236) Rowlinson, J. S. *Mol. Phys.* **2005**, *103*, 2821–2828.

(237) Lehtola, S. *J. Chem. Theory Comput.* **2023**, *19*, 2502–2517.

(238) Mardirossian, N.; Head-Gordon, M. *J. Chem. Phys.* **2016**, *144*, 214110.

(239) Peverati, R.; Truhlar, D. G. *Phys. Chem. Chem. Phys.* **2012**, *14*, 16187–16191.

(240) Oh, J. J.; Hillig, K. W.; Kuczkowski, R. L.; Bohn, R. K. *J. Phys. Chem.* **1990**, *94*, 4453–4455.

(241) Manchon, A.; Koo, H. C.; Nitta, J.; Frolov, S. M.; Duine, R. A. *Nat. Mater.* **2015**, *14*, 871–882.

(242) Tokatly, I. V. *Phys. Rev. Lett.* **2008**, *101*, 106601.

(243) Winkler, R., *Spin–Orbit Coupling Effects in Two-Dimensional Electron and Hole Systems*; Springer: 2003.

(244) Pausch, A.; Steinmetz, D.; Franzke, Y. J. Effects of the Molecular Berry Curvature in Relativistic Systems, Talk at WATOC, Oslo, Norway, 2025.

(245) Van Horn, M.; Cheragwandi, T.; List, N. H. *ChemRxiv* **2025**, DOI: 10.26434/chemrxiv-2025-x3fr7.

(246) Van Horn, M.; Cheragwandi, T.; List, N. H. *ChemRxiv* **2025**, DOI: 10.26434/chemrxiv-2025-xdhvl.

(247) Sugawa, S.; Salces-Carcoba, F.; Yue, Y.; Putra, A.; Spielman, I. B. *npj Quantum Inf.* **2021**, *7*, 144.

(248) Johnsson, M. T. Time reversal symmetry and the geometric phase, Ph.D. Thesis, University of Canterbury, 1998.

(249) Tajti, A.; Szalay, P. G.; Császár, A. G.; Kállay, M.; Gauss, J.; Valeev, E. F.; Flowers, B. A.; Vázquez, J.; Stanton, J. F. *J. Chem. Phys.* **2004**, *121*, 11599–11613.

(250) Yixi, W.; Zhang, Y.; Liu, Y. *J. Phys. Chem. A* **2025**, *129*, 11713–11724.

(251) Valeev, E. F.; Sherrill, C. D. *J. Chem. Phys.* **2003**, *118*, 3921–3927.

(252) Gauss, J.; Tajti, A.; Kállay, M.; Stanton, J. F.; Szalay, P. G. *J. Chem. Phys.* **2006**, *125*, 144111.

(253) Tajti, A.; Szalay, P. G.; Gauss, J. *J. Chem. Phys.* **2007**, *127*, 014102.

(254) Karton, A. *J. Phys. Chem. A* **2025**, *129*, 5692–5699.

(255) Imafuku, Y.; Abe, M.; Schmidt, M. W.; Hada, M. *J. Phys. Chem. A* **2016**, *120*, 2150–2159.

(256) Dyall, K. G. *Theor. Chem. Acc.* **2012**, *131*, 1172.

(257) Dyall, K. G.; Tecmer, P.; Sunaga, A. *J. Chem. Theory Comput.* **2023**, *19*, 198–210.

(258) Dyall, K. G. Dyall dz, tz, and qz basis sets for relativistic electronic structure calculations, Zenodo: 2023.

(259) National Institute of Standards and Technology Atomic Weights and Isotopic Compositions, `https://physics.nist.gov/cgi-bin/Compositions/stand_alone.pl?ele=&all=all`, 2025.

(260) Tiesinga, E.; Mohr, P. J.; Newell, D. B.; Taylor, B. N. The 2022 CODATA Recommended Values of the Fundamental Physical Constants (Web Version 9.0), `https://physics.nist.gov/constants`, 2024.

(261) Roos, B. O.; Lindh, R.; Malmqvist, P.-Å.; Veryazov, V.; Widmark, P.-O. *J. Phys. Chem. A* **2004**, *108*, 2851–2858.

(262) Widmark, P.-O.; Malmqvist, P.-Å.; Roos, B. O. *Theor. Chim. Acta* **1990**, *77*, 291–306.

(263) Peterson, K. A.; Figgen, D.; Goll, E.; Stoll, H.; Dolg, M. *J. Chem. Phys.* **2003**, *119*, 11113–11123.

(264) Weigend, F.; Furche, F.; Ahlrichs, R. *J. Chem. Phys.* **2003**, *119*, 12753–12762.

Danksagung

Während einer Promotion begegnet man zahlreichen Menschen. Einigen von ihnen möchte ich hier namentlich danken:

Ich danke meinem Doktorvater, Prof. Dr. Wim Klopper, für die Möglichkeit in seinem Arbeitskreis zu promovieren. Dort habe ich mich immer wohl gefühlt und er hat eine wunderbare Umgebung zum Lernen und Arbeiten geschaffen. Ich danke ihm für die Freiheit bei der Wahl meiner Forschungsthemen sowie für ergiebige fachliche Diskussionen.. Außerdem danke ich Prof. Dr. Florian Weigend für seine Rolle als Zweitbetreuer dieser Arbeit sowie informative, aber auch gelegentlich erheiternde Gespräche.

Amber Pausch gebührt mein außerordentlicher Dank für die intensive Zusammenarbeit, die ausführlichen Anmerkungen zu meiner Forschung sowie die tatkräftige Hilfe bei der Implementierung und die Korrektur dieser Arbeit.

Es gibt nur wenige Tage an denen ich meiner Lebensabschnittsgefährtin, Jasmin Muuß, nicht dankbar bin. Ihre tägliche Unterstützung, nicht nur während meiner Promotion, ist ein maßgeblicher Teil meines Lebens. Außerdem danke ich ihr für die gewissenhafte Korrektur dieser ihr fachfremden Lektüre. Weiterhin bin ich meinen Eltern unendlich dankbar für ihren Beistand in allen Lebenslagen. Ebenso bin ich all meinen Freunden dankbar, die meine wissenschaftliche und persönliche Entwicklung in so bedeutendem Maße mitgeprägt haben.

Darüber hinaus gilt mein besonderer Dank der gesamten Gruppe für Theoretischen Chemie am KIT. Anja Appenzeller und Nina Rauwolf danke ich für ihre Gesellschaft, vor allem auf verschiedenen dienstlichen Reisen. Ganz ausdrücklich möchte ich noch Angela Bihlmeier, Sebastian Höfener und Michael Harding für diverse Diskussionen mit teilweise stark unterschiedlicher fachlicher Relevanz danken.

Ich durfte einige Studierende während verschiedener Exkurse in die theoretische Chemie begleiten. Für die gemeinsame Forschung und gelegentlichen Schabernack danke ich Maximilian Kronenberger, Adrian Ellinger, Falko Sinaga, Lukas Hamm und Fabian Hofmann. Max wurde seitdem einer meiner besten Freunde und ich freue mich stets über soziale Interaktionen mit ihm. Adrian danke ich ebenfalls für die Korrektur dieser Arbeit.

Ich danke dem Curry-Gladiator für eine ganz besonders unterhaltsame Mittagspause in der Mensa des KITs.

Ich danke dem Sonderforschungsbereich 4f for Future, bei dem ich assoziiertes Mitglied des integrierten Graduiertenkollegs war.

Zuletzt danke ich Michael Katz für den Druck dieses Dokuments und unzählige tagerhellende Besuche als Kunde in seinem Unternehmen.